Probing Molecular Mechanisms of Mycobacterium Pathogenesis in Bone Cells

by Artemis Emily Milne
BSc (Hons).

Doctoral Thesis
Submitted to The University of Warwick
for the degree of
Doctor of Philosophy
in Molecular Biomedicine

Supervisor: Dr. Meera Unnikrishnan (Warwick Medical School) and Dr. Amit Singhal (Infectious Diseases Labs (ID Labs), A*STAR)
Warwick Medical School
Date of submission: February 28th 2023

Table of Contents

"I was taught that the way of progress was neither swift nor easy."

— Marie Curie, physicist, chemist, and winner of the 1903 and 1911 Nobel Prize in Physics

I. List of Figures

II. List of Tables

III. Acknowledgments

I start by thanking my supervisors, Associate Professor Meera Unnikrishnan, and Dr. Amit Singhal, for their elite mentorship throughout my PhD journey. A special thank you to Dr. Meera Unnikrishnan for awarding me this opportunity and taking me under your wing.

I am thankful to my review panel members, Professor Nick Waterfield, Associate Professor John James, and Professor Laurent Renia for their advice and inspiration. My gratitude must also extend to my collaborators, without whom this project would not have been possible. Dr. Menaka Rajapakse, your bioinformatics assistance has been invaluable. Dr. Guillaume Remy of Warwick Manufacturing Group, thank you for collaborating with Warwick Medical School and helping us with Micro-CT experiments. Thank you to Ivy Low and Andrew Chan, of the Singapore Immunology Network's Core Flow Cytometry Team, for your patience and for operating the cell sorter so seamlessly every time.

I also thank my friends at AS and MU labs, namely Louise Fraser, Andrea Lee, Mardiana Marzuki, Dr. Carey Lim, Kavana Bywater-Brenna, Dr. Pooja Agarwal, and Giridhar Chandrasekharan. A special thank you to Kavana Bywater-Brenna and Molly Watling for their companionship throughout a hectic final year and development of my thesis.

Finally, I express my deep gratitude to my parents, for all the unconditional support, encouragement and understanding. Making you both proud is my biggest motivation.

IV. Declaration

This thesis is submitted to the University of Warwick in support of my application
for the degree of Doctor of Philosophy. It has been composed by me and has not been submitted in a previous application for any degree.

The data and data analysis presented in this thesis was carried out by the author except for the following:

- Operation of Aria 5L FACS sorter by Ivy Low and assisted by Andrew Chan at Singapore Immunology Network Core Flow Cytometry Facility.
- Bulk RNA-sequencing: RNA extraction and library synthesis by Lolita Fong, Foo Shihui, and Shanshan Wu Howland of the Immunogenomics Team at Singapore Immunology Network.
- Bulk RNA-sequencing quality control and bioinformatics analysis by DESeq2, as well as assistance with downstream analysis with Ingenuity Pathway Analysis was carried out by Dr Menaka Rajapakse of The Computational Immunology Department at Singapore Immunology Network.
- Micro X-Ray Computed Tomography and data analysis of BCG infected mice femurs was carried out by Dr Guillaume Remy of Warwick Manufacturing Group.

Signed: Artemis Emily Milne
Date: 28th February 2023

V. Summary

Homeostasis of the bone is a tightly regulated process involving bone forming osteoblasts and bone resorptive osteoclasts, which are characterised by their multinucleation and large size. It has been demonstrated that *Mycobacterium tuberculosis* (*Mtb*) infection of mature multinuclear osteoclasts can lead to dysregulation of cytokines and chemokines, reprogramming of osteoclast development and disruption of resorption capabilities. However, mechanisms of pathogenesis remain unclear.

In this project, we first characterised the *in vitro* differentiated osteoclast-like cells (OCLs), followed by the effects of mycobacterial infection on OCLs in two models of infection using *M. bovis* BCG. Infection of OCLs *in vitro* show that osteoclast frequency and resorptive activity increased during mycobacterial infection. This was also observed in OCLs obtained from C57BL/6 mice infected intravenously with BCG. To understand the mechanisms involved in mycobacterial infection of OCLs, we conducted transcriptome analysis of infected OCLs from both *in vitro* and *in vivo* models.

Our data suggests that host cell death pathways are modulated during BCG infection. To explore further, we investigate apoptosis and pyroptosis using several immunological techniques. We also probe the involvement of the NLRP3 inflammasome during infection.

Our findings refine our understanding of how mycobacteria manipulate the osteoclasts to provide a favourable environment to survive, which may thus inform potential host directed therapy strategies.

VI. List of Abbreviations

Acronym	Meaning
≥3N	Greater than 3 nuclei
µCT	Micro-Computational Tomography
1-2N	1-2 nuclei
AFB	Acid fast bacilli
AIM	Absent in melanoma 2
Akt	Protein kinase B
ALOX	Lipoxygenase
ALP	Alkaline phosphatase
AM	Alveolar macrophage
ANOVA	Analysis of variance
APC	Antigen-presenting cell
APC (flow cytometry)	Allophycocyanin
ASC	Apoptosis-associated speck-like protein containing a caspase-1 recruitment domain
ATAC-seq	The assay for transposase-accessible chromatin with sequencing
ATCC	American type culture collection
ATP	Adenosine 5′-triphosphate
Atp6v0d2	V0 complex V-type proton ATPase subunit D2
ATPase	Adenosine triphosphatase
AV	Annexin VI
BCG	Bacillus Calmette–Guérin
BJTB	Bone and joint TB
BM	Bone marrow
BMD	Bone mineral density
BMDC	Bone marrow derived dendritic cell
BMDM	Bone marrow derived macrophage
BMM	Bone marrow macrophage
BMP	Bone morphogenetic protein

BMU	Basic multicellular unit
BP	Biological process
BSA	Bovine serum albumin
BSL	Biosafety level
BV650	Brilliant Violet 650™
CaP	Calcium-phosphate
CC	Cellular component
CCL	Chemokine ligand
cDNA	Complementary DNA
CFP-10	Culture filtrate protein 10
CFU	Colony forming unit
ChIP	Chromatin immunoprecipitation
CLEAR	Coordinated Lysosomal Expression and Regulation
CO_2	Carbon dioxide
Col1a1	Collagen type 1 alpha 1 chain
COPD	Chronic obstructive pulmonary disease
cpn	Chaperonin protein
CR	Complement receptor
CREB	cAMP response element binding protein
Ct	Cycle threshold
CTHCR1	Collagen Triple repeat containing 1
CTR	Calcitonin receptor
CTSK	Cathepsin K
CXCL	C-X-C motif chemokine ligand
DAMP	Damage associated patterns
DAP	Death associated protein
DAPI	4′,6-Diamidino-2-phenylindole
DC	Dendritic cell
DC-STAMP	DC-specific transmembrane protein
DEG	Differentially expressed gene
DM	Diabetes mellitus
DNA	Deoxyribonucleic acid
DPI	Days post infection

ECAR	Extracellular acidification rate
ELISA	Enzyme-linked immunosorbent assay
EMEM	Eagle's Minimum Essential Medium
EMP	Embryonic erythro-myeloid progenitor
EPTB	Extrapulmonary TB
ER	Endoplasmic reticulum
ERK	Extracellular signal-regulated kinase
ESAT-6	Early secretory antigenic 6 kDa
FACS	Fluorescence activated cell sorting
FADD	FAS-mediated death domain protein
FC	Fold change
FCS	Fetal calf serum
FDR	False discovery rate
FGF	Fibroblast growth factor
FITC	Fluorescein isothiocyanate
FMO	Fluorescence minus one
FSC	Forward scatter
GM-CSF	Granulocyte macrophage-colony stimulating factor
GO	Gene ontology
GSDMD	Gasdermin D
GSH	Glutathione
GTPase	Guanosine triphosphatase
HA	Hyaluronic acid
HDT	Host directed therapy
Hh	Hedgehog
HIF1α	Hypoxia-inducible factor 1-alpha
HIV	Human immunodeficiency virus
HLOQ	Highest limit of quantification
HRP	Horseradish peroxidase
HSC	Hematopoietic stem cell
I.V.	Intravenous
IBD	Inflammatory bowel disease
IFN	Interferon

IGF	Insulin-like growth factor
IGRA	Interferon gamma release assay
IL	Interleukin
IM	Interstitial macrophages
In ≥3N	Infected ≥3 nuclei
In 1-2N	Infected 1-2 nuclei
IOB	Infected without bacteria
IPA	Ingenuity pathway analysis
iPS	Induced pluripotent stem cell
ITGB3	Integrin Subunit Beta 3
IWB	Infected with bacteria
IκK	Inhibitory-κB Kinase
JAK	Janus kinase
kDa	Kilodalton
KO	Knockout
LAM	Lipoarabinomannan
LDH	Lactate dehydrogenase
LIF	Leukaemia inhibitory factor
LLOQ	Lowest limit of quantification
LPA	Lysophosphatidic acid
LPS	Lipopolysaccharide
MAPK	Mitogen-activated protein kinase
MCP	Monocyte chemoattractant protein
M-CSF	Macrophage colony-stimulating factor
MDR	Multi-drug resistant
MF	Molecular function
MFI	Median fluorescence intensity
MGC	Multinuclear giant cell
MHC	Major histocompatibility complex
MIP	Macrophage inflammatory protein
MLKL	Mixed-lineage kinase domain–like pseudokinase
MMP	Matrix metallopeptidase
MN	Monocyte

MOI	Multiplicity of infection
MR	Mannose receptor
mRNA	Messenger RNA
MRSA	Methicillin-resistant *S. aureus*
MSC	Mesenchymal stem cell
Mtb	Mycobacterium tuberculosis
mTOR	Mammalian target of rapamycin
MΦ	Macrophage
NAC	N-acetylcysteine
NAD	Nicotinamide adenine dinucleotide
NEAA	Non-Essential Amino Acid
NFATc1	Nuclear factor of activated T-cell c1
NF-κB	Nuclear factor-kappa B
NHO	Normal human osteoblast
NHS	National Health Service
NLR	Nod-like receptor
NLRC4	NLR family CARD domain-containing protein 4
NLRP3	Nucleotide-binding oligomerisation domain, leucine-rich repeat, and pyrin domain-containing 3
NO	Nitric oxide
NOD2	Nucleotide-binding oligomerisation domain-containing protein 2
ns	Not significant
NTM	Nontuberculous mycobacteria
OATB	Osteoarticular TB
OB	Osteoblast
OC	Osteoclast
OCL	Osteoclast-like cell
OCN	Osteocalcin
OCP	Osteoclast precursor
OCR	Oxygen consumption rate
OC-STAMP	Osteoclast stimulatory transmembrane protein
OD	Optical density
OOR >	Out of range, unable to extrapolate

OOR<	Out of range, unable to extrapolate
OPG	Osteoprotegerin
OPN	Osteopontin
OSCAR	Osteoclast-associated receptor
OSM	Oncostatin M
OSX	Osterix
ox-mtDNA	Oxidised mitochondrial DNA
OXPHOS	Oxidative phosphorylation
p.i.	Post infection
P/S	Penicillin and streptomycin
PAMP	Pathogen-associated molecular pattern
PB	Peripheral blood
PB (flow cytometry)	Pacific Blue
PBMC	Peripheral blood mononuclear cell
PBS	Phosphate Buffer Saline
PCA	Principal Component Analysis
PCD	Programmed cell death
PCR	Polymerase chain reaction
PerCP	Peridinin-chlorophyll-protein Complex Conjugate
PFA	Paraformaldehyde
pH	Potential of hydrogen
PI	Propidium iodide
PI3K	Phosphoinositide 3-kinase
PPD	Purified protein derivative
PRR	Pattern Recognition Receptor
PS	Phosphatidylserine
PTH	Parathyroid hormone
PTM	Post-translational modification
PUFA	Polyunsaturated fatty acid
RA	Rheumatoid arthritis
RANKL	Receptor activator of nuclear factor kappa-B ligand

RANTES	Regulated upon Activation, Normal T Cell Expressed and Presumably Secreted
RD1	Region of Difference 1
RIPA	Radioimmunoprecipitation assay
RIPK	Receptor-interacting protein kinase
RLU	Relative luminescence unit
RNA	Ribonucleic acid
ROI	Region of interest
ROS	Reactive oxygen species
RPKM	Reads per kilobase of exon per million reads mapped
RPM	Revolutions per minute
RPMI	Roswell Park Memorial Institute
RT	Room temperature
RT-qPCR	Reverse transcription-quantitative PCR
RUNX2	RUNX family transcription factor 2
SARS-CoV-2	Severe acute respiratory syndrome coronavirus 2
SATB2	Special AT-rich sequence-binding protein 2
SD	Standard deviation
SDS-PAGE	Sodium dodecyl-sulphate polyacrylamide gel electrophoresis
SIgN	Singapore Immunology Network
SLC6A4	Solute carrier family 6-member 4
SRC	Spare respiratory capacity
SSC	Side Scatter
SSRI	Serotonin reuptake inhibitors
STAT	Signal transducer and activator of transcription
T2DM	Type 2 diabetes mellitus
TB	Tuberculosis
TBP	TATA box-binding protein
TBST	Tris buffered saline + Tween
TCA	Tricarboxylic acid
TF	Transcription factor
TGF-β	Transforming growth factor beta
TLR	Toll-like receptor

TNF	Tumour necrosis factor
TRAP	Tartrate-resistant acid phosphatase
TST	Tuberculin skin test
TUNEL	Terminal deoxynucleotidyl transferase dUTP nick end labeling
Un ≥3N	Uninfected ≥3 nuclei
Un 1-2N	Uninfected 1-2 nuclei
WHO	World Health Organisation
WMG	Warwick Manufacturing Group
Wnt	Wingless signalling pathway
WT	Wild type
XDR	Extensively-drug resistant

Chapter 1 Introduction

1.1 Introduction

1.1.1.1 *Mycobacterium tuberculosis*

Mycobacterium tuberculosis (*M. tuberculosis, Mtb*), the causative agent of human tuberculosis (TB), is an aerobic, non-motile, non-capsulated and non-spore forming bacterium measuring 0.5 µm x 3 µm, encompassed by a thick cell wall rich in mycolic acids. It is a member of the *Mycobacteriaceae* family of the species of *Mycobacterium,* of which there are 170 currently recognised species. The *Mycobacteriaceae* family can be divided into three categories: *Mycobacterium tuberculosis* complex, Nontuberculous mycobacteria (NTM) and *Mycobacterium leprae.*

The genus *Mycobacterium* was postulated to originate for more than 150 million years, with an ancestral variant of *M. tuberculosis* originating from East Africa around 3 million years ago (Gutierrez, Brisse et al. 2005). Archaeological studies on Egyptian mummies have revealed the presence of skeletal deformities associated with tuberculosis, called Pott's deformities (Morse, Brothwell et al. 1964, Zimmerman 1979). Other early historical records and archaeological evidence show that other ancient civilisations such as Ancient Rome and Ancient Greece were also plagued by the disease (Daniel 2006). It was only in 1882 that the tubercle bacillus was officially identified by German microbiologist Robert Koch (Koch 1882).

1.1.1.2 Tuberculosis – Present Scenario

Despite being an ancient pathogen, tuberculosis (TB) continues to pose a threat to global health (WHO 2022). There were an estimated 10.6 million cases of infection recorded by the World Health Organisation (WHO) in 2021, which saw rising mortality due to a lack of healthcare resources brought on by the COVID-19 pandemic. *Mtb* is introduced into the airway, where it is phagocytosed by local alveolar macrophages (AMs). If AMs are not successful in eliminating the *Mtb,* it can continue to replicate intracellularly. As a result, AMs, and other surrounding

innate immune cells such as neutrophils and dendritic cells surround the bacilli or cells containing it in an attempt to encase the infection locally. This leads to the formation of a granuloma. Usually this is the hallmark of a latent or dormant infection.

Latent TB is an inactive form of the disease which presents asymptomatically - around 1.8 billion people, or a quarter of the world's population are currently infected (WHO 2022). This type can be diagnosed by a blood test or the tuberculin skin test (TST), which tests the skin's immune response to purified protein derivative (PPD) from heat-killed cultures of *Mtb*. However, this test is not specific for *Mtb* infection as PPD contains antigens that are also found in nontuberculous mycobacteria and the bacille Calmette-Guérin (BCG) vaccine (Andersen, Munk et al. 2000). More specific tests for TB infection have been developed over the last 20 years, such as the interferon gamma release assay (IGRA). This approach primarily uses the early secretory antigenic 6 kDa (ESAT-6) protein and culture filtrate protein 10 (CFP-10), which are antigens found in *Mtb* but not in BCG or other nontuberculous mycobacteria. In the IGRA, blood samples or circulating lymphocytes are incubated *in vitro* with *Mtb* specific antigens ESAT-6/CFP10 and interferon-gamma release is quantified upon activation. Commercially available intradermal skin tests targeting ESAT-6/CFP10 have recently become the new standard according to the WHO, and are known as TB antigen-based skin tests (TBSTs) (WHO 2022).

If the patient is immunocompromised and cannot contain the infection, active TB occurs due to the escape and spread of bacilli from the granuloma. Patients with active TB present with symptoms such as chest pains, loss of appetite, fever, weight loss, night sweats, fatigue and even coughing up blood (haemoptysis) (NHS, 2019). If left untreated, active TB can result in serious lung damage and death. There are several avenues of diagnostics for pulmonary active TB, depending on the access to resources available. For low-income countries, where healthcare resources are lacking, more traditional approaches are relied on. Symptom screening (e.g., persistent cough lasting for 2-3 weeks, fever, unintentional weight loss, night sweats), and epidemiologic factors (e.g., history

of TB exposure, travel to or residence in an area where TB is endemic) are considered. The diagnosis of active TB is then confirmed with an abnormal chest X-ray, isolation and identification of *Mtb* from a bodily fluid, secretion or tissue (e.g. microbiological culture of sputum and staining for acid fast bacilli (AFB) using the Ziehl-Neelsen method) (Pai, Nicol et al. 2016).

Traditional diagnostics are limited by their lack of sensitivity and propensity for false results with Marciniuk *et al*. documenting that 4.8 % of active TB patients present with a normal X-ray (Marciniuk, Mc Nab et al. 1999). In addition, the sensitivity of a single sputum is approximately 60 %, compared to solid mycobacterial culture from patient samples (Toman, Frieden et al. 2004). Mycobacterial culture is also limited as it requires 4–6 weeks for results to appear (Toman, Frieden et al. 2004). As such, these methods are subjective, non-specific and time consuming.

Therefore, newer approaches are being implemented. The Xpert MTB/RIF molecular test, which detects *Mtb* directly from clinical specimens, is one of the most widely used molecular tests for TB diagnosis today. It uses a hemi-nested real-time polymerase chain reaction (PCR) to amplify a *Mtb*-specific sequence of the *rpoB* gene with a 2–3 hr turnaround time. IGRAs can also be used to diagnose active TB. In addition, fluorescent AFB stains using auramine also reduce reading time compared with traditional AFB staining with Ziehl-Neelsen (Pai, Nicol et al. 2016).

There are several different treatments for TB, including antibiotics and anti-inflammatories. The treatment for pulmonary TB relies on long courses of several antibiotics – isoniazid, rifampicin, pyrazinamide, and ethambutol for first two months, followed by four months of isoniazid (INH) and rifampicin. For latent TB, treatment consists of rifampicin and isoniazid for three months or isoniazid for six months (NHS 2022).

The bacille Calmette-Guérin (BCG), inactivated / attenuated *M. bovis*, vaccine is the only effective vaccine for the prevention of TB, used since 1921. It has a 60-

80 % protective efficacy against severe forms of TB but does not confer protection to those who have already been exposed (Rodrigues, Mangtani et al. 2011). Also, the efficacy is only when the patient has been vaccinated in childhood (Trunz, Fine et al. 2006).

1.2 Extrapulmonary TB

Although TB primarily affects the lungs, up to an estimated 25 % of cases affect organs other than the lungs. This is known as extrapulmonary TB (EPTB). Common sites affected by EPTB include the lymph nodes, pleura, the genitourinary system, the central nervous system as well as bone and joints (Baykan, Sayiner et al. 2022).

EPTB is an increasing cause for concern for both the developing and developed world, and is steadily increasing in incidence across the globe (Ayed 2018). Host risk factors for EPTB include poverty, female gender, age ≥45 years, human immunodeficiency virus (HIV)-infection and low CD4 count (Ayed 2018, Qian, Nguyen et al. 2018). In Europe, migrants from South-East Asia and Sub-Saharan Africa were found to have the highest risks of EPTB complications, much higher than non-migrants (Hayward, Rustage et al. 2021).

The risk of EPTB in HIV-infected patients is very high, with one study showing a 50 % co-infection rate (Gomes da Rocha Dias, von Amann et al. 2016). Untreated HIV patients have severely depleted CD4 counts or dysfunction of $CD4^+$ T-cells which in turn leads to reduced IL-2 or interferon gamma (IFN-γ) production (Mehandru, Poles et al. 2004). As a result, this makes an individual more vulnerable to infections such as TB. The severity of immunosuppression is associated with the incidence of HIV co-infection with EPTB. EPTB is also notoriously difficult to diagnose, as clinical manifestations can be non-specific, and has been known to mimic other non-infectious conditions (Binesh, Zahir et al. 2013). In resource limited settings, this signifies a delay in EPTB diagnosis and treatment, leading to negatively impacted patient outcomes.

1.3 Bone and Joint Tuberculosis

Bone and joint TB (BJTB) is a form of EPTB that accounts for 6.7 % of TB cases in England, with the prevalence higher amongst immigrants from highly endemic countries (Broderick, Hopkins et al. 2018). In terms of world prevalence, there are an estimated 19-38 million cases (Held 2017). BJTB is likely caused by bacterial dissemination from the primary focus of infection (lung) to vertebrae or joints that have a rich vascular supply or are close in proximity to the lungs (Jabir 2017).

Symptoms of skeletal TB include severe back pain, stiffness, spinal abscess, neurological disorders, swelling of soft tissue, muscle weakness and TB-related meningitis. The spine and weight bearing joints are commonly infected sites, with 50 % of BJTB infections affecting the spine (Moon 2014). Spinal TB (tuberculosis spondylitis), also known as Pott's disease, frequently involves the lower thoracic and upper lumbar vertebrae areas of the spine. It results in kyphosis, a 'hunchback' disfigurement called 'Pott's spine' (Ansari, Amanullah et al. 2013). Spinal TB is the major manifestation of BJTB in older children and young adults, as the spine is more vascularised than in adults. There are also risks of serious deformities that impact child development, including bone destruction, spinal deformity, and paraplegia. Additionally, BJTB is significantly more common in underdeveloped countries with dense populations such as Chennai in India, where the incidence of spinal TB in children is 30 % of all TB cases (Moon, Kim et al. 2012). BJTB is characterised by mass bone resorption and chronic inflammation from the presence of *Mtb*.

Osteoarticular TB (OATB) is another manifestation of BJTB that is characterised by arthritis of weight-bearing joints such as knee, hip, or ankle, but it can also affect non-weight-bearing joints including the wrist and elbow. It is impossible to define the true incidence of OATB as there are no accessible epidemiological data, but it is estimated that OATB represents 1-3% of all TB cases (Agashe 2020).

Early diagnosis is crucial for effective treatment of BJTB but difficulties are associated with diagnosis. As such, Pott's disease may be asymptomatic and

painless in its early stages. BJTB diagnosis is still based on invasive and time-consuming methods and relies on culturing *Mtb* from biological fluids such as pleural, cerebral, synovial fluids collected by biopsy or from paraspinal abscess (Rajasekaran, Soundararajan et al. 2018). The IGRA and Xpert MTB/RIF tests show promise in diagnosing BJTB. In one study evaluating these tools in BJTB diagnosis, the sensitivity of IGRA was 81.4 %; Xpert MTB/RIF's sensitivity was 70.9 % whilst the combined sensitivity of both methods was 91.9 % (Tang, Yin et al. 2018). However, the hidden costs of the Xpert machine (installation, power supply, technical training) limits its use in low resource countries such as Nigeria (Abdurrahman, Emenyonu et al. 2014).

Available chemotherapies are sub-optimal due to poor drug penetration in extra-pulmonary sites and very long treatment durations of 6-18 months, which pose a financial burden to the patient as well as worsen their quality of life. Surgery is also necessary when there is vertebral instability, large abscesses and/or progressive deformity (Leonard 2017). Therefore, there is a huge need for improved, financially viable diagnostic markers to rapidly identify or rule out BJTB, as well as therapeutic interventions.

Many details of BJTB pathogenesis remain unclear. Unlike *Mtb*-macrophage interactions, which are well studied, little is known about how *Mtb* interacts with cells in extra-pulmonary locations. Previous studies have reported that *Mtb* infects major bone cell types, osteoblasts, and osteoclasts, leading to production of soluble mediators, but there is still much information missing (Wright 2002, Wright 2004, Hoshino 2014).

Considerable evidence states that *Mtb* can reside in the bone marrow (BM), providing a reservoir to confer survival. Fatima *et al* discovered *Mtb* in the BM of murine mice models treated with the antibiotic INH and found that bacilli were enriched with genes related to dormancy, with reduced expression of genes related to replication (Fatima 2020). Furthermore, BM mesenchymal stem cells (MSCs) were also found to provide a niche for dormant *Mtb* (Das 2013). Nevertheless, mechanisms underlying bone cell modulation by *Mtb* are poorly

understood. Bacterial determinants that control invasion and survival in bone cells and how they affect bone remodelling, a distinct feature of bone infections, are largely unknown. Thus, understanding the molecular basis of BJTB is first necessary for the development of improved diagnostic tools and design of novel therapeutic interventions.

1.4 Mycobacterial interactions with the host

1.4.1 Overview of Innate and Adaptive Immune Response

In the fight against foreign pathogens, the innate immune cells are the first line of protection. These cells aim to give a rapid but non-specific response compared to the adaptive immune cells. Macrophages and monocytes (MNs) play a crucial role during *Mtb* and other bacterial infections.

Transmission of *Mtb* first occurs from the expulsion of contaminated airborne particles (droplet nuclei) from the lungs of an infected person, typically when they cough or sneeze. The droplet nuclei containing infectious bacilli are then inhaled by another person in close contact and travel to the lung where they encounter the resident alveolar macrophages (AMs). During TB infection, the AMs are the main targets of *Mtb.* Meanwhile, infiltrating MNs enter the infection site and differentiate into interstitial macrophages (IMs) that are thought to be *Mtb*-restrictive and induce pro-inflammatory cytokine release, which stimulates the T-cell and adaptive immune response against *Mtb* (Huang 2018).

The failure of the host to fully eradicate *Mtb* bacilli results in either latent or active TB forms. The latent phase is characterised by the formation of granulomas composed of an aggregation of various innate and adaptive immune cells (macrophages, $CD4^+$/$CD8^+$ T-cells, DCs) to enclose *Mtb* infected macrophages and prevent further dissemination of bacilli. If the host becomes immunocompromised (e.g. co-infection with HIV, immunosuppressive treatments) or became exposed to a highly virulent *Mtb* strain, the equilibrium of the granuloma can become disrupted – *Mtb* begins to proliferate and induce

necrosis in the infected macrophages, resulting in the infection spreading throughout the lungs and beyond. This is known as the active phase of TB, which is able to be transmitted and is contagious (Sholeye, Williams et al. 2022)

1.4.2 *Mtb* / macrophage interactions

Alveolar macrophages (AMs) are phagocytes that detect, engulf, and destroy pathogens, dead cells, and particles larger than 0.5 μm that are recognised as 'non-self'. During infection, MNs and macrophages recognise *Mtb* through pattern recognition receptors (PRRs), which are receptors expressed on the surface of innate immune cells. PRRs recognise pathogen-associated molecular patterns (PAMPs). Stimulation of PPRs by PAMPs trigger cellular responses including antigen-presentation, phagosome maturation, inflammation, and programmed cell death (Maphasa, Meyer et al. 2020). The PRRs that have been implicated with *Mtb* infection include toll-like receptors (TLRs), complement receptors (CRs), and mannose receptors (MRs) to name a few (Underhill, Ozinsky et al. 1999, Ferguson, Weis et al. 2004, Kang, Azad et al. 2005). Binding of a PAMP from *Mtb* or other pathogen to a PRR can lead to several different outcomes in the AM, as illustrated in figure 1.1.

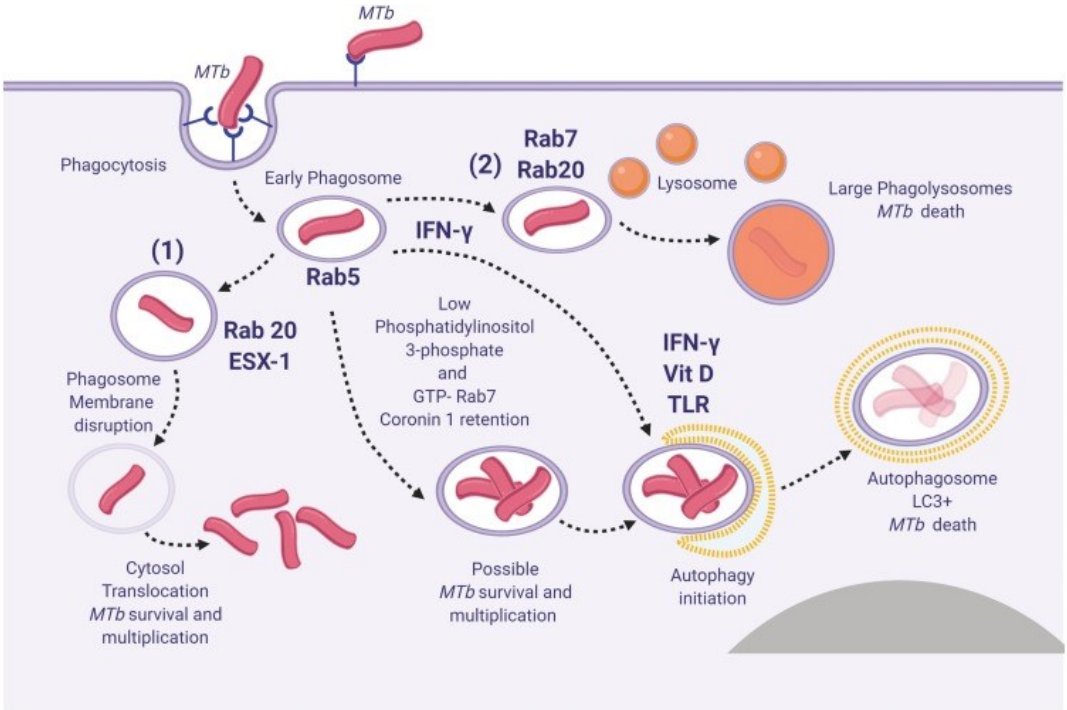

Figure 1.1: The different outcomes for intracellular Mtb – killing or survival

A key strategy used by Mtb is to preserve the characteristics of the early endosome, delay phagosome-maturation (through retention of Rab5, inhibition of PI3P and inhibition of EEA1) or escape the phagosome entirely (through the actions of Rab20-trafficking, and ESX-1). Otherwise, Mtb is killed by lysosomal degradation (Tăbăran, Matea et al. 2020).

If the PRR is an endocytic receptor, for example the mannose receptor (MR), this leads to phagocytosis and the production of anti-inflammatory cytokines, devoid of inducing an oxidative response (Nigou, Zelle-Rieser et al. 2001, Kang, Azad et al. 2005). This route of entry promotes survival of *Mtb.* Virulent *Mtb* contains mannose-capped lipoarabinomannan (ManLAM) on its surface which is recognised by the MR. Interaction between ManLAM and MR can impair or delay phagosome maturation into a lysosome (phagosome-lysosome fusion) (Kang, Azad et al. 2005).

Phagosome maturation is a sequential process whereby internalised pathogens are matured through membrane-bound phagosomes, acquiring more reactive oxygen species (ROS), nitrogen intermediates, lysosomal hydrolases, and antimicrobial peptides along the way, until a final fusion with a lysosome takes place. The environment becomes too acidic and toxic for pathogens to survive, and so the pathogen is digested by proteases and hydrolases. *Mtb* interference with the phagosome maturation process is a key strategy evolved for its survival intracellularly. *Mtb* can also escape the phagosome entirely, a trait shared with *L. monocytogenes* and *S. aureus* (Grosz, Kolter et al. 2014, Jamwal, Mehrotra et al. 2016).

AMs, which derive from yoke sac precursors of fetal MNs, can both control and permit intracellular *Mtb* infection (Hoeffel 2018). Whilst they have strategies to limit *Mtb* growth, they are less able to control infection than bone marrow monocyte-derived IMs. This may be due to their metabolism. As such, AMs mainly use fatty acid oxidation, which is more accommodating to *Mtb* growth, compared to IMs which have a glycolytic metabolism (Huang, Nazarova et al. 2018). Intracellular *Mtb* growth may also be facilitated by the alterations in lipid metabolism during infection of AMs which nutritionally benefits *Mtb* growth and

leads to the transformation of macrophages into foam cells, which are characterised by the accumulation of lipid bodies composed of triglycerides and cholesterol esters (Cumming, Addicott et al. 2018).

1.4.3 Relevance of inflammasomes in *Mtb* infection

As discussed, the host cell contains PPRs that sense extracellular pathogens, but they also have systems in place to sense pathogen components intracellularly. This involves inflammasomes, which regulate the inflammatory response of the host cell. Nucleotide binding and oligomerisation domain-like receptors (NLRs, e.g. NLRP3) and absent in melanoma 2 (AIM2)-like receptors (ALRs, e.g. AIM2) are such examples of inflammasomes (Sharma and Kanneganti 2016).

Inflammasomes are intracellular multimeric protein complexes found in the cytoplasm of myeloid origin cells that mediate the activation of caspase-1. Caspase-1 then cleaves pro- IL-1β/pro-IL-18 into their active forms of IL-1β/IL-18, of which are pivotal in *Mtb* infection and control. *Mtb* infection specifically has been linked to the activation of the NLRP3 and AIM2 inflammasomes and are the most well-studied in relation to *Mtb.* Whilst AIM2 inflammasome is activated by its specific stimuli, double-stranded DNA (or mt-DNA), NLRP3 is activated by a wider range of stimuli (such as TNF-α, IL-1β and LPS).

1.4.4 The NLRP3 inflammasome in *Mtb* infection

The NLRP3 inflammasome mediates the activation of caspase-1, cleavage of inactive IL-1β/IL-18 into their active forms and pyroptosis (an inflammatory form of cell death) in response to bacterial infection (figure 1.2). *Mtb* can either activate or inhibit the NLRP3 inflammasome, resulting in protective or damaging outcomes for the host (Rastogi and Briken 2022).

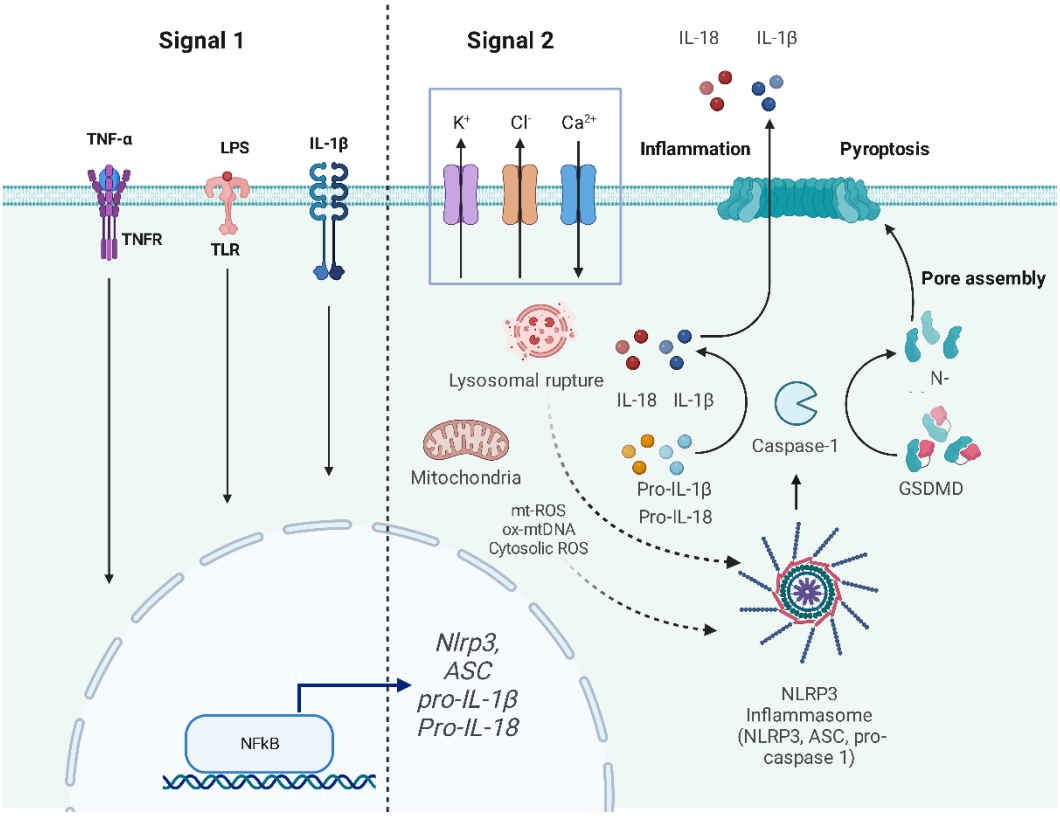

Figure 1.2: The signalling mechanism of the canonical NLRP3 inflammasome

The canonical NLRP3 inflammasome mechanism of action involving the priming signal (signal 1) such as TNF-α, LPS or IL-1β leading to the activation of transcription factor NF-κB and the upregulation of genes NLRP3, ASC pro-IL-1β *and* pro-IL-18. *NLRP3 then undergoes post-translational modifications (PTMs) to confer its activation. The activation signal is triggered by various signals (extracellular ATP, K^+ efflux, Cl^- efflux, Ca^{+2} influx, ox-mtDNA, lysosomal rupture and intracellular ROS production). (Created using BioRender).*

For the NLRP3 inflammasome to be activated, two signals are required. The first step is priming of the NLRP3 inflammasome. Priming is initiated by the binding of a PAMP from *Mtb* to a signalling PRR, such as TLR (2/4), TNF-R, and IL-1R. This causes the activation of transcription factor NF-κB, resulting in its translocation to the nucleus to drive expression of *NLRP3, ASC, pro-IL-1β, pro–IL-18 (*and *pro-caspase-11)* genes (Rastogi and Briken 2022). Caspase-8 and FAS-mediated death domain protein (FADD), and NOD1/2 are also involved in the priming step through the regulation of NF-κB activation. The second signal is the activator of

NLRP3 by a second stimulus, which may include extracellular ATP, potassium (K^+) efflux, chloride (Cl^-) efflux, calcium (Ca^{+2}) influx, oxidised mitochondrial DNA (ox-mtDNA), lysosomal rupture and intracellular ROS production (Zhou, Yazdi et al. 2011, Murakami, Ockinger et al. 2012, Rossol, Pierer et al. 2012, Shimada, Crother et al. 2012, Tang, Lang et al. 2017).

The second signal results in NLRP3 associating with adapter molecule apoptosis-associated speck-like protein containing a CARD (ASC). Once NLRP3 associates with ASC, pro-caspase-1 is recruited and oligomerises to form characteristic 'specks' or pyroptosomes (Fernandes-Alnemri, Wu et al. 2007, Lu, Magupalli et al. 2014). The NLRP3 inflammasome complex promotes pro-caspase-1 self-cleavage into active caspase-1, which then goes on to cleave pro-IL-1β and pro-IL-18. Caspase-1 also cleaves gasdermin D (GSDMD), which facilitates the release the N-terminal fragment to undergo oligomerisation and membrane pore formation. The GSDMD pores are responsible for pyroptosis and cytokine release, without the rupturing of the plasma membrane.

It is well known that NLRP3 and *Mtb* infection are intertwined. NLRP3 activation during *Mtb* infection has been found in several cell types: THP-1 monocyte-derived macrophages, primary human peripheral blood mononuclear cells (PBMCs), murine bone marrow derived macrophages (BMDMs), and murine bone marrow derived dendritic cells (BMDCs) (Mishra, Moura-Alves et al. 2010, Wong and Jacobs 2011, Dorhoi, Nouailles et al. 2012, Amaral, Riteau et al. 2018).

However, IL-1β or IL-18 release may be protective or harmful to the cell depending on the scenario. The protective effects of IL-1β are shown in $IL1B^{-/-}$ and $IL1R^{-/-}$ mice, which are extremely vulnerable to *Mtb* infection. This has been evidenced by a shorter survival time, a higher bacterial burden in the lungs and vast necrosis of pulmonary tissue in the $IL1B^{-/-}$ / $IL1R^{-/-}$ mice compared to the WT mice (Mayer-Barber, Barber et al. 2010, Mayer-Barber, Andrade et al. 2011). $IL18^{-/-}$ mice also show a higher bacterial burden in the lungs during *Mtb* infection (Sugawara, Yamada et al. 1999). Moreover, MN–derived macrophages from patients with genetic variants in NLRP3 secrete higher than expected levels of IL-

1β and display increased control over *Mtb* growth (Verma, Lerm et al. 2008, Eklund, Welin et al. 2014). The cellular mechanisms by which IL-1β offer host protection may involve an induction in apoptosis or autophagy signalling as well as increasing the maturation of phagosomes containing *Mtb* (Master, Rampini et al. 2008, Pilli, Arko-Mensah et al. 2012, Jayaraman, Sada-Ovalle et al. 2013).

The harmful role of IL-1β in *Mtb* was evidenced by studies analysing the correlation between increased IL-1β expression and severity of TB (Wilkinson, Patel et al. 1999, Zhang, Zhou et al. 2014). The dynamic effects of IL-1β signalling could be explained by the time course of infection. Per se, early in infection IL-1β confers protective effects as it mainly acts on innate immune cells. As infection progresses, IL-1β starts to act on different cell types, changing the response and thereby inducing inflammatory tissue damage (Silvério, Gonçalves et al. 2021).

1.4.5 *Mtb* induced host cell death

Naturally, programmed cell death (PCD) mechanisms (e.g., apoptosis and autophagy) of cells containing intracellular *Mtb* is an effective approach for innate cells in controlling infection, as it results in the bacilli being contained within dead macrophages so they can be phagocytosed by neighbouring cells. Non-PCD forms of cell death such as necrosis are beneficial to *Mtb* survival as it results in its extracellular dissemination and spread. *Mtb* infection is associated with many forms of PCD and non-PCD forms of cell death, but pyroptosis, apoptosis, autophagy and necroptosis are amongst the most well studied. These four pathways are summarised in figure 1.3.

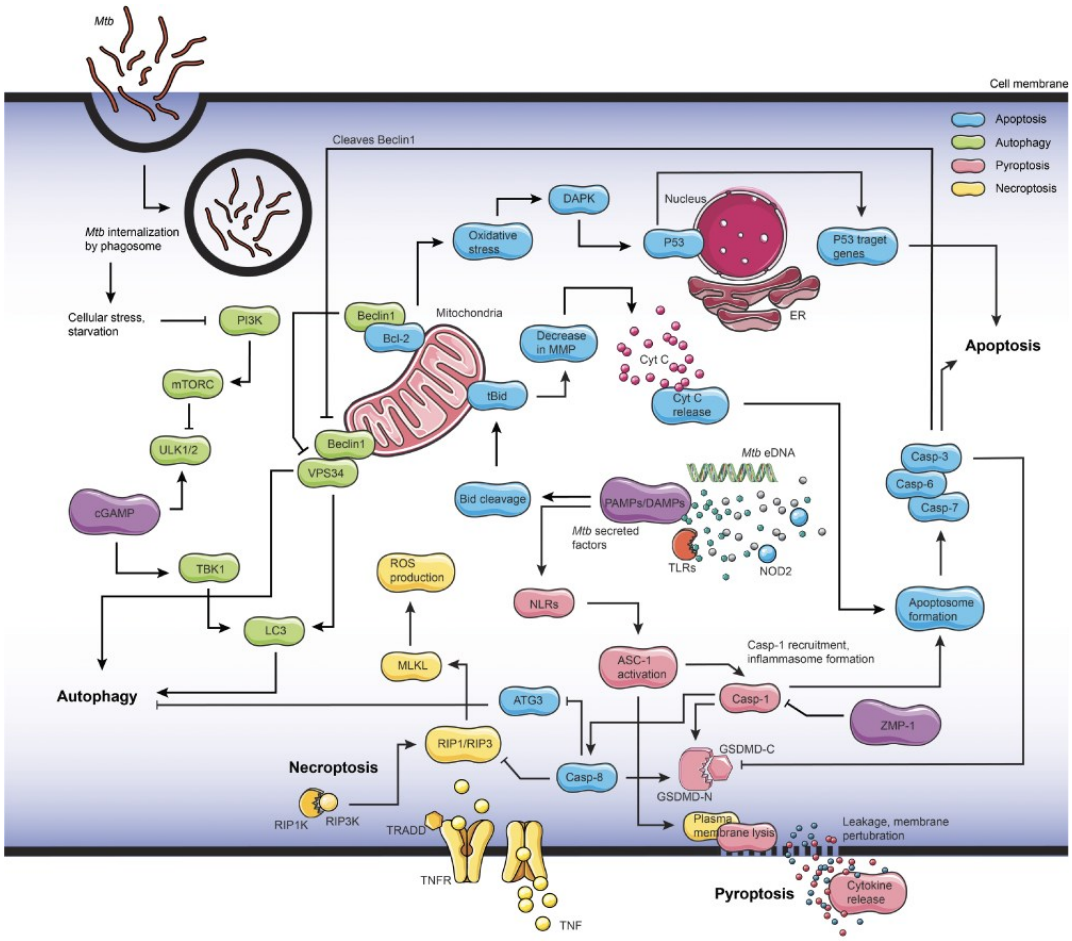

Figure 1.3 Key host cell death pathways involved in Mtb infection

Apoptosis, autophagy, pyroptosis and necroptosis and their key signalling pathway components (Nisa, Kipper et al. 2022).

1.4.6 Pyroptosis

Pyroptosis, dependent on activation of the NLRP3 inflammasome (or other inflammasomes such as the NLR family CARD domain-containing protein 4, NLRC4) is an inflammatory form of cell death. It has been discovered that *Mtb* causes caspase-1/NLRP3/GSDMD-mediated pyroptosis of human MNs and macrophages (Beckwith, Beckwith et al. 2020). This was found to be type VII secretion system (ESX-1) mediated or caused by the damage to the plasma membrane during phagocytosis of *Mtb.* Both of these cause K^+ efflux, activation of NLRP3-dependent IL-1β release, and pyroptosis which in turn permits the spread of *Mtb* to surrounding cells (Beckwith, Beckwith et al. 2020).

1.4.7 Apoptosis

Apoptosis is a form of PCD that can be phenotypically distinguished by cell shrinkage, DNA fragmentation, exposure of phosphatidylserine (PS) on the outer layer of the cell membrane and fragmentation of cellular components into membrane-bound apoptotic bodies, followed by phagocytosis by neighbouring cells (Saraste and Pulkki 2000). Apoptosis of infected cells is beneficial for the host during *Mtb* infection as limits inflammation compared to necrosis, an inflammatory form of cell death induced by *Mtb* (Yorulmaz 2015).

The capacity for *Mtb* to induce cell death in innate immune cells such as AMs has been well noted in the literature, with several modes of death associated with infection (apoptosis, necroptosis, pyroptosis, and ferroptosis) (Nisa, Kipper et al. 2022). Extensive evidence supports the association of *Mtb* with both induction and inhibition of apoptosis in AMs, through several identified *Mtb* proteins. ESAT-6, the PGRS domain of Rv0297 (Rv0297PGRS), *Mtb* Ag MPT83 (Rv2872), and the *Mtb*-derived TLR2 ligand, Rv1016c lipoprotein have all been shown to induce apoptosis in macrophages via distinct mechanisms (Wang, Zuo et al. 2017, Grover, Sharma et al. 2018, Lin, Chang et al. 2019).

Mtb is also able to inhibit cell apoptosis for its own benefit. Several identified *Mtb* factors include mannose-capped lipoarabinomannan (MANLAM), LpqT, mycobacterial acyl carrier protein (Rv2244) and SP110b. Mannose-capped LAM induces antiapoptotic B-cell CLL/lymphoma 2 family member A1 (Halder, Kumar et al. 2015). LpqT perturbs TLR2-dependent inflammatory signalling along with apoptosis (Li, Feng et al. 2018). Rv2244 inhibits apoptosis via the ROS/JNK signalling pathway (Paik, Choi et al. 2019). Also, IFN-inducer nuclear protein SP110b has been shown to modulate nuclear factor-κB (NF-κB) activity causing the downregulation of TNF-α, along with NF-κB induced antiapoptotic gene expression (Leu, Chen et al. 2017).

1.4.8 Autophagy

Autophagy is a mechanism by which cells maintain homeostasis and survival by degrading unwanted cellular components or bacteria in LC3-associated autophagosomes that commence lysosomal degradation. This process may or may not result in cell death. Autophagy is referred to as xenophagy when the process is directed at bacteria to eliminate them and was first shown in *Mtb* infection of macrophages (Gutierrez, Master et al. 2004).

Autophagy is a protective mechanism for the host during *Mtb* infection. Extensive evidence shows that a suppression in autophagy increases *Mtb* survival, while its stimulation (through IFN-γ signalling) increases *Mtb* killing (Gutierrez, Master et al. 2004, Dutta, Kathania et al. 2012, Sakowski, Koster et al. 2015). *Mtb* has acquired tactics to evade elimination by autophagy. For instance, virulent *Mtb* strains were shown to prevent RAB7-mediated autophagosome maturation into autolysosomes (Chandra, Ghanwat et al. 2015). Additionally, *Mtb* was found to express a miRNA (miR-155) that resulted in the inhibition of known autophagy related genes (ATG family and LC3) in human primary DCs (Etna, Sinigaglia et al. 2018).

1.4.9 Necroptosis

Necroptosis is another form of host cell death induced by *Mtb.* It is a form of programmed necrosis, inflammatory cell death that is caspase-independent and does not activate IL-1β and IL-18. Cell death by this pathway is described by the construction of the necrosome, which involves the phosphorylation of receptor-interacting protein kinase 1 (RIPK1), RIPK3, mixed-lineage kinase domain–like pseudokinase (MLKL), and the inhibition of apoptosis-associated caspase-8. MLKL oligomerises to form pores in the cell membrane, which results in cytoplasm swelling, leakage and production of damage associated patterns (DAMPs). Cell death by necroptosis results in enhanced *Mtb* replication and spread, thereby detrimental to the host. However, there seems to be negative feedback crosstalk between autophagy and necroptosis as it was reported that

autophagy inhibits necroptosis, and necroptosis can promote autophagy (Nikoletopoulou, Markaki et al. 2013).

1.4.10 Ferroptosis

More recently, a new pathway of regulated necrosis has been described, termed ferroptosis. It is characterised by iron dependent lipid peroxidation due to excessive iron. Specifically, increased iron participates in the catalysis of the oxidation of phospholipids containing polyunsaturated fatty acids (PUFAs) residues in Fenton reactions. Lipid peroxidation and the formation of lipid reactive oxygen species (lipid ROS) eventually reaches toxic levels in the cell and induces cell swelling, rupture, and death (Cheng and Li 2007, Du and Guo 2022). Ferroptosis is implicated during *Mtb* infection, as increased iron levels have been correlated with increased risk of active pulmonary TB and it has been reported that *Mtb* induces ferroptosis in macrophages *in vitro* and *in vivo* (Amaral, Costa et al. 2019).

1.5 Bone homeostasis in the host immune response

1.5.1 Bone and Bone Remodelling

The bone is a metabolically active organ that makes up the skeleton, which is important for movement, support and protection of internal organs, and calcium and phosphate storage. Bone is made up of an osteoid matrix and hydroxyapatite crystal, but it also contains water, non-collagenous proteins, lipids, and specialised bone cells. The bone as a whole is made up of two structurally distinct types – cortical bone and trabecular bone (Kenkre and Bassett 2018).

Cortical bone is the outer dense layer and is solid with penetrating vascular canals. It has an outer periosteal surface that contains blood vessels, nerve endings, bone cells, as well as an inner, endosteal surface that is adjacent to the marrow. Trabecular bone makes up the honeycomb-like structure on the

endosteal surface of cortical bone, and constitutes a fine network of connecting plates and rods (Kenkre and Bassett 2018). The bone is a highly dynamic organ that undergoes constant modelling and remodelling through the coordinated activities of bone cells called osteoblasts, osteoclasts, and osteocytes. The functions of these bone cells are summarised in table 1.1.

Table 1.1 The function and location of osteogenic cells, osteoblasts, osteocytes and osteoclasts in the human body *(Biga 2022).*

Bone Cells		
Cell type	**Function**	**Location**
Osteogenic cells	Develop into osteoblasts	Endosteum, cellular layer of the periosteum
Osteoblasts	Bone formation	Endosteum, cellular layer of the periosteum, growing portions of bone
Osteocytes	Maintain mineral concentration of matrix	Entrapped in matrix
Osteoclasts	Bone resorption	Endosteum, cellular layer of the periosteum, at sites of old, injured, or unneeded bone

Bone modelling denotes the actions of bone-forming osteoblasts and bone-resorbing osteoclasts simultaneously at separate locations with the goal of changing bone shape which is important during development. In bone remodelling, osteoblasts and osteoclasts act on the same bone surface, with osteoblast activity following osteoclast activity. It is how the adult skeleton adapts to changes in mechanical loading or replaces damaged bone (Sims and Martin 2020). Under normal physiological conditions, the rate of resorption equals the rate of formation, so that the overall volume of bone stays the same, with the functions of osteoclasts and osteoblasts tightly regulated to work in a reciprocal manner. Bone remodelling occurs in structures known as basic multicellular units (BMU) (Jilka 2003). Each BMU is encapsulated by osteocytes, which are inert bone-lining cells. Bone remodelling takes place over 100-200 days and consists of five steps: activation, resorption, reversal, formation, and termination, as condensed in figure 1.4. The process can be activated by mechanical stress or by hormonal signals such as the parathyroid hormone (PTH). Secretion of PTH is triggered in response to reduced calcium levels and binds to the PTH receptor on osteoblasts, initiating the expression of receptor activator NF-kB ligand (RANKL) and macrophage colony stimulating factor (M-

CSF) (Jacome-Galarza, Percin et al. 2019). RANKL and M-CSF, which are also supplied by osteocytes and bone marrow stromal cells, in turn stimulate the differentiation of mononuclear precursor cells of the monocyte macrophage lineage into mature osteoclasts (osteoclastogenesis).

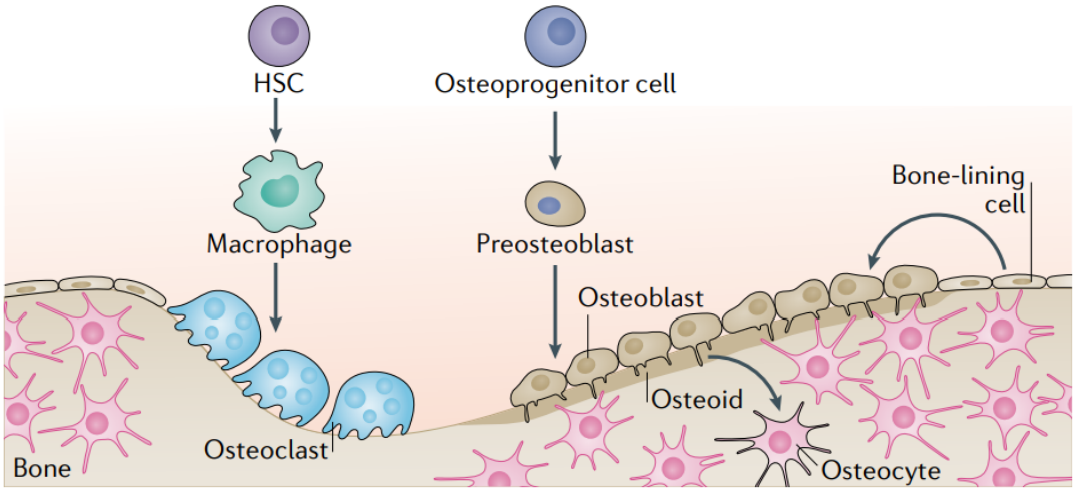

Figure 1.4: Bone remodelling to maintain bone homeostasis under normal physiological conditions.

The actions of bone forming osteoblast cells and bone resorbing osteoclasts work in tandem inside the BMU so that the rate of bone formation matches the rate of bone resorption (Salhotra, Shah et al. 2020).

Osteoclasts are multinucleated giant cells that have the exclusive ability to reabsorb bone mineral, which normally takes around 2 weeks. Through the cytoskeleton reorganisation in osteoclasts, they are able to adhere to the bone surface and displace the cells that are already there (Ferrier, Xia et al. 1994). Through the adherence of the osteoclast on the surface, they form a sealing zone and a ruffled border that increases surface area of secretion into the resorption pit (lacunae). This also prevents the potential diffusion of damaging proteolytic enzymes and other resorbing factors into the surrounding quiescent bone. Osteoclasts pump protons (H^+) generated by carbonic anhydrase II whereby the H^+-ATPase pumps H^+ into lacunae, a process coupled to Cl^- transport through Clcn7. This mobilises the inorganic components of the bone (Kenkre and Bassett 2018). Tartrate-resistant acid phosphatase (TRAP), also secreted by osteoclasts, also solubilises the inorganic components of bone (Katsimbri 2017).

Furthermore, osteoclasts perform the polarised secretion of cathepsin K (CTSK), a protease which hydrolyses the organic components of bone (e.g. collagen).

Following bone resorption, osteoclasts undergo apoptosis to prevent excess resorption (Katsimbri 2017). The reversal phase follows resorption, which typically takes 4-5 weeks. The exact coupling mechanism and the reversal phase is not well elucidated but transforming growth factor beta 1 (TGF-β) and insulin-like growth factor-1 (IGF-1) have been found to be released and activated by the acidic pH caused by osteoclasts secretions during resorption (Xu 2018). Secretion of clastokines (cytokines derived from osteoclasts), including the complement factor C3a or collagen triple repeat containing 1 (CTHCR1), from osteoclasts results in osteoblast progenitor cells (such as mesenchymal stem cells and bone lining cells) being recruited to the lacunae where they differentiate into mature osteoblasts (Takeshita 2013). The regulation of osteoblast differentiation as well as function involves the wingless (Wnt) signalling pathways, key players being Lrp5 (Wnt co-receptor regulating bone formation) and Sclerostin/Scl (a putative Lrp5-antagonist) (Day, Guo et al. 2005, Yorgan and Schinke 2014). The formation stage takes 4-6 months. Osteoblasts secrete osteoid (the unmineralised bone matrix) into the lacunae. Osteoid is rich in type 1 collagen and forms the new bone matrix (Charles and Aliprantis 2014). Osteoid is continually secreted by the osteoblasts until the entire resorption pit is filled. The new bone matrix is then mineralised over time by the deposition of hydroxyapatite crystals and calcium amongst collagen fibrils. Due to this high mineral content, bone is mechanically rigid and has weight-bearing strength (Katsimbri 2017). Around 30 days after osteoid formation, the termination phase occurs. This is where the bone matrix further is calcified and osteoblasts either undergo apoptosis, form bone lining cells and / or differentiate into osteocytes, which make up 95 % of all cells in the bone (Katsimbri 2017). Bone lining cells form a thin layer which cover the surface of bone, functioning to regulate the movement of calcium and phosphate ions and can also be reactivated back into osteoblasts. Osteocytes function to maintain bone integrity, sensing mechanical forces and maintain mineral homeostasis through the secretion of calcium and phosphate ions from the bone tissue (table 1.1).

1.6 Osteoclasts – macrophages of the bone

Osteoclasts function as the innate immune cells of the bone, thus are highly regulated to appropriately respond to stress and inflammatory changes in their microenvironment. Osteoclasts are regulated by tightly controlled mechanisms of differentiation and display a diversity of origin. During embryonic development and postnatal development, osteoclasts derive from the embryonic erythro-myeloid progenitor (EMP) lineage (Yahara 2020). During adulthood however, osteoclasts are derived from the bone marrow (BM) hematopoietic stem cells (HSCs). Osteoclasts share this origin with cells such as monocytes (MN), macrophages (MΦ), and dendritic cells (DCs). Although the BM and blood are the primary sources of osteoclast progenitors in humans and mice, they can also be found in HSCs within the liver, spleen, thymus and lymph nodes (Udagawa, Takahashi et al. 1990, Blin-Wakkach, Wakkach et al. 2004, Xing, Xiu et al. 2012, Marino, Logan et al. 2014).

1.6.1 Osteoclastogenesis

Osteoclastogenesis refers to the development of multinucleated osteoclasts via the fusion of their precursors. The master regulator of osteoclastogenesis was identified as the receptor activator of nuclear factor kappa-B/ receptor activator of nuclear factor kappa-B ligand/ osteoprotegerin (RANKL/RANK/OPG) signalling axis (Lacey 1998, Yasuda 1998, Takayanagi 2021). Osteoclast progenitors/precursors (OCP) express c-FMS, the receptor for macrophage colony stimulating factor (M-CSF). Upon binding of MCSF to c-FMS, survival and proliferation of osteoclast precursor cells are activated through extracellular signal-regulated kinase (ERK) and Akt signalling pathways. RANKL is secreted by osteoblasts, osteocytes, chondrocytes, osteocytes, and T-cells under pathological conditions. RANKL binds to RANK on the surface of OCPs and induces further differentiation through the recruitment of TRAF6, which activates MAPKs, c-fos, NF-κB, Akt and nuclear factor of activated T cells 1 (NFATc1). NFATc1 is a transcription factor involved in the expression of many osteoclast genes such as

tartrate resistant acid phosphatase (TRAP, *ACP5*) and osteoclast-associated receptor (*OSCAR*) (Arai, Miyamoto et al. 1999, Takayanagi, Kim et al. 2002, Kearns, Khosla et al. 2008). Osteoprotegerin (OPG) is secreted by osteoblasts and osteocytes and is a soluble decoy receptor for RANKL. RANKL binds OPG with a higher affinity than the RANK receptor, preventing the differentiation of common myeloid progenitors into mature osteoclasts. (Katsimbri 2017). Thus, the RANKL:OPG ratio is key in regulating osteoclast-mediated bone resorption.

OCPs fuse with one another to form mature multinucleated osteoclasts. It is proposed that OCPs do this selectively and recognise their fusion partners based on factors such as nuclearity, intracellular heterogeneity and mobility (Hobolt-Pedersen, Delaissé et al. 2014). It has been found that CD44, along with $\alpha_v\beta_3$ integrin, regulate motility when OCPs and fusion partners migrate and adhere together during multinucleation. $\alpha_v\beta_3$ is an integrin that is a receptor for vitronectin – composed of integrin alpha V and integrin beta 3 (CD61). $\alpha_v\beta_3$ is found at the podosomes at the leading edge of osteoclasts (Yahara, Nguyen et al. 2022). Osteoclast fusion factor, DC-specific transmembrane protein (DC-STAMP) (also known as CD47) and syncytin-1 are involved in OCP fusion (Hobolt-Pedersen, Delaissé et al. 2014, Søe, Hobolt-Pedersen et al. 2015, Søe 2020). In studies with mice deficient in DC-STAMP, d2 isoform of vacuolar (H^+) ATPase (v-ATPase) V0 domain (ATP6v0d2) and osteoclast stimulatory transmembrane protein (OC-STAMP), only osteoclast-like cells with a single nucleus were found (Yagi, Miyamoto et al. 2005, Lee, Rho et al. 2006, Miyamoto, Suzuki et al. 2012). These findings highlight the significance of these proteins for multinucleation during osteoclastogenesis – osteoclasts are comprehensively defined as having 3 nuclei or above.

With the advent of single cell-based methods, the molecular switch triggering terminal differentiation of osteoclasts was identified as Cbp/p300-interacting transactivator with Glu/Asp-rich carboxy-terminal domain 2 (cited2) (Tsukasaki, Huynh et al. 2020). Key markers during osteoclastogenesis are summarised in figure 1.5.

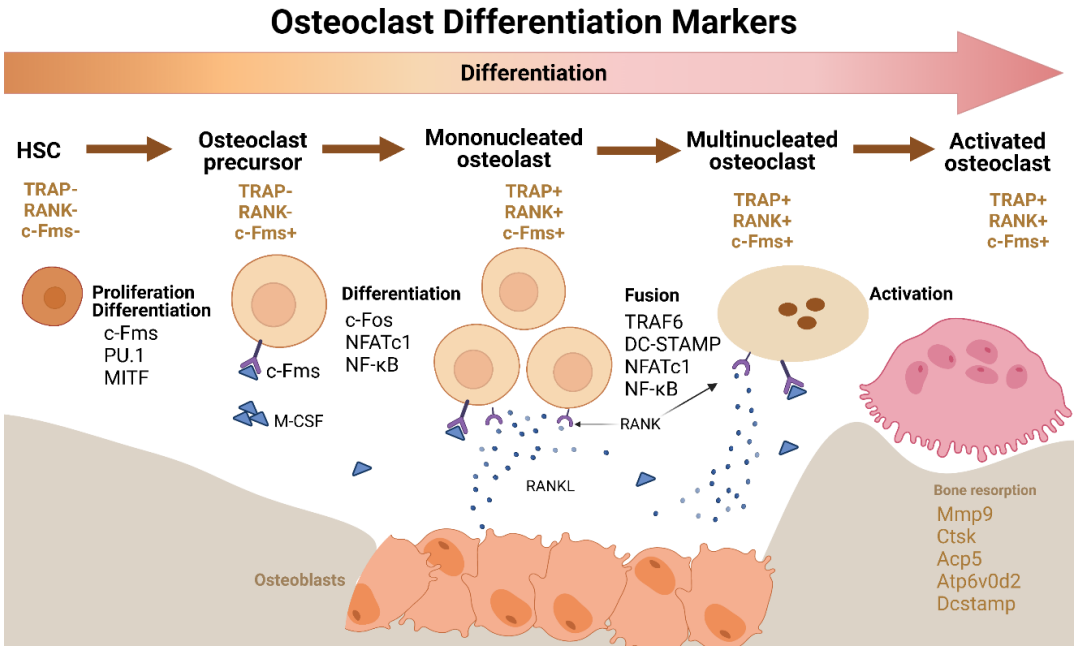

Figure 1.5 Markers expressed during osteoclast differentiation under physiological conditions

Osteoclasts are derived from HSCs in the BM which undergo differentiation into osteoclasts controlled by M-CSF and RANKL signalling pathways (created with BioRender).

1.6.2 Role of osteoclasts in immunity

Although osteoclasts are primarily responsible for breaking down bone tissue, they also play an important role in the immune system.

Due to their shared lineage with macrophages/monocytes, osteoclasts share many characteristics of innate immune cells. Under pathological conditions, they have been shown to partake in antigen presentation, crosstalk with T-cells, along with immune modulation via the release of several different cytokines and other immune mediators that can help to fight infection and disease. The immune

functions of osteoclasts are depicted in figure 1.6.

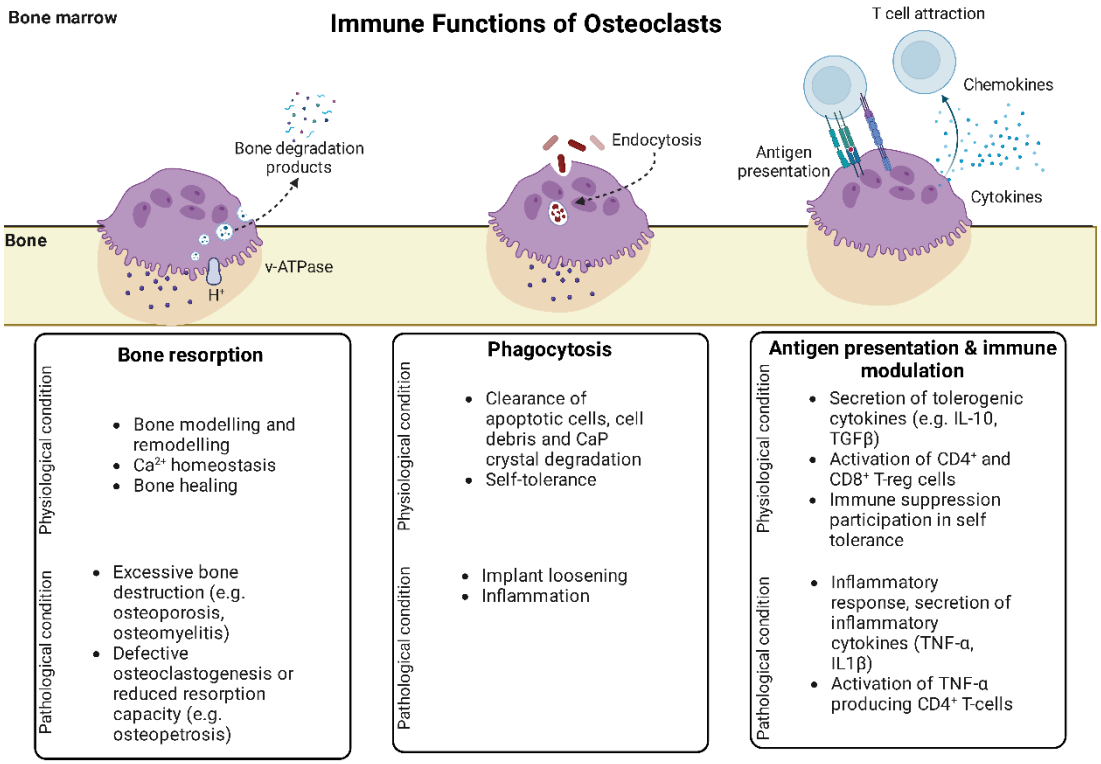

Figure 1.6 The immune functions of osteoclasts during physiological and pathological conditions.

Apart from bone resorption, osteoclasts and innate immune cells share properties of phagocytosis, antigen presentation and immune modulation (Madel 2019). (Created with BioRender).

1.6.3 Phagocytic activity of osteoclasts

Naturally, the most familiar function of osteoclasts is phagocytosis, a characteristic shared with macrophages. Their phagocytic properties not only degrade the bone within the lacunae extracellularly but can of course phagocytose large particles such bacteria, other microorganisms, and abnormal or dead cells. Professional phagocytes (MNs, neutrophils, DCs, osteoclasts) possess receptors that can recognise different microbial components and altered cells, including non-opsonic receptors (e.g. scavenger receptors, C-lectin and lectin-like receptors) and opsonic receptors (e.g. complement receptors, Fc-receptors). This binding results in the invagination of the cell membrane and

formation of a phagocytic synapse with directed cytoskeleton remodelling to engulf particles into phagosomes (Madel 2019).

Phagocytosis by osteoclasts has been demonstrated for large particles such as calcium-phosphate (CaP) crystals (strengthens the bone matrix in mineralised bone), which are too large to undergo normal resorption (Heymann, Guicheux et al. 2001). It has also been shown that osteoclasts recognise damaged or apoptotic neighbouring chondrocytes, osteocytes and even apoptotic thymocytes (immature T-cells) *in vitro* (Soskolne 1978, Boabaid, Cerri et al. 2001, Harre, Keppeler et al. 2012). The capacity of osteoclasts to perform phagocytosis is independent of resorption – as non-polarised osteoclasts can still undergo phagocytosis (Stenbeck and Horton 2000).

1.6.3.1 Antigen-presentation

Antigen presentation is a characteristic displayed by phagocytic cells of myeloid origin. DCs are the most renowned antigen presenting cell (APC). DCs partially degrade the ingested particles to allow degraded peptides to process and present those peptides/antigens via major histocompatibility complex (MHC-II) for antigen presentation. While MHC-I molecules are found on all cells and are used to present intracellular antigens, MHC-II molecules are only found on professional APCs and are used to present exogenous ('non-self') antigens (Madel 2019). Professional APCs that present antigens via MHC-I and MHC-II and bind the T-cell receptor (TCR) found on $CD8^+$ and $CD4^+$ T-cells, respectively. This TCR signalling activates naïve T-cells. The secretion of cytokines by APC also controls the state of differentiation of activated T-cells into regulatory immunosuppressive T-cells or effector T-cells (Th1, Th2, Th17) which promote the inflammatory response.

Interestingly, osteoclasts share these traits of APCs and properties of antigen presentation. Human osteoclasts were shown to express both MHC-I and MHC-II and could engulf soluble antigens on the cell surface, as well as express cytokines IL-1β, IL-6, IL-10, TGF-β, and TNF-α which resulted in activation of both (helper) $CD4^+$ and $CD8^+$ (cytotoxic) T-cells (Li, Hong et al. 2010, Ibáñez, Abou-Ezzi et al.

2016). Moreover, it was found that murine osteoclasts differentiated *in vitro* from macrophages and DCs expressed MHC-II and were capable of presenting antigens as effectively as DCs. This highlights that, although the origin of the osteoclast may differ, their function as an APC is an inherent characteristic of the osteoclast. *In vivo* studies also confirmed the constitutive expression of MHC-II and that antigen presentation had no impact on the cells ability to resorb bone (Ibáñez, Abou-Ezzi et al. 2016).

1.6.3.2 Immune modulation

In recent years, advancements in the understanding of crosstalk between osteoclasts and immune cells have taken place. Under normal physiological conditions, osteoclasts secrete IL-10 and TGF-β which induce immunosuppressive regulatory T-cells (T-reg) which in turn participates in a negative feedback loop, inhibiting osteoclastogenesis and bone resorption (Li 2010). However, in pathogenic conditions, the secretion of TNF-α and IL-1β by osteoclasts activates $CD8^+$ T-cells to produce TNF-α, although the crosstalk between these cells and osteoclasts in inflammatory conditions is unclear (Ibáñez, Abou-Ezzi et al. 2016). Additionally, in pathogenic conditions, osteoclasts can also be derived from immature $CD11c^+$ DCs, with comparable expression of markers and resorption ability to osteoclasts derived from MNs (Alnaeeli, Penninger et al. 2006). Notably, DC-derived osteoclasts stimulate higher levels of proinflammatory cytokines TNF-α, IL-6 and IL-1β and more effectively induce TNF-α^+ $CD4^+$ T-cells compared to MN-derived osteoclasts (Ibáñez, Abou-Ezzi et al. 2016). Moreover, several cytokines have been associated with pro/anti-osteoclastogenic roles, as summarised in table 1.2. In inflammatory conditions where the levels of TNF-α, IL-6 and IL-1β are high, this drives the differentiation of pathogenic osteoclasts (Tamura 1993, Cao 2016, Luo 2018).

Table 1.2 Key pro/anti-osteoclastogenic cytokines *(Amarasekara, 2018).*

Cytokine	Action
Osteoclastogenic cytokines	
RANKL	Induces OC differentiation, survival, proliferation, and maturation
M-CSF	Induces OC differentiation, survival, proliferation, and maturation
TNF-α	Induces RANKL and RANK expression, stimulates OC differentiation
IL-1α	Induces RANKL and OC marker expression, activates MITF induction
IL-1β	Induces RANKL expression and OC differentiation
IL-6	Induces RANKL expression and OC marker expression
IL-7	Induces RANKL expression and TNF-α expression, activates STAT5
IL-8	Induces RANK-mediated NFATc1 activation
IL-11	Induces OC differentiation, increases OC progenitor cells
IL-15	Induces TNF-α and RANKL expression, stimulates OC differentiation
IL-17	Induces RANKL, TNF-α, IL-1 and IL-6 expression
IL-23	Induces RANKL and RANK expression, stimulates IL-17 producing Th17 cell expansion
IL-34	Induces OC differentiation, activates STAT3/Smad7 signalling pathway
Anti-osteoclastogenic cytokines	
OPG	Inhibits OC differentiation (a decoy receptor of RANKL)
IFN-α	Downregulates c-Fos expression
IFN-β	Inhibits RANK- and TLR5-mediated OC differentiation; downregulates JAK1/STAT3/c-Fos signalling pathway
IFN-γ	Inhibits RANKL- and TNF-α-induced OC differentiation; stimulates OC apoptosis
IL-3	Downregulates c-Fms, PU.1, c-Fos, and TNFR expression
IL-4	Inhibits RANKL-induced NFATc1 induction; downregulates TNF-α, IL-1, IL-6, and RANKL expression
IL-10	Downregulates NFATc1, IL-1, TNF-α, and IL-6 production; induces OPG expression
IL-12	Inhibits RANKL- and TNF-α-induced OC differentiation
IL-27	Inhibits RANKL-induced signalling pathway; downregulates IL-17-mediated Th17 cell differentiation
IL-33	Inhibits RANKL-induced OC differentiation; induces OC apoptosis

1.7 Osteoblasts

Osteoblasts are uni-nucleated cells that synthesise the bone and are derived from mesenchymal stem cells (MSCs), which also give rise to myoblasts (muscle), chrondrocytes (cartilage) or adipocyte (fat) lineages. Osteoblastogenesis is characterised by four stages: commitment, proliferation, maturation and mineralisation. Each stage is distinguished by the expression of specific molecular markers (figure 1.7). Several signalling pathways including hedgehog (Hh), Wnt, Notch, bone morphogenetic protein (BMP) and transforming growth factor-beta (TGFβ) are factors involved in osteoblastogenesis.

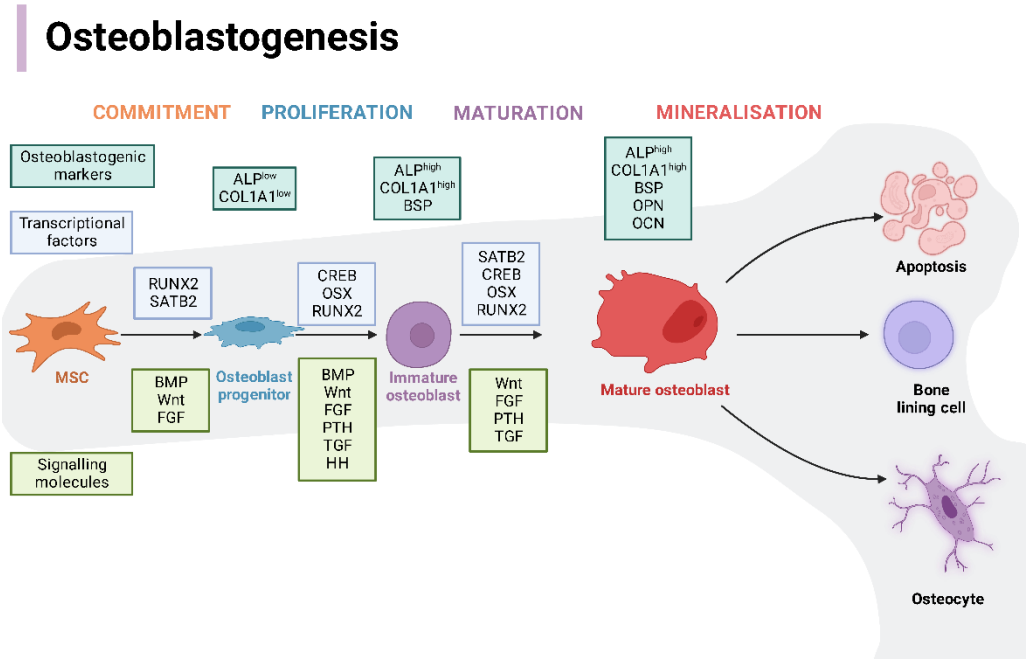

Figure 1.7 Key signalling events in osteoblastogenesis

Osteoblastogenesis is characterised by four stages - commitment, proliferation, maturation and mineralisation - each stage is distinguished by the expression of specific molecular markers (created using Biorender).

1.7.1 Osteoblastogenesis

The differentiation of MSCs into preosteoblasts is controlled transcriptionally by RUNX family transcription factor 2 (Runx2) (Stein, Lian et al. 2004). Once activated, the cells undergo BMP, Wnt and FGF signalling in the commitment phase and become classified as preosteoblasts. Preosteoblasts are described by low concentrations of markers alkaline phosphatase (ALP) and collagen type 1 alpha 1 chain (COL1A1). The proliferation phase denotes the differentiation of the osteoblast progenitor to an immature osteoblast with high concentrations of ALP and COL1A1. Transcriptional regulators are cAMP response element binding protein (CREB), Osterix (OSX) and RUNX2 and signalling occurs through the BMP, Wnt, Fibroblast growth factors (FGF), Parathyroid hormone (PTH), TGF and Hedgehog (HH) pathways (Rutkovskiy, Stensløkken et al. 2016).

The maturation stage which gives rise to the mature osteoblast. Mature osteoblasts are characterised by ALP, COL1A1, osteopontin (OPN), osteocalcin

(OCN), Bone sialoprotein (BSP) markers. Once osteoblastogenesis is completed, they undergo the mineralisation phase. Matrix mineralisation involves the enrichment of the matrix with osteocalcin, which promotes mineral deposits which strengthen the bone. Osteoblasts end up either becoming terminally differentiated bone-lining cells, osteocytes or undergo PCD by apoptosis (Rutkovskiy, Stensløkken et al. 2016).

1.8 Disorders of the Bone

The carefully controlled process of bone remodelling can be perturbed by a variety of events, including hormonal and metabolic changes. If bone homeostasis is disturbed, this can lead to various bone disorders such as osteoporosis, osteoarthritis, and rheumatoid arthritis (excessive bone resorption) or spondylosis (excessive bone formation), as summarised in table 1.3. Disorders due to excess osteoclast activity and bone resorption are more common and have a tendency to be accompanied by hormone deficiencies after the menopause, rheumatoid arthritis, cancer metastasis to the bone, corticotherapy and also due to extended period of sedentary / bedridden lifestyle (e.g. spinal cord injury) (Croucher 2016, Coury 2019, Madel 2019).

Table 1.3 Conditions caused by imbalance in bone homeostasis *(adapted from* (Harty and Jones 2021)*).*

Bone remodelling disorders	**Mechanism**	**Clinical features**	**Treatments**
Osteoporosis	Bone resorption > bone formation	Low bone mass and bone strength, fragile bones	Calcium, vitamin D, selective oestrogen receptor modulator (SERM), oestrogen, bisphosphonates, RANKL antagonists, calcitonin
Oestrogen-deficiency bone loss	Bone resorption > formation	Low bone mass and bone strength	Calcium, vitamin D, oestrogen, bisphosphonates, RANKL antagonists, calcitonin, PTH
Paget's disease of the bone	↑ local bone turnover	Local bone pain and fragility, hearing loss, high-output heart failure	Bisphosphonates
Chronic kidney disease-mineral and bone disorder	↓ Excretion of phosphate ↓ of $1,25(OH)_2D$ (calcitriol) Secondary ↑PTH	Diseased bone that is prone to fracture	Phosphate restriction and binders, calcitriol, or its analogues
Osteoarthritis	Bone resorption > formation	Joint pain, stiffness, and locomotor restriction	Nonsteroidal anti-inflammatory drugs (NSAIDs), Corticosteroids
Spondylosis	Bone formation > resorption	Tingling, numbness, weakness, lack of coordination	NSAIDs, muscle relaxants, opioids

Osteomyelitis refers to the inflammation of the bone caused by pathogenic infection by bacteria, mycobacteria, or fungi. It can result from the dissemination of the pathogen from surrounding tissue, systemic infection, or direct contact/trauma due to injury or trauma. *Staphylococcus aureus* is to blame for two-thirds of all skeletal infections, with an antimicrobial resistance presenting an additional burden for its treatment - up to 50 % of cases of *S. aureus* osteomyelitis are caused by methicillin-resistant *S. aureus* (MRSA) (Dudareva, Hotchen et al. 2019, Masters, Ricciardi et al. 2022). In osteomyelitis, *S. aureus* promotes osteoclast differentiation via stimulation of pro-osteoclastogenic IL-1β, IL-6, and TNF-α, and elicits osteoblast apoptosis (Yoshii 2002, Zwerina, 2004, Dapunt 2014). Less commonly, osteomyelitis is caused by other pathogens such as *Enterococcus* spp., *Pseudomonas aeruginosa*, *Escherichia coli* and

Cutibacterium acnes. It is important to note that whilst most cases of osteomyelitis are due to a single pathogen, polymicrobial infections are common in trauma or fracture related cases in the foot or ankle (Masters 2022). Figure 1.8 represents the main pathogens other than *S. aureus* responsible for osteomyelitis.

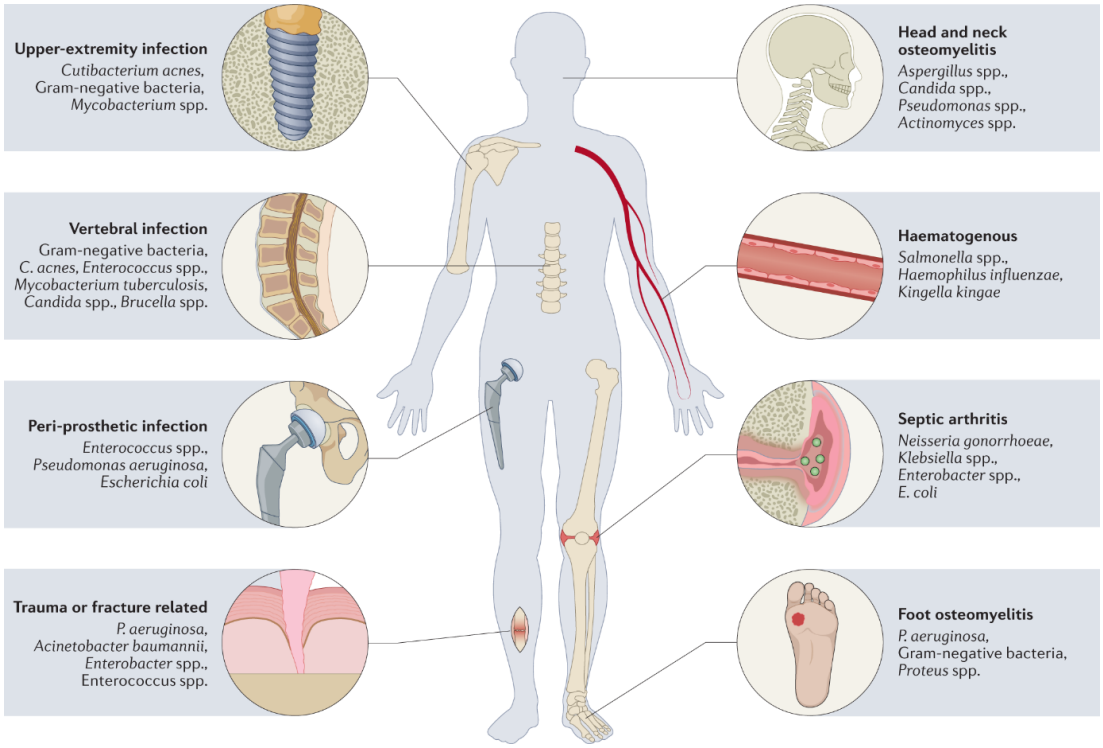

Figure 1.8 Schematic showing pathogens other than S. aureus responsible for bone infections in humans

The human skeleton can be affected by numerous different pathogens other than S. aureus. Mycobacteria primarily infects the upper extremities and the vertebrae (Masters, 2022).

As mentioned, the bone is classified into two structurally distinct types which are – trabecular and cortical. Trabecular bone has a hollow structure which is highly vascularised and therefore oxygen rich. This microenvironment is therefore more favourable for intracellular pathogens such as *Mtb* to reside in compared to cortical bone, which contains more bone matrix, is more mineralised and compact, less vascularised, and less oxygenised (Jabir 2017). In fact, TB is known to especially affect bones that are rich in red bone marrow (Jabir 2017). Spinal TB or Pott's disease, characterised by chronic inflammation and massive bone

resorption of the spinal vertebrae, is a common manifestation of BJTB. A contributing factor could be its proximity to the lungs containing the alveolar macrophages (AMs). Interestingly, a connection between inflammation of the lungs brought on by conditions like cystic fibrosis, asthma, and chronic obstructive pulmonary disease (COPD) and severe acute respiratory syndrome coronavirus 2 (SARS-CoV-2) has been linked to systemic bone loss (Qiao, Lau et al. 2022). This is also true of *Mtb* infection, which begins in the respiratory tract and spreads to the bones and joints through the blood (Jabir, 2017).

1.9 *Mtb* interactions in the bone microenvironment

1.9.1 *Mtb* interactions with Osteoclasts

Raynaud-Messina *et al* presented two hypotheses for the pathogenesis of Spinal TB or Pott's disease, which leads to aberrant bone resorption accompanied with chronic inflammation. Firstly, they posed that it could be initiated because of abnormal activation of macrophages and their precursors to the infection site, which then release proinflammatory, pro-osteoclastogenic cytokines which result in the pathogenesis. This has not been validated (Raynaud-Messina, Verollet et al. 2019). The second hypothesis is that osteoclasts themselves can be targeted by *Mtb* and reprogrammed into abnormal overactivity (Raynaud-Messina, Verollet et al. 2019). It is likely a combination of both factors. Meghji *et al* established a dose-dependent increase in the bone resorption and osteoclast number in response to the sonicates of *Mtb* to explants of murine calvarial bone, reporting chaperonin protein (cpn) 10 to be responsible for the osteolytic activity (dissolution of bone). The cpn10 protein is a potent stimulator of bone resorption, induces osteoclast recruitment, and is apparently as potent as osteolytic cytokine IL-1 (Meghji, White et al. 1997).

Hoshino *et al.* (2014) discovered that *Mtb* could infect osteoclasts directly. They demonstrated that internalisation of H37Rv virulent *Mtb* strain in both mononuclear osteoclast precursors and mature multinuclear osteoclasts (Hoshino 2014). Infection of osteoclast precursor cells saw an increase in

production of proinflammatory cytokines (TNF-α, IL-6 and IL1-β), a characteristic shared with macrophages. Interestingly, TNF-α, IL-6 and IL1-β are pro-osteoclastogenic cytokines and the authors suggest that osteoclastogenesis of these precursors are favoured during infection (Hoshino 2014). In comparison, *Mtb* infection of mature osteoclasts lead to the incapacitation of the production of pro-inflammatory cytokines TNF-α, IL-6 and IL1-β but resulted in a different expression profile of chemokines (CCL5, CCL17, CCL20, CCL22, CCL24, and CCL25) (Hoshino 2014). Also, when *Mtb*-infected mature osteoclasts were visualised with electron microscopy, there was no endosome/phagosome membrane surrounding the intracellular bacilli. This shows that intracellular *Mtb* was able to escape from the phagosome, which could have allowed the population to rapidly expand. Notably, *Mtb* infection of mature multinuclear osteoclasts lead to dysregulation of cytokines and chemokines, reprogramming osteoclast development (Hoshino 2014).

Mtb infection was also shown to influence the number of osteoclasts (Liu, Jia et al. 2015, Yi, Li et al. 2018, Liu, Zhou et al. 2020). In a rabbit model of osteoarticular tuberculosis, Liu *et al* discovered that the frequency of osteoclasts increased, while the frequency of osteoblasts decreased (Liu, Jia et al. 2015). Likewise, in osteoarticular tuberculosis bone samples from affected TB patients, the number of osteoclasts in the legions similarly increased compared to bone samples from patients with osteoarthritis alone (Liu, Zhou et al. 2020). Liu *et al* supported their findings by showing a possible mechanism of pathogenesis of osteoarticular tuberculosis involving TNF-α. For this, they showed that TNF-α treatment inhibited apoptosis of osteoclasts infected with *Mtb* by activating autophagy (Liu, Zhou et al. 2020).

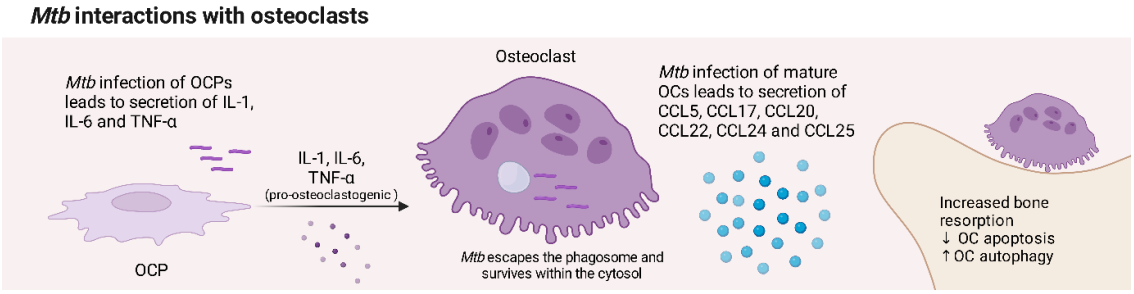

Figure 1.9 Schematic to summarise the known interactions between Mtb and osteoclasts during bone TB

Mtb infects both OCPs and mature osteoclasts and leads to differing responses resulting in increased bone resorption.

1.9.2 *Mtb* interaction with Osteoblasts

As discussed, TB osteomyelitis is characterised by uncontrolled inflammation and severe bone loss. The exploration into *Mtb* interactions with osteoblasts has been limited so far but it has been indicated that osteoblasts can participate in the host response against *Mtb*. Early studies show that human osteoblasts secrete chemokines known to attract leukocytes in response to *Mtb* infection. A study using normal human osteoblasts (NHO) and osteoblast-like cell line MG-63 and infecting them with *Mtb* showed secretion of the chemokines interleukin (IL)-8, inducible protein (IP)-10, RANTES, and monocyte chemoattractant protein (MCP)-1 (CCL2). Nuclear localisation of (AP)-1, transcription factor activator protein of promoter regions of IL-8, RANTES, MCP-1, and IP-10 was also observed (Wright and Friedland 2002). Another study by the same authors showed that harvested medium from *Mtb* infected MG-63 drove gene expression and secretion of CXCL8 and CCL2 from primary human MNs. This was discovered to be regulated in part by IL-1 and TNF-α using IL-1R and anti-TNF-α blockades (Wright and Friedland 2004).

The role of osteoblast apoptosis in *Mtb* infection has also been studied. Yi *et al* have shown that *Mtb* lysate significantly induced osteoblast apoptosis, along with enhancing RANKL expression and decreasing osteoprotegerin (OPG) expression *in vitro* (Yi, Li et al. 2018). Transcriptomic techniques were employed to identify

mycobacterial genes important for the *in vivo* pathogenesis of bone TB. Transcriptomic profiling of *Mtb* within abscesses or necrotic bone TB patient samples using whole genome microarrays revealed metabolic switching of *Mtb* to a hypo-metabolic state combined with cell wall remodelling to a strengthened state to enhance survival (Kaur, Sharma et al. 2022). Kaur *et al* then developed an *in vitro* infection model of osteoblasts using the MC3T3 osteoblast cell line. Transcriptome analysis of *Mtb* from the infection model revealed virulence genes *Rv1046c, DppD* and *PE_PGRS26* that were also found in human bone TB microarray data (Kaur, Sharma et al. 2022).

1.9.3 Relevance of EPTB strain in bone dysfunction

Notably, an ancestral variant of *Mtb* with high rates of bone dissemination was found with a functional variant in the ESX-5 secreted effector EsxM. This variant of EsxM was able to alter the macrophage cytoskeleton, enhance motility, and was associated with granuloma efflux and particularly dissemination into the bone (Saelens, Sweeney et al. 2022). Furthermore, a 2016 study found that strains of *Mtb* differ in affinity for human osteoblasts of the SaOS-2 cell line, human alveolar epithelial cells (A549) and murine alveolar macrophages (MHS) *in vitro* (Sarkar, Dlamini et al. 2016). Drug susceptible, multi-drug resistant (MDR) and extensively-drug resistant (XDR) *Mtb* strains were used. The MDR and XDR strains had a higher invasion capacity for the A549 and MHS cells, compared to SaOS-2 (Sarkar, Dlamini et al. 2016). However, the drug susceptible strain exhibited a higher propensity for SaOS-2 cells (Sarkar, Dlamini et al. 2016). It was proposed that EPTB development can be dependent upon the particular *Mtb* strain, as they likely have differing aptitudes for passing through the alveolar epithelial lining, as well as affinity for cells outside of the lungs (Sarkar, Dlamini et al. 2016).

1.10 Project rationale and aims

The specific molecular interactions in mycobacterial infection of the bone remain unknown. Due to the extensive evidence connecting osteoclasts to the immune response, we aimed to investigate the phenotypic and transcriptomic response of bone cells during mycobacterial infection.

We first aimed to validate and characterise the differentiation protocol of murine bone marrow cells into osteoclast-like cells (OCLs). Then, with *in vitro* and *in vivo* infection models, we aimed to decipher the infection-dependent phenotypic changes and analyse the transcriptome to identify differentially expressed genes upon infection.

Hypothesis

We hypothesise that tuberculosis osteomyelitis, which is characterised by mass bone resorption and inflammation, is due to a dysregulation of bone homeostasis due to an overactivity of osteoclasts. The increased frequency of osteoclasts evidenced in previous literature may be due to an increase in the fusion of osteoclast precursors and involves the release of pro-osteoclastogenic factors which drives this process.

Specific aims for this project are:

• To characterise the osteoclast-like cells (OCLs) from murine bone marrow cells.

- Phenotypic characterisation using molecular, microscopic, and immunological methods.
- Transcriptomic characterisation by bulk RNA-sequencing.

• To investigate the effect of BCG infection on bone cells *in vitro.*

- Employ immunological, molecular, microscopic, and transcriptomic techniques to investigate OCLs during *in vitro* infection.
- Use *in vitro* assays to determine effect of BCG infection on MG-63 osteoblast-like cell line.
- Transcriptomic analysis of *in vitro* infected OCLs.

- To investigate the effect of BCG infection on bone cells *in vivo.*
  - Use of Micro-Computational Tomography (μCT) to study the alterations in bone structure during infection.
  - Transcriptomic analysis of OCLs from BCG infected mice.

Chapter 2 Methods and Materials

2.1 Eukaryotic cell line culture

Osteoblast-like cells of the MG-63 cell line (ATCC) were maintained in Eagle's Minimum Essential Medium (EMEM) (Sigma, M5650) with 10 % foetal bovine serum (FBS), 2 mM L-glutamine and 1 % non-essential amino acids (NEAA). Sub-culturing was carried out using the recommended sub-cultivation ratio of between 1:4 and 1:8 every 3-5 days using the standard trypsin-EDTA method. Medium renewal was done 2-3 times a week. Cells were incubated in T75 flasks at 37°C, 5 % CO_2.

Monocytes of the THP-1 cell line (ATCC) were maintained in RPMI medium (Sigma) supplemented with 10 % FBS, 2 mM L-glutamine. When the cell concentration reached $8x10^5$ cells /ml the cells would be subcultured by the addition of the desired volume of cells in spent media to a new T75 flask and topped up to 10 ml with fresh media. THP-1 cells were also incubated in T75 flasks at 37°C, 5 % CO_2.

2.2 Primary cell culture

2.2.1 Ethics statement

All mouse procedures performed at the Infectious Diseases Labs (ID Labs) and Singapore Immunology Network (SIgN) were reviewed and approved by the BRC (Biological Resource Centre), A*STAR Institutional Animal Care and USE Committee (IACUC #181399). The guidelines for housing and care of laboratory animals were followed in accordance with institutional regulations of the National Advisory Committee for Laboratory Animal Research (NACLAR).

NLRP3 knockout (KO) mice were obtained from Dr Jurg Tschopp, University of Lausanne. NLRP targeting vector was electroporated into C57BL/6 embryonic stem (ES) cells (Ozgene). Southern blot analysis was used to identify

homologous recombinant ES and then microinjected into C57BL/6 blastocysts. Offspring were backcrossed to C57BL/6 mice. PCR of the tail genomic DNA confirmed the germline transmission (Martinon 2006).

2.2.2 Murine osteoclast-like cell generation

6–12-week-old donor C57BL/6 WT or knockout mice were killed using CO_2 inhalation and cervical dislocation. Two leg bones from each mouse were harvested and hair was removed along with muscle as cleanly as possible, using a C-fold where needed. Bones were soaked in 70 % ethanol for 5-10 mins, then washed once in PBS. The ends of bones were cut, and bone marrow was flushed out with PBS using a 25-G needle through a 70 μM cell strainer. Cell aggregates were separated as well as possible using a 1 ml syringe and a 25-G needle by drawing the cell suspension in and out of the syringe. Then, cell suspension was flushed through a 70 μm cell strainer and into a 50 ml conical centrifuge tube. Following this, cells were centrifuged for 7 mins at 1500 rpm, 4°C. Cells were re-suspended in 2 ml ACK lysis buffer and left at room temperature for 5 mins. Osteoclast media (α-MEM, 5 % FBS, 2 mM L-glut, 50 μM β-ME, 1 % P/S) was used to top up to 20 ml for neutralisation. The suspension was spun down for 5 mins, 1500 rpm, 4°C followed by re-suspension in 3 ml osteoclast medium. Cells were counted on a haemocytometer using the trypan blue exclusion method and plated at $1x10^6$ /ml in 6 well plates overnight.

The next day, the non-adherent cells were removed by pipetting media up and down and transferred into a 50 ml Falcon tube and centrifuged at 1500 rpm for 7 mins at 4°C. Viable cells were counted and plated at $0.4x10^6$ /ml with 30 ng/ml rh-MCSF for 2 days. On day three, total media was changed and supplemented with 30 ng/ml rh-MCSF and 30 ng/ml rh-RANKL. On day six, half the media was removed and replenished with OCL media supplemented with 60 ng/ml rh-MCSF and 60 ng/ml rh-RANKL. OCLs were harvested at day seven.

A schematic of the methodology is shown in figure 2.1.

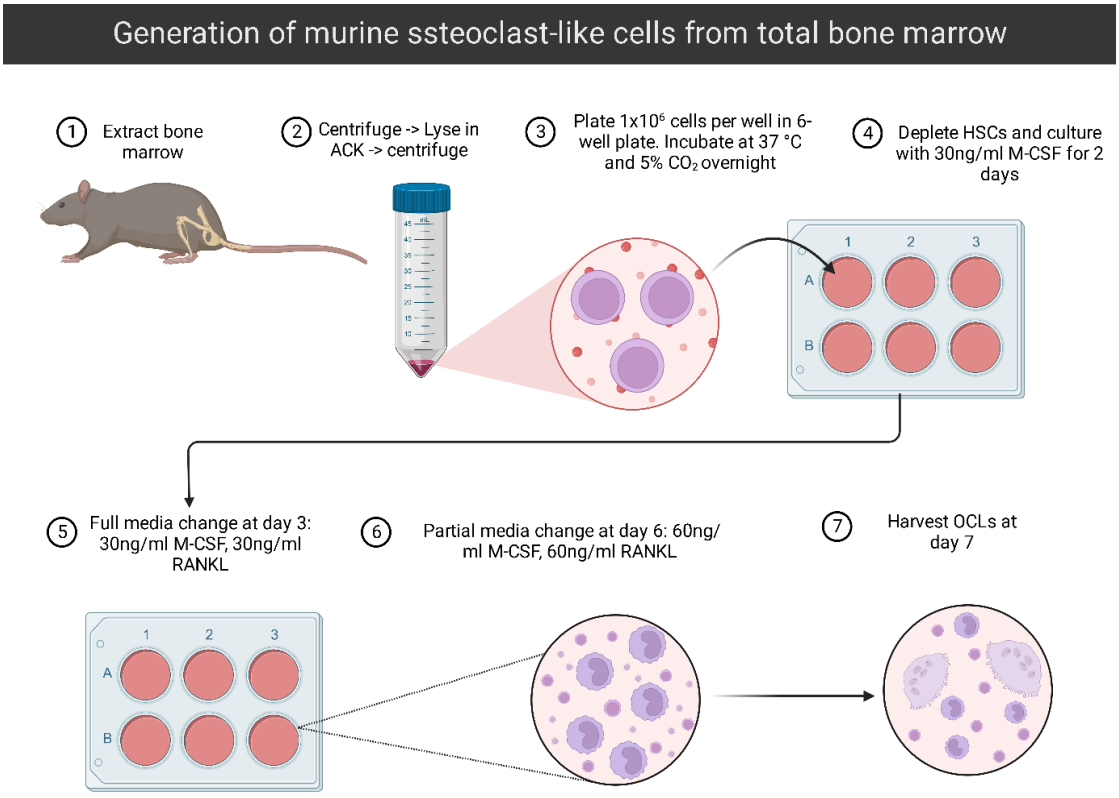

Figure 2.1: Schematic diagram for generating osteoclast-like cells (OCLs) from murine bone marrow cells involving a 7-day differentiation under the influence of M-CSF and RANKL *(created using BioRender).*

2.2.3 Preparation of osteoclast-like cells for sorting

For preparation of osteoclast-like cells for FACS, media was removed from wells. Cells were washed once with FACS sort buffer (1X PBS, 2 % FCS, 0.5 M EDTA) and incubated with 500 µl Accutase (StemCell) at 37°C for 30 mins. After extensive washing with PBS, detached cells were collected in a 50 ml falcon tube containing FACS sort buffer and were centrifuged at 1500 rpm for 5 mins at 4°C. Then, cells were re-suspended in 1 ml FACS sort buffer and stained with Hoechst 33342 (1:500) and AmCyan (1:1000) incubated for 15 mins on ice and underwent a final FACS sort buffer wash. Cells were filtered through a 100 µm nylon mesh prior to sorting with an Aria II 5L. Singlets with 1–2 nuclei (1-2N) and ≥3 nuclei (≥3N) were selected by a histogram display of Hoechst fluorescence and sorted into separate tubes with OCL media containing FBS.

2.2.4 Immunophenotyping of osteoclast-like cells

Aria II 5L can be used to simultaneously sort and analyse cells. Protocols were followed as above to generate, detach and stain OCLs with Hoechst 33342 and AmCyan. For further analysis of surface markers, cells were stained with antibodies against CD44, CD45, Gr-1 and CD51 (details in table 2.1) for 25 mins on ice in the dark followed by washing with FACS sort buffer. Cells were filtered through a 100µm nylon mesh prior to sorting with an Aria II 5L. Samples were analysed on FlowJo Version 10.6.1.

Table 2.1 Immunophenotyping panel for murine osteoclast-like cells by flow cytometry

Ab	Labelling	Isotype/ Host	Clone	Cat.-Nr.	Company	Dilution
LIVE/DEAD™	AmCyan	-	-	L34957	Invitrogen	1/1000
Fc (mouse) CD16/32	-	Rat IgG2a, λ	93	101319	Biolegend	1/80
Hoechst 33342	DAPI	-	-	62249	Thermo Fisher	1/1000
Gr-1	PE	Rat IgG2b, κ	RB6-8C5	108407	Biolegend	1/400
CD45	FITC	Rat IgG2b, κ	30-F11	103107	Biolegend	1/400
CD44	BV650	Rat IgG2b, κ	IM7	103049	Biolegend	1/400
CD51	Biotin	Rat IgG1, κ	RMV-7	104103	Biolegend	1/800
Streptavidin	APC	-	-	405207	Biolegend	1/100

2.2.4.1 Immunophenotyping of murine bone marrow cells

Total bone marrow was extracted from the hind legs of 6–12-week-old donor C57BL/6 mice that had been killed using CO_2 inhalation and cervical dislocation. Staining was performed following the panel as below on the day of sacrifice on two million bone marrow cells per sample. Controls included were unstained cells, cells only stained with live/dead stain, Fluorescence Minus One (FMO) control with all markers stained except CD115. Samples were acquired on a BD LSRFortessa™ and analysed on FlowJo Version 10.6.1. The panel for immunophenotyping of BM cells is shown in table 2.2.

Table 2.2 Immunophenotyping panel for murine bone marrow by flow cytometry

Ab	Labelling	Isotype/Host	Clone	Cat.-Nr.	Company	Dilution
LIVE/DEAD ™	AmCyan	-	-	L34957	Invitrogen	1/1000
Fc (mouse)	TruStain FcX™ (anti-mouse CD16/32)	Rat IgG2a, λ	93	101319	Biolegend	1/80
CD3	PerCP-Cy5.5	Rat IgG2b, κ	17A2	100217	Biolegend	1/200
c-Kit (CD117)	Super Bright 436 (PB)	Rat IgG2b, κ	2B8	105819	Biolegend	1/400
CD11b	BV650	Rat IgG2b, κ	M1/70	101239	Biolegend	1/400
CD27	PE-Cy7	Armenian Hamster IgG	LG.3A10	124215	Biolegend	1/800
CD45R (B220)	FITC	Rat IgG2a, κ	RA3-6B2	554880	BD Pharm	1/100
CD70	PE	Rat IgG2b, κ	FR70	104605	Biolegend	1/200
CD115	APC	Rat IgG2a, κ	AFS98	135509	Biolegend	1/100

2.3 Mycobacterial culturing

Liquid cultures of *M. bovis* BCG were grown at 37°C, shaking at ~180 rpm in Middlebrook 7H9 broth supplemented with 10 % albumin, dextrose, catalase (ADC), 0.05 % sterile Tween-80 and 0.5 % glycerol. Solid cultures of *M. bovis* BCG were sustained on 7H11 agar plates supplemented with 10 % ADC and 0.5 % glycerol. BCG-GFP and BCG-ds red cultures were cultured in the same way as the wild type, except with the addition of 50 µg/ml hygromycin. Optical densities to be measured using a spectrophotometer at a wavelength of 600 nm. Cultures were incubated at 37°C, 5 % CO_2.

To create frozen glycerol stocks, 900 µl of log phase BCG culture (OD of 0.4 – 0.8) was mixed with 300 µl of autoclaved sterile 80 % glycerol in a cryo-tube to give a final concentration of 20 % glycerol in 1.2 ml. Stocks were stored in a –80˚c freezer. CFU of working stocks was determined after 1 week whereby the bacteria were plated on 7H11 agar with the following dilutions: 10^{-4} ,10^{-5}, 10^{-6}

and 10^{-7}. After 2 weeks of incubation at 37°C, 5 % CO_2, the colonies were counted to determine the number of colonies/ml using the following equation:

$$\text{CFU/ml: } \frac{no.of\ colonies\ X\ dilution\ factor}{Amt\ used\ during\ plating}\ X\ 1000$$

2.4 BCG infection assay models

2.4.1 *In vitro* BCG infection model for osteoblast-like cells

Adherent cells (MG-63, at 70-80 % confluence, at passage below 15) were seeded at 50,000 cells per well of 96 well plate or 200,000 cells per well of 24 well plate or 500,000 cells per well of 6-well plate, with antibiotic-free media the day before infection. Working BCG stocks of a pre-determined CFU were thawed and diluted in 10 ml antibiotic-free media and centrifuged for 10 mins at 3800 rpm, followed by sonication for 5 mins. Antibiotic-free media was then used to top up BCG and added to cells at an MOI of 5:1. One well was trypsinised and used for counting of cells for MOI. Cells were incubated for 3 h at 37°C, 5 % CO_2. Then, infected cells were washed with PBS to remove extracellular BCG and antibiotic-free media was replaced for subsequent time points. For CFU determination, cells were washed with PBS and then lysed in 0.06 % SDS for 10 mins. Lysates were plated in dilutions of PBS at 10^0, 10^{-1}, 10^{-2}, 10^{-3} on 7H11 agar and incubated at 37°C for 14 days after which colonies were counted and CFU was determined as described above.

2.4.2 *In vitro* OCL BCG infection model for osteoclast-like cells

In vitro infection of OCLs took place at day 6 of the differentiation protocol listed (fig 2.1). One well was trypsinised and used for counting of cells for MOI. Then, cells were infected with BCG at an MOI of 5 for 3 hrs. Upon this, infected cells were washed with PBS to remove extracellular bacteria and media was replaced to a final concentration of 45 ng/ml rh-RANKL and rh-MCSF. Uninfected cells were subjected to a partial media change (half the media was

removed and replaced with 60 ng/ml rh-MCSF and 60ng/ml rh-RANKL so the final concentration was 45 ng/ml).

2.4.3 *In vivo* BCG infection model

6–12-week-old mice were infected intra-venously (i.v) with 10^6 BCG in 100 µl PBS and control age and gender matched mice were injected i.v with PBS alone. After 30 days as indicated, mice were sacrificed alongside control mice. BM cells were differentiated into OCLs following the protocol shown in figure 2.1.

2.5 TRAP staining

Tartrate-resistant acid phosphatase (TRAP) is a known marker for osteoclasts and staining for this marker was performed to visualise its activity during differentiation or to compare its activity during uninfected and infected states. TRAP staining was conducted using a TRAP staining kit (Wako, catalogue No: 294-67001) on OCLs during differentiation at specified time points or at day 7. Media was removed from OCLs in a 24 well plate and cells were washed with PBS. PBS was removed and 500 µl of pre-cold fixative (4 % PFA in PBS) was added and incubated on ice for 10 mins. Cells were washed 3 times with PBS and 500 µl of Ethanol/Acetone 50 : 50 v/v was added and incubated for 1 minute at −20°C. Cells were washed 3 times with PBS. TRAP stain solution was prepared. For 1 ml: Sodium tartrate soln. (× 10): 100 µl. TRAP substrate soln. A: 900 µl. TRAP substrate soln. B: 10 µl. 250 µl/well of TRAP stain was added and the plate was incubated at 37°C for 15~45 mins. The reaction was stopped by diluting the reaction solution by washing with distilled water. Cells were imaged using an EVOS light microscope at 4X and 20X magnification. Cells that were $TRAP^+$ with 3 or more nuclei were counted from 20X non-overlapping images so that a total of at least 100 cells were counted.

2.6 ALP staining

Alkaline phosphatase (ALP) is an enzyme secreted by osteoblasts and is a marker of osteoblast differentiation. ALP staining was conducted using an ALP

staining kit (Wako, catalogue No: 294-67001) to visualise ALP activity of osteoblast-like cell line MG-63 during uninfected and *in vitro* BCG infected conditions. Media was removed from MG-63 cells in a 24 well plate and cells were washed with PBS. PBS was removed and 500 µl of pre-cold fixative (4 % PFA in PBS) was added and incubated on ice for 10 mins. Cells were washed 3 times with PBS and 500 µl of Ethanol/Acetone 50 : 50 v/v was added and incubated for 1 min at –20°C. Cells were washed 3 times with PBS. 250 µl of the premixed ALP substrate solution was added to each well, the plate was covered to prevent the wells from drying and placed at 37°C for 15~45 mins. The reaction was then stopped by diluting the wells with 2 ml of DDW per well, followed by removal of the solution from the wells and washing of the wells thrice more. Cells were imaged using an EVOS light microscope at 4X and 20X magnification. ImageJ was used to quantify ALP activity. The FIJI plugin Trainable Weka Segmentation was used to quantify ALP activity.

2.7 Reverse transcription polymerase chain reaction

2.7.1 RNA extraction

RNA work was carried out in an RNAse free environment. Firstly, cells were lysed in TRIzol and 0.2 ml chloroform was added for every 1 ml TRIzol used. Sampled were shaken vigorously for 15 sec and incubated at room temperature for 3 mins. Samples were then centrifuged at max speed for 10 mins at 4°C. Then, the upper colourless aqueous phase was added to a new Eppendorf tube along with 1 volume of 70 % ethanol to the clear lysate and these were mixed by pipetting. The Qiagen RNeasy (Catalogue No: 74106) protocol was followed for RNA extraction and all subsequent centrifugations were carried out at room temperature at max speed. Up to 700 µl of sample was loaded onto the RNeasy mini column. Samples were then centrifuged for 15 sec. Then, the flow through was discarded, but not the collection tube. 700 µl of Buffer RW1 was loaded into the same RNeasy mini column and centrifuged again for 15 sec and flow through was discarded. The column was transferred into a new collection tube and 500 µl Buffer RPE was added onto the column and centrifuged for 15 sec

and flow through was again discarded. Another 500 µl Buffer RPE was added to the column and centrifuged for 2 mins. Flow through was discarded and RNA was eluted with 30-50 µl RNase-free water in a 1.5 ml RNAse free collection tube by centrifugation for 1 min. Eluted RNA was stored at –80°C.

The concentration of RNA was measured in ng/µl using a Nanodrop 2000 spectrophotometer (Thermo Scientific). The A260/A230 and A260/280 ratios were also recorded. A A260/A230 ratio between 2.0 – 2.2 was considered pure, as this ratio highlighted contaminants that absorb at 230 nm. A A260/280 ratio of 2.0 was considered pure, as a number below this would suggest the presence of protein, phenol or other contaminants that absorb at 280 nm.

2.7.2 Reverse transcription of RNA

For cDNA synthesis, the Bio-Rad iScript Advanced cDNA Synthesis Kit for RT-qPCR (Bio-Rad, Catalogue No: 1725038) was used. Briefly, (as in table 2.4) each 20µl reaction mastermix consisting of an input of 2 µg RNA template, iScript Advanced Reverse Transcriptase, 5x iScript Advanced Reaction Mix was incubated at 46°C for 20 mins for reverse transcription in a thermocycler. To inactivate the reverse transcriptase, the reaction was incubated at 95°C for 1 min and held at 4°C.

Table 2.3 cDNA synthesis reaction set-up

Component	**Volume per Reaction (µl)**
5x iScript Advanced Reaction Mix	4
iScript Advanced Reverse Transcriptase	1
RNA sample	Variable (2 µg)
Nuclease-free water	To 20
Total volume per reaction	20

2.7.3 Designing PCR primers

Primers for RT-qPCR were ordered from Integrated DNA Technologies (https://sg.idtdna.com/) and primers were designed using National Centre for

Biotechnology Information (NCBI) Primer Blast (https://www.ncbi.nlm.nih.gov/tools/primer-blast/)

Primers were designed according to the following considerations:

- Product size: 100-180bp
- Primer size: 18-22bp
- Primer Tm: 58-62°C
- Primer GC%: < 50 %
- Sequence type: Linear

Mouse primers used are listed in table 2.4. Human primers are listed in table 2.5.

Table 2.4 Mouse primers used for RT-qPCR

Target	**F/R**	**Sequence (5'-3')**
Mouse *NFATc1*	F	TCATCGGCGGGAAGAAGATG
Mouse *NFATc1*	R	GTCCCGGTCAGTCTTTGCTT
Mouse *CTSK*	F	GAAGGGAAGCAAGCACTGGA
Mouse *CTSK*	R	CCATGTTGGTAATGCCGCAG
Mouse *CTR*	F	TCACAAGCACGCGGACAATGT
Mouse *CTR*	R	TGCCAACCATTATCCACGCCA
Mouse *Acp5*	F	GGCCGGCCACTACCCCATCT
Mouse *Acp5*	R	GCCGGCCCCACTCAGCACATAG
Mouse *Dc-stamp*	F	TTTGCCGCTGTGGACTATCTGC
Mouse *Dc-stamp*	R	GCAGAATCATGGACGACTCCTTG
Mouse *Atp6v0d2*	F	ACGGTGATGTCACAGCAGACGT
Mouse *Atp6v0d2*	R	CTCTGGATAGAGCCTGCCGCA

Table 2.5 Human primers used for RT-qPCR

Target	**F/R**	**Sequence (5'-3')**
Human *ALP*	F	ATGGGATGGGTGTCTCCACA
Human *ALP*	R	CCACGAAGGGGAACTTGTC

Human *RUNX2*	F	CACTGGCGCTGCAACAAGA
Human *RUNX2*	R	CATTCCGGAGCTCAGCAGAATAA
Human *COL1A1*	F	GCTCGTGGAAATGATGGTGC
Human *COL1A1*	R	ACCCTGGGGACCTTCAGAG
Human *RANKL*	F	AGAGCGCAGATGGATCCTAA
Human *RANKL*	R	TTCCTTTTGCACAGCTCCTT
Human *TLR2*	F	GGCCAGCAAATTACCTGTGTG
Human *TLR2*	R	AGGCGGACATCCTGAACCT
Human *TLR4*	F	TGGTGGAAGTTGAACGAATGG
Human *TLR4*	R	AGGACCGACACACCAATGATG

2.7.4 Real-time Quantitative Polymerase Chain Reaction (RT-qPCR)

The previously obtained cDNA was used to determine gene expression using the iTaq Universal SYBR Green Supermix (Bio-Rad, Catalogue No: 172-5122). RT-qPCR for gene expression was performed using a CFX Connect™ Real-Time PCR Detection System (Bio-Rad) according to the iTaq Universal SYBR Green Supermix protocol. The previously obtained cDNA was diluted with RNAse free water so that the input amount was 1 µg, with the reaction set up as in table 2.6. Reactions were performed in duplicate or triplicate and relative normalised expression was automatically calculated by the Bio-Rad CFX Manager 3.1 software.

Table 2.6 Reaction setup for RT-qPCR

Reaction Setup		
Component	**Volume per 20µl reaction**	**Final concentration**
iTaq Universal SYBR Green supermix (2x)	10 µl	1x
Forward and reverse primers	Variable	1 µg
DNA template	Variable	cDNA: 100 ng-100 fg
H_2O	Variable	-
Total reaction mix volume	20 µl	-

2.8 Bulk RNA-sequencing

2.8.1 RNA isolation and sequencing library construction

Bulk RNA-sequencing was conducted to provide insight into transcriptomic changes upon OCL differentiation (chapter 3) or identify differentially expressed genes upon *in vitro* or *in vivo* BCG infection (chapter 5). RNA isolation and library construction of murine samples (as in figure 2.3) was performed by Lolita Fong and Foo Shihui of the Immunogenomics Team at Singapore Immunology Network (SIgN). The sorting strategy used by FACS and the number of cells collected for all 37 samples is shown in figure 2.2 and table 2.7.

Table 2.7: The number of cells after FACS used per library for each sample for bulk RNA-sequencing for 37 samples.

Sample Description	Sample amount
Uninfected OCLs with 1-2 nuclei	1192872
Uninfected OCLs with >3N nuclei	13204
Infected OCLs with 1-2 nuclei	2001727
Infected OCLs with >3 nuclei	17795
Uninfected OCLs with 1-2 nuclei	1694132
Uninfected OCLs with >3N nuclei	110323
Infected OCLs with 1-2 nuclei	1404227
Infected OCLs with >3 nuclei	74882
Uninfected OCLs with 1-2 nuclei	3881036
Infected OCLs with 1-2 nuclei	3113985
Infected OCLs with >3 nuclei	78420
Uninfected OCLs with 1-2 nuclei	4006987
Infected OCLs with 1-2 nuclei	2722766
Infected OCLs with >3 nuclei	156811
In vitro infected OCLs with 1-2 nuclei	647463
In vitro infected OCLs with 1-2 nuclei	776558
In vitro infected OCLs with >3 nuclei	13650
Uninfected OCLs with >3N nuclei	58399
In vivo infected OCLs with 1-2 nuclei	849583
In vivo infected OCLs with >3 nuclei	69755
In vivo infected OCLs with 1-2 nuclei	1207736
In vivo infected OCLs with >3 nuclei	59094
Osteoclast precursor cells from WT mouse 1	800000
OCLs with 1-2N nuclei from WT mouse 1	1.1x10^6
OCLs with >3N nuclei from WT mouse 1	60102
Osteoclast precursor cells from WT mouse 2	800000
OCLs with 1-2N nuclei from WT mouse 2	1.12x10^6
OCLs with >3N nuclei from WT mouse 2	469931
Osteoclast precursor cells from BCG mouse 1	800000
OCLs with 1-2N nuclei from BCG mouse 1	790724
OCLs with >3N nuclei from BCG mouse 1	17396
Osteoclast precursor cells from BCG mouse 2	800000
OCLs with 1-2N nuclei from BCG mouse 2	1.05X10^6
OCLs with >3N nuclei from BCG mouse 2	16524
Osteoclast precursor cells from BCG mouse 3	800000
OCLs with 1-2N nuclei from BCG mouse 3	996471
OCLs with >3N nuclei from BCG mouse 3	16436

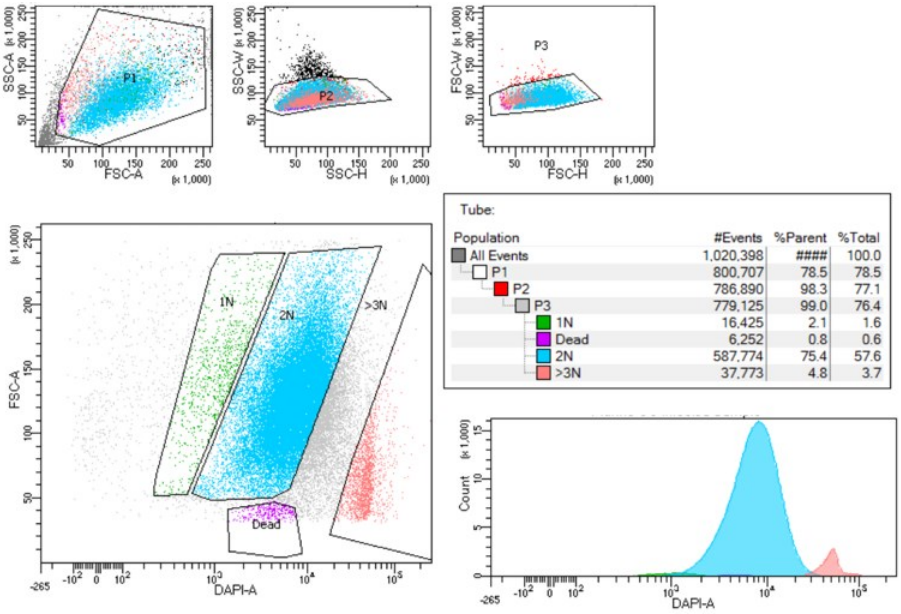

Figure 2.2: Sorting strategy used by Aria 5 sorter to analyse and separate 1-2N cells from ≥3N cells.

Total RNA was extracted using Arcturus PicoPure RNA Isolation kit, with the inclusion of a DNAse treatment to remove DNA contaminants (Thermo Fisher Scientific) according to the manufacturer's protocol. All mouse RNA samples were analysed on Agilent Bioanalyser for quality assessment with RNA Integrity Number (RIN), with RIN=1 representing mostly degraded RNA and RIN=1 mostly intact. The RIN numbers from the samples ranged from 5.3 to 10, with a median of 9.8. cDNA libraries were prepared using 0.5 ng of total RNA using the SMARTSeq v2 protocol (Picelli, Faridani et al. 2014) with the following modifications: 1. Addition of 20 μM TSO; 2. Use of 200 pg cDNA with 1/5 reaction of Illumina Nextera XT kit. The length distribution of the cDNA libraries was monitored using a DNA High Sensitivity Reagent Kit on the Perkin Elmer Labchip. All samples were subjected to an indexed paired-end sequencing run of 2x151 cycles on an Illumina HiSeq 4000 system (26 samples/lane).

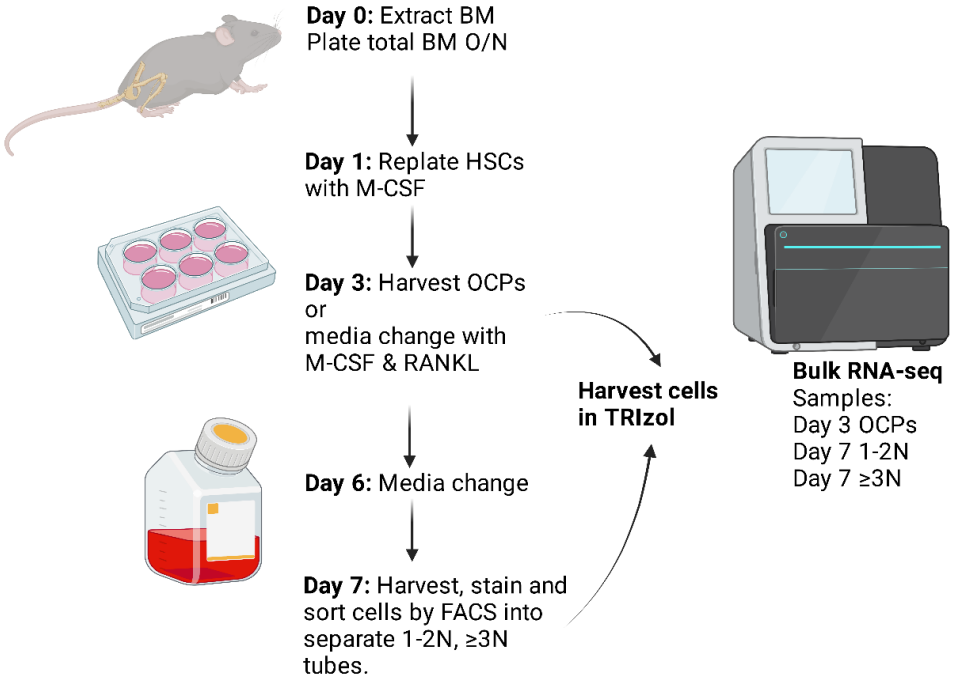

Figure 2.3 Schematic of bulk RNA-sequencing experimental workflow for sorted murine OCLs

C57BL/6 mice samples (cells at day of differentiation stimulated with M-CSF) or sorted day 7 cells (1-2N, ≥3N) were harvested in TRIzol and stored at -80°C before being sent for bulk RNA-sequencing. 2 infection models were used (in vitro and in vivo). For in vitro BCG infection, cells were infected with MOI:5 at day 6 (3 hrs, remove extracellular BCG, harvest, and sort cells at 24 hrs p.i.) For in vivo infection, mice were infected with a CFU 10^6 BCG for 30 days, sacrificed and cells were differentiated as normal for 7 days, harvested and sorted at day 7.

2.8.2 RNA-sequencing quality control

Quality control for the raw reads was performed by the analysis of sequence quality, GC content, and the presence of adaptors and low-quality reads, using MultiQC on the total of 37 samples that were sent for bulk RNA-sequencing. Samples are listed below with the statistics of assigned reads (%) and assigned reads (millions) generated by MultiQC are shown in table 2.8.

Table 2.8 Statistics of assigned reads (%) and assigned reads (millions) generated by MultiQC.

Un=uninfected. In=infected. OCP=osteoclast precursor. In vivo = in vivo infected sample. In vitro = in vitro infected sample. 1-2N=1-2 nuclei. ≥3N=≥3 nuclei.

Sample Name	FeatureCounts: % Assigned Reads	FeatureCounts: Assigned Reads (Millions)
R11647_R: *In vitro*: Un 1-2N	85.20%	28.5
R11648: *In vitro*: Un ≥3N	84.10%	32.8
R11649: *In vitro:* In 1-2N	85.10%	26.6
R11650: *In vitro*: In ≥3N	84.10%	26.6
R11651: *In vitro*: Un 1-2N	83.60%	23.7
R11652: *In vitro*: Un ≥3N	77.70%	26.7
R11653: *In vitro*: In 1-2N	83.50%	20.1
R11654: *In vitro*: In ≥3N	77.40%	29.7
R11655: *In vitro*: Un 1-2N	83.50%	21.2
R11657: *In vitro*: In 1-2N	84.90%	16.4
R11658: *In vitro*: In ≥3N	81.70%	24.1
R11659: *In vitro*: Un 1-2N	84.10%	28.7
R11661: *In vitro*: In 1-2N	84.90%	24.1
R11662: *In vitro*: In ≥3N	85.50%	29.7
R11669: *In vitro*: In 1-2N	85.50%	26.3
R11673: *In vitro*: In 1-2N	85.10%	29.2
R11674: *In vitro*: In ≥3N	80.90%	23.3
R11676: *In vitro*: Un ≥3N	77.50%	24.5
R11677: *In vivo*: In 1-2N	83.30%	38.3
R11678: *In vivo*: In ≥3N	74.30%	30.6
R11681: *In vivo*: In 1-2N	81.70%	30.4
R11682: *In vivo*: In ≥3N	74.80%	31.2
R11683: *In vivo*: Un OCP	83.20%	25
R11684: *In vivo*: Un 1-2N	83.70%	29.1
R11685: *In vivo*: Un ≥3N	81.00%	31.7
R11686: *In vivo*: Un OCP	83.40%	25.4
R11687: *In vivo*: Un 1-2N	83.50%	29.9
R11688: *In vivo*: Un ≥3N	80.20%	27.4
R11689_R: *In vivo*: In OCP	84.70%	41.9
R11690: *In vivo*: In 1-2N	84.30%	28
R11691: *In vivo*: In ≥3N	81.10%	29.2
R11692: *In vivo*: In OCP	84.10%	31.2
R11693: *In vivo*: In 1-2N	83.40%	29
R11694: *In vivo*: In ≥3N	78.00%	30.5
R11695: *In vivo*: In OCP	84.10%	26.3
R11696: *In vivo*: In 1-2N	83.40%	35.8
R11697: *In vivo*: In ≥3N	78.60%	34.7

To avoid confusion in downstream analysis, *in vitro* and *in vivo* BCG infected samples were analysed separately.

Most of the samples passed 80% of the reads being mapped to the reference genome (*Mus* Musculus *ENSMUSG*). Reads were assigned to features of type 'exon' in the input annotation grouped by gene_id in the reference genome (*Mus* Musculus) using featureCounts3 (version 1.5.1). Sequence alignment was done with GRCm38 genome and used the annotation file gencode.VM22.annotation.gtf to estimate feature counts. The raw counts table was filtered to remove genes with near-zero counts, filtering on counts per million (CPM).

2.8.3 Bulk RNA-sequencing data processing and identification of differentially expressed genes

DESeq2 was performed to identify differential expression of genes (DEGs). Compared to the reference *Mus* Musculus genome, the parameters used were Log2FC|≥0.6| and *padj*<0.05.

2.8.4 Gene Ontology Enrichment Analysis

Gene Ontology (GO, http://geneontology.org/) enrichment analysis of the DEGs was accomplished using the TopGo R package to assess for significant biological processes, molecular functions, and cellular components, with $P < 0.05$ being considered significantly significant for enriched terms.

2.8.5 IPA Enrichment Analysis

Ingenuity pathway analysis (IPA) was operated using the IPA software (version 70750971; Ingenuity Systems; Qiagen China Co., Ltd.). The input gene lists were

genes with FDR<0.05. The Fisher's Exact Test is used by IPA to calculate the statistical significance (*p*-value) of overlap between the input genes and molecules that are annotated in established canonical pathways and up-regulators.

2.8.6 BioPlanet Enrichment Analysis

Online tool EnrichR (https://maayanlab.cloud/Enrichr/) was used to perform gene set enrichment analysis of the BioPlanet 2019 gene set library. BioPlanet is a comprehensive resource that collects all known operational human biological pathways (Huang, Grishagin et al. 2019). The *p*-value is calculated from Fisher's Exact Test which is a proportion test that assumes a binomial distribution and independence for probability of any gene belonging to any set. Reported ontology terms from BioPlanet were limited to the top five terms for each condition, sorted by *p*-value.

2.8.7 MetaCore Enrichment Analysis

Enrichment analysis of differentially expressed genes was performed to discover gene ontology (GO) terms and enriched networks using MetaCore Build 6.24.67895 from Clarivate Analytics. Differentially expressed genes were mapped onto pre-defined process networks to identify significantly altered process networks. Reported GO processes or process networks from MetaCore were restricted to the top five terms for each condition, sorted by *p*-value.

2.9 Stimulation of TLR2/4 in MG-63

Adherent cells (MG-63) were seeded at a density of $5x10^4$ cells/well on 24-well plates and left to adhere for 24 hrs. The next day, cells were stimulated at various concentrations of LPS/*Pam*2CSK4 (100 ng/ml, 1 µg/ml and 2 µg/ml) for

3 hrs in a final volume of 200 µl/well. After supernatants were collected, they were centrifuged at 4°C and 1500 rpm for 5 mins. Supernatants were stored at –20°C.

2.10 NLRP3 inflammasome activation

At day 7 of differentiation, OCLs were left untreated (control) or primed with 1 µg/ml of LPS for 4 hrs followed by treatment with 5 µM of nigericin (Nig.) for 1 h.

2.11 Apoptosis induction

At day 7 of differentiation OCLs were challenged with staurosporine (1µM) for 4 hrs to stimulate cell death by apoptosis

2.12 ELISA

After supernatants were collected, they were centrifuged at 4°C and 1500 rpm for 5 mins. Supernatants were stored at –20°C. Then, a Costar 96-well flat-bottom ELISA plate was coated with 50 µl/well capture antibody diluted 1:250 in PBS overnight at 4°C. The next day, wells were washed 3 times with PBST (PBS-0.05 % Tween 20). The next steps were carried out at room temperature. The plate was then blocked for 1 hr with 150 µl/well PBS – 0.05 % Tween 20 –1 % BSA (blocking buffer) followed by a wash 3 times with PBST. 50 µl/well of the standards and samples were added to the respective wells and incubated for 2 hrs. All standards and samples were diluted in blocking buffer. After 2 hrs, the plate was washed 3 times with PBST. The detection biotin labelled antibody was added at 50 µl/well at a dilution of 1:250 in blocking buffer and the plate was incubated for 1 hr. The plate was again washed 3 times with PBST and the Streptavidin-HRP antibody was added at 70 µl/well at a dilution of 1:2000 and incubated at 20 – 30 mins.

A final 6 washes of the plate with PBST were performed. 90 µl/well detection buffer was added, and the plate was incubated in the dark until a colour change was observed. Once this was seen, 50 µl/well Stop solution was added and the plate was covered in foil to protect from the light until the plates are read with a Microplate reader TECAN Infinite® 200 PRO at 490 nm with the subtraction of the absorbance at a reference wavelength (between 620 and 650 nm). ELISA Kits used are listed in table 2.9.

Table 2.9 Human and mouse ELISA kits used

Target	**Company**	**Catalog No.**
Mouse CXCL2	R&D Systems	DY452-05
Mouse CXCL1	R&D Systems	DY453-05
Mouse TNF- α	R&D Systems	DY401-05
Mouse IL-6	R&D Systems	DY406-05
Mouse IL-1α	R&D Systems	DY400-05
Human IL-1β	Invitrogen	88-7261-22

2.13 Cytokine profiling by Luminex

Cytokine analysis of 50 µl of infected/uninfected OCL supernatant was performed using the mouse Cytokine/Chemokine Convenience 36-Plex ProcartaPlex Panel 1 with the following pre-determined targets: [bead region]:

Chemokines: ENA-78 (CXCL5) [57], Eotaxin (CCL11) [62], GRO alpha (CXCL1) [43], IP-10 (CXCL10) [22], MCP-1 (CCL2) [51], MIP-1 alpha (CCL3) [47], MIP-1 beta (CCL4) [72], MIP-2 alpha (CXCL2) [55], RANTES (CCL5) [44]

Cytokines: G-CSF (CSF-3) [12], GM-CSF [42], IFN alpha [30], IFN gamma [38], IL-1 alpha [56], IL-1 beta [19], IL-2 [20], IL-3 [14], IL-4 [26], IL-5 [27], IL-6 [28], IL-9 [34], IL-10 [13], IL-12p70 [39], IL-13 [35], IL-15/IL-15R [54], IL-17A (CTLA-8) [52], IL-18 [66], IL-22 [33], IL-23 [37], IL-27 [36], IL-28 [64], IL-31 [76], LIF [18], MCP-3 (CCL7) [48], M-CSF [21], TNF alpha [45]. The protocol as stated by the manufacturers was followed.

2.14 Other flow cytometry methods

2.14.1 TLR2/TLR4 expression analysis

$0.5x10^6$ MG-63 cells per well were seeded on a 6 well plate. 24 hrs were allowed for the cells to adhere. 24 hrs later, 1 well was used for tryspinsation and counting of cells for MOI. Cells were infected with GFP-BCG for 3 hrs at an MOI 1:5. Extracellular bacteria were removed after 3 hrs, and media was replaced with antibiotic free EMEM. Cells were placed in incubation at 37°C for the 24-hr time point. Cells were washed with PBS, detached with Accutase and were collected and spun down at 1500 rpm for 5 mins at 4°C. After washing with PBS, cells were centrifuged again at 1500 rpm for 5 mins at 4°C. Supernatant was discarded and the pellets were re-suspended in 2 ml PBS. For live dead staining, 1 µl of AmCyan was added to 1 ml of sample and incubated in the dark for 15 min at 4°C. 2 ml FACs buffer was added, followed by centrifugation for 5 mins at 1500 rpm at 4°C. 200 µl FACS buffer was added, and Fc block was performed.

After washing, samples were stained with antibodies TLR2-PE (Biolegend, 1:20, Catalog No.392305) and TLR4-APC (Biolegend, 1:20, Catalog No. 312815). Following incubation at 4°C for 25 mins, samples were washed with 150 µl FACS buffer, centrifuged down at 1500 rpm for 5 mins at 4°C and pellets were re-suspended in 200 µl 2 % PFA. Cells were kept on ice and samples were run on the Fortessa 4L flow cytometer. Isotype controls used were PE Mouse IgG2a, κ Isotype Ctrl (FC) and APC Mouse IgG2a, κ Isotype Ctrl (FC) Antibody.

2.14.2 Analysis of apoptotic cells using Annexin V/ PI

Annexin V/PI experiments were carried out using APC Annexin V Apoptosis Detection Kit with PI (Biolegend, Cat.-Nr. 640932). OCLs were infected according to the infection assay protocols. At 24 hrs post-*in vitro* infection, or 30 days post *in vivo* infection, infected and uninfected OCLs were detached with Accutase after being washed with PBS. Cells were centrifuged at 1500 rpm at RT

for 5 mins. The viable cell density was determined using the trypan blue exclusion method. Cells were stained with Hoechst 33342 (1:1000) and washed and resuspended in 100 µl Annexin-binding buffer (10 mM HEPES, 140 mM NaCl and 2.5 mM $CaCl_2$ pH 7.4). Cells were stained with 5 µl of annexin V-APC and cells were incubated at 15 mins at RT. After incubation, cells were washed with Annexin-binding buffer. 100 µl Annexin-binding buffer was added and 2.5 µl Propidium Iodide (PI) stain was added. Then, cells underwent a final wash in Annexin-binding buffer. As soon as possible, the cells were analysed using a BD FACSymphony™ A5 Cell Analyzer.

2.15 Immunoblotting

Infection assays were carried out with BCG MOI 5. Cells were pelleted, washed in cold PBS, and lysed in Radioimmunoprecipitation assay buffer (RIPA) buffer (Thermo Scientific) containing 1X Halt protease and phosphatase single-use inhibitor cocktail (Thermo Scientific), incubated on ice, and centrifuged at max-speed at 4°C for 10 min. The supernatant was collected, and aliquots were stored in a -80°C freezer. To determine the concentration of protein in lysates, Pierce Detergent Compatible Bradford Assay (Thermofisher Scientific) was used. 20-50 µg protein was formulated in 4X Laemmli sample buffer (BioRad) and loaded onto Mini-PROTEAN® TGX Stain-Free™ Precast Gels (BioRad) and run at 120 V. Blots were blocked with 5 % BSA in TBST (Tris-buffered saline plus Tween20) for 1 hr at room temperature and incubation of the membranes with primary antibodies occurred overnight at 4°C. The next day, membranes were washed thrice with TBST and underwent a 1 hr incubation at room temperature with secondary (-HRP) antibodies. After washing the blots again, they were visualised with Luminata Forte Western HRP substrate (EMD Millipore LUF0500). Stripping of blots for blocking and re-probing was performed using Abcam mild stripping buffer (glycine, Sodium dodecyl sulphate, Tween20 and distilled water pH 2.2) followed by 3 washes in TBST. Antibodies used are listed in table 2.10:

Table 2.10 List of antibodies used in immunoblot

Target (anti-)	Host species	Molecular weight (kDa)	Company	Catalog No.	Dilution
β-actin	Mouse	43	Cell Signalling	3700S	1:2000
Caspase 3	Mouse	32, 19, 17	Cell Signalling	14220S	1:1000
NLRP3	Rabbit	118		15101S	1:1000
ASC	Rabbit	22	Cell Signalling	67824	1:1000
Anti-rabbit HRP	Rabbit	-	Cell Signalling	7074	1:5000
Anti-mouse HRP	Mouse	-	Cell Signalling	7076	1:5000

2.16 Cytotoxicity Assays

Cytotoxicity of cells was measured using the CytoTox 96® Non-Radioactive Cytotoxicity Assay (Promega). Adherent cells (MG-63, osteoclast-like cells) were seeded into 96-well plates at a density of 50,000 cells per well in 100 µl and each condition was performed in triplicate.

A no cell control with just media was used to determine the background fluorescence of the media. Untreated cells were used as a vehicle-only control, and maximum LDH release was determined for positive control wells.

Cells were infected with BCG MOI:5 for 3 hrs, followed by removal of extracellular bacteria and incubation of the cells for the desired time points. To generate a Maximum LDH Release Control, 10 µl of 10X Lysis Solution (per 100 µl original volume) was added to the positive control wells 45 mins before adding CytoTox 96® Reagent. After the desired incubation time point(s), 50 µl aliquots from all test and control wells were transferred to a fresh 96-well flat clear bottom plate. 50 µl of the CytoTox 96® Reagent was added to each sample aliquot and the plate was protected from light and incubated for 30 mins at room temperature. Then 50 µl of Stop Solution was added to each well. Finally, the absorbance at 490 nm was read within 1 hr using a plate reader.

To determine the results, the averages of the no cell control wells were calculated and subtracted from the values of the rest of the experimental wells. With these corrected values, the percentage of cytotoxicity was determined using the following equation.

$$\text{Percentage cytotoxicity} = \frac{Experimental\ LDH\ Release\ (OD490)}{Maximum\ LDH\ Release\ (OD490)}\ X\ 100$$

2.17 Caspase-1 Quantification

The CaspaseGlo-1 Inflammasome Assay (Promega, G9951) was used according to the manufacturer's instructions to quantify levels of caspase-1 in osteoclast-like cell supernatants at the specified time points. To eradicate non-specific caspase-mediated cleavage, the proteasome inhibitor MG-132 was used to determine caspase-1 specific activity. The GloMax® Discover System plate-reader was used to measure the luminescence.

2.18 Caspase-3/7 quantification

The CaspaseGlo-3/7 Assay (Promega, G8090) was used according to the manufacturer's instructions to quantify levels of cell mediated caspase-3/7 release. The GloMax® Discover System plate-reader was used to measure the luminescence.

2.19 Micro-CT

Micro-CT was performed using Tescan Unitom XL by Dr Guillaume Remy of Warwick Manufacturing Group (WMG). Software used for analysis was Acquila, Panthera and VG Studio Max 2022.1. This work was possible due to the NXCT grant.

Information about the scans are found in table 2.11.

Table 2.11 Parameters used in micro-CT analysis of BCG infected mouse femurs

Methodology	**Sample**
Equipment Used	Tescan Unitom XL
Software Used	Acquila
	Panthera
	VG Studio Max 2022.1
Conditions	
Exposure Voltage (kV)	100
Exposure Power (W)	15
Exposure Time (ms)	300
Filters	
Material	N/A
Thickness (mm)	
Information about the Scan	
Voxel Size (µm)	4.091
No. of Projections	2783
Frame per Projection	5

2.20 Statistical Analysis

All experiments shown in this thesis were independently repeated at least thrice unless otherwise stated. Statistical analyses were performed in GraphPad Prism software (version 9). Data normality testing was carried out using GraphPad Prism normality and lognormality tests, assuming normal (Gaussian) distribution. The distribution tests included Anderson-Darling test, D'Agostino-Pearson omnibus normality test, Shapiro-Wilk normality test, and Kolmogorov-Smirnov normality test with Dallal-Wilkinson-Lillie for *P*-value. If data passed normality testing, parametric tests were then used. If not, nonparametric tests were used. Details of which statistical tests were selected are shown in figure legends. Results were considered statistically significant at according to p-value thresholds, whereby not significant (ns) is represented by $P > 0.05$, $*P < 0.05$, $**P < 0.01$, $***P < 0.001$ and **** $P < 0.0001$.

Chapter 3 Generation and validation of a differentiation protocol for murine bone marrow into osteoclast-like cells

3.1 Introduction

The study of osteoclasts has been possible since the 1970's, when it was determined that osteoblasts and osteoclasts are derived from different lineages – osteoblasts arising from pluripotential mesenchymal cells (MSCs) and osteoclasts from haemopoietic stem cells (HSCs). In the body, osteoclast precursors (OCPs) are found in the bone marrow (BM), peripheral blood and spleen and are stimulated to differentiate under the influence of the cytokines receptor activator of NF-κB ligand (RANKL) and macrophage colony-stimulating factor (M-CSF).

To study interactions of the *Mycobacterium* with osteoclasts, it is important to have *in vitro* systems in place. Studying osteoclasts comes with the limitation that there are currently no specific commercially available cell lines for osteoclasts; primary cells must be used, or macrophage cell lines can be differentiated to form osteoclasts. There are several methods to obtain mature osteoclasts *in vitro* and appropriate protocols can be selected to suit individual research goals.

This chapter will focus on the generation and validation of the murine osteoclast-like cells (OCLs) differentiated from BM cells. OCLs were first characterised using known osteoclast markers. We were also able to reproduce a recent technique of sorting and separating osteoclast-like cells according to their multinucleation into cells with 3 or more nuclei (≥3N) and 1-2 nuclei (1-2N) by flow cytometry cell sorting (Madel 2018). We then further characterised the sorted 1-2N and ≥3N cells by performing transcriptomic analysis, which is novel.

3.1 Results

3.1.1 Optimisation of osteoclast extraction and differentiation protocol

Primary murine bone marrow (BM) cells were differentiated into functional osteoclast-like cells (OCLs). Total BM from the hind legs (tibia and femur) from 6–12-week-old donor C57BL/6 mice was flushed with PBS through a cell strainer with a 25-G needle into a 50 ml conical centrifuge tube. Cells were then centrifuged, re-suspended in ACK lysis buffer to lyse red blood cells, centrifuged again, re-suspended in osteoclast media and viable cells were then plated overnight. The next day, non-adherent cells were re-plated with 30 ng/ml recombinant human M-CSF for 2 days. Growth medium was changed at day 3, and the medium was changed partially again at day 6. Finally, OCLs were harvested at day 7.

Before a 7-day protocol was established, a 9-day protocol of differentiation was followed. This involved an extension of incubation time from 7 days to 9 days after the partial media change at day 6.

To characterise these cells throughout a time course, we used the histochemical technique to stain for tartrate-resistant acid phosphatase (TRAP). This is the most common method been used to confirm the presence of osteoclasts *in vitro*. TRAP, encoded by the gene *Acp5*, is highly expressed by osteoclasts, and is secreted to dephosphorylate bone matrix phosphoproteins such as osteopontin and bone sialoprotein during bone resorption. The TRAP stain involves the formation of insoluble maroon dye deposits at the sites of activity at an acidic pH (Newa, Bhandari et al. 2011). Only cells that show this TRAP staining, with 3 or more nuclei (≥3N) are defined as osteoclasts.

TRAP staining was performed at day 3, 5, 7 and 9 of differentiation and imaged with an EVOS light microscope with the brightfield setting at 4X and 20X magnification. Representative images are shown in figure 3.1. At day 3 and day 5, OCLs are clearly not present as they are in day 7. At day 9, it appears that the cells have died.

Previous reports have indicated that for full osteoclast differentiation from murine BM cells, 7-10 days of differentiation is needed (Yazid, Ariffin et al. 2010). It is known that osteoclasts do not survive very long in culture, and once they form, they survive for a maximum of 1-2 days and then die primarily by apoptosis (Chevalier, Çolakoğlu et al. 2021). Hence, we decided that OCLs should be used within 7 days whilst they are viable and not be studied beyond this time.

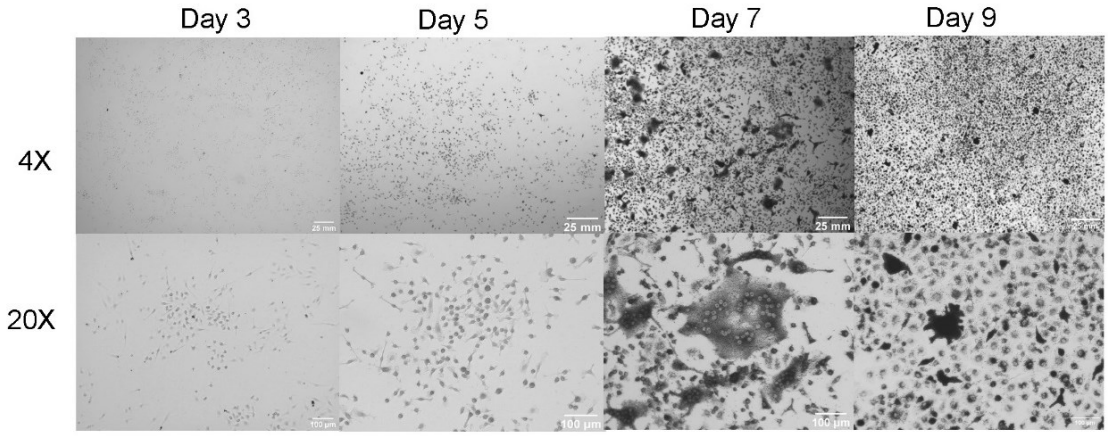

Figure 3.1 Histochemical characterisation of osteoclast-like cells by TRAP staining

TRAP staining was conducted on osteoclast like cells at day 3, 5, 7 and 9 of differentiation. An osteoclast is defined as a giant cell that is TRAP positive, with 3 or more nuclei. Representative brightfield images are shown at 4X (scale bar: 25 mm) and 20X magnification (scale bar: 100 µm).

3.1.2 Validation of osteoclast-like cells at day 7

Next, we investigated the relative expression of selected markers of osteoclasts at day 7 versus day 3 to prove that the cells at day 7 were expressing the bone resorption genes at significantly higher levels. Parent cells at day 3 of

differentiation were chosen as the control, as by then the BM cells had undergone 48 hrs of M-CSF stimulation prior to RANKL stimulation. As M-CSF stimulation causes monocyte to macrophage differentiation involving transcription factors PU.1 and MITF, and osteoclasts cannot be formed independently of RANKL signalling (although osteoclastogenesis can be RANKL independent with the involvement of other factors such as TNF-α and IL-1 (Liao, Feng et al. 2021)), cells at day 3 were called osteoclast precursors (OCPs). The relative expression of genes such as *Nfatc1, Ctsk, Acp5, Atp6v0d2, Ctr and Dc-stamp* (relative to β-actin) in OCPs at day 3 were compared to differentiated cells (OCLs) at day 7.

Nuclear factor of activated T cells 1 (NFATc1) is one of the master transcriptional regulators of osteoclastogenesis. It binds to the promoter regions of other resorption genes *Acp5, Ctsk, Ctr, Dc-stamp* and *Atp6v0d2* to promote their transcription (Takayanagi, Kim et al. 2002, Matsumoto, Kogawa et al. 2004, Kim, Kim et al. 2005). Cathepsin K (CTSK) is an osteoclast-secreted matrix metalloproteinase which cleaves type I collagen of the bone matrix at several sites (Kirschke 2007). The calcitonin receptor (CTR) is the osteoclast-specific receptor for the hormone calcitonin and is expressed highly on osteoclasts. Calcitonin secretion is triggered by increased serum Ca^{2+}, which results in calcitonin binding to CTR, and induces inhibition of osteoclast-mediated bone resorption via the loss of the ruffled border, retraction of the cell and suppression of cell motility (Copp and Cheney 1962, Chambers, Athanasou et al. 1984, Keller, Catala-Lehnen et al. 2014). ATPase H^+ transporting v0 subunit d2 (ATP6V0D2), a component of the proton pump vacuolar-ATPase that mediates acidification of the bone resorption lacunae, is also osteoclast-specific (Wu, Xu et al. 2009). Dendritic cell specific transmembrane protein (DC-STAMP) cooperates with osteoclast stimulatory transmembrane protein (OC-STAMP) to regulate osteoclast cell-cell fusion in osteoclasts (Chiu and Ritchlin 2016).

We noticed a strong increase in osteoclast marker gene expression in the day 7 samples compared to day 3 OCPs, especially *Nfatc1, Ctsk, Acp5 and Atp6v0d2*

(figure 3.2). A high level of variation was seen for *Ctr* and *Dc-Stamp* expression between experiments.

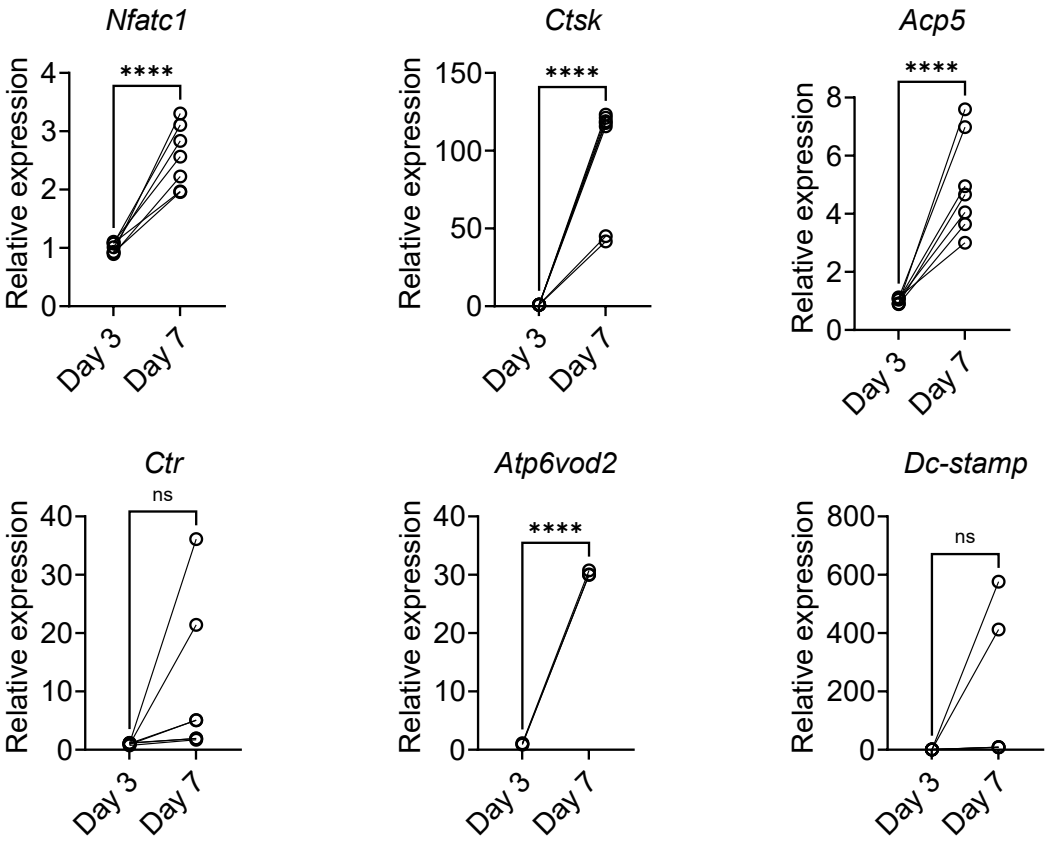

Figure 3.2 OCLs express bone resorption markers significantly more than OCPs

Relative expression of bone resorption genes at day 7 vs day 3 of differentiation. Data were normalised to the housekeeping gene β-actin to obtain ΔCq. The fold change in genes of interest relative to untreated samples was determined using the 2−ΔΔCq method. Each experiment was carried out in duplicate, and the mean of the duplicates were plotted. Each experiment was carried out at least thrice. Statistical analysis was conducted using student's paired t-test. Each dot represents an average value of a given experiment, performed in triplicate. Significant expression differences were found between day 7 and day 3 for genes Nfatc1 (P<0.0001, N=7), Ctsk (P<0.0001, N=7), Acp5 (P<0.0001, N=7), Atp6v0d2 (P<0.0001, N=3) but not Ctr (P<0.0840, N=7) and Dc-stamp (P=0.1358, N=5).

3.1.2.1 Separation of osteoclasts from their precursors based on their multinucleation

Working with primary differentiated cells gives rise to the issue of culture heterogeneity with most cells still being precursors that are exposed to

osteoclastogenic conditions. There is also a lack of surface markers that are specific for osteoclasts. Until recently, most studies on osteoclasts do not attempt to separate mature osteoclasts from their precursors and cells are analysed all together, which leads to inconsistent results and introduces bias from the precursor cells. However, we were able to consistently reproduce a novel technique of sorting and separating cells based on their multinucleation (Madel 2018). In this study, we defined mature resorbing osteoclasts as being $TRAP^+$, with 3 or more nuclei.

At day 7 of differentiation, cells were detached using Accutase, as it has been shown that osteoclasts are resistant to trypsinisation (Chambers 1979, Heinemann, Adam et al. 2021). Accutase is the preferred choice of detachment with many researchers and is used to avoid damage to cell surface proteins (Merrild, Pirapaharan et al. 2015, Madel 2018). Detached cells were then stained using the vital dye Hoechst 33342 prior to sorting on an Aria II 5L. The details of the sorter settings are described in detail in the Materials and Methods (section 2.2.3).

As a control experiment, cells at day 0 (BM cells) were compared to cells at day 7 (figure 3.3A,B) which shows a clear increase in size and granularity of cells at day 7 vs day 0, as well as an uptake of Hoechst at a population of higher fluorescence (≥3N).

Sorting gates were set according to size, granularity, and Hoechst fluorescence, with 50,000 events recorded for analysis.

To probe the multinucleation of cells over a time course of differentiation, cells were stained at day 2, 5 and 7 (figure 3.3C). The emergence of OCLs in ≥3N subpopulation only appears at day 7 within the heterogenous mixture of cells and accounts for a small fraction of the total population (figure 3.3C-D) with an average ≥3N frequency of 4.067 % compared to 92.47 % for 1-2N cells. As osteoclasts are defined as having 3 or more nuclei, the ≥3N fraction is the

population that is more specifically of interest. The 1-2N population are called pre-OCLs.

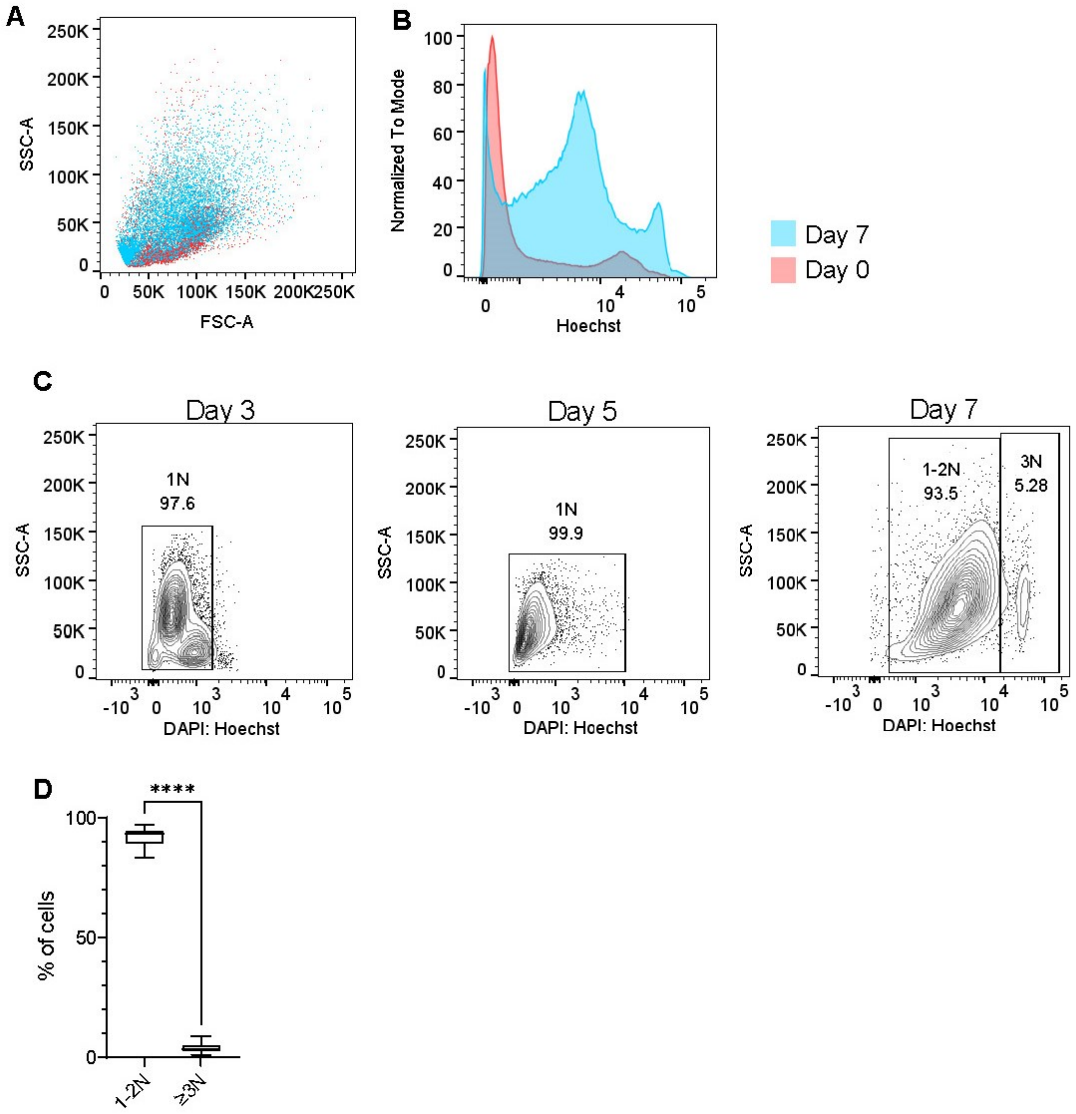

Figure 3.3 Characterisation of OCLs by multinucleation

(A) Overlay plot showing the increased size and granularity of OCLs at day 7 compared to BM cells at day 0 and (B) Histogram overlay showing the increased Hoechst uptake at a higher fluorescence at day 7 compared to day 0. Gated on single and live cells. (C) flow cytometry plots to show the uptake of Hoechst stain at day 3, 5 and 7 of differentiation. Gated on single cells (doublet discrimination) and live cells, analysed using FlowJo 10.6.1. (D) Compiled data in the form of a box and whisker plot showing min to max percentages of 1-2N cells compared to ≥3N cells. Mann-Whitney test, P<0.0001.

The 1-2N and ≥3N cells were then sorted into separate collection tubes containing OCL media for transcriptomic validation by bulk RNA-sequencing (methods and materials section 3.1.3).

3.1.2.2 Surface expression of immunophenotypic markers in osteoclast-like cells

After establishing a method of separating cells based on their multinucleation, we investigated whether there were any immunophenotypic differences between 1-2N and ≥3N cells. For this, we analysed the surface expressions of CD45, Gr-1, CD44 and CD51 markers. CD45 is marker of mature HSCs excluding mature erythrocytes and platelets (McKinney-Freeman, Naveiras et al. 2009). However, it may play a role in bone remodelling as it was shown that in CD45 KO osteoclasts showed perturbed bone remodelling and unusual morphology, attributed to defective cell fusion (Shivtiel, Kollet et al. 2008). Gr-1 (also known as Ly6G)w is a granulocyte / neutrophil marker and was chosen as a negative marker as osteoclasts do not express Gr-1. CD44 is a receptor for ligands hyaluronic acid (HA), along with osteopontin (OPN), collagen, and laminin (Kim and Kumar 2014). It is essential for the fusion of pre-osteoclasts – CD44 specific antibodies and CD44 ligands for HA and OPN have been shown to perturb macrophage fusion and osteoclastogenesis (Chellaiah, Kizer et al. 2003, Chabadel, Bañon-Rodríguez et al. 2007, Chang, Kim et al. 2007). The most specific marker for osteoclasts is CD51, which is a vitronectin receptor α chain, integrin αV and has been demonstrated to initiate bone resorption by mediating OPN adhesion to osteoclasts (Madel 2019). Therefore, OCLs would be expected to be $CD45^{+}Gr\text{-}1^{-}CD44^{+}CD51^{+}$.

Immunophenotyping was performed at day 7 to show surface markers within the mixture of cells during differentiation (figure 3.4A). At day 7, the gating strategy shown in figure 3.4 was used to investigate the differences between 1-2N and ≥3N. The frequency of $CD45^{+}$ $Gr\text{-}1^{-}$ $CD44^{+}$ $CD51^{+}$ immunophenotype between 1-2N and ≥3N cells expressed as a frequency of parent was analysed (figure 3.4B). The frequency of parent refers to the percentage of cells out of the parent

population, which is the population one level up. Here, we refer to the frequency of parent as being the frequency of $CD44^+$ $CD51^+$ cells out of the $CD45^+$ $Gr\text{-}1^-$ population. Notably, the frequency of parent population for $CD51^+$ OCLs is higher in ≥3N compared to 1-2N (12.68% vs 7.960 %, respectively). When CD51 expression alone was examined, as this is the most specific marker for osteoclasts, ≥3N cells were found to have a higher median fluorescence intensity (MFI) of CD51 than 1-2N cells (figure 3.5A-B). Taken together, from this data it can be concluded that immunophenotypically, 1-2N and ≥3N cells are different and that there are more OCLs in ≥3N cells.

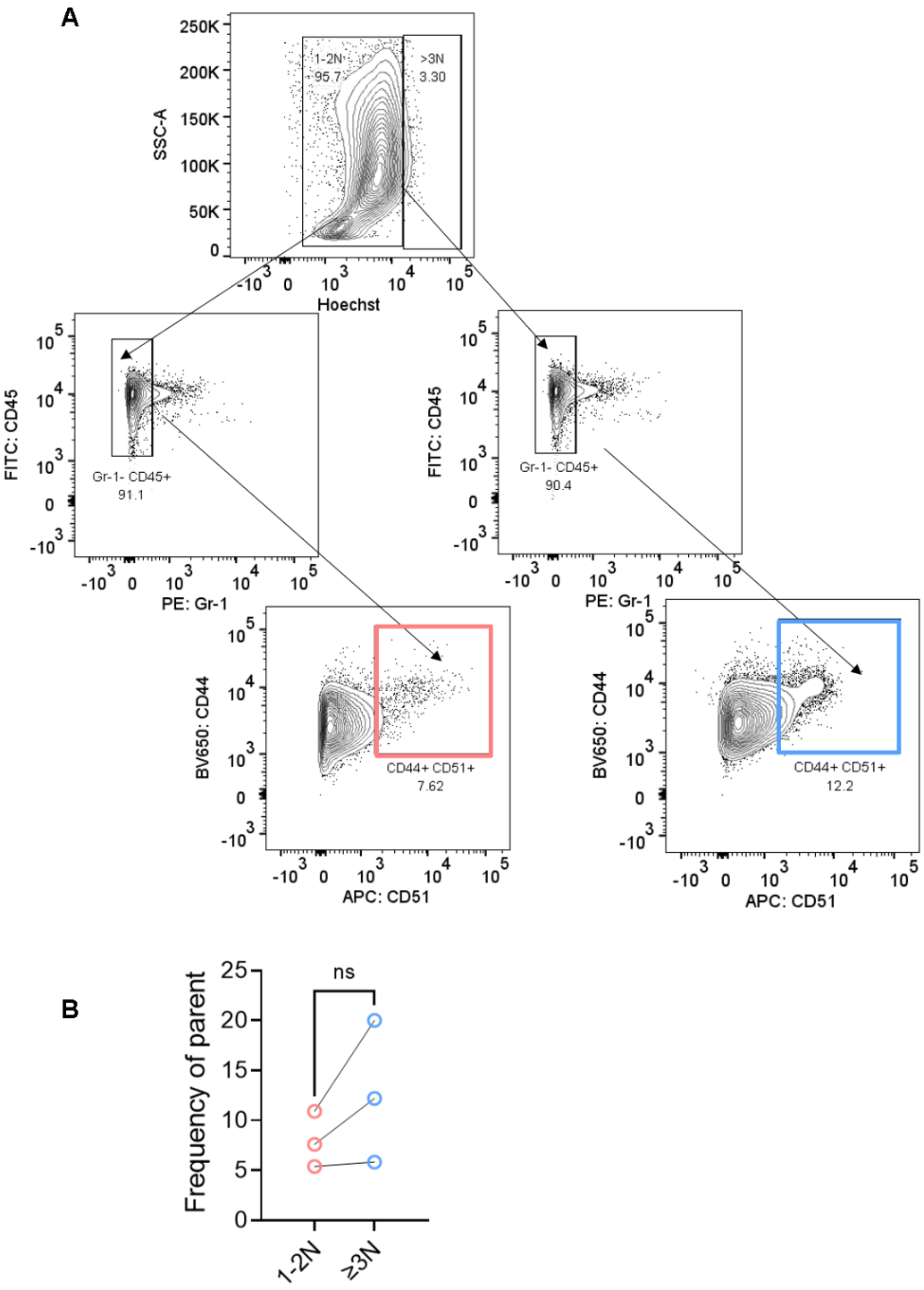

Figure 3.4 Characterisation of osteoclast-like cells by surface markers

(A) Immunophenotyping gating strategy of OCLs at day 7 of the differentiation protocol. Gated on single and live cells. (B) compiled frequency of CD44⁺ CD51⁺ out of the parent CD45⁺ Gr-1⁻ population for 3 independent experiments. Statistically analysed using student's paired t-test (P=0.1999).

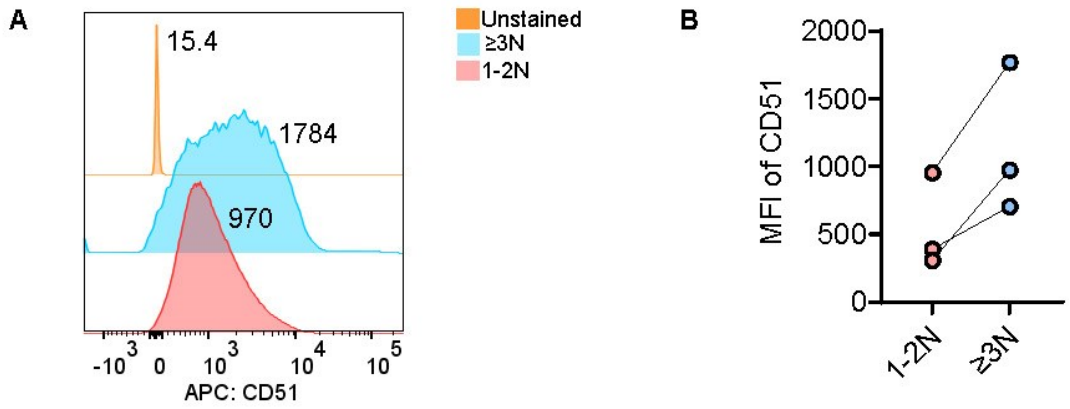

Figure 3.5 Characterisation of OCLs by CD51 expression

(A) Surface expression of CD51 by MFI on 1-2N vs ≥3N cells. (B) Half offset histogram of one representative experiment showing the MFI of 1-2N, ≥3N cells compared to the unstained control and (F) compiled MFI of CD51 from 3 independent experiments. Gated on single and live cells. Statistically analysed using student's paired t-test, with no significant differences found between 1-2N and ≥3N cells (P=0.0561).

3.1.3 Transcriptomic validation of osteoclast-like cells

To investigate the transcriptomic differences between 1-2N and ≥3N cells compared to OCPs at day 3, bulk RNA-sequencing was performed. A schematic of the workflow is shown in figure 3.6A. Differential gene expression (DEG) analysis of RNA-sequencing data was performed using the DESeq2 package of R statistics. Details of the sequencing and analysis are found in materials and methods (section 2.8). To investigate the changes in gene expression across the 3 groups, unbiased hierarchical clustering was used. As such, DEGs were separated into 4 distinct clusters (figure 3.6B).

Each cluster showed significant transcriptomic changes when expressed as Z-scores of average expressions across the same condition for each cluster (figure 3.7). The degree of statistical significance between groups was determined by Wilcoxon test, of which the *p*-values are listed in Table SA1, Appendix. Gene Ontology (GO) Enrichment and Ingenuity pathway analysis (IPA) was then

carried out on the genes within each cluster. The genes for each cluster are listed in Table SA2, (Appendix) and the important ones are indicated in figure 3.6B.

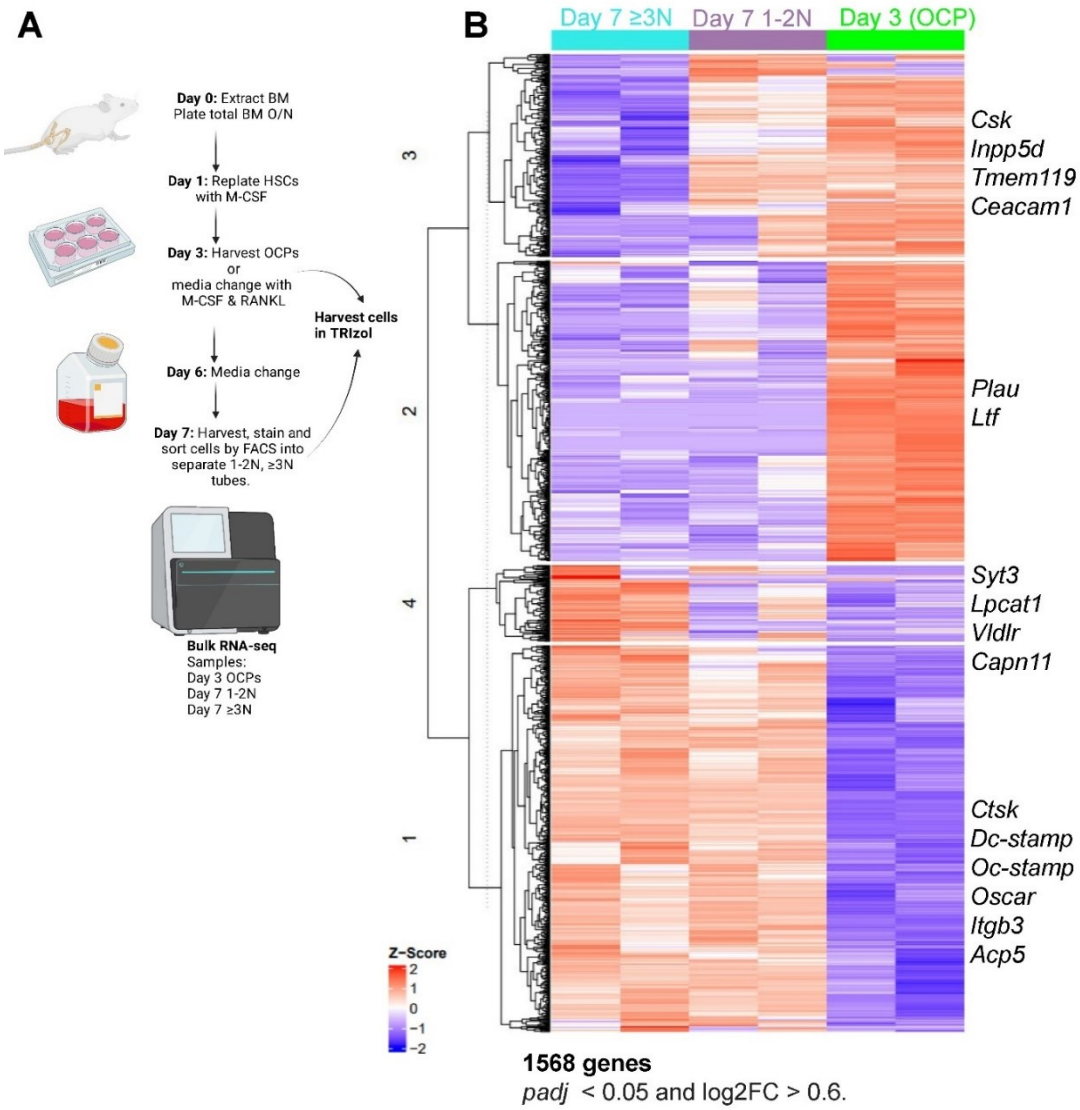

Figure 3.6 Transcriptomic validation of osteoclast-like cells and precursors

(A) Schematic of workflow for transcriptomic analysis of murine OCLs by bulk RNA-sequencing. (B) Heatmap of differentially expressed genes in day 7 ≥3N, day 7 1-2N and day 3 OCPs. The heatmap is based on log2RPKM normalised counts of 1568 differentially expressed genes as identified by DESeq2, unbiased hierarchical clustering creating 4 distinct clusters with the top genes annotated. Colour key gradient scale indicates upregulation in red and downregulation in blue. Key genes are annotated on the heatmap.

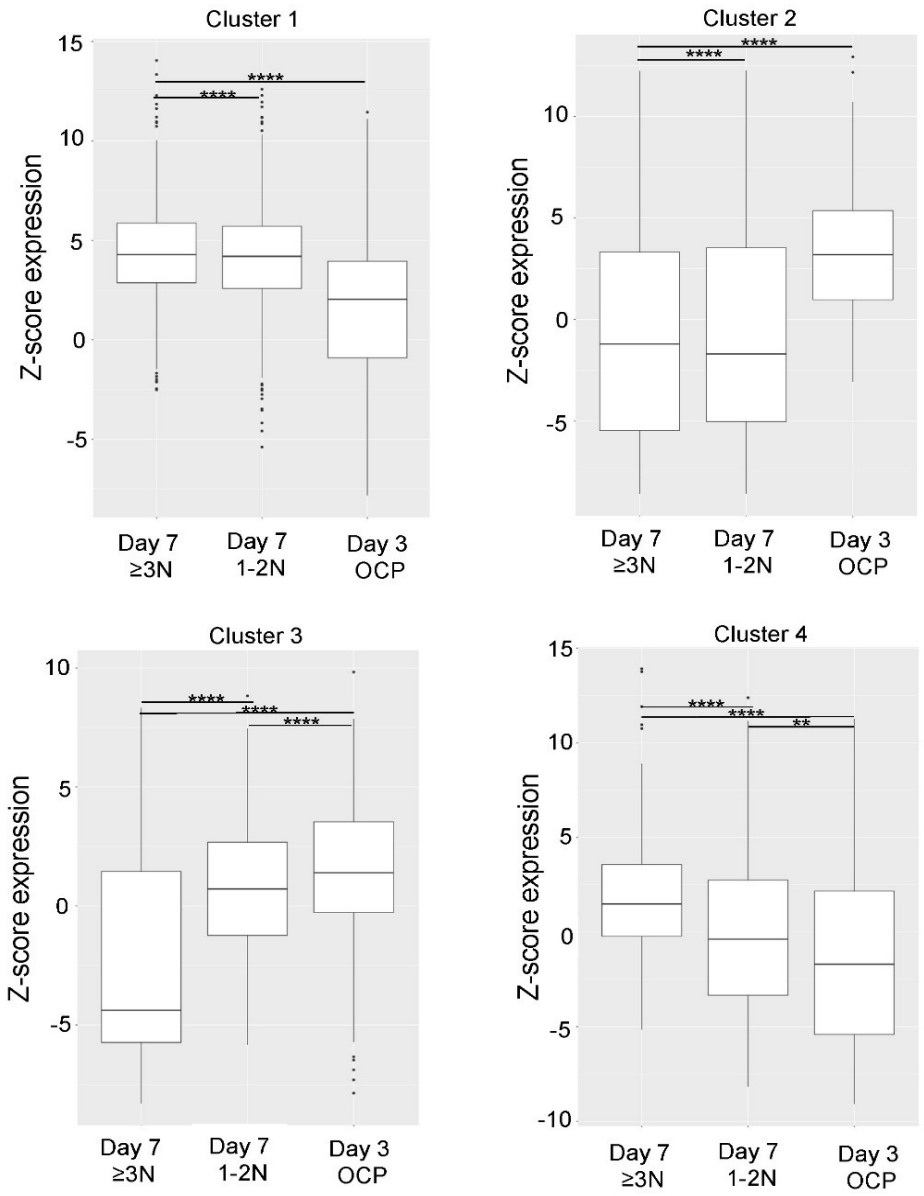

Figure 3.7 Global transcriptomic changes among clusters 1, 2, 3, 4 to differentiate OCPs from OCLs.

Box plots for Z-score of gene expressions averaged over the same conditions for N=4 clusters. Statistical significance was determined by Wilcoxon statistical tests to validate the degree of significance in Z-score of gene expressions averaged over the same condition (p-values are in Table SA1).

Cluster 1 represents genes that were upregulated in day 7 cells (both in 1-2N and ≥3N) compared to day 3 OCPs (figure 3.6B, 3.7). These included genes involved

in the positive regulation of osteoclast differentiation, bone resorption and positive regulation of bone resorption: *Ctsk*, *Dc-stamp*. *Oc-stamp*, *Oscar*, *Itgb3*, and *Acp5*. GO analysis of cluster 1 genes revealed presence of genes associated with proton-transporting ATPase activity (table 3.1). These were *Atp6v1h, Atp6v0b*, *Atp6v1a, Atp6v1e1, Atp6v0e, Atp6v0c, Atp6v0d2, Tcirg1, Atp6ap1, Atp6v1c1,* and *Atp6v1d*. This is anticipated since osteoclasts use membrane V-ATPases at the ruffle border to secrete protons into the lacunae to generate an acidic pH for resorption (Wu 2009).

Table 3.1 List of GO Terms identified in Gene Enrichment Analysis for transcriptomic validation of OCLs

GO analysis using R package 'TopGo' from the unbiased clustered analysis of 1568 differentially expressed genes.

Gene Enrichment Analysis			
Cluster	**Ontology**	**Term**	***P*-value**
1	BP	Cellular response to interferon-beta	1.200E-14
1	MF	Proton-transporting ATPase activity, rotational mechanism	4.800E-13
1	BP	Defence response to virus	3.100E-12
1	MF	Identical protein binding	6.700E-12
1	BP	Antigen processing and presentation of exogenous peptide antigen	2.000E-09
2	BP	Neutrophil chemotaxis	4.100E-11
2	BP	Antigen processing and presentation of exogenous peptide antigen via MHC class II	2.900E-09
2	BP	Neutrophil extravasation	1.500E-08
2	BP	Leukocyte migration involved in inflammatory response	5.900E-08
2	MF	Integrin binding	2.100E-07
3	BP	Negative regulation of bone resorption	4.300E-05
3	BP	Regulation of small GTPase mediated signal transduction	8.400E-05
3	MF	TBP-class protein binding	1.900E-04
3	MF	ATP binding	1.900E-04
3	MF	Opioid receptor binding	2.300E-04
4	MF	NADH dehydrogenase (ubiquinone) activity	1.800E-04
4	MF	Calcium ion binding	3.500E-04
4	BP	Positive regulation of morphogenesis of an epithelium	7.200E-04
4	BP	Regulation of nephron tubule epithelial cell differentiation	1.020E-03
4	BP	Negative regulation of execution phase of apoptosis	1.230E-03

Cluster 2 represents genes that were downregulated in day 7 cells (in both 1-2N and ≥3N) compared to day 3 OCPs. The top GO terms enriched were neutrophil chemotaxis along with antigen processing and presentation of exogenous peptide antigen via MHC class II. This includes genes *Plau* and *Ltf*. Of note, downregulation of *Plau* and *Ltf* genes upon osteoclastogenesis has been shown previously (Toor, Wani et al. 2021).

Cluster 3 included genes that are specifically downregulated in day 7 ≥3N cells. As anticipated, the top GO process enriched in cluster 3 genes was the negative regulation of bone resorption which include *Csk, Inpp5d, Tmem119, Ceacam1* genes (Table 3.1). The GO terms enriched for cluster 3 genes were regulation of small GTPase mediated signal transduction (*Foxm1, Adgrg1, Kitl, Nup62, Madd, Ralgapa2, Amot, Rap1gap2, Gpr35, Lpar6, Arhgap19, P2ry10*) and MF TBP-class protein binding (*Ahr, Rnf4, Ruvbl2, Hnrpf*). Although TBP-2 has been associated with impairment of human osteoclastogenesis before, the involvement of the genes from our data seems to be novel (Aitken 2004).

Cluster 4 represents genes that were largely upregulated in ≥3N only compared to 1-2N and OCPs. From GO analysis, there was an enrichment of NADH dehydrogenase (ubiquinone) activity (*Nd4, Nd5* and *Nd6*), indicating a higher energetic requirement by ≥3N cells compared to 1-2N cells. Also enriched in cluster 4 were genes involved in calcium ion binding processes (*Actn1, Arsa, Plcd1, Syt3, Lpcat1, Vldlr, Dchs1, Capn11, Gnptab, Calml4)* (table 3.1).

In conclusion, GO enrichment analysis attributed novel genes ≥3N specific clusters 3 and 4, unravelling transcriptomic differences between 1-2N and ≥3N cells.

3.1.4 Clustered Analysis: Ingenuity Pathway Analysis (IPA)

To get a deeper insight from the transcriptomic data we also performed Ingenuity pathway analysis (IPA) using the IPA software (version 70750971; Ingenuity

Systems; Qiagen China Co., Ltd.) on the DEGs from each cluster of the heatmap (fig 3.6B). The Fisher's Exact Test was used by IPA to calculate the statistical significance (*p*-value) of overlap between the genes of each cluster and molecules that are annotated in established canonical pathways and up-regulators. The top 5 canonical pathways are listed in table 3.2 and upstream regulators in table 3.3.

Table 3.2 List of top 5 canonical pathways identified by IPA analysis from the unbiased clustered analysis of 1568 differentially expressed genes

Cluster	Top canonical pathway	*p*-value
1	Phagosome Maturation	1.38E-12
	Activation of IRF by Cytosolic Pattern Recognition Receptors	4.46E-11
	CLEAR Signalling Pathway	1.44E-10
	Iron homeostasis signalling pathway	2.48E-10
	Oxidative Phosphorylation	2.65E-10
2	B Cell Development	1.17E-12
	Granulocyte Adhesion and Diapedesis	2.03E-12
	Agranulocyte Adhesion and Diapedesis	1.07E-09
	Th2 Pathway	3.99E-07
	Antigen Presentation Pathway	6.15E-07
3	Pentose Phosphate Pathway (Oxidative Branch)	1.46E-03
	Colorectal Cancer Metastasis Signalling	2.00E-03
	Role of Macrophages, Fibroblasts and Endothelial Cells in Rheumatoid Arthritis	2.57E-03
	G-Protein Coupled Receptor Signalling	6.40E-03
	Melanocyte Development and Pigmentation Signalling	7.23E-03
4	Regulation of Cellular Mechanics by Calpain Protease	6.10E-04
	Mitochondrial Dysfunction	8.97E-04
	Sirtuin Signalling Pathway	1.72E-03
	Phospholipases	3.09E-03
	Methylglyoxal Degradation VI	4.33E-03

IPA analysis of cluster 1 genes (upregulated in day 7: 1-2N and ≥3N cells) revealed the enrichment of phagosome maturation and the oxidative phosphorylation pathway (table 3.2). The genes included for phagosome maturation were *Atp6ap1*, *Atp6ap2*, *Atp6v0b*, *Atp6v0c*, *Atp6v0d2*, *Atp6v0e1*, *Atp6v1a*, *Atp6v1b2*, *Atp6v1c1*, *Atp6v1d*, *Atp6v1e1*, *Atp6v1g1*, *Atp6v1h*, *B2m*, *Ctsk*, *Ctss*, *Dctn4*, *Hla-A*, *Hla-E*, *M6pr*, *Prdx2*, *Rac2*, *Tap1*, *and Tcirg1*. For oxidative

phosphorylation, the genes included were: *Atp5f1d, Cox6c, Cox7a2l, Cox8a, Cyc1, Mt-Atp6, Mt-Co3, Mt-Cyb, Mt-Nd1, Mt-Nd2, Ndufv1, Sdha, Sdhb, Sdhc, Sdhd, Uqcrc1, Uqcrc2, and Uqcrfs1.* Osteoclasts display phagocytic properties not just in the resorption of bone material, but they can also ingest pathogens, abnormal or dead cells which is essential for bone remodelling and homeostasis (Madel 2019). Oxidative phosphorylation is also the main bioenergetic source for osteoclast formation due to the rearrangement of the cytoskeleton, which requires large amounts of ATP, as well as the migration of osteoclasts along the bone surface (Lemma 2016).

IPA analysis of cluster 2 genes (downregulated in day 7: 1-2N and ≥3N cells) highlighted the enrichment of B-cell development pathway (table 3.2). Granulocyte adhesion and diapedesis was also highlighted by IPA (table 3.2). Notably, *Ly6G* is Gr-1 – the expression of Gr-1 is downregulated at day 7 is shown at both the transcriptomic (day 3 vs day 7) and surface expression level (day 2, day 5, day 7) during differentiation (figure 3.4, table 3.2).

IPA of cluster 3 genes which were downregulated in day 7 ≥3N cells only, found pentose phosphate pathway (PPP) (oxidative branch) as the top term, annotated by genes *G6pd* and *H6pd* (table 3.2). The PPP functions to generate DNA/RNA precursors and is split into the oxidative phase and non-oxidative phase. The oxidative phase produces NADPH which donates electrons in anabolic reactions. *G6pd* encodes for the gene glucose-6-phosphate dehydrogenase which converts G6P into ribose 5 phosphate and produces NADPH.

IPA of cluster 4 of genes which were upregulated in day 7 ≥3N cells only, found regulation of cellular mechanics by calpain protease (genes *Actn1, Capn11, Capn6, Pxn*) and mitochondrial dysfunction (with annotated genes *Mt-Co1, Mt-Nd4, Mt-Nd5, Mt-Nd6, Ucp2*) as the top canonical pathways (table 3.2).

IPA analysis also found interesting changes in top upstream regulators of the respective pathways (table 3.3). The upstream regulators identified can include

transcription factors (TFs) or any small molecule or gene known to regulate gene expression. The overlap *p*-value was calculated using Fisher's Exact Test and determines whether the overlap between the DEGs in each cluster and the genes in the Ingenuity Knowledge Base. The significance is attributed to $p < 0.01$.

Table 3.3 List Top 5 upstream regulators identified by IPA analysis from the unbiased clustered analysis of 1568 differentially expressed genes

Cluster	Top upstream regulators	*P*-value	Predicted Activation
1	Irgm1	5.55E-32	Inhibited
	Lipopolysaccharide	8.92E-32	Activated
	PNPT1	1.65E-31	Inhibited
	Ifnar	8.29E-31	Activated
	TRIM24	5.51E-28	Inhibited
2	Lipopolysaccharide	8.29E-44	Inhibited
	GATA2	2.93E-37	Inhibited
	IL4	9.58E-35	Inhibited
	Dexamethasone	1.84E-33	
	TNF	4.41E-29	Inhibited
3	Lipopolysaccharide	7.75E-09	Inhibited
	IFNG	1.58E-06	Inhibited
	TNF	5.01E-06	Inhibited
	PTPRR	5.78E-06	
	TCF4	7.12E-06	Activated
4	MRPL12	2.95E-08	
	ALKBH7	2.05E-07	
	DAP3	2.96E-07	Activated
	Actinonin	9.70E-07	Inhibited
	PSMB11	1.66E-06	Inhibited

Cluster 1 (genes upregulated in day 7 cells compared to day 3) showed that lipopolysaccharide (LPS) mediated stimulation is predicted to be activated. LPS is known to promote the mitogen-activated protein kinase (MAPK) pathway and promote cyclooxygenase-2 (COX-2) expression in murine macrophage cell line RAW 264.7, promoting their differentiation into osteoclasts (Hou, Guo et al. 2013). It was also shown that in RAW 264.7, when primed with RANKL and then treated with LPS, the TNF-α secreted regulates osteoclastogenesis (AlQranei, Senbanjo et al. 2021). Among cluster 2 (downregulated in day 7 cells) as well as cluster 3 (downregulated in day 7 ≥3N only) LPS and TNF were predicted to be inhibitory of genes downregulated in osteoclastogenesis, which is instinctual since TNF and LPS are pro-osteoclastogenic.

Upstream regulator analysis also highlighted *Ifnar* (interferon alpha/beta receptor 1 (IFNA-R1) signalling in activated state among cluster 1 genes. IFNAR1 is the low affinity component of a heterodimeric IFN receptor, with high affinity IRNAR2 being the other component. Type 1 IFNs compromising of cytokines such as IFN-α and IFN-β signal through this IFNAR receptor. Type 1 interferon signalling activates the Janus kinase (JAK)-signal transducer and activator of transcription (STAT) (JAK-STAT) signalling cascade, usually in MNs in response to viral infections. In the context of osteoclastogenesis, the roles of IFNs are still being unravelled. Nevertheless, it has been shown that mice deficient in IFN signalling components including IFNAR1, interferon regulatory factor 1 (IRF1), IRF9, and STAT1 display reduced bone density along with increased osteoclastogenesis compared to wild type (WT) mice, pointing to the roles of IFN signalling in negative feedback loops in osteoclastogenesis and homeostasis (Place 2021).

Among cluster 4 genes (upregulated in day 7 ≥3N only) DAP3 was predicted to be activated. Interestingly, *Dap3* (death associated protein 3) was found to be the top upstream regulator and is a mitochondrial ribosomal small subunit protein essential for mitochondrial homeostasis, participating in the extrinsic pathway for apoptosis and TNF associated cell death pathways. It acts upstream of caspase 8 and 9 and downstream of IFN-γ, TNF-α and Fas ligand (Kim, Chae et al. 2007, Takala, Ramji et al. 2022). *Dap3* was identified as an important novel gene which is associated with bone mineral density in rats (Alam 2014).

3.1.4.1 Bone resorption markers in day 7 ≥3N vs day 7 1-2N and day 3 OCP cells

In the RNA-sequencing data, we then looked for the osteoclast specific genes that had been tested previously using RT-qPCR (*Dc-stamp, Ctsk, Acp5*), as shown in figure 3.2. These genes were significantly upregulated at day 7 (both in 1-2N and ≥3N), although there were no significant differences between expression of these genes between 1-2N and ≥3N (figure 3.8).

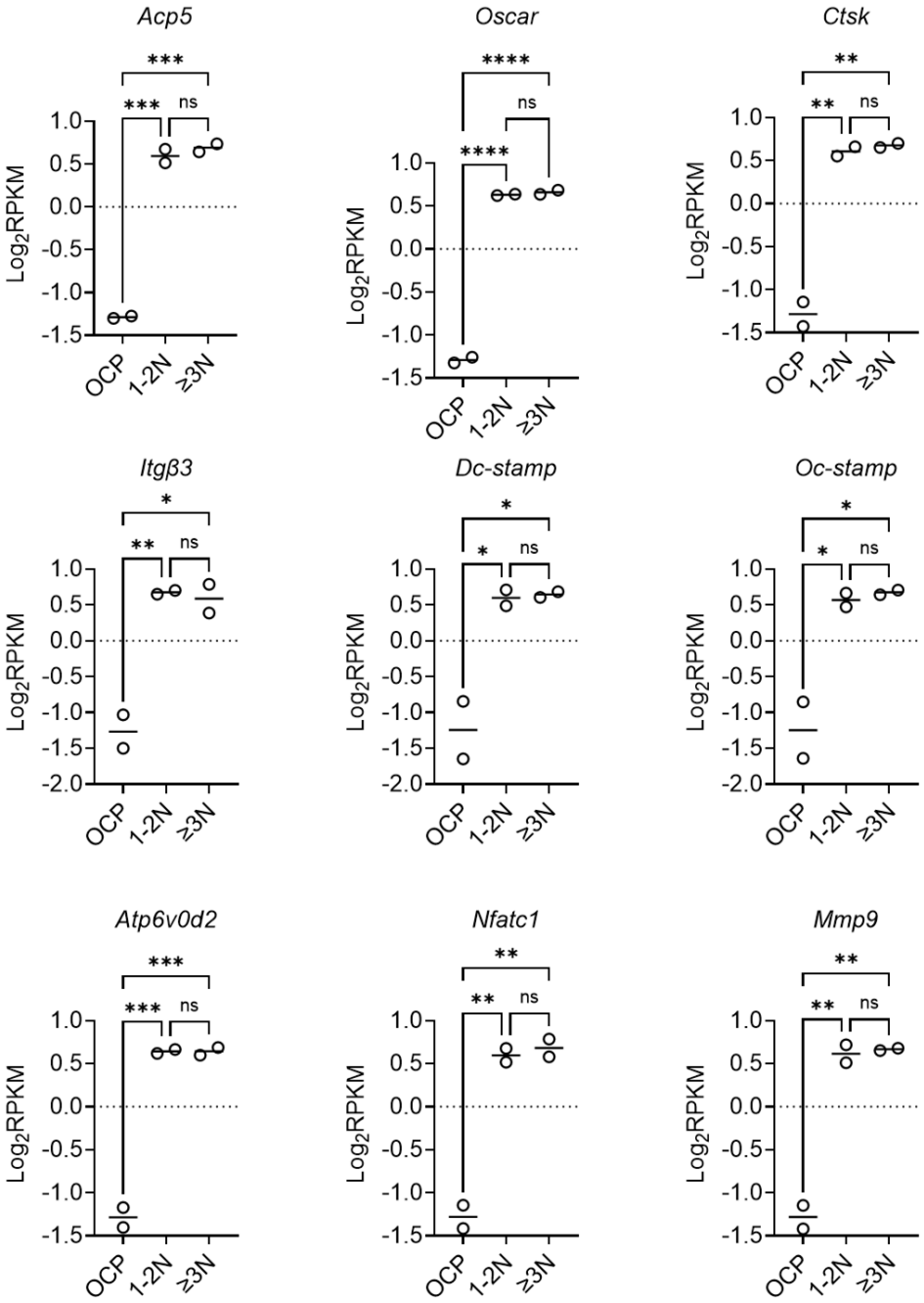

Figure 3.8 Relative expression values (log2RPKM) of bone resorption genes enriched in cluster 1, upregulated in day 7 (1-2N & ≥3N) compared to day 3 OCPs

Statistical analysis was performed using One-Way ANOVA, with no significant differences found between 1-2N and ≥3N cells across all bone resorption genes.

3.2 Discussion

The study of osteoclasts is important with the emerging interest in the field of osteoimmunology. The differentiation of primary murine BM into osteoclasts gives rise to a heterogeneous population and day to day variation. Although in the body, OCPs are found in the PB and spleen (Root 2021, Yahara 2022), we focused on those that are derived from the BM.

Mature osteoclasts can be isolated directly from rabbits by obtaining the long bones (tibia and femur) of a 2–4-day-old rabbit which briefly involves mincing the bones finely into small pieces in culture medium, transferred to a 50 ml conical tube and vortexed forcefully and plated overnight in Petri dishes, and the cells are gently washed with PBS to remove stromal and non-adherent cells (Marino, Logan et al. 2014). Isolation of mature rat osteoclasts from 2–4-day old rats or osteoclast precursors from 7-9 day old mice can also be carried out in the same general way by finely mincing the long bones followed by subsequent processing steps (Boyde, Ali et al. 1984, Chambers, Revell et al. 1984, Arnett and Dempster 1986, Marino, Logan et al. 2014). The earliest studies of osteoclasts were carried out using these methods and are rarely used nowadays. It is also impractical to source new-born mice as it relies on the constant successful breeding of mice stock, as well as a short window of time to isolate the desired cells.

A commonly used method to generate human osteoclasts is to obtain samples of fresh peripheral/venous blood or a buffy coat and use the standard Ficoll-Paque method to isolate human PBMCs. An optional step would be to purify $CD14^+$ cells (which constitute ~10 % of PBMC population) by magnetic bead separation to purify monocytes from the other cell populations. The cells are then cultured in the presence of M-CSF and RANKL for 4-6 days (Henriksen, Karsdal et al. 2012).

Moreover, the murine macrophage cell line RAW 264.7 can be differentiated into osteoclasts with variable concentrations of MCSF and RANKL (with 20–

100 ng/ml). Although this method would have avoided ethical considerations, immortalised cell lines do not behave the same way as primary cells.

Interestingly, osteoclasts can also be derived from induced pluripotent stem cells, human iPS cell line with up to 40 days of differentiation with various growth factors and cytokines over the following phases: mesoderm induction, haematopoietic specification, haematopoietic expansion and maturation, and differentiation into osteoclasts (Grigoriadis, Kennedy et al. 2010). We veered away from this specialist and novel technique as it is not well established but it is an exciting prospect for future researchers.

We finally decided to derive osteoclast-like cells (OCLs) from murine BM using a 7-day protocol, after establishing that 9 days was too long. Although this protocol presented the limitation that it would produce a heterogenous mix of cells, it allowed the optionality of studying the effects of mycobacterial infection on OCLs derived from knock-out mice.

Before studying the effects of mycobacterial infection, it was imperative to first characterise the cells derived from this method. One method we used was to characterise the cells by their nuclei number, as osteoclasts are defined as having 3 or more nuclei (although they can have up to 100 nuclei) (Marino 2014). To date, only one study has been published which endeavours to purify and characterise multinucleated cells with 3 and more nuclei (≥3N cells) with the use of vital dye (Hoechst 33342) and sorting using FACS (Madel 2018). Madel *et al.* used BM $CD11b^+$ precursor cells as their control to compare against 1-2N and ≥3N cells, highlighting a difference in their differentiation strategy. To generate their OCLs, murine $CD11b^+$ monocytes were isolated from the murine BM cells using microbeads for magnetic separation, whereas we used an adherence method of plating the total BM overnight to deplete the adherent MSCs from culture.

CD11b is an integrin family member that is expressed on the surface of leukocytes including MNs, neutrophils, natural killer (NK) cells, granulocytes, and macrophages. However, it has been shown that both $CD11b^+$ and $CD11b^-$ populations of BM have osteoclastogenic potential (Root 2021). Due to the lack of clarity to whether $CD11b^+$ cells have increased potential for OCL formation, we decided not to purify $CD11b^+$ monocytes; instead plating the total BM population for stimulation with RANKL and M-CSF, as we intended to mimic the differentiation process that occurs *in vivo* as closely as possible.

Madel *et al.* were able to show that the sorted ≥3N cells were pure, functioning, and viable (Madel 2019). They demonstrated that sorted ≥3N cells retained a higher matrix dissolution activity and bone resorption capacity than 1-2N cells. Though we showed the increased expression of CD51 av-integrin (marker of differentiated osteoclasts) among ≥3N cells compared to 1-2N cells (figure 3.5), our transcriptomic analysis by RNA-sequencing did not reveal significant differences between the bone resorption genes in 1-2N and ≥3N cells (figure 3.8). To measure the correlation between resorptive activity and nuclei number, functional assays would need to be performed. A positive correlation between nuclei number per osteoclast and volume of resorption pit has been made by Piper *et al* (Piper 1992), but another study found that osteoclasts with >10N underwent resorption more actively compared to small ones (with 2–5N) (Lees 2001). As such, a reason for no obvious changes in osteoclast resorption genes could be that we had investigated only the small difference between 1-2N and ≥3N.

Furthermore, Madel *et al.* note that the mean number of OCLs obtained after sorting corresponded to about 1 % of total cells seeded at the beginning of the differentiation. Our experience did not match this. We found around 0.005-0.003 % based on 20 million initial cells seeded. We also noted that our method presents limitations in that it fails to recover giant cells with many nuclei. These cells are especially 'sticky' and resist detachment from the bottom of the plate even after several rounds of Accutase treatment and PBS washes. Use of 0.1 %

gelatin to coat culture plate wells did not improve this either. This means that analysis done by the cell sorter may underrepresent the true populations of cells within the culture plate. Moreover, this purification method of OCLs was troublesome and time consuming. Depending on the day, between 5,000-100,000 ≥3N cells would be collected by the cell sorter, with 100,000-600,000 1-2N cells. The use of a 100 μM mesh to filter the cells before sorting to generate a single cell suspension could explain the few numbers of cells in this population. As osteoclasts can range from 10 - 300 μM, osteoclasts over 100 μM would have been filtered out and the data on these lost.

We attempted several times to recover the ≥3N OCLs in order to visualise them with immunofluorescence. To do this, we tried seeding the sorted cells onto chamber slides pre-treated with poly-L-lysine, left them to adhere overnight, and then fixed and stained the next day. We avoided leaving the cells for longer than a day as the cells were fragile after sorting and faced some problems recovering enough cells ≥3N to seed onto chamber slides in the first place. The issue of not recovering enough ≥3N cells presents a technical limitation to the downstream studies that could be carried out. As ≥3N cells recovered after sorting were <5 % of the total, this meant that to study the 'pure' OCLs we would incorporate transcriptomic methods such as bulk RNA-sequencing where fewer cells can be used.

Immunophenotyping of the OCLs also presented challenges. This technique of characterising the cells is limited by the fact that, at the time of experimentation, there are few specific known markers of mature osteoclasts that are not also present on other myeloid lineage cells or precursors. Our staining panel to define OCLs as $CD45^{+}Gr\text{-}1^{-}CD44^{+}CD51^{+}$ provides a robust method for screening surface markers but could have also been refined. CD11b can be used as a surface marker for OCPs but many granulocytes also express this marker which could have led to overestimation of OCPs. To overcome this, we used Gr-1 as a granulocyte marker. $CD11b^{+}/Gr\text{-}1^{-/lo}$ cells could have been identified as they have a 60-70 % potential to differentiate into $TRAP^{+}$ mononuclear osteoclasts when cultured

with M-CSF and RANKL (Yao 2006). Another way we could have refined our immunophenotyping panel further would be to use a staining scheme to distinguish macrophages ($CD11b^{+}$ $CD68^{+}$ $CD115^{+}$ $CD265^{low}$) from OCPs ($CD11b^{low}$ $CD68^{+}$ $CD115^{+}$ $CD265^{+}$) (Patel, Shi et al. 2022).

Transcriptomic profiling of murine osteoclast differentiation has been performed previously, but on the total cell populations (Toor, Wani et al. 2021). These authors found that genes *Pheta1*, *Hagh*, *Gfpt1* and *Nol4* that have not been previously associated with osteoclasts were upregulated during osteoclastogenesis of primary murine BM. Meanwhile, novel genes that were downregulated included *Plau*, *Ltf*, *Sell* and *Zfp831.* Our data also showed *Plau* and *Lft* to be downregulated in day 7 cells compared to day 3 OCPs (figure 3.6B). The *Plau* gene encodes a secreted serine protease (uPA) that converts plasminogen to plasmin. The receptor for uPA is uPAR, and it was discovered that this is expressed in osteoblasts and osteoclasts (Furlan 2007). Importantly, uPAR deficient mice show a phenotype of increased bone mineral density (BMD), increased osteoblast formation, decreased osteoclastogenesis and delayed cytoskeletal remodelling in mature osteoclasts (Furlan 2007).

From our data, DEGs that were upregulated in day 7 ≥3N only compared to day 7 1-2N and OCPs (cluster 4) showed there was enrichment of NADH dehydrogenase (ubiquinone) activity (*Nd4, Nd5* and *Nd6;* figure 3.6B), indicating a higher energetic requirement for ≥3N cells compared to 1-2N. Indeed, during oxidative phosphorylation (OXPHOS), the NADH-ubiquinone dehydrogenase (complex I) is the main entry point for electrons to catalyse the oxidation of NADH. Seven out of the 44 subunits of complex I are encoded by mitochondrial genes, including *Nd4*, *Nd5*, and *Nd6.* Osteoclasts require a large amount of energy to migrate along the bone surface, as well as secrete degrading proteases and H^{+} ions into the resorption lacuna, all of which require ATP. OXPHOS produces 17 times more ATP per molecule of glucose than glycolysis, and evidence shows osteoclasts have densely packed mitochondria and high expression of OXPHOS

enzymes. As such, OXPHOS is the prevalent bioenergetic pathway utilised by osteoclasts during formation (Li, Lee et al. 2020).

Transcriptomic analysis of sorted day 7 ≥3N, day 7 1-2N and day 3 OCP cells also highlighted that cells at day 7 express genes related to osteoclast differentiation and bone resorption and can be called osteoclast-like cells. Although significant differences in relative bone resorption between day 7 ≥3N and day 7 1-2N cells were not prevalent, the mRNA levels for several processes are significantly higher in ≥3N cells than 1-2N. These include calcium ion binding (*Actn1, Arsa, Plcd1*, *Syt3, Lpcat1, Vldlr, Dchs1, Capn11, Gnptab,* and *Calml4),* shown in table 3.1, cluster 4. Ca^{2+} signalling is important during osteoclastogenesis - Ca^{2+} oscillations in the cytoplasm mediated by RANKL to upregulate NFATc1 during osteoclast differentiation (Okada, Okabe et al. 2020). NADH activity (*Nd4, Nd5* and *Nd6*) and negative regulation phase of apoptosis (*Gm20594,* and *Fzd3*) are also noteworthy processes that are enriched in ≥3N cells compared to 1-2N.

As further experiments rely on this method of purifying ≥3N OCLs, it was important to have a thorough approach to validating the differentiation protocol. The ≥3N population seems to be distinct on the transcriptomic level in several processes, which is why we continued to analyse them separately from 1-2N cells in further studies.

Chapter 4 Elucidating the response of bone cells during mycobacterial infection

4.1 Introduction

It has been shown that *Mtb* can persist both in human bone marrow (BM) cells *in vitro* as well as the BM stem cells of *Mtb* infected mice (Raghuvanshi, Sharma et al. 2010, Das, Kashino et al. 2013). Viable bacilli have also been found in the BM of TB patients that had undergone long-term anti-TB drug treatment (Das, Kashino et al. 2013).

In contrast, bone cell interactions with mycobacteria and their precise cellular locations within bones are not well characterised. Mycobacteria are generally thought to cause a deregulation of bone homeostasis, possibly through an imbalance of the receptor activator of NF-κB ligand (RANKL)/osteoprotegerin (OPG) axis (Lacey 1998, Yasuda 1998, Takayanagi 2021). Furthermore, it was found that serum OPG levels in samples from patients with spinal TB were severely decreased compared to non-TB patients (Ma, Jin et al. 2022). In the same study, it was confirmed that *Mtb* could internalise inside human bone tissue derived osteoblasts with a dose-dependent increase of the CD40 mRNA expression and interleukin 6 (IL-6) secretion (Ma, Jin et al. 2022).

Studies of *Mtb* infection of osteoclasts derived from human PBMCs show increasing evidence linking *Mtb* infection to an increase in osteoclast number (Hoshino 2014, Liu, Zhou et al. 2020). These studies show that, in addition to the indirect effects of the inflammatory response of surrounding immune cells, the pathogenesis of bone TB could also be driven by the direct infection of bone cells themselves. This could contribute to disease progression. Therefore, in this chapter, we aim to define the phenotypic changes occurring more closely during mycobacterial infection of bone cells.

M. bovis bacilli Calmette-Guérin (BCG), the attenuated vaccine strain, was used as a model for *Mtb,* as it shares 99 % genome sequence similarity with virulent *Mtb* and can be handled under BSL2 laboratory conditions (Brosch 2002). Furthermore, during the time of my PhD (Oct 2019 – March 2022) BSL3 in Singapore was not available for TB work as COVID-19 work was prioritised.

We report on both the phenotypic changes on osteoblast-like cell line MG-63 during *in vitro* BCG infection and in osteoclast-like cells derived from primary murine bone marrow. Immunological methods such as flow cytometry and ELISA were used to study various immunotypic changes at the cellular level, and to further investigate potential biomarkers of infection. We then delve deeper into the osteoclast response to infection, using an *in vivo* model of infection to show phenotypic changes in osteoclasts, and investigate changes in the whole bone architecture using μ-CT.

4.2 Results

4.2.1 *In vitro* BCG infection of osteoblasts

Using the osteoblast cell line MG-63, an *in vitro* infection protocol using BCG was first optimised. The day before infection, when MG-63 cells reached 70-75 % confluence at a passage below 15, they were re-seeded at the appropriate density for the culture plate. On the day of infection, the MG-63 cells were counted to determine the multiplicity of infection (MOI). BCG infection was conducted at a MOI of 5 for 3 hrs, followed by a PBS wash to remove extracellular bacteria. Time points of 3 hrs and 24 hrs post infection (p.i.) were used.

First, we investigated the intracellular presence of mycobacteria in MG-63 using flow cytometry and CFU assays. Cells infected with fluorescent strain of BCG (m-Cherry) were harvested and stained at 3 and 24 hrs p.i. Flow cytometry shows percentage of cells containing bacteria at 3-hrs p.i. and persistence at 24-hrs p.i. (figure 4.1A-B). Uptake and persistence of BCG inside MG-63 was compared to THP-1 monocytes. THP-1 monocytes were used as a positive control as these cells

are well known to phagocytose BCG. Using flow cytometry for MG-63, a low percentage uptake of 2.6 % was observed at 3 hrs p.i. (figure 4.1A, C), increasing to 4.1 % at 24 hrs p.i. (figure 4.1B, C). THP-1 saw a percentage invasion of 9.9 % at 3 hrs p.i., increasing to 50.3 % at 24 hrs p.i., respectively. CFU counts using 7H11 agar plates from infected MG-63 showed that viable BCG was able to reside and persist intracellularly, and bacterial numbers changed from 72333 CFU/ml at 3 hrs p.i., to 56518 CFU/ml at 24 hrs p.i., to 53222 CFU/ml at 48 hrs p.i. (figure 4.1D). For THP-1 cells, bacterial load was one log10 higher at all time points tested (figure 4.1D). From this data, it can be concluded MG-63 shows a weak ability to uptake bacteria, compared to phagocytic cell line THP-1. Despite this,

there is intracellular persistence of bacilli across all time points tested in MG-63.

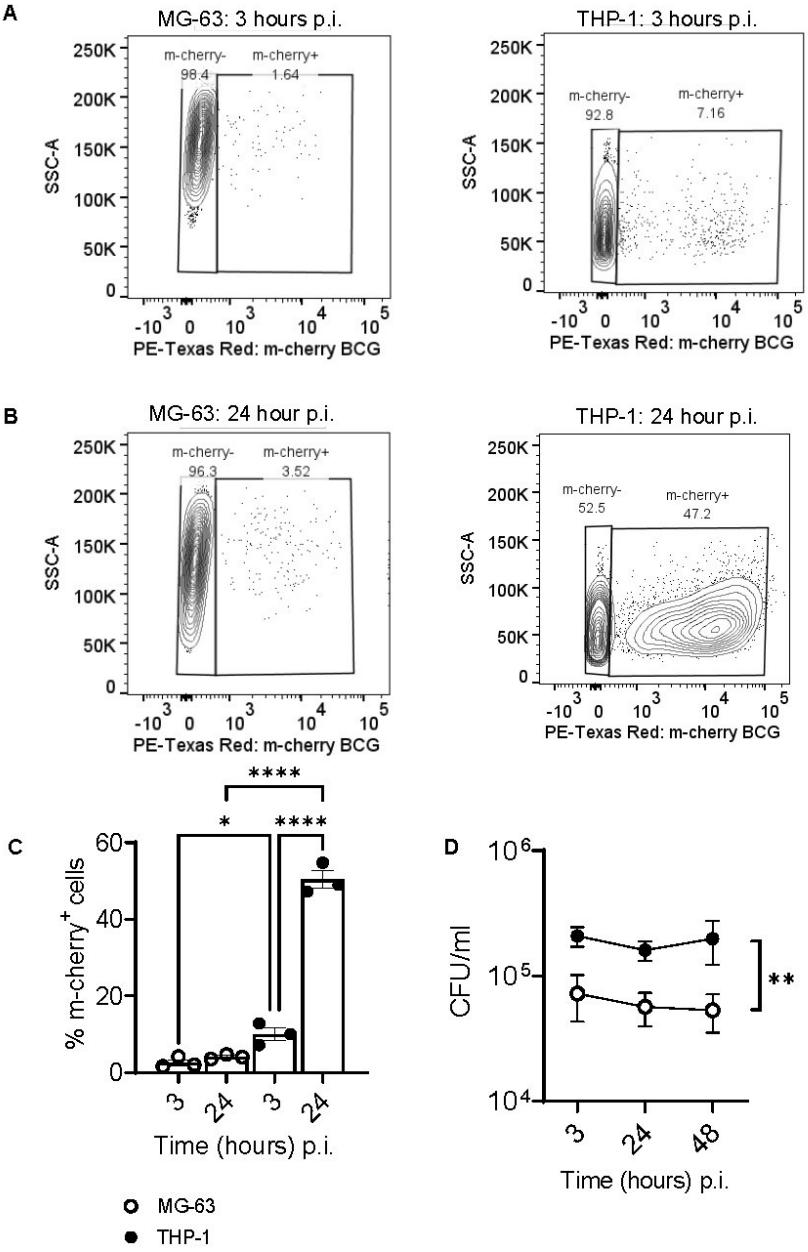

Figure 4.1 BCG is internalised and survives within osteoblast-like cell line MG-63

*(A) Contour plots with outliers displayed showing BCG uptake at 3 hrs p.i. for MG-63 and THP-1 cells. (B) Contour plots with outliers displayed showing BCG persistence at 24 hrs-p.i. for MG-63 and THP-1 cells. (C) Compiled data of BCG uptake at 3 and 24 hrs p.i. of MG-63 and THP-1. Statistical analysis was performed using Two-Way ANOVA for differences between cell type (MG-63 or THP-1) and time and interactions between cell type*time. Cell type had a significant effect ($F_{1,8}$=202.1, P<0.0001) and a main effect of time ($F_{1,8}$= 332.5, P<0.0001) and a significant interaction between cell type*time ($F_{1,8}$=174.6, P<0.0001). (D) Infection assay: CFU/ml of intracellular BCG at 3 vs 24 hrs p.i. in MG-63 and THP-1 cells. Statistical analysis was performed by unpaired t-test for differences between MG-*

*63 and THP-1 at respective time point. There were significant differences between the CFU/ml of MG-63 and THP-1 (*P=0.0012).*

4.2.2 Bone formation markers are not altered by *in vitro* BCG infection

Osteocalcin (OCN), a bone formation marker, was reported to be poorly expressed in tissues of spinal TB patients compared to non-infected patients (Izawa 2015). Other bacterial infections of the bone have shown to perturb bone formation. For example, *S. aureus* infection can inhibit bone formation as well as expression of bone formation genes (alkaline phosphatase (*ALP*), collagen 1 (*COL1A1*), *RUNX2*, and osteocalcin (*OCN*) in human primary osteoblasts and in the cell line MG-63 (Kassem, Lindholm et al. 2016). Hence, we tested a selection of bone formation markers with the aim of uncovering whether the relative expression of these markers was changed during infection.

RT-qPCR was used to compare the relative expression of bone formation genes in MG-63 during uninfected and 24 hrs p.i infected states using the methods and materials described in section 2.7. Osteogenic marker genes selected were *ALP*, *COL1A1*, osterix (*SP7*), *RUNX2*, RANKL (*TNFSF11*), *OCN* and bone sialoprotein (*BSP*) (figure 4.2 A). Of the genes tested, only relative gene expressions of *ALP* and *TNFSR11* were significantly increased during infection compared to the uninfected control.

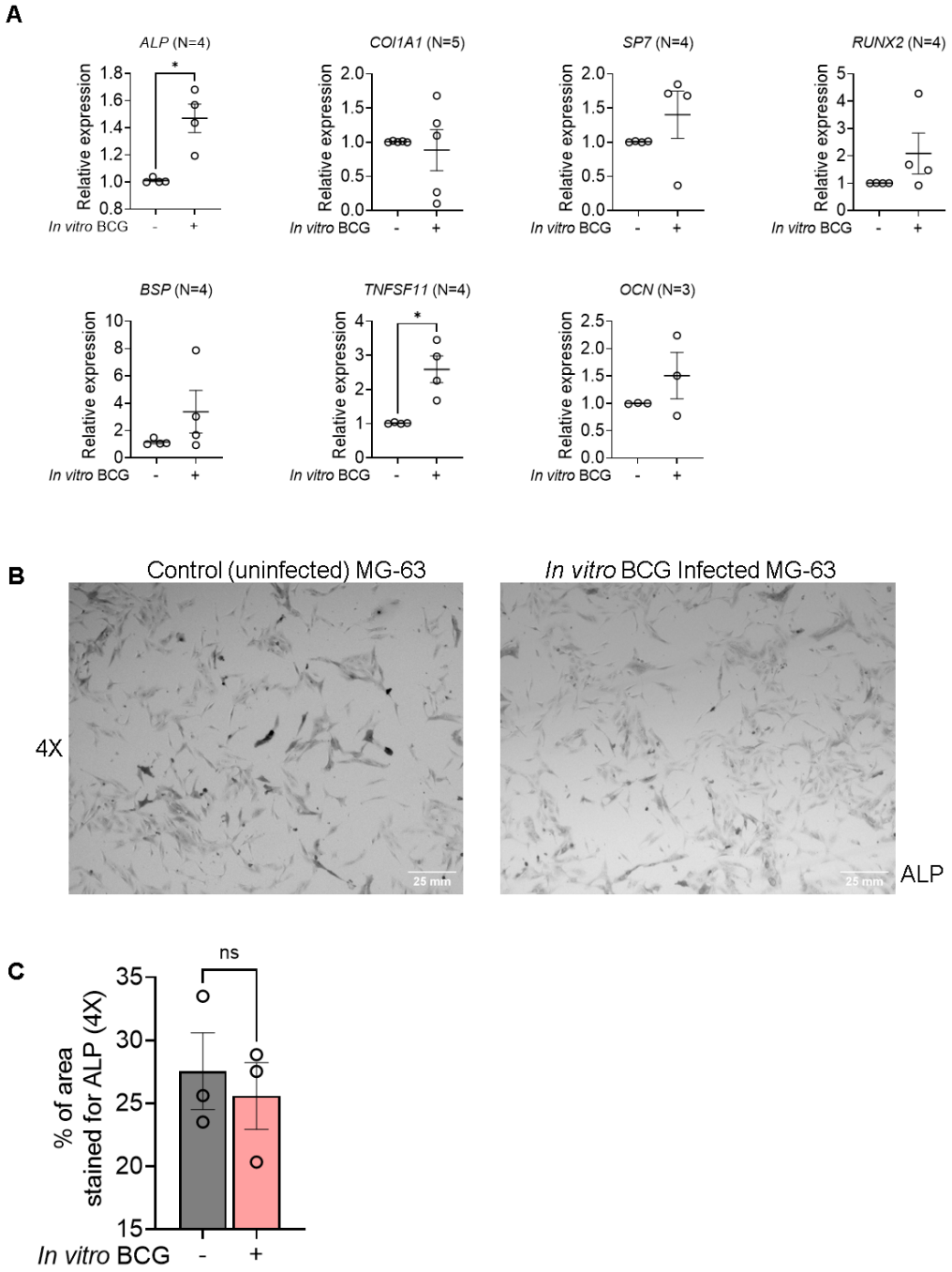

Figure 4.2 The effect of in vitro BCG on bone formation markers in osteoblast-like cell line MG-63

(A) RT-qPCR for bone formation genes ALP, COL1A1, SP7, RUNX2, BSP and TNFSF11. Data were normalised to the housekeeping gene β-actin to obtain ΔCq. The fold change in genes of interest relative to uninfected samples was determined using the $2^{-\Delta\Delta Cq}$ method. Experiments were performed in triplicate and the mean of triplicates are plotted. N=4 experiments. Mean ± SD are plotted. ALP and RANKL was significantly increased upon infection, Mann Whitney test. ALP: P=0.0286, TNFSF11: P=0.0286. (B) Representative images of Alkaline Phosphatase (ALP) stained MG-63 cells uninfected and in vitro infected with BCG at 4X (scale bar: 25mm) (C) Compiled quantification of ALP. Images were collected from 5 different fields of view at 4X magnification and quantified using the WEKA trainable

segmentation tool in the Fiji plugin for ImageJ. Mean ± SD are plotted, N=3, Unpaired t-test, P=0.6516.

To probe the activity of ALP further, a histochemical staining method for ALP was used as described in section 2.6. MG-63 were seeded at 200,000 cells per well of 24 well plates and ALP histochemical staining was carried out on uninfected and infected MG-63 after 24 hrs p.i. Images were taken on EVOS at 4X magnification for at least 5 non overlapping fields of view. No significant differences could be seen in the images during uninfected vs infected by eye (figure 4.2B). For quantification of ALP, the FIJI plugin - ImageJ Trainable Weka Segmentation was used to calculate the amount of ALP staining on uninfected versus infected cells. The average ALP quantification of the 5 images for uninfected and infected was taken and plotted in figure 4.2C. In contrast to the increased relative expression of *ALP* during infection, the quantification of histochemical staining showed a non-significant decrease in ALP activity in the infected cells.

4.2.3 Osteoblasts display a weak proinflammatory response to *in vitro* BCG infection

TLR2/4 signalling has been well studied in mycobacterial infection of macrophages; TLR activation triggers intracellular signalling cascades and the activation of NF-κB (Kawai 2007). However, little is known about how *Mtb* infection modulates the osteoblast response and if TLR2 and TLR4 are involved. Therefore, we next investigated the effects of BCG on selected proinflammatory markers in osteoblasts: TLR2, TLR4 and IL-1β.

TLR2 and TLR4 surface expression was assessed by using flow cytometry, quantifying median fluorescence intensity (MFI) and RT-qPCR for relative gene expression in MG-63 cells. THP-1 cells were used as the positive control as it is known that TLR2 and TLR4 expression increases during mycobacterial infection (Gao, Wu et al. 2019).

For MG-63, it was found that TLR2 surface expression was significantly increased during infection from a mean MFI of 97.4 to 200.3, a 2.06-fold increase (figure 4.3A). In comparison, BCG infection of THP-1 cells resulted in the MFI increasing from a mean of 30.6 to 84.5, a 2.76-fold increase (figure 4.3A). For TLR4, surface expression on MG-63 cells was decreased from a mean MFI of 1505 to 640.8 upon BCG infection, a 0.43-fold decrease. Whereas, as expected, THP-1 displayed an increase of an MFI of 180.2 to 273.3, a 1.52-fold increase (figure 4.3B).

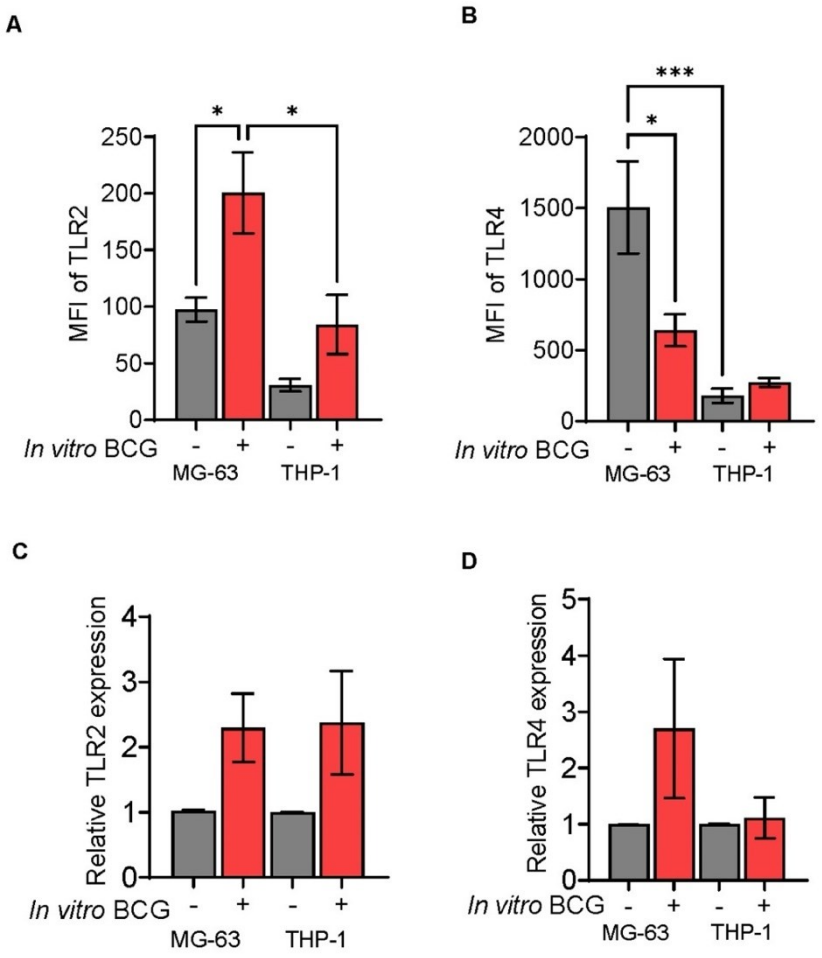

Figure 4.3 Differential modulation of TLR2 and TLR4 expression in MG-63 and THP-1 cells by in vitro BCG

*(A) Median Fluorescence intensity (MFI) of TLR2 surface expression on MG-63 and THP-1 cells, normalised to the isotype control PE Mouse IgG2a, κ Isotype Ctrl (FC) antibody fluorescence of PE (TLR2) measured by flow cytometry. N=4. One-way ANOVA ($F_{3,11}$ = 9.121, P=0.0025) and Tukey's multiple comparisons test showed significant differences between uninfected and infected MG-63 *P=0.0239, and infected MG-63 and infected THP-1 *P=0.0152. (B) MFI of TLR4 surface expression on MG-63 and THP-1 cells, normalised to the isotype control APC Mouse IgG2a, κ Isotype Ctrl (FC) Antibody fluorescence of APC (TLR4) measured by flow cytometry.*

*N=4. One-way ANOVA (F3,15= 1.75, P=0.0003) and Tukey's multiple comparisons test showed significant differences between uninfected and infected MG-63 *P=0.0238, and uninfected MG-63 and uninfected THP-1 ***P=0.0004. (C) Relative expression of TLR2 in uninfected and infected MG-63 and THP-1 cells, normalised to the housekeeping gene β-actin to obtain ΔCq. The fold change in genes of interest relative to uninfected samples was determined using the $2^{-\Delta\Delta Cq}$ method. Mean ± SD are plotted, N=4. One-way ANOVA showed no statistically significant differences. (D) Relative expression of TLR4 in uninfected and infected MG-63 and THP-1 cells, normalised to the housekeeping gene β-actin to obtain ΔCq. The fold change in genes of interest relative to uninfected samples was determined using the $2^{-\Delta\Delta Cq}$ method. Mean ± SD are plotted, N=4. One-way ANOVA showed no statistically significant differences.*

Modulation in TLR2 in BCG infected MG-63 cells was also found at the mRNA expression level where the relative gene expression of *TLR2* increased by 2.30-fold upon infection (figure 4.3C). BCG infected THP-1 cells similarly showed a 2.37-fold increase of *TLR2* gene expression (figure 4.3C). Both MG-63 and THP-1 saw a non-significant increase in relative TLR4 mRNA expression upon infection (figure 4.3D). Taken together, our data highlights a few important aspects of TLR2/4 in osteoblasts: (1) MG-63 cells demonstrate higher protein expression of TLR2 and TLR4 relative to THP-1 cells (figure 4.3A,B). (2) BCG infection reduced TLR4 protein expression in MG-63 cells which is the opposite of what was found in THP-1 cells, where BCG infection increased TLR4 protein expression (figure 4.3B). The use of LPS and Pam2CSK4 could have been used as controls to strengthen this data, as well as intracellular staining of TLR2 and TLR4 to show internalisation of the receptors upon activation.

TLR signalling results in downstream production of IL-1β (Medzhitov 1997), therefore we investigated whether MG-63 produced IL-1β in response to BCG challenge. For this, ELISA was performed on the supernatants of uninfected and BCG infected MG-63 cells. Initially, I aimed to determine the optimal concentration of TLR4 ligand LPS and TLR2 ligand Pam2CSK4, enough to stimulate MG-63 cells. Three concentrations were tested: 100 ng/ml, 1 μg/ml, and 2 μg/ml stimulation for 4 hrs, and IL-1β release was measured (figure 4.4A). Of note, stimulation with either LPS or Pam2CSK4 at the respective concentrations failed to give rise to a statistically significant increase in IL-1β.

BCG infection induced an average of 38.4 pg/ml IL-1β at 3 hrs p.i., increasing to 133 pg/ml at 24 hrs p.i. (figure 4.4B).

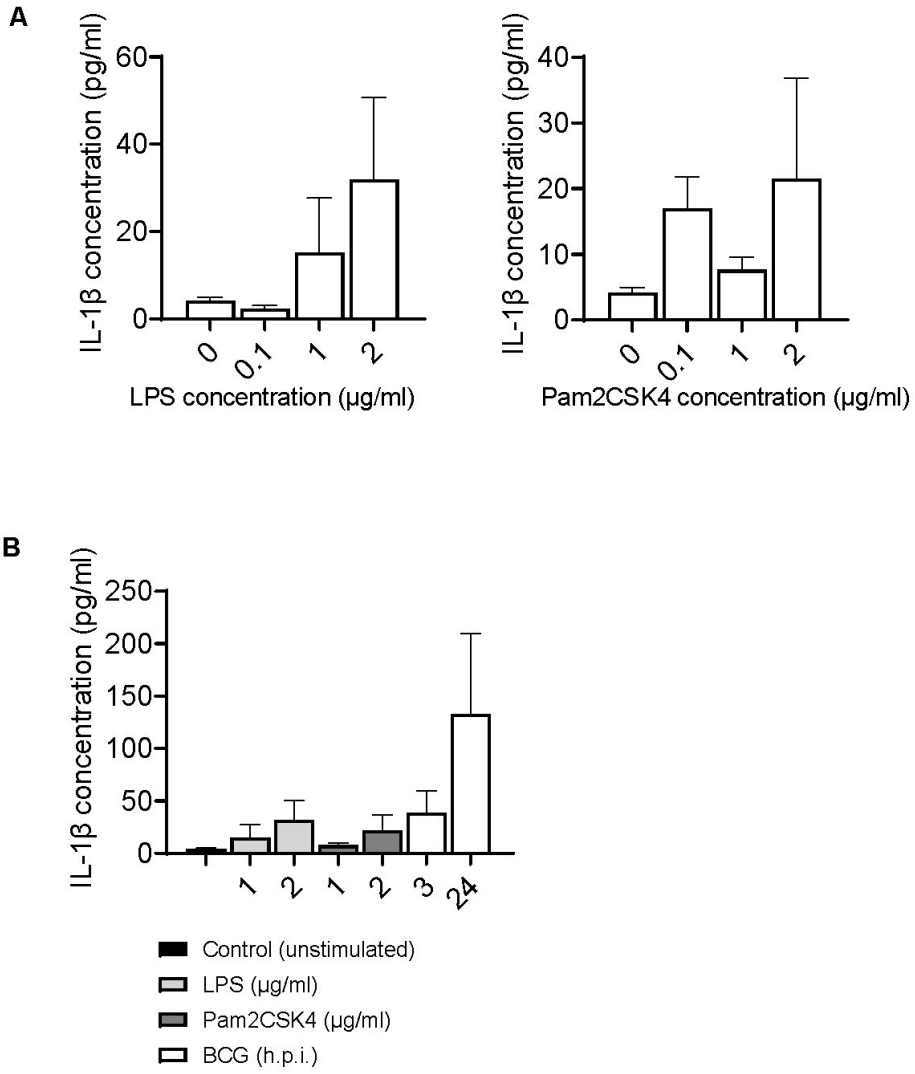

Figure 4.4 Proinflammatory cytokine IL-1β is weakly induced in MG-63 osteoblasts by in vitro BCG

(A) Quantification of IL-1β in response to 100ng/ml, 1µg/ml and 2µg/ml LPS stimulated MG-63 cells. N=4. One-Way ANOVA showed no significant differences between unstimulated MG-63 (control) levels of IL-1β and the test concentrations of LPS ($F_{3,15}$ = 2.050, P=0.1501). Quantification of IL-1β in response to 100ng/ml, 1µg/ml and 2µg/ml Pam2CSK4 stimulated MG-63 cells. One-Way ANOVA showed no significant differences between unstimulated MG-63 (control) levels of IL-1β and the test concentrations of Pam2CSK4 ($F_{3,11}$= 0.9843, P=0.4355) (C) Quantification of IL-1β from MG-63 in response to LPS, Pam2CSK4 and BCG at 3 hrs and 24 hrs p.i. One-Way ANOVA showed no significant differences in IL-1β concentration between groups ($F_{6, 22}$= 2.104, P=0.0939). Graphs show mean ±SD, N=4.

BCG exhibited a weak invasive phenotype with MG-63 cells compared to THP-1 (figure 4.1), which possess active Fc and C3b receptors due to their monocytic characteristics. This lack of active uptake of bacteria could justify the low percentage invasion seen in MG-63 and therefore correlate with the weak proinflammatory response of IL-1β (figure 4.1, figure 4.4). MG-63 phenotypically is a fibroblast-like cell type and is not actively phagocytic. Although it has not been determined how exactly bacteria are able to internalise within osteoblasts, the uptake of *S. aureus* is facilitated by adhesins, with the major player being FnBPs on the surface of *S. aureus* which interact with Fn receptors (e.g. α5β1 integrins) on the osteoblast cell surface (Foster 2014). It is possible mycobacteria utilise a similar strategy to internalise within the osteoblast.

Nonetheless, we found a significant induction in *TNFSF11* gene expression (figure 4.2A), *TLR2* gene and TLR2 protein expression (figure 4.3A, C) and a slight induction of IL-1β (figure 4.4B) all of which are pro-osteoclastogenic mediators. Hence, we decided to probe further into the response of osteoclast-like cells during mycobacterial infection.

4.2.4 *In vitro* BCG infection of osteoclasts

To study osteoclast responses to *in vitro* BCG infection, OCLs were infected by m-Cherry-BCG at day 6 of differentiation as described in the methods and materials section 2.4.2, for 3 hrs at an MOI:5 followed by removal of extracellular bacteria and incubation until 24 hrs post infection. Infections were performed only up to 24 hrs so that OCLs would not be cultured past 7 days, as multiple reports have shown that they die very quickly in culture (only surviving 1-2 days once they reach maturity) (Akchurin 2008, Chevalier 2021).

Flow cytometry data (figure 4.5A-C) showed that the percentage of m-Cherry^{+} OCLs increased from an average of 32.6 % at 3 hrs p.i. to 51.3 % at 24 hrs p.i. This was not reflected in the CFU assay which quantifies viable intracellular bacteria (figure 4.5D). For OCLs at 3 hrs p.i., there was a mean of 85022 CFU/ml, dropping to 5854 CFU/ml at 24 hrs p.i. The increase in fluorescence and reduction in

CFU/ml at 24 hrs p.i. for OCLs may be explained by the loss of cells during the wash step prior to lysis or cells lysing bacteria into the media.

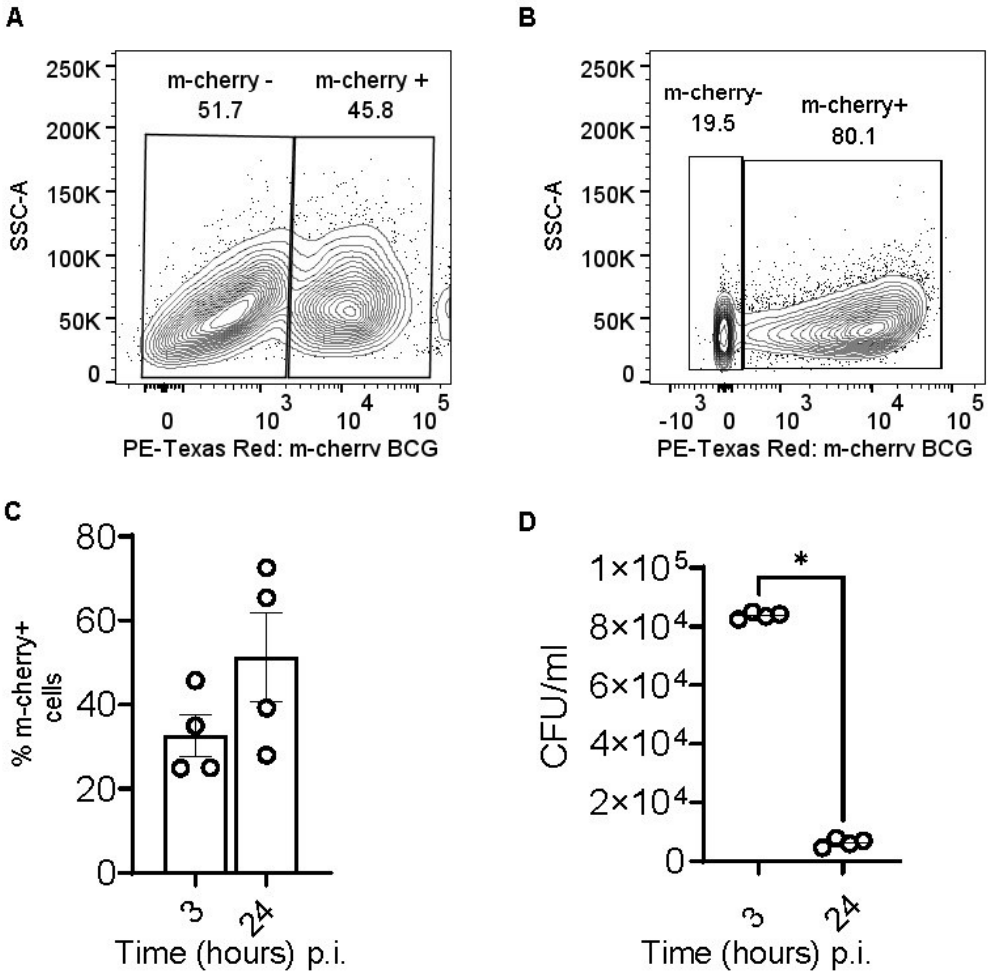

Figure 4.5 BCG is internalised by osteoclast-like cells

Contour plots with outliers displayed showing BCG uptake at 3 hrs (A) vs 24 hrs-p.i. (B) for OCLs. (C) Compiled data of BCG uptake at 3 and 24 hrs p.i. of OCLs (unpaired t-test, P=0.1621). (D) CFU assay quantifying viable intracellular BCG at 3 vs 24 hrs p.i. in OCLs (Mann Whitney test, P=0.0286).

At 24 hrs p.i. we could also separate the 1-2N OCLs from ≥3N OCLs using Hoescht staining of the nuclei and evaluated whether BCG is preferential to either cell type, (figure 4.6). We found that BCG does not have a propensity for 1-2N or ≥3N cells - both populations show similar percentages of m-Cherry^{+} cells (figure 4.6 B). However, there is more variation in the persistence of BCG within ≥3N cells compared to 1-2N (figure 4.6B). Taken together with figure 4.5D which shows a

13-fold reduction in CFU/ml between 3 and 24 hours, it could be postulated that ≥3N cells inhibit intracellular BCG growth more effectively than 1-2N cells.

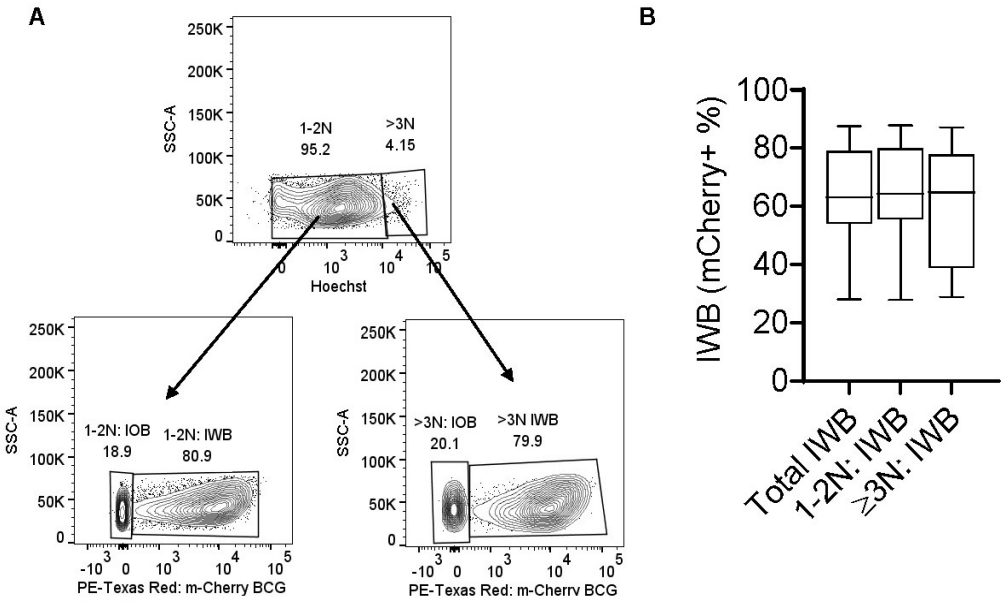

Figure 4.6 BCG infects 1-2N or ≥3N cells equally

(A) Representative gating strategy of m-cherry BCG infected cells at 24 hrs p.i. Contour plots divide 1-2N and ≥3N cells into separate contour plots depicting IOB (infected without bacteria) and IWB (infected with bacteria). (B) Box and whisker plot of compiled data of the percentages of IWB from total, 1-2N and ≥3N cells. Data was analysed using One Way ANOVA and found no statistical differences. N=12.

4.2.5 Increase in osteoclast number and their resorption activity during *in vitro* BCG infection

We measured osteoclastic activity using several methods. Firstly, we distinguished if there was any difference between the frequency of osteoclasts in culture upon infection with TRAP staining. Increased TRAP activity is known to be enhanced in the presence of increased bone resorption, as its serum level correlates with the absolute number of osteoclasts and resorption markers (Mira-Pascual 2019). Increased TRAP staining in OATB bone samples from TB patients was also increased compared to osteoarthritis control samples, suggesting the mycobacteria had a role to play in the increase in TRAP staining/activity (Liu, Zhou et al. 2020).

At 24 hrs p.i or day 7, TRAP⁺ cells containing 3 or more nuclei (≥3N) were counted at 20X per field of view from at least 7 non overlapping images so that at least 100 cells were counted in total per well. As shown in figure 4.7A-B, we saw a trend in the increase in osteoclast numbers in BCG infected OCLs compared to the control.

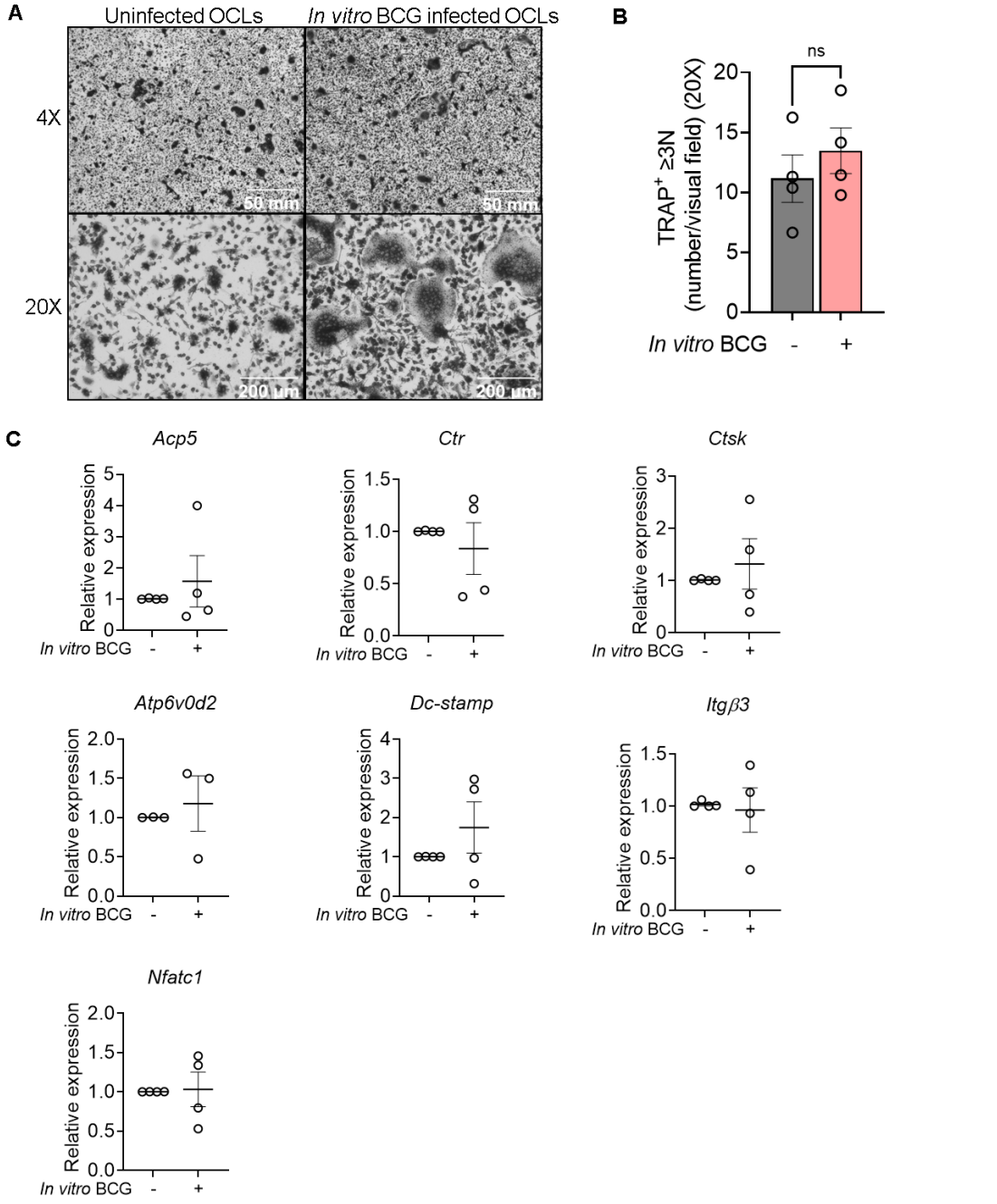

Figure 4.7 The effect of in vitro BCG on bone resorption markers in osteoclast-like cells

(A) Representative images of TRAP stained OCLs from control (uninfected) and in vitro BCG infected cells at 4X (scale bar: 50mm) and 20X (scale bar: 200µm) (B) Quantification of TRAP⁺ OCLs containing 3 or more nuclei. N=4, unpaired t-test, P=0.4301. (C) Real-time PCR for bone resorption genes Nfatc1, Acp5, Ctr, CTSK, Atp6v0d2, Dc-Stamp and Itgb3 for in vitro infected OCLs. Data were normalised to the housekeeping gene β-actin to obtain ΔCq. The fold change in genes of interest relative to uninfected samples was determined using the $2^{-\Delta\Delta Cq}$ method. Experiments were performed in triplicate and the mean of triplicates are plotted. Mean ± SD are plotted. The number of experiment replicates are stated on each graph. Statistical analyses were performed using unpaired t-test or Mann-Whitney test. No results were statistically significant.

To investigate whether the increase in TRAP activity in BCG infected OCLs was related to an increase in the expression of bone resorption genes, we conducted RT-qPCR for *Nfatc1, Acp5 Ctr, Ctsk, Atp6v0d2, Dc-stamp* and *Itgβ3*. The data showed that there were no changes in the mRNA expression of bone resorption genes upon infection (figure 4.7C). Therefore, the increase in BCG-mediated TRAP activity is not linked to an increase in bone resorption markers.

4.2.6 *In vitro* BCG infection expands OCL frequency through an increase in multinucleation

Our TRAP activity assay (figure 4.7A) indicates an increase in large OCLs upon BCG infection, therefore we decided to probe whether this was linked to an increase in the multinucleation or fusion events between the precursors with 1 or 2 nuclei.

Using a Hoechst 33342 staining method (see Methods 2.2.3), uninfected OCLs and *in vitro* infected OCLs were isolated on a cell sorter based on their multinucleation. The frequency ≥3N cells was markedly increased upon *in vitro* infection, whereas there were no significant differences between the frequency of 1-2N cells (figure 4.8 A-B). The average percentage of ≥3N in uninfected OCL culture was 3.91 % compared to 9.35 % in BCG-infected OCLs. The increase of the ≥3N fraction of cells suggests an increase in the multinuclear phenotype and increase in the number of osteoclasts in the culture, which was also highlighted by TRAP staining (figure 4.7A).

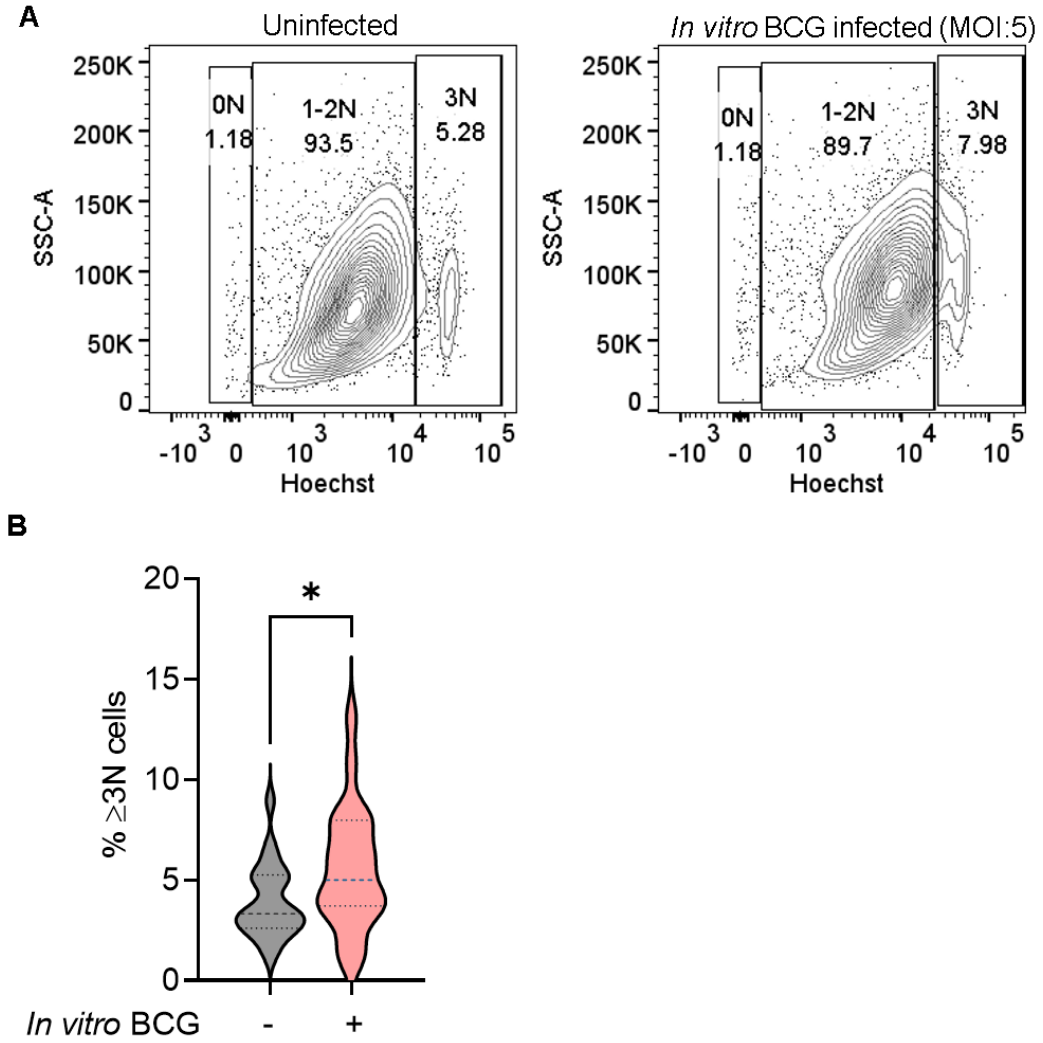

Figure 4.8 BCG infection in vitro expands frequency of multinucleated OCLs.

(A) Representative contour plot with outliers of OCLs from an uninfected control OCLs and OCLs that had been infected in vitro with BCG (MOI:5) for 3 hrs followed by a 24-hr time point. Gated on single and live cells. (B) Violin plot depicting compiled percentages of ≥3N cells in culture from uninfected control mice and OCLs that were infected in vitro with BCG MOI 5 for 3 hrs followed by a 24-hr time point. Statistical analyses were performed using Mann-Whitney test (the data is not normally distributed) and showed significant differences: P=0.0342. N=22.

4.2.7 *In vitro* BCG infection modulates cytokine/chemokine profiles in OCLs

Osteoclasts participate in paracrine signalling, engaging in communication with adjacent and other immune cells. To study whether BCG induced cytokine and chemokine release from OCLs upon infection, we conducted cytokine profiling of

supernatants collected from uninfected and *in vitro* infected OCLs using Luminex multiplex assays and ELISAs. In Luminex analysis, values for IL-3, IL-9, IL-23, IL-17A (CTLA-8), IL-28, IL-22 IL-31 from both uninfected and infected samples were lower than the Lower Limit of Quantification (LLOQ) and therefore unable to estimate (out of range, unable to extrapolate; OOR>). All data for IP-10 (CXCL10) could also not be extrapolated as the values were above than the Higher Limit of Quantification (HLOQ) and out of range, unable to extrapolate (OOR<). The raw data from Luminex experiments are included in Appendix Tables SB1 and SB2. The samples were run as 4 replicates from 2 different experiments, which used a total of 4 mice for each group (uninfected versus infected).

A heatmap was generated using the data (figure 4.9A). Some samples gave rise to data that was detected for the uninfected condition, but not for infected (OOR<), (MCP-1 (CCL2), MIP-2 α (CXCL2), MIP-1β (CCL4), GRO-α (CXCL1)), these were included in the heatmap where the HLOQ was plotted but not featured the scatter plots. Uninfected sample values from G-CSF (CSF-3), IL1-β, IL-2, M-CSF, IL-4, IL-5, IFN-α, IL-9, IL-12p70, IL-13, IL-15, IL-1α were OOR< but the infected sample values were within the limits. Similarly, these were included in the heatmap but not the scatter plots to give a gist of general changes in cytokine and chemokine expressions upon infection.

The only data that were plotted individually were values that were detected within the range of quantification or were able to be extrapolated. This includes IL-10, LIF, IL-27, RANTES (CCL5), IL-6, TNF-α, MIP-1α (CCL3), MCP-3 (CCL7), Eotaxin (CCLL11) and IFN-γ (figure 4.9B). From the data of the cytokines that were within the range, IL-10, RANTES (CCL5), MIP-α (CCL3), MCP-3 (CCL7), IL-6 and Eotaxin (CCL11) were significantly increased upon infection. Out of these, RANTES (CCL5), MIP-α (CCL3), MCP-3 (CCL7), IL-6 and Eotaxin (CCL11) have been shown to stimulate osteoclastogenesis (Yukie 2009, Wintges 2013, Kindstedt 2017, Jordan 2018).

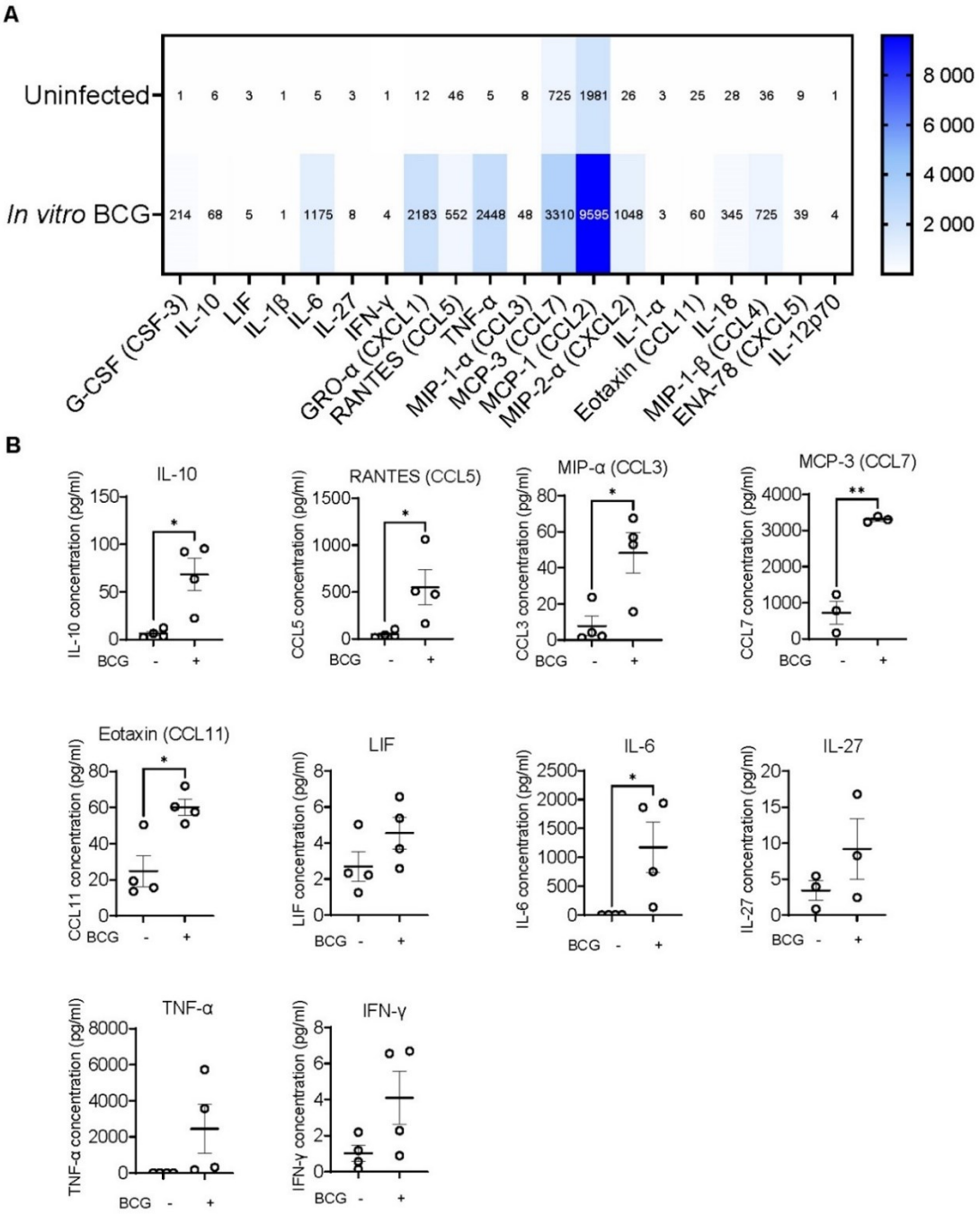

Figure 4.9 In vitro BCG infection induces pro-osteoclastogenic and proinflammatory cytokine release

Luminex assay of a panel of pre-determined panel of cytokines released into the supernatant by uninfected OCLs and OCLs infected in vitro with BCG MOI 5 at a 24-hr time point (N=4 mice). (A) Heatmap of cytokine panel assay of cytokine levels that were determined by Luminex including values that were within range, or able to be extrapolated. Values that were <OOR or >OOR are plotted as the HLOQ or LLOQ accordingly. The mean of side-by-side replicates were plotted with a double gradient colourmap. (B) Scatter plots of cytokines upregulated during in vitro BCG infection with values within the range detected by Luminex, replicates denoted by dots on the graph. Graphs show mean ±SD with individual values plotted. Statistical

analyses were performed using Student's unpaired t-test. IL-10: P=0.0108; RANTES (CCL5): P=0.0362; MIP-α (CCL3): P=0.0177; MCP-3 (CCL7): P=0.0012; Eotaxin (CCL11): P=0.0105.

CCL2, CXCL2, CCL4, TNF-α and CXCL1 do not fully quantify the cytokine release upon infection due to the infected values being out of range, higher than the HLOQ. The supernatants for infected samples would need to be diluted and repeated. For TNF-α and IL-6, the variation may have come because the supernatants were in frozen storage at -20°C prior to the experiment. Individual ELISAs were also performed for IL-1β, CXCL2, IL-6 and TNF-α (figure 4.10). This similarly showed a significant increase of IL-6 upon infection. In both Luminex assays and ELISA, no significant increase in IL-1β was found upon infection.

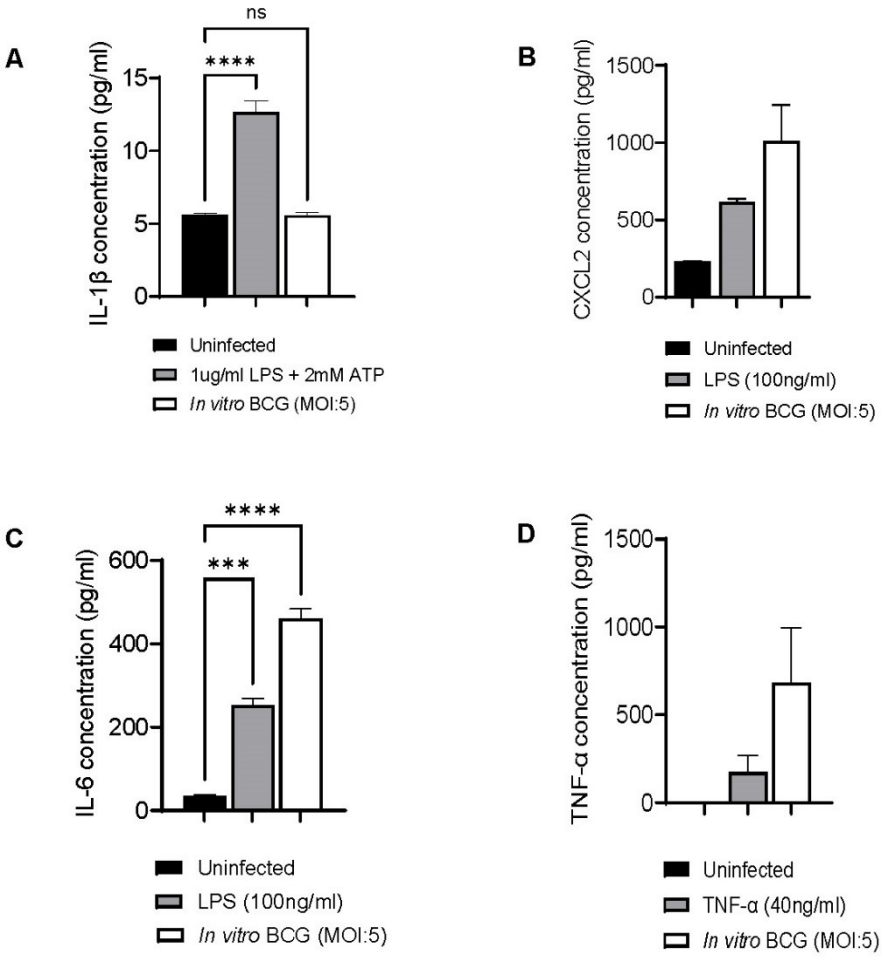

Figure 4.10 In vitro BCG infection induces osteoclastogenic and proinflammatory cytokine release

(A) Quantification of IL-1β in response to 1μg/ml LPS for 4 hrs followed by 1 hr of 2mM ATP treatment, and in vitro BCG infection. N=3. Analysis was performed using One-Way ANOVA. Tukey's multiple comparison test showed significant differences

between uninfected levels of IL-1β and the test concentrations of LPS + ATP positive control (P<0.0001). (B) Quantification of CXCL2 in response to 100ng/ml LPS for 4 hrs, and in vitro BCG infection for 3 hrs followed by 24-hr time point. N=3. Analysis was performed using One-Way ANOVA. (C) Quantification of IL-6 in response to 100ng/ml LPS for 4 hrs, and in vitro BCG infection for 3 hrs followed by 24-hr time point. N=3. Analysis was performed using One-Way ANOVA. Tukey's multiple comparison test showed significant differences between uninfected levels of IL-6 and the test concentrations of LPS positive control (P=0.0002) and uninfected versus BCG infection (P<0.0001). (D) Quantification of TNF-α in response to 40ng/ml TNF-α for 3 hrs, and in vitro BCG infection for 3 hrs followed by 24-hr time point. N=4. Analysis was performed using One-Way ANOVA.

4.2.8 *In vitro* BCG infection of OCLs does not alter surface receptors

We next evaluated the effect of BCG infection on the $CD45^{+}Gr\text{-}1^{-}CD44^{+}CD51^{+}$ immunophenotype. For this, uninfected and BCG-infected (24 hrs p.i) OCLs were stained followed by flow cytometry. The frequency of $CD45^{+}Gr\text{-}1^{-}CD44^{+}CD51^{+}$ cells did not change significantly between uninfected and infected for both 1-2N and ≥3N cells (figure 4.11). The frequency of parent refers to the percentage of $CD44^{+}CD51^{+}$ out of the parent $CD45^{+}Gr\text{-}1^{-}$ population. For *in vitro* infection, the average frequency of parent for uninfected 1-2N cells was 16.16 % and infected 1-2N cells was 16.33 % whereas for ≥3N cells, the average frequency of parent for uninfected was 15.90 % and infected was 16.67 %.

Surface expression of CD51 (vitronectin receptor subunit alpha), a marker of mature osteoclasts, also did not show any change between uninfected and infected cells, both for 1-2N and ≥3N population (figure 4.12). The mean CD51 MFI for uninfected 1-2N was 549.6 and *in vitro* infected was 596.9. The mean CD51 MFI for uninfected ≥3N was 1149 and *in vitro* infected ≥3N was 1228.

Taken together, our data is suggesting that the $CD45^{+}Gr\text{-}1^{-}CD44^{+}CD51^{+}$ immunophenotype is not altered during BCG infection. How this relates to osteoclastogenesis is limited by the lack of mature osteoclast-specific surface markers.

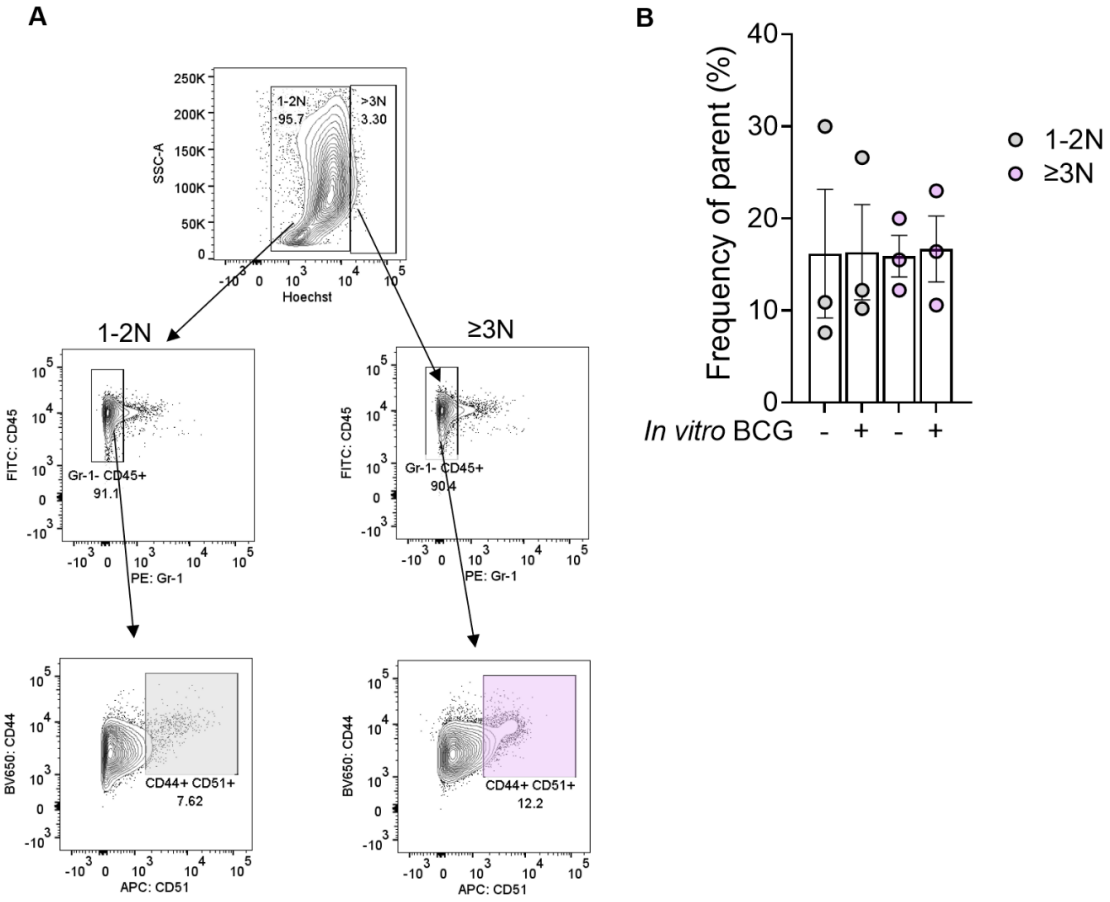

Figure 4.11 In vitro BCG does not significantly alter OCL immunophenotype

(A) Representative gating strategy for flow cytometry analysis of 1-2N and ≥3N cells for a CD45⁺ Gr-1⁻ CD44⁺ CD51⁺ immunophenotype. Cells are pre-gated on single cells by doublet discrimination and live cells (AmCyan). (B) Scatter plot with bar of compiled frequency of parent values. The percentage of events (CD44⁺CD51⁺) in this population out of the parent population (CD45⁺Gr-1⁻) for 1-2N and ≥3N cells in OCLs from uninfected mice and OCLs from age and gender matched mice that had been infected in vitro with BCG MOI 5 for a 24-hr time point. Statistical analyses were performed using two-way ANOVA and revealed no statistically significant differences in 1-2N cells upon infection and ≥3N cells upon infection.

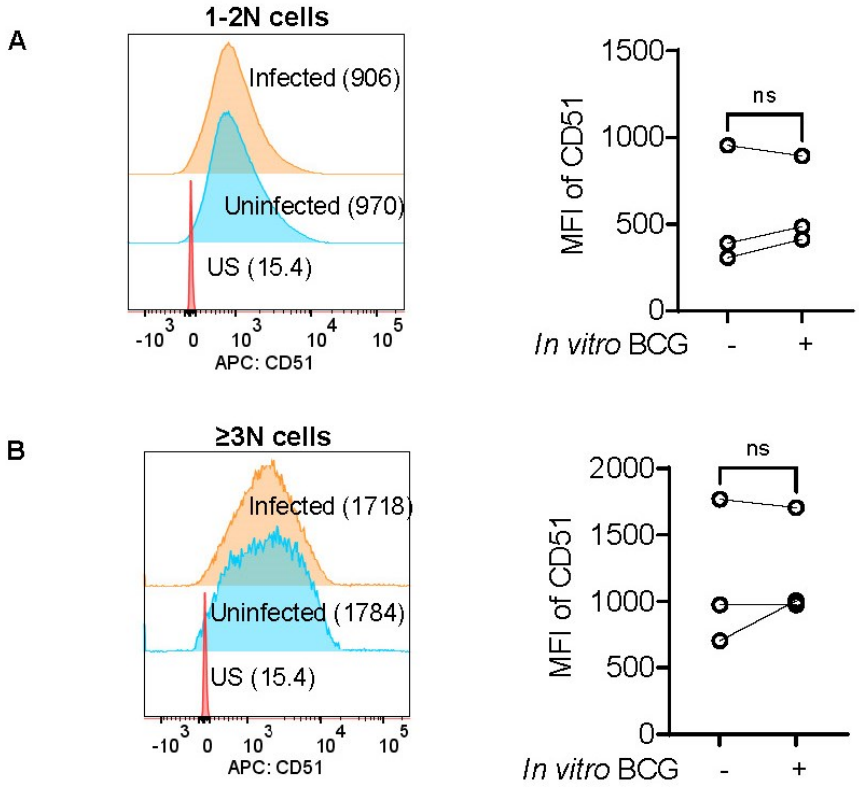

Figure 4.12 In vitro BCG does not significantly alter surface expression of CD51

(A) Representative median fluorescence intensity (MFI) half-offset histogram overlays of CD51 fluorescence in unstained (US) (control) cells, uninfected and infected cells and before-after plot with compiled CD51 MFI normalised to unstained controls. Statistical analyses were performed using unpaired t-test, but no statistically significant differences were found in CD51 expression in 1-2N (P=0.8608). (B) Representative MFI half-offset histogram overlays of CD51 fluorescence in unstained (control) cells, uninfected and infected cells, and before-after plot with compiled CD51 MFI normalised to unstained controls. Statistical analyses were performed using unpaired t-test, but no statistically significant differences were found in CD51 expression in ≥3N (P=0.8527) upon in vitro BCG infection.

4.2.9 *In vivo* infection model

An *in vivo* EPTB infection model was next established. This involved the intravenous (i.v.) injection of 10^6 BCG for a period of 30 days to ensure mycobacteria had sufficient time to establish a systemic infection and reach the bone marrow, which is how bone TB can manifest. After 30 days post infection (dpi), BM cells were harvested and differentiated into OCLs for 7 days (figure 4.13).

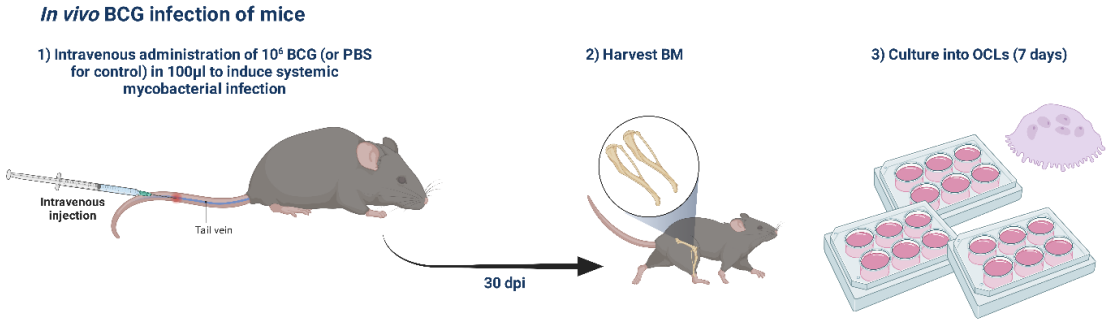

Figure 4.13 Schematic diagram of in vivo BCG infection.

Age and gender matched C57BL/6 mice were injected I.V. with 10^6 BCG in 100 µl or 100 µl PBS as a control for 30 days, after which they were sacrificed, and the BM was harvested and differentiated into OCLs. There was no second stimulation with BCG during differentiation.

4.2.10 The effect of *in vivo* BCG on osteoclast number and activity

The effect of *in vivo* BCG on OCLs was studied using TRAP stain and nuclear staining analysis, as described for *in vitro* infected OCLs (methods and materials section 2.2.3, 2.5). After 7 days of *in vitro* culture, OCLs from mice infected *in vivo* were stained using a TRAP staining kit along with their respective mock infected controls (figure 4.14A, B). Frequency of 1-2N, ≥3N cells was also analysed using the previously described flow cytometry method.

The OCLs from *in vivo* BCG-infected mice displayed a significant increase in TRAP activity, with an average of 12.61 $TRAP^+$ ≥3N OCLs per field of view at 20X magnification compared to 7.57 for mock infected (figure 4.14A, B). This is different from *in vitro* infected OCLs, where a non-significant slight increase was observed upon BCG infection (figure 4.7B). The expansion of ≥3N cells rose from 3.80 % in mock-infected to 4.35 % in BCG-infected (figure 4.14C). In our *in vitro* experiments however, we saw a significant increase in ≥3N cells (figure 4.8B).

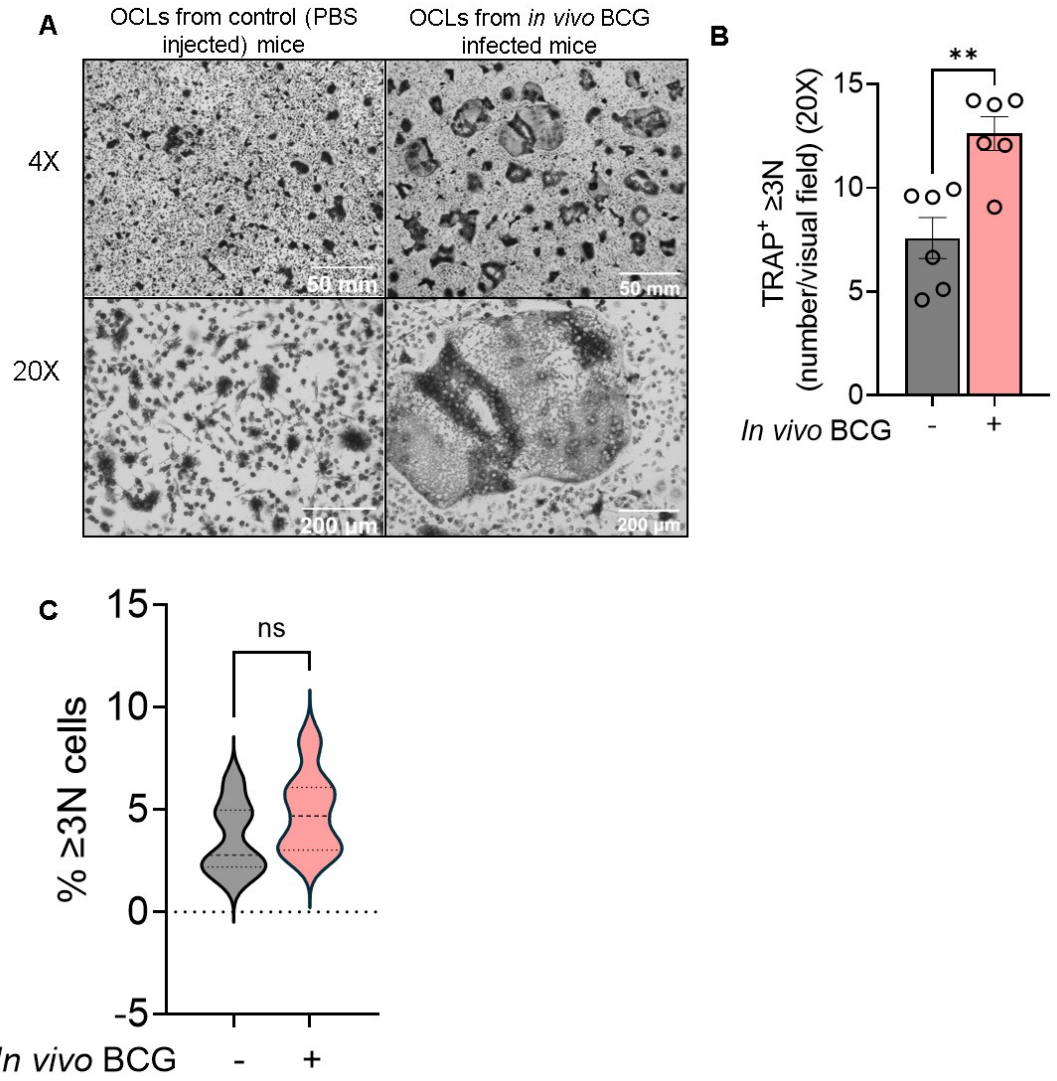

Figure 4.14 In vivo BCG infection increases TRAP activity and multinucleation of OCLs

(A) Representative images of TRAP stained OCLs from control (mock infected) and OCLs from mice infected in vivo with BCG at 4X (scale bar: 25mm) and 20X (scale bar: 50µm) (B) Quantification of TRAP⁺ OCLs containing 3 or more nuclei. N=6, unpaired t-test, P=0.0028. (C) Violin plot depicting compiled percentages of ≥3N cells in culture from PBS infected control mice and OCLs from age and gender matched mice that were infected with 10^6 BCG for 30 days. Statistical analyses were performed using Mann-Whitney test and showed no significant differences: P=0.5787. N=7.

4.2.11 *In vivo* BCG infection effect on cytokine and chemokine profiles from OCLs

Luminex assays were performed to determine whether the proinflammatory and pro-osteoclastogenic effects seen from *in vitro* BCG infection (figure 4.9)

translated to *in vivo.* The raw data is found in Appendix Table SB3. The samples were not diluted prior to processing so some values presented outside the ranges of detection. Both mock infected and infected sample values for IL-4 were lower than the Lower Limit of Quantification (LLOQ) and unable to extrapolate (OOR>). Also uninfected and infected sample data for IP-10 (CXCL10) could not be extrapolated as the values were above than the Higher Limit of Quantification (HLOQ) and unable to extrapolate (OOR<). In this analysis, 3 replicate samples were included (3 control mice and 3 BCG infected mice for a total of 6 mice) (figure 4.15).

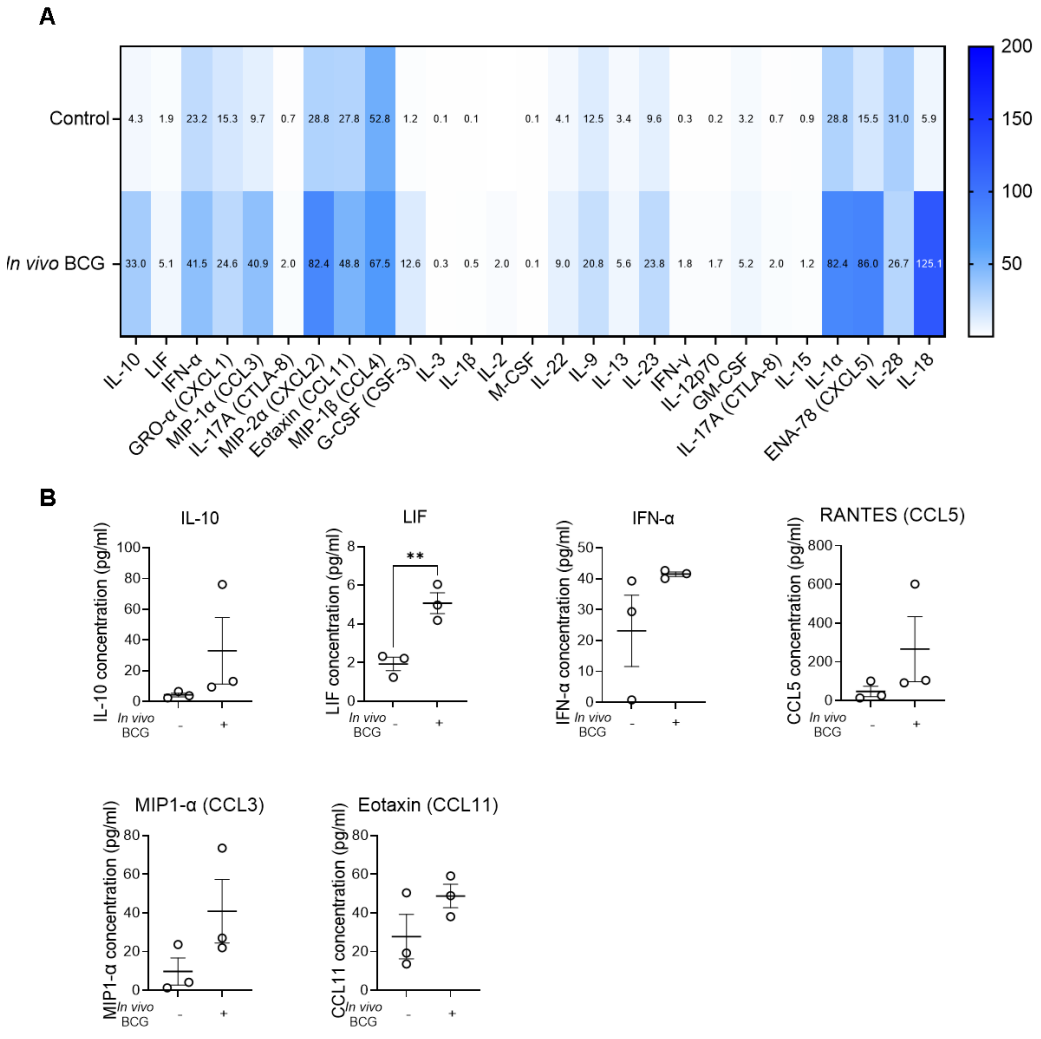

Figure 4.15 Cytokine profiling of OCLs from in vivo BCG infected mice

Luminex assay of a pre-determined panel of cytokines released into the supernatant by OCLs from mock infected mice and OCLs from mice infected in vivo with BCG. Culture supernatants at day 7 of differentiation were used. (A) Heatmap of cytokine panel assay of cytokine levels that were determined by Luminex including values that were within range, or able to be extrapolated. The mean of side-by-side replicates were plotted with a double gradient colourmap. N=3. (B) Scatter plots of

*cytokines upregulated during in vivo BCG infection with values within the range detected by Luminex, replicates denoted by dots on the graph, with each dot representing one mouse. Graphs show mean ±SD with individual values plotted. Statistical analyses were performed using Student's unpaired t-test, LIF: **P=0.0081.*

A heatmap was generated of the cytokines with data that were included within the range of detection or that could be extrapolated (figure 4.15A). IL-6, TNF-α, MCP-3 (CCL7) and CCL2 were excluded from the heatmap due to high variation within the replicates which skewed the axis. Of the cytokines that were both within range and had N=3 for mock infected and N=3 for infected, scatter plots were generated.

Similar to the *in vitro* infection data, an increase in IL-10, MIP-1α (CCL3), RANTES (CCL5), Eotaxin (CCL11) and LIF was found in the culture supernatant of OCLs from *in vivo* infected mice (figure 4.15B). Of these cytokines, only LIF was significantly increased upon *in vivo* infection. Regardless of the mode or time of infection, these chemokines and cytokines appear to be linked to the osteoclast response to mycobacterial challenge.

4.2.12 Analysis of cell populations in BM of *in vivo* BCG infected mice

The data so far has suggested that for both *in vitro* and *in vivo* infection, BCG induces an increased osteoclast number, frequency, activity, and their inflammatory response. Next, we aimed to investigate whether BCG could reprogram HSCs in the BM towards osteoclastogenic potential. For this, we analysed the OCP populations among the BM cells of mock vs BCG-infected mice at 30 days p.i. using flow cytometry. We hypothesised that an increase in the OCPs in the BM during infection could be responsible for the increased multinucleated, resorptive osteoclasts observed among *in vitro* differentiated BM cells from BCG-infected mice (figure 4.14).

To evaluate the frequency of OCPs the BM cells were stained with antibodies against CD117 (c-Kit), CD115, B220, CD11b, CD27, CD3 and CD70 markers. Three gating strategies were used to ensure thorough analysis. The frequency of OCPs in the BM was expressed as a percentage of live cells in the analysis.

Xiao *et al* demonstrated that a rare BM population of c-Kit^{+}CD115^{+}B220^{-}CD11b^{low} CD27^{low} cells (i.e. 0.3%) had higher potential for osteoclastogenesis than c-Kit^{+}CD115^{+}B220^{-}CD11b^{low} CD27^{high} cells (Xiao 2013). Therefore, we looked for the c-Kit^{+}CD115^{+}B220^{-}CD11b^{low}CD27^{low} and c-Kit^{+}CD115^{+}B220^{-}CD11b^{low} CD27^{high} cells in the BM of uninfected and BCG-infected mice (figure 4.16A). We considered both of them as OCPs. When these two populations were analysed separately, we found a trend of low frequency for both of them in BM of BCG-infected mice (figure 4.16 B,C). Combining the frequency of two populations resulted in significantly decreased OCPs in BCG-infected mice (mean of 0.348 %) compared to the control mice (mean of 0.696 %) (figure 4.16D).

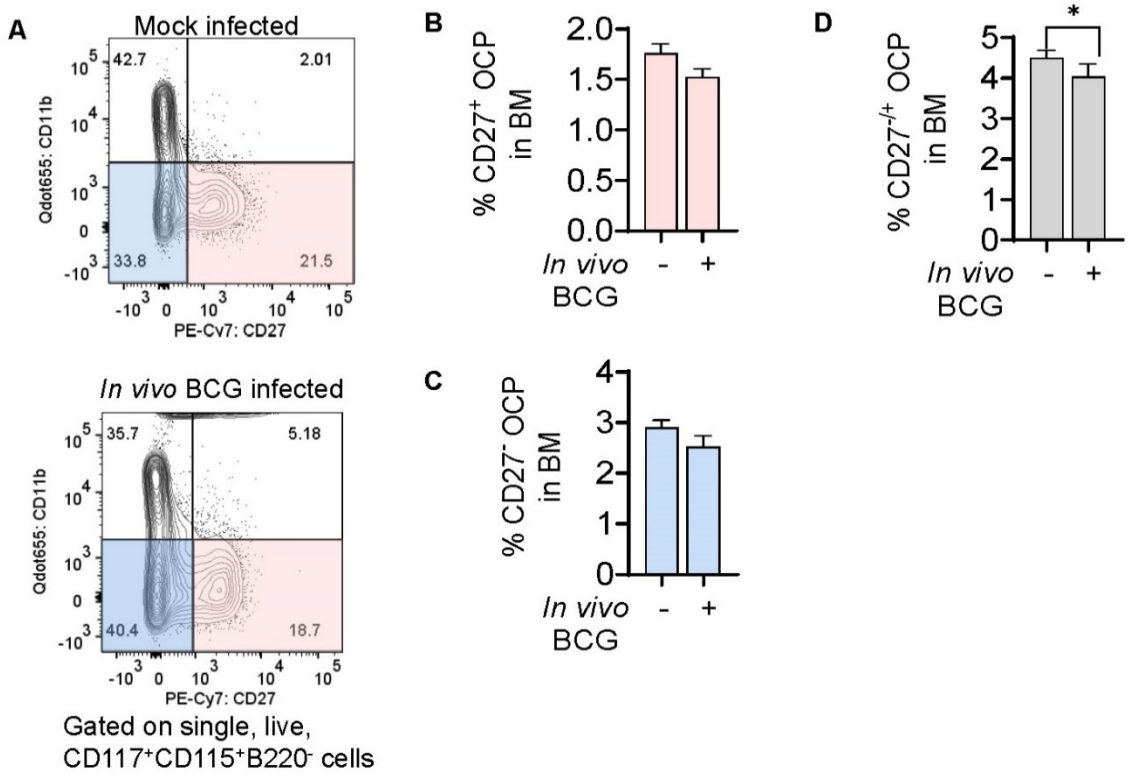

Figure 4.16 Frequency of CD117^{+}CD115^{+} B220^{-}CD11b^{low} in the BM of BCG infected mice decrease compared to mock infected mice

(A) Representative contour plots with outliers of mock-infected and in vivo BCG infected mice showing single, live, CD117⁺CD115⁺B220⁻CD11b^{low} CD27⁺/CD27⁻ cells. (B) Bar graph showing the percentage of CD117⁺CD115⁺B220⁻CD11b^{low}CD27⁺ cells in the BM expressed as a percentage of total live cells. Student's unpaired t-test (P=0.0877). (C) Bar graph showing the percentage of CD117⁺CD115⁺B220⁻ CD11b^{low} CD27⁻ cells in the BM expressed as a percentage of total live cells. Student's unpaired t-test (P=0.1840). (D) Bar graph showing the percentage of CD115⁺B220⁻ CD11b^{low} cells in the BM expressed as a percentage of total live cells. Student's unpaired t-test (P=0.0422). CD117 is also known as c-Kit.

We also utilised the strategy adopted by Jacome-Galarza *et al*, who characterised BM OCPs as CD3⁻B220⁻CD11b^{low}CD117⁺CD115⁺ (Jacome-Galarza 2013). Using this characterisation, we found a 2-fold reduction in OCPs among BM cells of BCG infected mice compared to BM from control mice (0.344 % in controls and 0.1582 % in BCG-infected mice, figure 4.17).

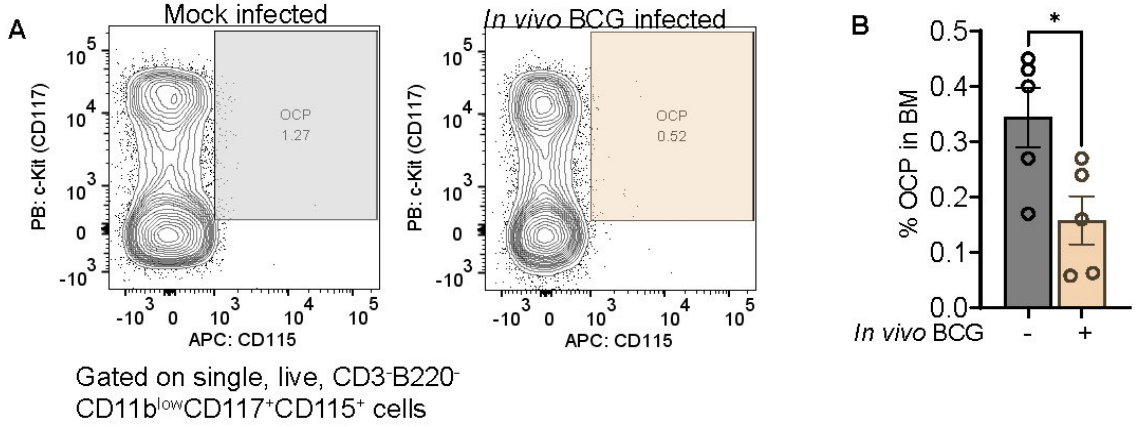

Figure 4.17 Frequency of CD3⁻B220⁻CD11b^{low}CD117⁺CD115⁺ OCPs in the BM of BCG infected mice decrease compared to mock infected mice

(A) Representative contour plots with outliers of mock infected vs in vivo infected BM of mice, showing single, live, CD3⁻B220⁻CD11b^{low}CD117⁺CD115⁺cells. (B) Frequency of OCPs - CD3⁻B220⁻CD11b^{low}CD117⁺CD115⁺cells expressed as a percentage of total live cells. Statistical analysis was performed using Student's unpaired t-test (P=0.0277). N=5.

The third gating strategy defines 'early OCPs' in BM as CD3⁻CD11b⁻ CD115⁺CD117⁺ cells (figure 4.18A) (Thompson 2020). When this gating was used, the frequency of early OCPs was found to be reduced in BCG-infected mice (0.2714 %) compared to the control mice (0.538 %, figure 4.18B). However, for CD3⁻ CD11b⁺ CD115⁺CD117⁻ 'late OCPs', we did not find any difference between

BCG-infected and control mice (figure 4.18C). The distinction between early and late OCPs comes from the previous finding that the 'late' OCP cell populations are more enriched for osteoclastogenic potential (Jacquin, Gran et al. 2006).

In summary, analysis using all three gating strategies indicated reduced OCPs in BCG-infected mice. Therefore, it can be reasoned that BCG-infected mice may have more mature circulating osteoclast precursors in the BM. This is highlighted by the observation of an increase in multinucleated OCLs in *in vitro* differentiated BM from BCG-infected mice (figure 4.14B)

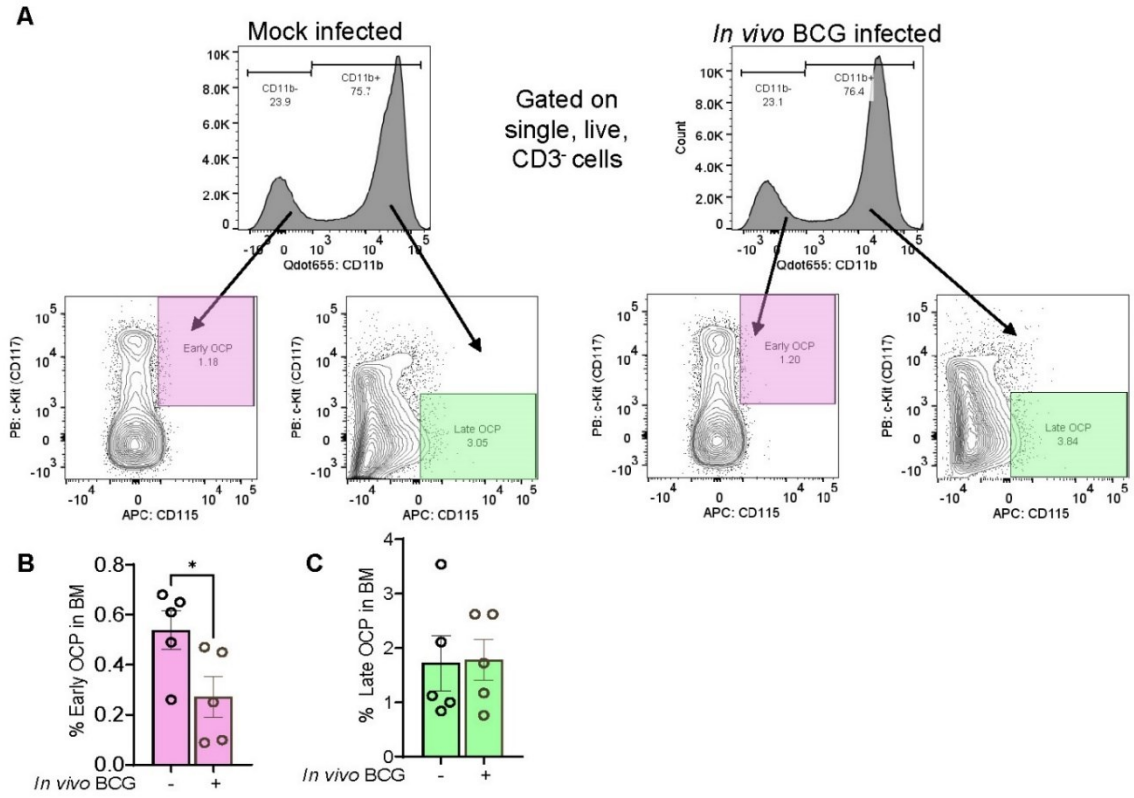

Figure 4.18 Frequency of 'early'/'late' OCPs in the BM of BCG infected mice decrease compared to mock infected mice

(A) Representative contour plots with outliers of mock infected vs in vivo infected BM of mice, gated on single, live CD3⁻ cells. (B) Percentage of early OCPs - CD3⁻CD11b⁻CD115⁺CD117⁺ cells expressed as a percentage of total live cells. Statistical analysis was performed using Student's unpaired t-test (P=0.0451) (C) Percentage of late OCPs - CD3⁻CD11b⁺CD115⁺ CD117⁻ cells expressed as a percentage of total live cells. Statistical analysis was performed using Student's unpaired t-test (P=0.9314).

In the BM, osteoclasts are differentiated under the influence of M-CSF and RANKL. M-CSF mediates the proliferation and survival of OCPs whereas RANKL promotes the differentiation of OCPs into mature OCs and is released by osteoblasts and osteocytes, although it can also be produced by other immune cells such as activated $CD4^+$ T cells. Cross talk between RANKL secreting T cells with OCPs causes bone loss during chronic immune activation. Hence, we hypothesised that mycobacterial infection leads to an increase in OCPs in the bone marrow (Xiao 2013).

Due to this crosstalk between OCPs and T-cells, we next analysed the T-cell populations in the BM as described before (Xiao 2013). The gating strategies are illustrated in figure 4.19). No difference in $CD3^+CD70^+$ T-cell frequency was observed between control and BCG-infected mice (figure 4.19A). However, we noticed a non-significant increase in $B220^+CD70^+$ T-cell frequency in the BM of BCG-infected mice (0.602 %) compared to control mice (0.472 %, figure 4.19B).

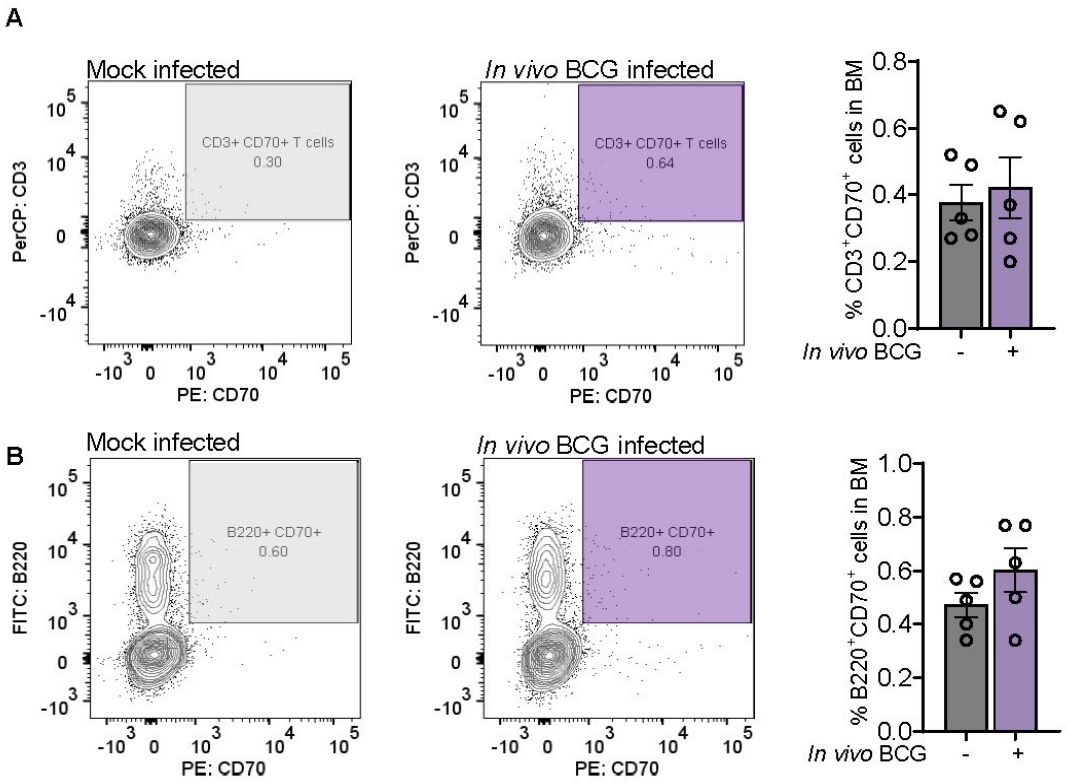

Figure 4.19 Frequency of T-cells in the BM of BCG infected mice compared to mock infected mice

(A) Representative contour plots with outliers of mock infected vs in vivo infected BM of mice, showing single, live $CD115^+CD3^+CD70^+$ cells and percentage of

$CD3^+CD70^+$ T-cells in the bone marrow expressed as a percentage of total single and live cells. Statistical analysis was performed using Student's unpaired t-test (P=0.6876). N=5. (B) Representative contour plots with outliers of mock infected vs in vivo infected BM of mice, showing single, live $CD115^+B220^+CD70^+$ cells and percentage of $B220^+CD70^+$ B/T-cells in the bone and percentage of $B220^+CD70^+$ T-cells in the bone marrow expressed as a percentage of total single and live cells. Statistical analysis was performed using Student's unpaired t-test (P=0.2039). N=5.

4.2.13 *In vivo* BCG infection deregulates homeostasis of the bone towards resorption on the macroscale

Bone porosity can be an indicator of bone fragility. Due to observation of the reduced OCPs (figure 4.16-4.18 and increased OCLs (figure 4.14) and their overactivation from the BM of BCG-infected mice, we hypothesised that femurs from BCG-infected mice would have increased porosity and decreased cortical thickness, when compared to mock infected control mice femurs. To evaluate this, we performed Micro-Computed Tomography (μCT), which is a gold standard method to study the phenotype of the bone in small animals such as mice and rats. μCT is widely used to quantify the three-dimensional geometry of the bone and quantify micro-structures.

The femurs from control and BCG-infected mice (30 days post i.v. infection) were harvested post-mortem for μCT analysis. Tescan Unitom XL was operated with the parameters detailed in the methods and materials (section 2.19). The best resolution was chosen that allows identification of all bone channels, including the smallest ones. Trabecular bone refers to the porous bone composed of trabeculated bone tissue found at the ends of long bones like the femur and has a higher turnover rate compared with the cortical bone. Cortical bone refers to the thick outer surface of typically a long bone and is found in the femur. The femurs contain both trabecular bone and cortical bone and representative cross sections of cortical and trabecular bone are shown in figure 4.20A. Figure 4.20B shows representative slices of bone from the epiphysis of a mock and BCG infected mouse femur, and figure 4.20C shows the same for the diaphysis. For porosity and thickness analysis, the epiphysis of both ends combined was

analysed separately to the diaphysis due to the differences in the incidence of trabecular and cortical bone.

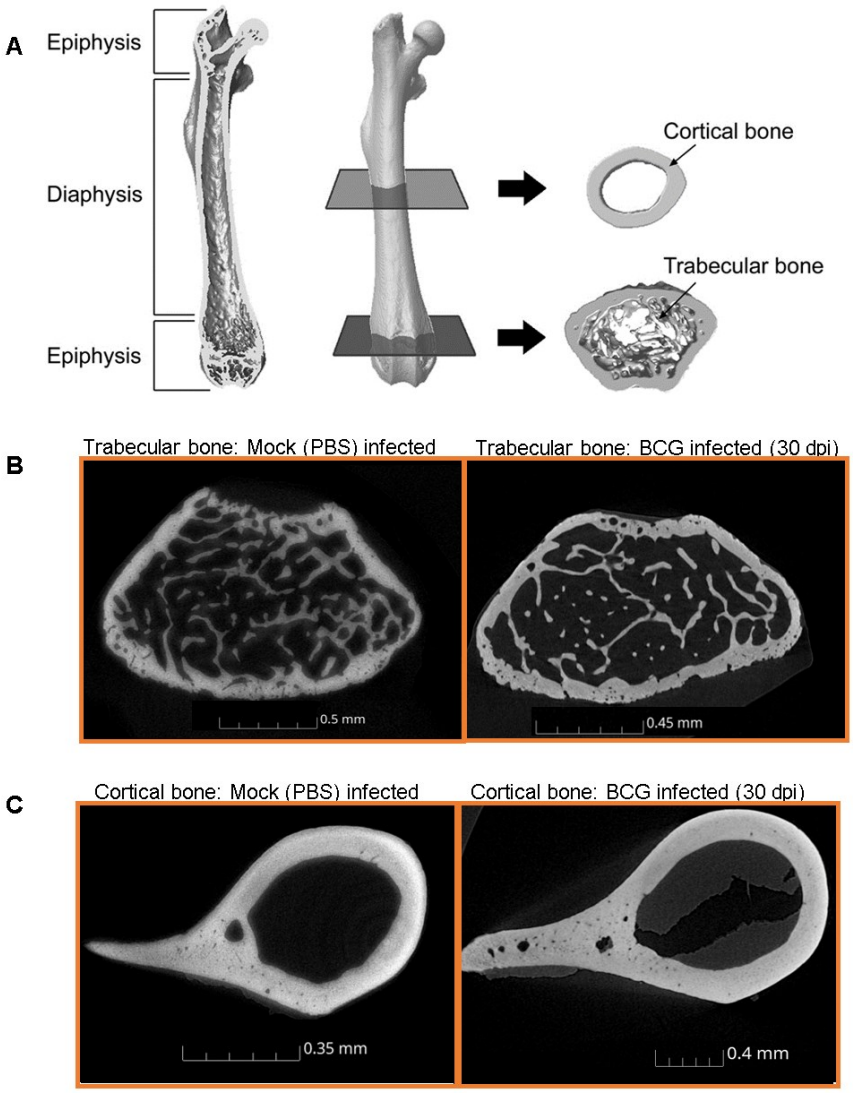

Figure 4.20 Micro-CT analysis of femurs from mock infected and BCG infected mice

(A) Schematic of a mouse femur to illustrate the parameters used for X-Ray Computed Tomography analysis. The femur is split into epiphysis and diaphysis. (B) Representative images of epiphysis bone tissue taken from the same coordinates from mock infected mouse femur and an age and gender matched BCG-infected mouse for 30 days. (C) Representative images of diaphysis bone tissue taken from the same coordinates from mock infected and BCG-infected mouse femur.

As mock-infected and infected mice were age and gender matched, it was possible to assess the differences in porosity and bone thickness with various regions of interest (ROIs). User independent analysis for porosity was performed using VGEasyPore, part of the VG Studio Max 2022.1 software. The diaphysis and epiphysis were analysed separately (figure 4.21A-B). The diaphysis refers to the tubular shaft portion of the bone between the proximal and distal ends of the bone whereas the epiphysis refers to these wider sections of bone at each end. The material volume of the ROI (diaphysis and epiphysis) was determined (figure 4.21C,D), along with the ratio of the sum of the pore volume (defect volume) which was expressed as a percentage of the material volume (figure 4.21E,F).

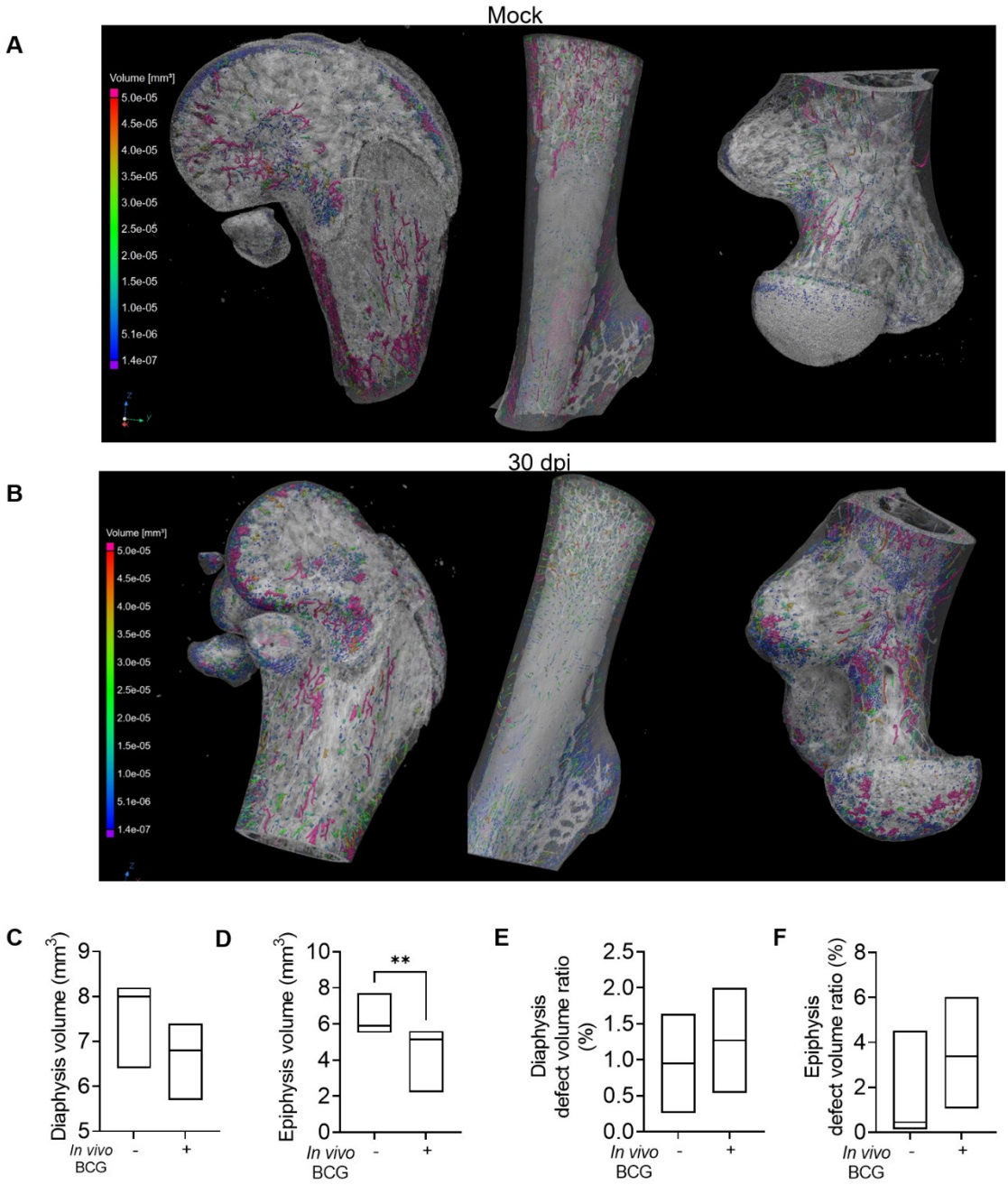

Figure 4.21 User independent porosity analysis of femurs from BCG infected mice versus mock infected mice

(A) Representative images of porosity analysis conducted by VGEasyPore of epiphysis and diaphysis from mock infected mouse femur and (B) age and gender matched BCG-infected mouse (C) Floating bar plots to show the combined volumes for diaphysis for mock infected and BCG-infected mice femurs. Line at median. N=3, Mann-Whitney test found no significant differences. (D) Floating bar plots to show the combined volumes for the epiphysis for mock infected and BCG-infected mice femurs. Line at median. N=3, Mann-Whitney test, P=0.0087. (E) Floating bar plots to show the defect volume ratio (the volume of the sum of the pores expressed as a percentage of the total bone volume) of the diaphysis for mock infected and BCG-infected mice femurs. Line at median. N=3, Mann-Whitney test found no significant differences. (F) Floating bar plots to show the defect volume ratio (the volume of

the sum of the pores expressed as a percentage of the total bone volume) of epiphysis for mock infected and BCG-infected mice femurs. Line at median. N=3, Mann-Whitney test found no significant differences.

As seen in figure 4.21D, there was a significant reduction in epiphysis volume for infected mice femurs. The defect volume ratio of both the epiphysis and diaphysis displayed non-significant increases for infected mice femurs.

User independent analysis for thickness was carried out with VG Studio Max 2022.1 for average thickness in mm for each ROI between mock infected and BCG infected diaphyses and epiphyses (figure 4.22).

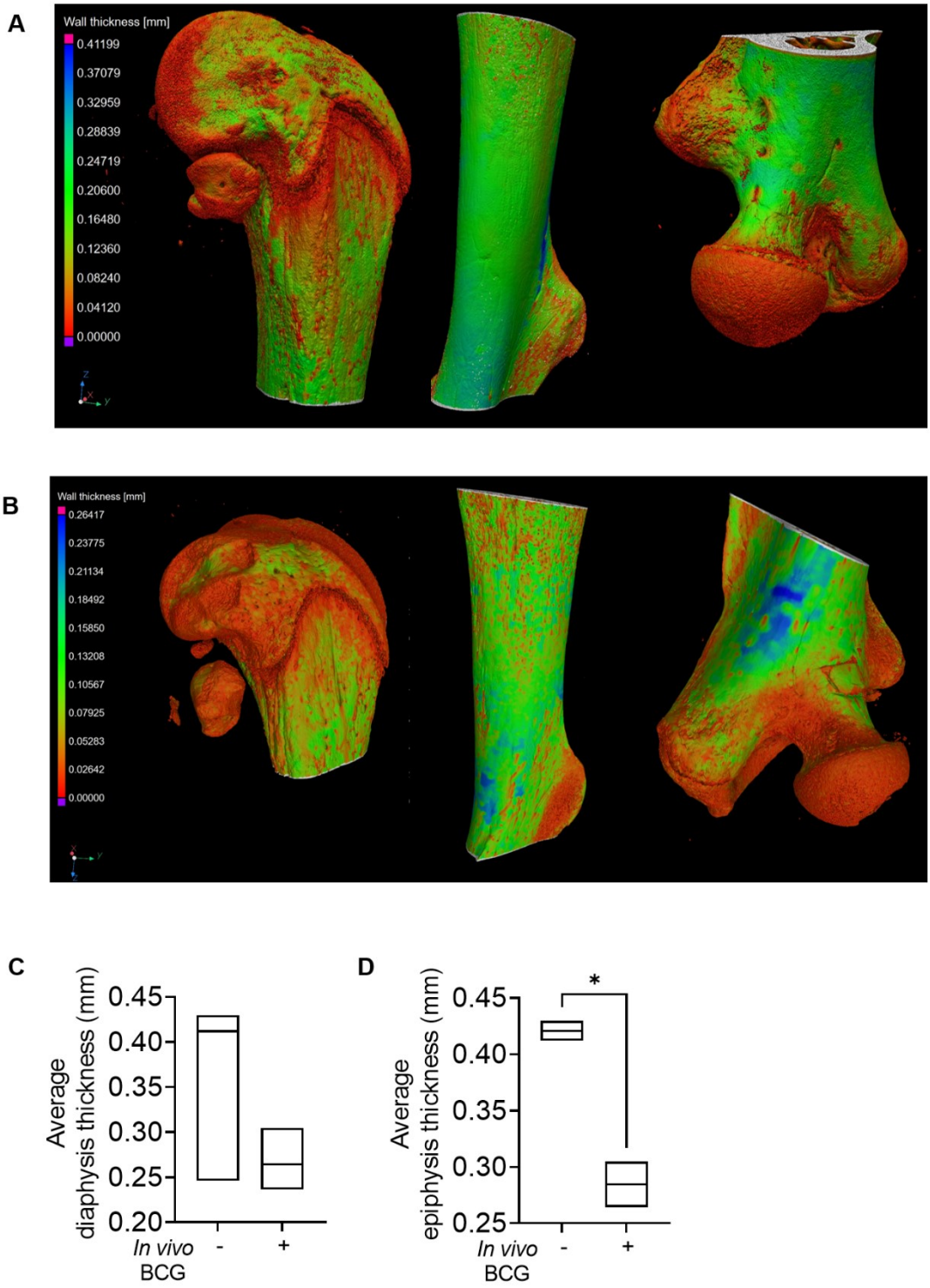

Figure 4.22 User independent thickness analysis of femurs from BCG infected mice versus mock infected mice

(A) Representative images of thickness of epiphysis and diaphysis from mock infected mouse femur and (B) age and gender matched BCG-infected mouse. Analysed with VG Studio Max 2022.1. (C) Floating bar plots to show compiled average thickness of diaphysis between mock infected and BCG-infected mice femurs. Line at median. N=3, Mann-Whitney test showed no significant difference. (D) Floating bar plots to show compiled average thickness of epiphysis between

mock infected and infected mice femurs. Line at median. N=3, Mann-Whitney test, P=0.0286.

A significant reduction in average epiphysis thickness in BCG infected was found compared to mock infected (figure 4.22C-D). In conclusion, a reduction in epiphysis volume (and therefore porosity) and thickness relates to an overactivity of osteoclast-mediated resorption during BCG infection.

4.3 Discussion

Bone and joint TB often presents with symptoms of non-specific pain and swelling, frequently mimicking other conditions such as osteosarcoma. This generally leads to delays in diagnosis and treatment. We noticed that there is a gap in the research for biomarkers and cellular mechanisms of bone and joint TB (Sigal 2017), therefore this work aimed to explore and characterise the phenotypic changes that occur during infection of bone cells, to more closely define molecular infection-specific changes that could be targeted for future diagnostic and treatment methods.

After establishing that BCG persists intracellularly inside osteoblast-like cell line MG-63 and osteoclast-like cells derived from murine BM, we probed for evidence of change in bone formation or resorption markers during infection using molecular and histochemical methods. RT-qPCR on RNA isolated from uninfected and BCG-infected MG-63 did not show any significant changes for bone formation markers, except for an increase in relative *TNFSF11* (RANKL) gene expression and surprisingly, an increase in relative *ALP* gene expression (figure 4.2A). Histochemical ALP staining showed an insignificant reduction in ALP activity (figure 4.2B-C). A reduction in ALP activity and increase in RANKL expression is in line with published studies of infected osteoblasts with other bacteria. For example, human osteoblasts (PromoCell, Heidelberg, Germany) that were exposed to biofilm conditioned media (BCM) from clinical wound isolates of *S. aureus* displayed a reduction in ALP activity, as measured by a spectrometric assay. In the same study relative levels of RANKL in osteoblasts were increased

significantly upon exposure to BCM of *S. aureus* (Sanchez, Ward et al. 2013). Another study of infected primary human osteoblasts and MG-63 cells showed that *S. aureus* infection inhibited bone formation as well as expression of bone formation genes (Kassem, Lindholm et al. 2016).

Serum level of ALP is currently used as a diagnostic marker of Paget's disease, bone infections and osteomyelitis with marked elevated (≥4 times normal limit) total alkaline phosphatase (T-ALP) levels indicative of increased osteoblastic activity. Interestingly, it has been suggested to be a useful tool for the differential diagnosis of pulmonary tuberculosis and sarcoidosis but ALP as a marker for bone specific TB would need to be investigated further (Tural Önür, Iliaz et al. 2016). Along with reduced ALP activity and increased *TNFSF11* expression, MG-63 displayed other phenotypic changes that favour bone loss during infection, such as some proinflammatory IL-1β release (figure 4.4B).

TLR2 and TLR4 are expressed on MG-63 osteoblasts and are involved in cytokine secretion in the inflammatory response, albeit at higher levels compared to THP-1 monocytes (figure 4.3A-B). TLR2 and TLR4 are constitutively and highly expressed on human monocytes and highly during osteoclast differentiation. According to a study, human primary osteoblasts express TLR4 at high levels, but TLR2 is barely detectable (Larousserie, Bsiri et al. 2017). TLR2 recognises mycobacterial cell wall components such as lipoarabinomannan (LAM) and lipomannan (LM) and their activation induce the NF-κB and MAPK pathways leading to the production of pro-inflammatory cytokines and chemokines. In human primary monocytes stimulated by *Mtb* antigen (Ag), TLR2 activation is required for ROS generation, along with MAPK pathway-dependent expression of CXCL8 and CCL2 (Lee 2009).

In this study, TLR2 surface protein and mRNA expression increased upon BCG infection of MG-63. This is in line with previous investigations into other bacterial infections of osteoblasts in relation to TLR2. *S. aureus* infection of murine MC3T3-E1 osteoblast cell line resulted in increased TLR2 surface expression measured by flow cytometry (Garcia-Moreno, Jordan et al. 2022). The increase in TLR2

surface and relative gene expression in MG-63 during BCG infection gives the impression that MG-63 could have a role in the pro-inflammatory response to infection. Indeed, TLR2 targeting by *S. aureus* results in increased RANKL and periosteal/endosteal osteoclast formation and bone resorption (Kassem, Lindholm et al. 2016). Kim *et al*. also described an induction of proinflammatory cytokines by TLR2 activation in osteoblasts, resulting in RANKL production (Kim, Yang et al. 2013).

Interestingly, we found that the surface expression of TLR4 was downregulated upon BCG infection whereas the relative mRNA expression was insignificantly upregulated. As expected, surface TLR4 expression in THP-1 cells increased upon infection. Previous studies reported that 24-hr LPS activation in THP-1 cells or PMA activated THP-1 cells resulted in an increased TLR2/4 expression and supports our use of THP-1 as a positive control (Lv, He et al. 2017). It has been shown that, in human primary osteoblasts, stimulation with LPS resulted in no significant change in TLR4 expression (through flow cytometry and RT-qPCR), differing from what we observed (Muthukuru and Darveau 2014). Nevertheless, Muthukuru *et al* carried out LPS challenge for 1 week to study the chronic effects of TLR4 activation in mice where they observed no change.

Notably, we have shown that MG-63 has a higher baseline of TLR4 expression compared to THP-1. TLR4 is a promiscuous receptor activated by a diverse range of stimuli in the bone marrow microenvironment, the best characterised being LPS. TLR4 activation is linked to increased RANKL and M-CSF expression which, in addition to osteoclastogenesis, also promotes osteoanabolic Wnts secretion (Wnt3a and Wnt5a) which is involved in osteoblast differentiation and proliferation (Alonso-Pérez, Franco-Trepat et al. 2018). TLR4 surface downregulation upon BCG infection of MG-63 cells could be explained by the internalisation of the receptor upon activation, as the relative expression of *TLR4* is increased upon infection. We found evidence of some proinflammatory response from the possible modulation of TLR2 and TLR4 (figure 4.3), resulting in some IL-1β secretion (figure 4.4B) and *RANKL* induction (figure 4.2A) by BCG-infected MG-63 cells. Both IL-1β and RANKL are involved in osteoclastogenesis.

To ascertain whether the proinflammatory response was TLR2/4 mediated, future experiments with knockdowns of TLR2/4 in MG-63 could be performed.

Our investigations into MG-63 interactions with BCG lead to the observation that only a small percentage of bacteria are internalised at 3 and 24 hrs p.i. (<5 %) (figure 4.1). Therefore, the phenotypic changes we saw in the cells might represent the indirect effects of infection, or paracrine signalling between bystander and bacilli-infected cells. To expand on the interactions between osteoblasts and osteoclast precursors, a trans-well experimental set up could be performed to infect osteoblasts and determine whether osteoclastogenesis occurs in the OCPs.

Working with osteoblast-like cell line MG-63 presents limitations. As it is a cancer cell line derived from an osteosarcoma patient, it behaves differently to primary cells. Most cell lines are derived from cancer cells and have already altered metabolism and enhanced Warburg metabolism, highlighting the need to use primary cells. It was found that infection of primary BMDM and murine macrophage like cells J774A.1 cells with *Listeria monocytogenes* induced a high induction of glucose uptake and glycolysis in primary BMDMs but not in J774A.1 cells as they already had this due to their cancer origin. The consensus is that the Warburg effect does not inhibit bacterial replication.

Further infection experiments were therefore conducted using primary murine bone marrow cells differentiated *in vitro* into osteoclast-like cells (OCLs). We were able to develop *in vitro* and *in vivo* models of BCG infection. The *in vitro* model involved infection of the OCLs at day 6 of differentiation at an MOI of 5, meanwhile the *in vivo* model involved the intravenous infection of the mice themselves at a CFU of 10^6 BCG for 30 days. For the control, mice were infected with 100 µl PBS. An improved control could have been heat killed mycobacteria and the presence of BCG within the bone could have been confirmed using CFU plating from the BM cells on the day of sacrifice. Osteoclasts share many common signalling pathways with macrophages, the primary target of *Mtb*. Indeed, *Mtb* infection of macrophages themselves release anti-bacterial nitric oxide (NO)

which drives the fusion of macrophages into multinuclear giant cells (MGCs) (Gharun, Senges et al. 2017). MGCs resemble osteoclasts and their production under pathological conditions are stimulated with M-CSF or granulocyte macrophage colony stimulating factor (GM-CSF) and interleukins (IL-4, IL-13) (Ikeda 1998). However, MGCs are different to osteoclasts in that they do not resorb bone and their cellular role is less well defined. Our results show an increase in multinucleation of pre-osteoclasts during infection (figures 4.8, 4.14). This finding is consistent with other studies involving mycobacterial infection of the bone. A 2015 study found that in a rabbit model of osteoarticular TB, the number of osteoclasts in the spine increased (while the number of osteoblasts decreased) (Liu, Jia et al. 2015). Another 2020 study found that in TRAP stained osteoarticular tuberculosis bone samples from affected TB patients, the number of osteoclasts was increased compared to osteoarthritis control samples (Liu, Zhou et al. 2020). The phenomenon of multinucleation is similarly seen when bovine macrophages are infected with *M. bovis;* the formation of MNGCs, which is a hallmark of the tuberculosis granuloma, occurs (Queval, Fearns et al. 2021). *Mtb* also produces MNGCs in human and animal models. The formation of MNGCs is relevant in the pathogenesis of pulmonary TB, but multinucleation of osteoclasts and their precursors brings into question what this means for skeletal TB pathogenesis.

It is widely accepted that there is a positive association between the number of nuclei per osteoclast and resorptive activity (Boissy, Saltel et al. 2002). In Paget's disease of bone, where excessive fusion of OCPs drives pathogenesis, OCLs are characterised by hyper-multinucleation, increased IL-6 expression, with the disease resulting in enhanced bone resorption (Reddy, Menaa et al. 1999). However, multinucleation itself may not be an indicator of increased osteoclast function. Indeed, it was found that a mutation in SNX10 increases the fusion of OCPs resulting in dysfunctional osteoclasts with defective ruffled borders and osteopetrosis, as they were unable to resorb bone *in vitro* (Stattin, Henning et al. 2017). Nonetheless, as well as an increase in multinucleation, we found increased TRAP activity (figures 4.7, 4.14) and other markers of osteoclast activity (figures 4.9, 4.15) during *in vitro* and *in vivo* BCG infection. From Luminex and ELISA

experiments, IL-10, MIP-1α (CCL3), RANTES (CCL5), Eotaxin (CCL11) and LIF as well as CXCL1 and CXCL2 were found to be upregulated in the culture supernatant from both *in vitro* infected OCLs (significantly) and those derived from BCG-infected mice (non-significantly). Of these factors, CXCL1, CXCL2, MIP-1α (CCL3), RANTES (CCL5), Eotaxin (CCL11) and LIF are well noted to be pro-osteoclastogenic (Yukie 2009, Wintges 2013, Kindstedt 2017, Jordan 2018).

Proinflammatory CXCL1 and CXCL2 are chemokines which are ligands of the G-protein coupled receptor CXCR2 (IL-8RB). CXCR2 is expressed on various cells such as macrophages, neutrophils, and epithelial cells and their primary role is to attract neutrophils to sites of injury. CXCL1 and CXCL2 have been shown to have roles in osteoclastogenesis and have been shown to stimulate osteoclast formation from BM adipocytes, commonly found in ageing and obesity (Hardaway, Herroon et al. 2015). Markedly, murine OCPs were found to express CXCL2 upon RANKL stimulation through JNK and NF-kB signalling pathways, and osteoclast formation was blocked through antagonisation of CXCR2 (Ha, Choi et al. 2010). Serum CXCL2 levels were also induced in patients who had undergone joint replacement in the bone tissue surrounding bacterially infected implants (Dapunt, Maurer et al. 2014).

More *in vivo* studies confirmed the osteoclastogenic effects of CXCL1 along with CCL2 (monocyte chemoattractant protein-1, MCP-1). CCL2 was undetected in our Luminex data in the culture supernatant of both *in vitro* and *in vivo* infected OCL samples, due to being higher than the HLOQ. In an ovariectomised rat model of bone loss, the reduced bone mineral density (BMD) measured by μ-CT correlated significantly with increased serum levels of CXCL1 and CCL2. Serum levels of CXCL1 and CCL2 from human patients with age associated or postmenopausal associated osteoporosis were also inversely correlated with their BMD measurements, suggesting CXCL1 and CCL2 may be novel markers of bone loss (Hu, Wang et al. 2020). CCL2 has been clearly implicated during osteoclast formation at various stages and its roles are pro-survival and pro-differentiation. During the early stage of differentiation, MSCs produce CCL2 which acts through its receptor CCR2 to attract OCPs (Sumi, Abe et al. 2018). CCL2 can also reverse

the inhibition of human osteoclastogenesis by GM-CSF *in vitro;* osteoclastogenesis is also inhibited with anti-CCL2 antibody treatment (Kim, Day et al. 2005).

Eotaxin (CCL11), which was upregulated in the culture supernatant from *in vitro* infected OCLs, as well as those differentiated from BM of BCG-infected mice, has been posed as a novel mediator of inflammatory bone disease. For example, serum levels of CCL11 are increased in inflammatory diseases with disturbed bone remodelling (Kindstedt, Holm et al. 2017). Curiously, IL-10 is the only anti-osteoclastogenic cytokine that was upregulated during both *in vitro* and *in vivo* infected OCL samples. IL-10 can inhibit osteoclastogenesis by preventing the expression of the master transcriptional regulator NFATc1 as well as its translocation to the nucleus (Evans and Fox 2007). It also can downregulate proinflammatory IL-1, IL-6 and TNF-α synthesis (Houri-Haddad, Soskolne et al. 2007). Overall, the cytokine/chemokine profiling showed a reprogramming towards osteoclastogenic activity.

Interestingly, the induction of the pro-osteoclastogenic factors was less strongly induced from OCLs differentiated from the BM of BCG infected mice. This may be explained by the 30-day long BCG exposure in addition to 7 days of differentiation into OCLs, which could have weakened the response. To mitigate this, the blood serum of the mice could have been processed for Luminex at 30 dpi, but this would not give insight into the OCL-specific response.

As we found an increase in the osteoclast frequency and activity in both *in vitro* and *in vivo* infection models, we went on to test a hypothesis on whether this was due to the perturbation in osteoclast progenitors (OCPs) in the BM of BCG-infected mice. We found decreased OCPs in the BM of BCG-infected mice (figure 4.16, 4.17, 4.18). OCP frequency has been shown to be increased in the BM of mouse models of inflammatory erosive arthritis ($CD11b^{-/lo}Ly6C^{hi}$) and the BM and periphery during chronic *Porphyromonas gingivalis* infection of mice ($CD11b^{+}c\text{-}fms^{+}Ly6C^{hi}$) (Butler, Brodin et al. 2012, Charles, Hsu et al. 2012, Jiang, Huang et al. 2022).

However, the OCP population is heterogeneous and not phenotypically uniform. Our study did not cover c-fms^{+}Ly6C^{hi} markers so it is possible this phenotype of OCP did increase during BCG infection. Also, we did not consider OCPs circulating in the peripheral blood (PB). Interestingly, it has been found that human peripheral blood monocytes have increased osteoclast differentiation potential compared to bone marrow monocytes (Kylmäoja, Nakamura et al. 2018). It would have been interesting to see whether there were changes in the circulating OCPs from BCG infected mice. Furthermore, due to the heterogeneity of origin of osteoclasts and their precursors (MNs and DCs are phenotypically varied and can also give rise to OCPs), the increase in osteoclast activity we saw (figures 4.7, 4.9, 4.14, 4.15), could have been due to the recruitment of other kinds of precursors.

In our study we did not look at the osteoblast precursor populations in the BM. In a malnourished mice model of inflammatory challenge, there was an expansion of MSCs and promotion of differentiation of BM MSCs into adipocytes rather than osteoblasts, in parallel with increased osteoclast activity (Osorio, Gugala et al. 2022). As EPTB patients disproportionately come from low socioeconomic backgrounds where they are more likely to be malnourished, inflammatory challenge by *Mtb* in this context could more likely lead to bone TB. Our experiments did not consider factors such as diet or age of the mice, but this is an interesting future direction.

Finally, we strengthen our hypothesis that mycobacteria interfere with the homeostasis of the bone by investigating the macrostructure of the bone. μ-CT data gave us insight into the bone architecture where thickness and porosity were investigated. As bone thickness and porosity are directly related to bone strength, these parameters are important when researching bone specific pathologies. In skeletal TB as well as other conditions such as osteoporosis and osteoarthritis, trabecular bone volume, trabecular thickness and trabecular number are substantially decreased. Our findings show that BCG-infected mice femurs had decreased thickness and increased porosity versus the mock infected mice (figures 4.21, 4.22). This was more significant in the epiphysis than the

diaphysis (figure 4.22B,C). In the pathogenesis of TB of long bones, *Mtb* begins in the epiphysis spreading to the adjacent joint (Jabir 2017), so it is intuitive that the epiphysis has been disproportionately more affected. Other assays like the OsteoAssay could be used to further study bone resorption.

Collectively, results presented in this chapter provide evidence for phenotypic changes in osteoclasts that favour osteoclastogenesis and result in bone loss. The next chapter focuses on the transcriptomic reprogramming of OCLs occurring during both *in vitro* and *in vivo* infection of osteoclast-like cells and probing the findings from the transcriptomic analysis.

Chapter 5 Transcriptomic reprogramming of OCLs during infection

5.1 Introduction

Bulk RNA sequencing (RNA-Seq) is a useful tool to determine RNA expression and identify novel genes in response to certain pathogenic conditions. There has been growing use of functional genomic tools such as RNA-seq to study *Mtb* in recent years (Arnvig, Comas et al. 2011, Pellin, Miotto et al. 2012, Lin, de Sessions et al. 2016). These studies have mainly focused on identifying genes paramount to *Mtb* survival, particularly in the context of infection within macrophages. Dual RNA-seq to dissect the response of the macrophage and *Mtb* has been conducted as well; Pisu *et al.* found that alveolar macrophages supported *Mtb* growth by increasing access to iron and fatty acids, whereas interstitial macrophages inhibited *Mtb* growth by sequestering iron and producing more nitric oxide (Pisu, Huang et al. 2020).

In terms of the host response to *Mtb* infection to different strains, murine BMDMs infected with either a hyper- (R5527) or hypovirulent (R1507) Beijing *Mtb* clinical isolate had undergone RNA-sequencing by Leisching *et al*. Pathway analysis highlighted that in the hypervirulent strain infection, stress-induced and growth inhibitory Gadd45 signalling pathway were activated. Upstream regulators of interferon activation such IRF3 and IRF7 were predicted to be upregulated in hypovirulent-infected BMDMs (Leisching, Pietersen et al. 2017). Transcriptomic profiling of human PBMCs stimulated with *Mtb* PPE57 showed an enrichment of type I interferon signalling genes including IRF7 (Yi, Hu et al. 2021).

RNA-seq in the context of EPTB has been fruitful in revealing the responses of human macrophages when infected with different strains of *Mtb* (López-Agudelo, Baena et al. 2022). Interestingly, RNA-seq revealed that a *Mtb* strain associated with high rates of bone dissemination carried an ancestral full-length version of EsxM (a type VII-secreted effector) rather than the truncated form that is found in most modern day *Mtb* strains (López-Agudelo, Baena et al. 2022).

Furthermore, the ancestral EsxM variant was shown to be associated with higher rates of extrapulmonary dissemination through the changes in macrophage actin dynamics and enhancement of macrophage motility (López-Agudelo, Baena et al. 2022).

However, transcriptomic analysis of *Mtb* infected osteoclasts has not been reported yet. In this chapter, I explore the transcriptomic reprogramming of OCLs during BCG infection. To this end, RNA-seq libraries were prepared from RNA isolated from *in vitro* infected OCLs or from OCLs differentiated from BM of BCG-infected mice and downstream analysis was performed. By unravelling the differences in the transcriptome of infected and uninfected OCLs, modulations in cell death pathways in infected OCLs were found, which led to further investigations into involvement of the NLRP3 inflammasome.

5.2 Results

5.2.1 Transcriptomic analysis of response of OCLs to *in vitro* BCG

To investigate the mechanisms behind the phenotypic changes seen during BCG infection, we conducted bulk RNA-seq of uninfected and *in vitro* BCG infected OCLs that were sorted by FACS into 1-2N and ≥3N populations (figure 5.1A). OCLs were sorted into 15 ml falcon tubes containing α-MEM, centrifuged at 1500 rpm at 4°C, lysed in TRIzol and stored at – 80C° before being sent for bulk RNA-sequencing. RNA extraction and bulk RNA-sequencing was performed using Arcturus PicoPure RNA Isolation kit (Thermo Fisher Scientific) according to the manufacturer's protocol. cDNA libraries were prepared using 0.5 ng of total RNA using the SMARTSeq v2 protocol (Picelli, Faridani et al. 2014). Quality control and initial bioinformatics analysis was conducted according to the pipeline in figure 5.1B.

To investigate the impact of *in vitro* BCG infection on OCLs, differential gene expression (DEGs) analysis was performed to compare the differences in cells with 1-2 nuclei (1-2N) and more than 3 nuclei (≥3N). Three-four biological

replicates for Uninfected (Un) 1-2N, Un ≥3N, infected (In) 1-2N and In ≥3N were used. One sample was removed from the analysis as it was identified as an outlier from the PCA plot (R11649: *In vitro:* In 1-2N (Figure SC1, Appendix).

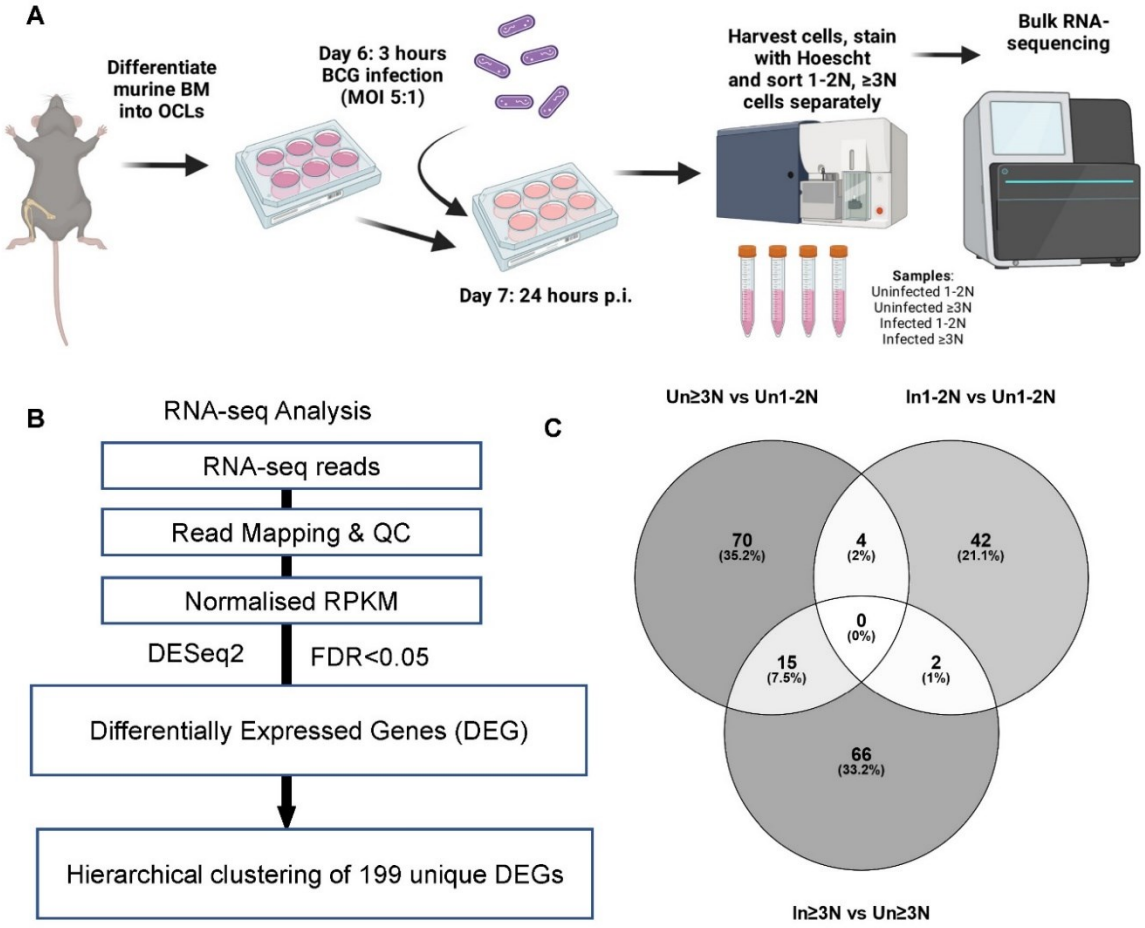

Figure 5.1 Bulk RNA-seq workflow and analysis for transcriptomic analysis of in vitro BCG infected OCLs

(A) Schematic diagram to illustrate infection protocol and sample processing for bulk RNA-seq. (B) RNA-seq analysis pipeline. (C) Venn diagram (created using Venny 2.1.) generated from three comparison groups totalling 220 total genes which give rise to 199 unique DEGs. The 199 DEGs were used to create the heatmap and subsequent clustered analysis of RNA-seq data (see figure 5.2).

The output from DESeq2 gave rise to DEGs, where a False Discovery Rate (FDR)<0.05 and cut off Log_2FoldChange > |0.6| were adhered to. Pairwise comparisons led to the identification of 89 DEGs between Un 1-2N vs Un ≥3N; 48 DEGs between Un 1-2N vs In 1-2N and 83 DEGs between Un ≥3N vs In ≥3N (summarised in table 5.1). The raw DEGs from these comparisons are listed in

Table SC1 in the Appendix. The interplay between these comparisons gave rise to 199 unique DEGs, as shown in the Venn diagram in figure 5.1C.

Table 5.1 Number of differentially expressed genes (DEGs) identified by DESeq2 analysis and pair-wise comparisons between nuclear number and in vitro BCG infection.

Pairwise comparisons	Number of DEGs	Upregulated	Downregulated
Un ≥3N vs Un 1-2N	89	19 (21%)	70 (79%)
In 1-2N vs Un 1-2N	48	27 (56%)	21 (44%)
In ≥3N vs Un ≥3N	83	55 (66%)	28 (34%)

5.2.2 Clustered analysis of *in vitro* BCG infected OCLs

Unbiased hierarchical clustering was applied to evaluate how gene expression varied among the 4 groups (Un 1-2N, Un ≥3N, In 1-2N and In ≥3N), dividing the common 199 DEGs into 5 distinct clusters (figure 5.2). Significant transcriptomic changes among 4 groups were found in clusters 1, 3 and 4 (figure 5.3). On the other hand, transcriptomic differences within clusters 2 and 5 did not show any differences among 4 groups, so were not considered further. The significance of transcriptomic changes between groups were determined by Wilcoxon statistical tests, of which the *p*-values are listed in Table SC2, Appendix. Table SC3 in the Appendix lists the genes in each cluster. Infection dependent clusters are defined as clusters that show a definitive difference between uninfected (Un 1-2N, Un ≥3N) and infected (In 1-2N, In ≥3N) sample groups. Cluster 1 shows genes that are downregulated in In vs Un and cluster 4 shows genes that are upregulated in In vs Un.

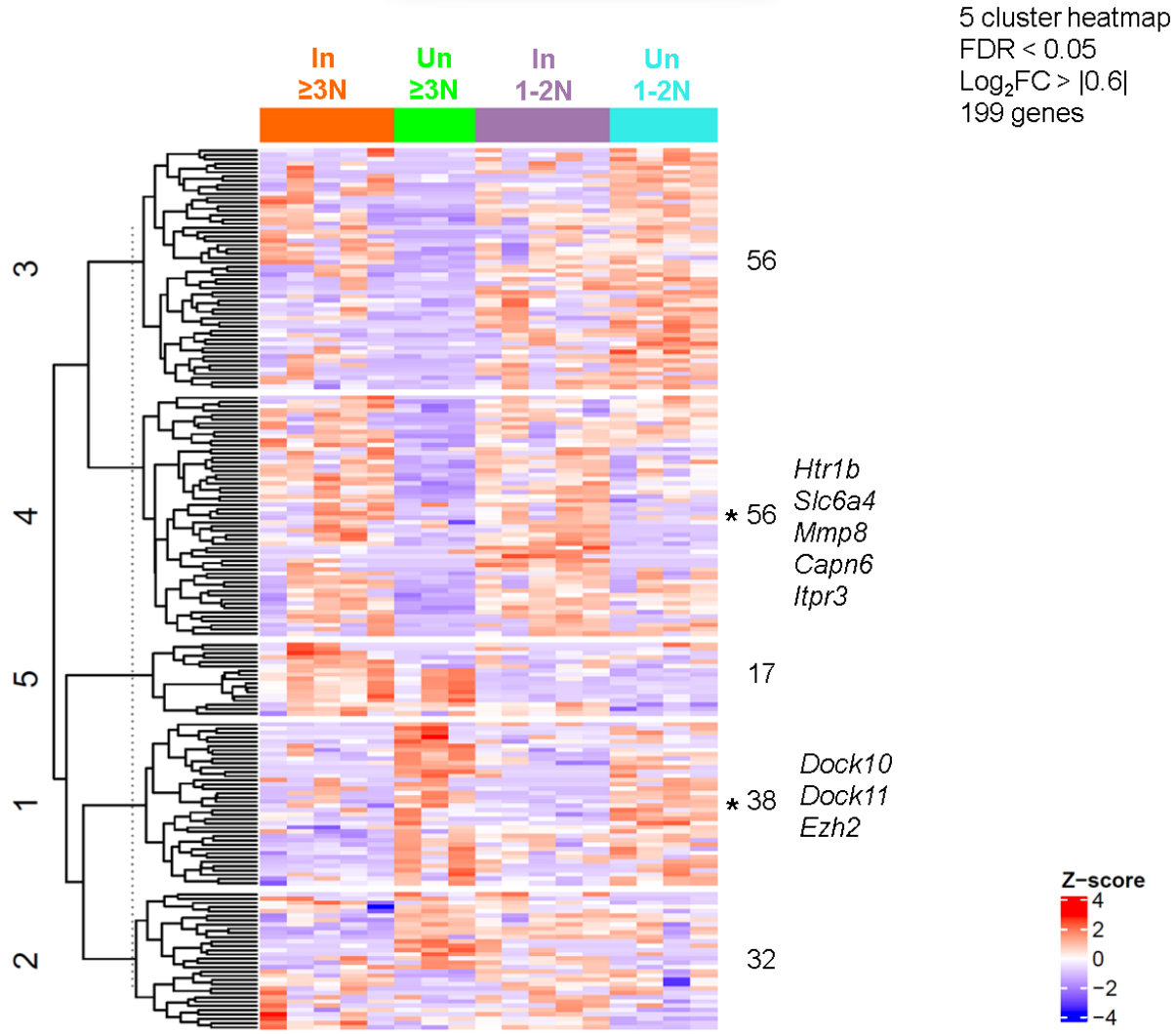

Figure 5.2 Heatmap of 199 unique DEGs for in vitro dataset

Heatmap of differentially expressed genes in uninfected 1-2N (Un 1-2N), infected 1-2N (In 1-2N), uninfected ≥3N (Un ≥3N), infected ≥3N (In ≥3N) OCLs. The heatmap is based on log2RPKM normalised counts of 199 DEGs from the output of DESeq2 with cut-offs at FDR<0.05 and Log2FoldChange > |0.6|. Unbiased hierarchical clustering created 5 distinct clusters with the top genes annotated. Colour key gradient scale indicates upregulation in red and downregulation in blue. Asterisks depict infection dependent clusters. The number of genes in each cluster is annotated. Key genes are annotated.

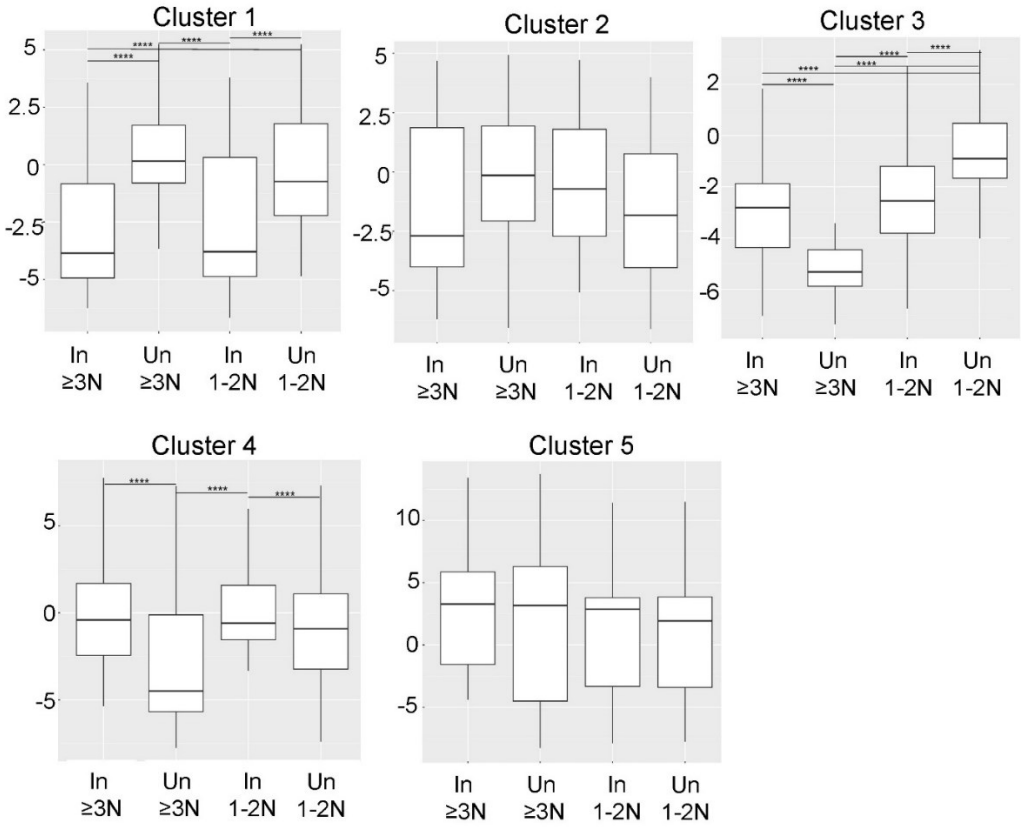

Figure 5.3 Significant transcriptomic changes were found in clusters 1, 3 and 4

Box plots for Z-score of gene expressions averaged over the same conditions for N=5 clusters and of the same condition on each cluster. Significance of transcriptomic changes were determined by Wilcoxon statistical tests (p-values in Table SC2, Appendix).

Gene Ontology (GO) for biological processes and molecular functions and Ingenuity Pathway Analysis (IPA) for top canonical pathways were carried out on clusters with significant infection-dependent transcriptomic changes (clusters 1 and 4). Additionally, I used publicly accessible informatics resource BioPlanet (2019) as it catalogues all pathways with their healthy and disease state annotations. The top 5 GO terms enriched or those that met the criteria for $p<0.05$ are listed in figure 5.4 for cluster 1 and 4. The top canonical pathways found by IPA for all clusters are listed in Table SC4 in the Appendix.

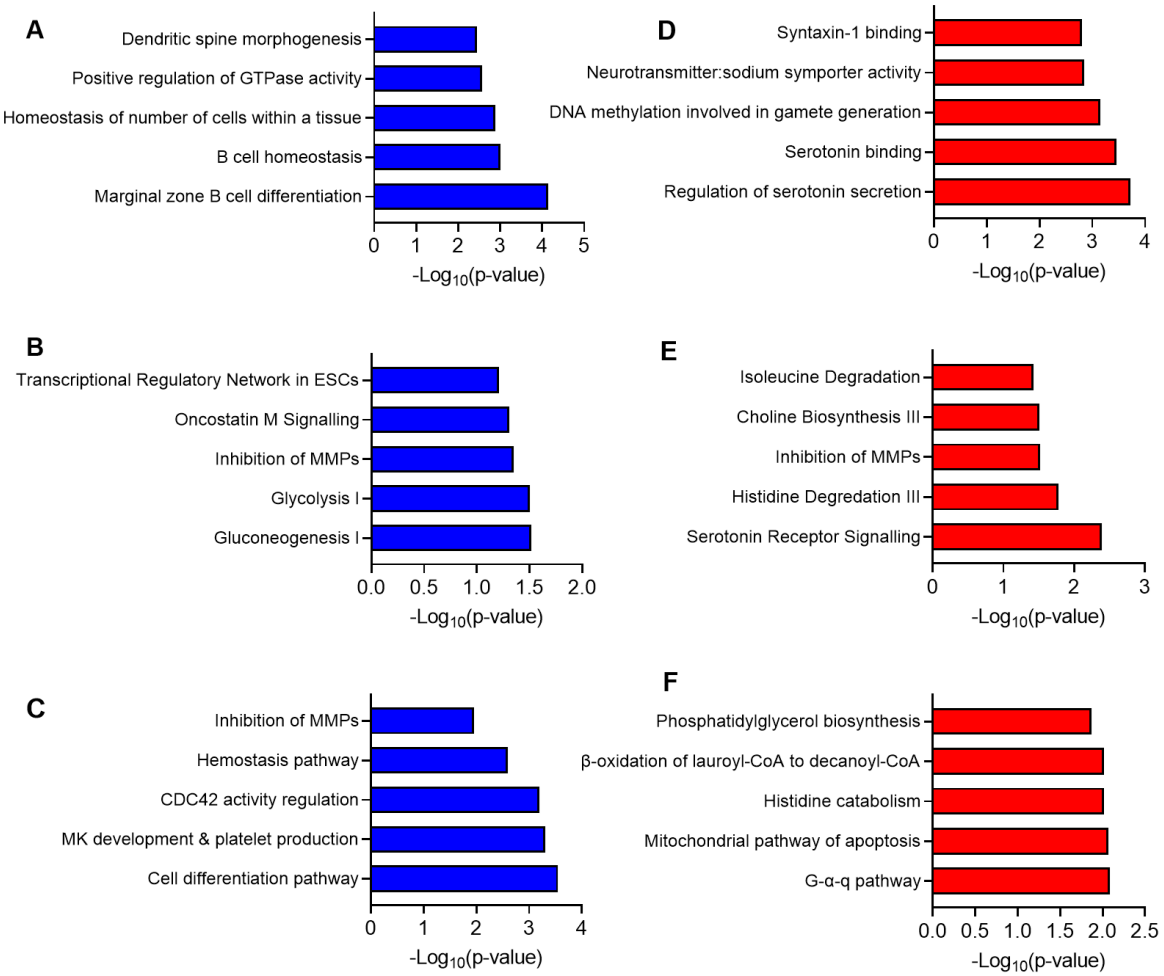

Figure 5.4 Enrichment analysis of cluster 1 and cluster 4 genes

Enrichment analysis of 38 DEGs downregulated in in vitro BCG infection (A) Top 5 BPs and MFs from GO enrichment analysis. (B) Top 5 canonical pathways from IPA analysis. (C) Top 5 processes highlighted from BioPlanet (2019) enrichment analysis. Enrichment analysis of 56 DEGs upregulated in in vitro BCG infection (E) Top 5 BPs and MFs from GO enrichment analysis. (F) Top 5 canonical pathways from IPA analysis. (G) Top 5 processes highlighted from BioPlanet (2019) enrichment analysis.

GO enrichment analysis of BCG infection-specific (downregulation) cluster 1 genes, interesting transcriptomic changes were demonstrated, such as the downregulation of GTPase activity regulation genes *Dock10*, *Dock11* and *Ezh2* (figure 5.4A). *Dock10* and *Dock11* genes were also highlighted under processes of marginal zone B cell differentiation and B cell homeostasis. Inhibition of matrix metalloproteinases (MMPs) was also picked up by IPA and BioPlanet (2019) analysis, concerning gene *Timp3,* encoding for a tissue inhibitor or MMPs. Timp3

acts on MMP9, MMP13 and MMP13; all of which are known to be promote osteoclast activity. IPA analysis of cluster 1 highlighted gluconeogenesis and glycolysis as the top canonical pathways (figure 5.4B). Metabolic reprogramming of macrophages by *Mtb* is well noted as a pro-survival mechanism, with many studies demonstrating that *Mtb* infection shifts macrophages towards aerobic glycolysis from OXPHOS, which is regulated by hypoxia-inducible factor 1-alpha (HIF1-α) and interferon-gamma (IFN-γ) (Lachmandas, Boutens et al. 2016, Marín Franco, Genoula et al. 2020). As such, the osteoclast may redirect metabolism in response to mycobacteria as well. However, only one gene (*Eno2*) was highlighted by IPA, involving the pathways of gluconeogenesis I and glycolysis I.

Cluster 4, infection specific upregulation, found an enrichment of serotonin receptor signalling genes *Htr1b* and *Slc6a4* from GO and IPA analysis (figure 5.4D,E). IPA analysis of cluster 4 genes also found an inhibition of matrix metalloproteases (MMP) genes *Mmp8* and *Tfpi2*. Interestingly, BioPlanet analysis found that the mitochondrial pathway of apoptosis: multidomain Bcl-2 family was enriched (figure 5.4F). The genes enriched were *Capn6* and *Itpr3*. *Capn6* has been shown to have an inhibitory role in apoptosis. *Itpr3* (or *Ip3r3*) is the receptor for inositol 1,4,5-trisphosphate, and is a Ca^{2+} channel enriched at ER-mitochondria contact sites where it provides Ca^{2+} for transport into the mitochondria and has been shown to have a proliferative and anti-apoptotic role in cells (Avalle 2019).

5.2.2.1 Pairwise analysis of *in vitro* BCG infected OCLs

Due to the few numbers of genes in each cluster and to ensure a comprehensive analysis, we also performed enrichment analysis of pairwise comparisons of DEGs from the comparisons Un 1-2N vs In 1-2N (48 DEGs) as well as Un ≥3N vs In ≥3N (83 DEGs). For reference, raw DEGs for these comparisons are listed in Table SC1, Appendix. I used MetaCore software for enrichment analysis of cell processes with upregulated / downregulated DEGs analysed separately. Top 5 enriched processes for each comparison are listed in table 5.2. Top canonical pathways for the pairwise comparisons identified by IPA are listed in Table SC5, Appendix.

Table 5.2 Enrichment analysis of pairwise comparisons

MetaCore analysis of GO process enrichment analysis for upregulated and downregulated genes. Upregulated and downregulated genes were analysed separately.

Comparison	**Enrichment by GO processes**	***p*-value**
In 1-2N vs Un 1-2N (27 genes upregulated in In 1-2N)	Myeloid leukocyte mediated immunity	3.34E-06
	Leukocyte degranulation	3.39E-05
	Myeloid cell activation involved in immune response	4.57E-05
	Regulation of canonical Wnt signalling pathway	4.75E-05
	Establishment of centrosome localisation	5.81E-05
In 1-2N vs Un 1-2N (21 genes downregulated in In 1-2N)	Regulation of vacuole fusion, non-autophagic	5.30E-06
	NADH regeneration	1.14E-04
	Glucose catabolic process to pyruvate	1.14E-04
	Canonical glycolysis	1.14E-04
	Glycolytic process through glucose-6-phosphate	1.52E-04
In ≥3N vs Un ≥3N (55 genes upregulated in In ≥3N)	Regulation of serotonin secretion	7.80E-08
	Cellular response to temperature stimulus	5.53E-07
	Negative regulation of gamma-aminobutyric acid secretion	1.18E-06
	Adenylate cyclase-inhibiting serotonin receptor signalling pathway	1.62E-06
	Negative regulation of serotonin secretion	2.80E-06
In ≥3N vs Un ≥3N (28 genes downregulated in In ≥3N)	Response to lipid	2.34E-08
	Lipoxin biosynthetic process	4.33E-08
	Lipoxin metabolic process	6.93E-08
	Lipoxygenase pathway	1.19E-06
	Regulation of cell death	1.83E-06

From the enrichment analysis of the 27 genes upregulated in In 1-2N vs Un 1-2N, we found an enrichment of processes relating to myeloid leukocyte mediated immunity and myeloid cell activation involved in immune response (table 5.2). Highlighted genes included *Trem1*, *Mmp-8*, *C19orf59 (Mcemp1)*, *Complexin 2*, *Complexin (Cplx1).* Due to OCL's shared lineage with myeloid leukocytes and given these cells are 1-2N, this is expected. NADH regeneration, glucose catabolic process to pyruvate and canonical glycolysis were processes enriched in the 21 downregulated genes of In 1-2N vs Un 1-2N comparison, highlighting genes *Eno* and *Eno2.*

In contrast, MetaCore enrichment analysis of In ≥3N vs Un ≥3N did not show any genes relating to myeloid cell activation. In ≥3N vs Un ≥3N, with 55 genes upregulated and 28 genes downregulated upon infection respectively. Again, an enrichment in the regulation of serotonin secretion was found from the analysis of 55 upregulated genes. Of the 28 genes downregulated, regulation of cell death was an enriched biological process (*Nr4a1, Ccn2, Id3, Timp3, Gata1, Alox12, Irak3, Rnf144b, Hpgd, Eno2*). *Alox12* and *Hpgd* genes showed overlap with the lipoxygenase pathway, along with *Alox15*. The downregulation of *Alox12* and *Alox15* is notable as overexpression of these genes sensitise cells to cell death by ferroptosis (Dolma 2003).

5.2.3 Transcriptomic analysis of OCLs from *in vivo* BCG-infected mice

To investigate whether transcriptomic changes seen in *in vitro* BCG-infected OCLs were also mirrored in OCLs differentiated from BM of BCG-infected mice, we conducted bulk-RNA sequencing on sorted OCLs generated from BM cells of BCG-infected mice. Mock infected and uninfected are terms used interchangeably in this section to mean the control OCLs from PBS-injected mice. The experimental and analysis workflow is illustrated in figure 5.5 A-B. The PCA plots for *in vivo* samples show variance between them, included in figure SC2, Appendix. Pairwise comparisons are summarised in table 5.3. The raw DEGs for each comparison are found in table SC6, Appendix.

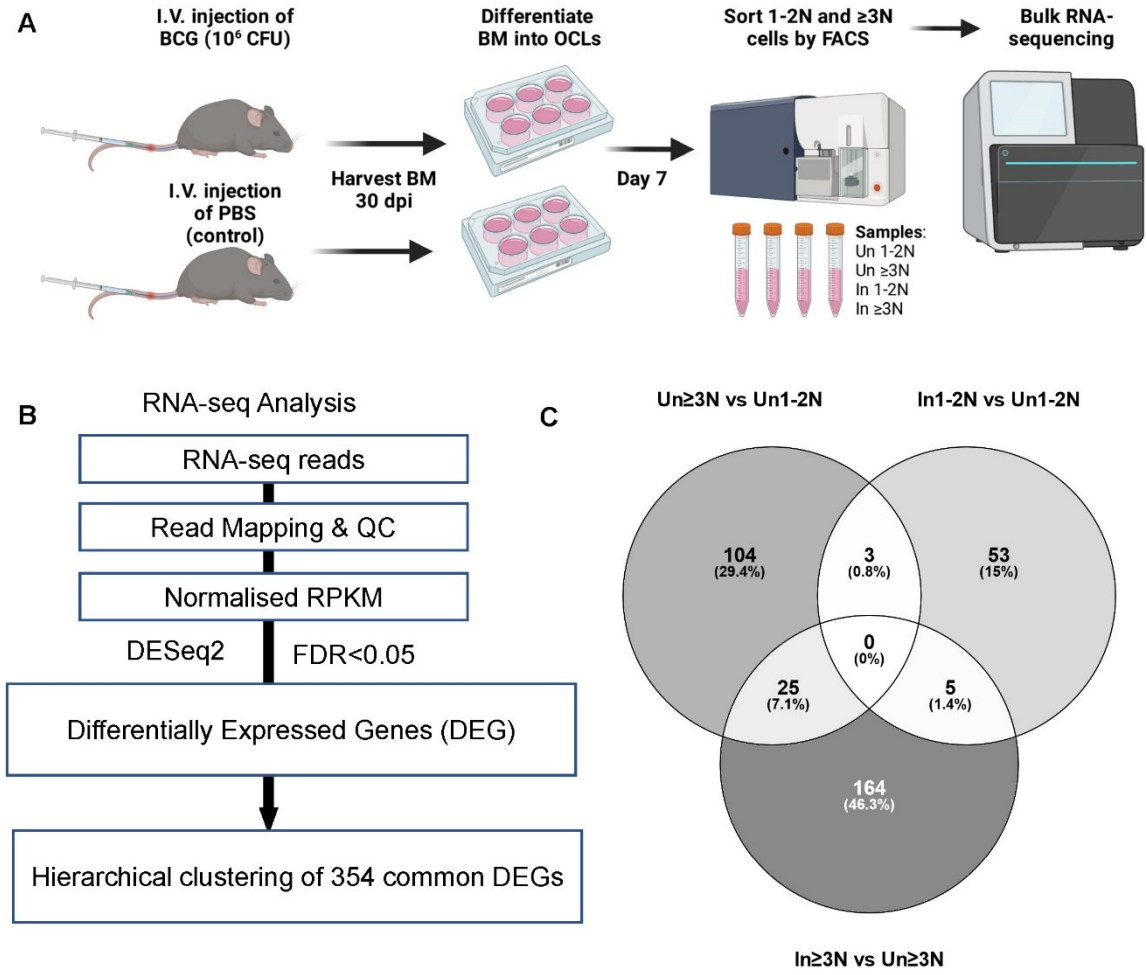

Figure 5.5 Bulk RNA-seq workflow and analysis for transcriptomic analysis of OCLs from uninfected and BCG-infected mice

(A) Schematic diagram to illustrate infection protocol and sample processing for samples for bulk RNA-seq. (B) RNA-seq analysis pipeline. (C) Venn diagram to illustrate the overlap of DEGs from comparisons Un≥3N vs Un1-2N (132 DEGs) In 1-2N vs Un 1-2N (61 DEGs) as well as In ≥3N vs Un ≥3N (195 DEGs), which totals 388 DEGs and 354 unique DEGs. 354 common DEGs were used to create hierarchical clustering heatmap used for clustered analysis. Created using Venny 2.1.

Table 5.3 Number of differentially expressed genes (DEGs) identified by DESeq2 analysis and pair-wise comparisons between nuclear number and in vivo BCG infection.

Pairwise comparisons	Number of DEGs	Upregulated	Downregulated
Un ≥3N vs Un 1-2N	132	39 (30%)	93 (60%)
In 1-2N vs Un 1-2N	61	53 (87%)	8 (13%)
In ≥3N vs Un ≥3N	195	151 (77%)	43 (23%)

5.2.3.1 Clustered analysis of OCLs from *in vivo* BCG-infected mice

Unbiased hierarchical clustering was used to segregate the 354 unique DEGs identified among four groups of *in vivo* OCLs. This gave rise to 5 distinct clusters, with clusters 1, 3 and 4 being infection dependent (figure 5.6). Significant transcriptomic changes were found in clusters 1, 2, and 3 (figure 5.7). Clusters 4 and 5 did not show significant changes so were not considered for further analysis. The significance of transcriptomic changes was determined by Wilcoxon statistical tests, of which the *p*-values are listed in the table SC7, Appendix.

The raw DEGs for each cluster are listed in table SC8, Appendix. Cluster 1, which consists of 76 DEGs downregulated upon *in vivo* BCG infection in ≥3N OCLs found the top enriched terms to be calcium ion binding (*Syt3, Lpcat1, Capn11, Fat3, Gnptab, Chp1, Calml4, Heg1*), adenosine receptor signalling pathway (*Adora2a* and *P2ry12*) as well as cytoplasmic microtubule organisation (*Ccdc88a, Spast,* and *Chp1*) (figure 5.8A).

IPA analysis of genes in cluster 1 downregulated in BCG infection in ≥3N OCLs also enriched the necroptosis signalling pathway (*Capn11, Chp1, Tnip1*), emphasising modulation of cell death again (figure 5.8B).

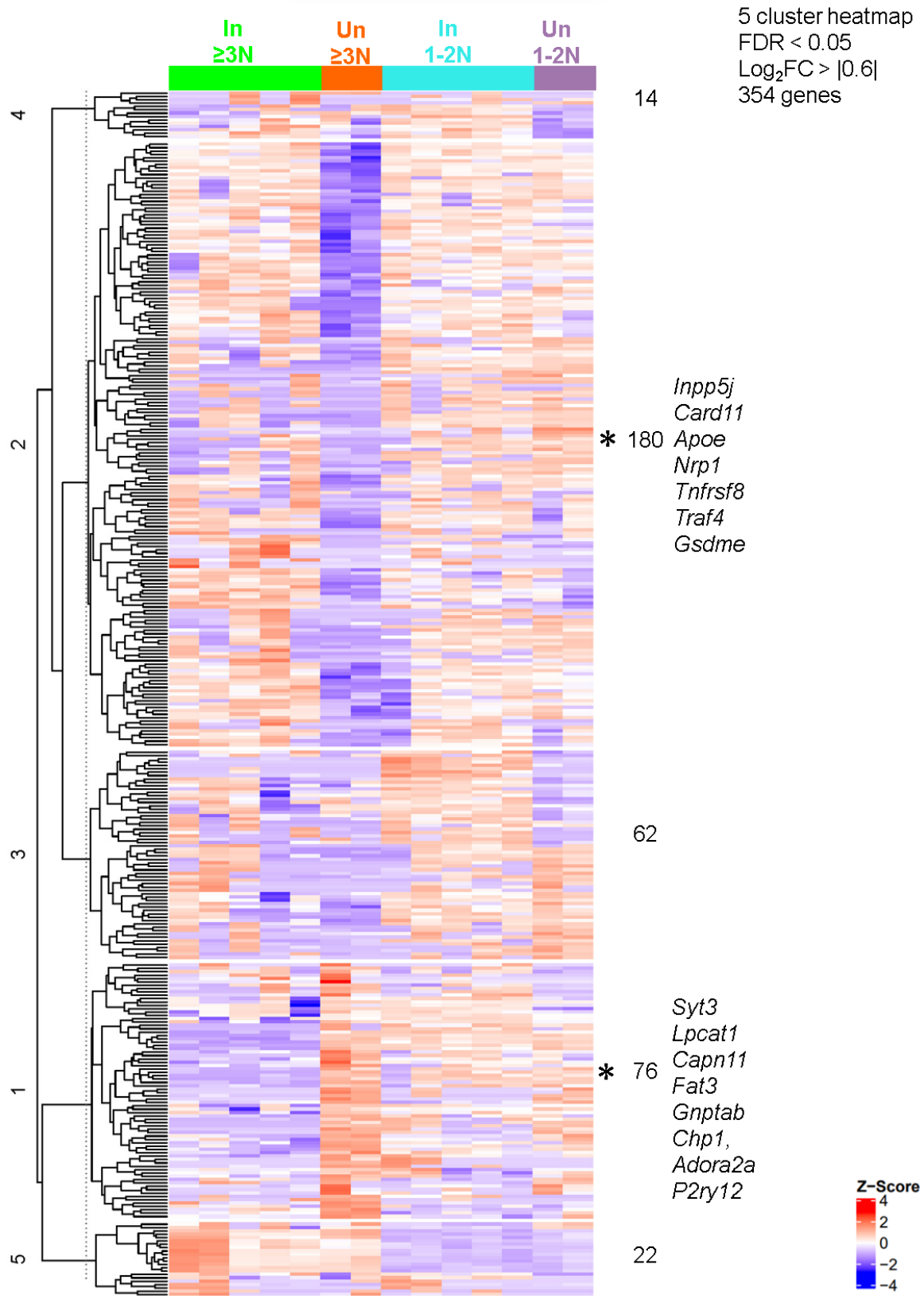

Figure 5.6 Clustered analysis of OCLs from in vivo BCG-infected mice versus mock infected mice

Heatmap of differentially expressed genes in uninfected 1-2N, infected 1-2N, uninfected ≥3N, infected ≥3N OCLs. The heatmap is based on log2RPKM normalised

counts of 354 DEGs as identified by DESeq2 with cut-offs at FDR<0.05 and Log_2FoldChange > |0.6|. Unbiased hierarchical clustering created 5 distinct clusters with the top genes annotated in clusters 1 and 4. The number of genes in each cluster is also annotated. Colour key gradient scale indicates upregulation in red and downregulation in blue. Asterisks depict infection dependent clusters.

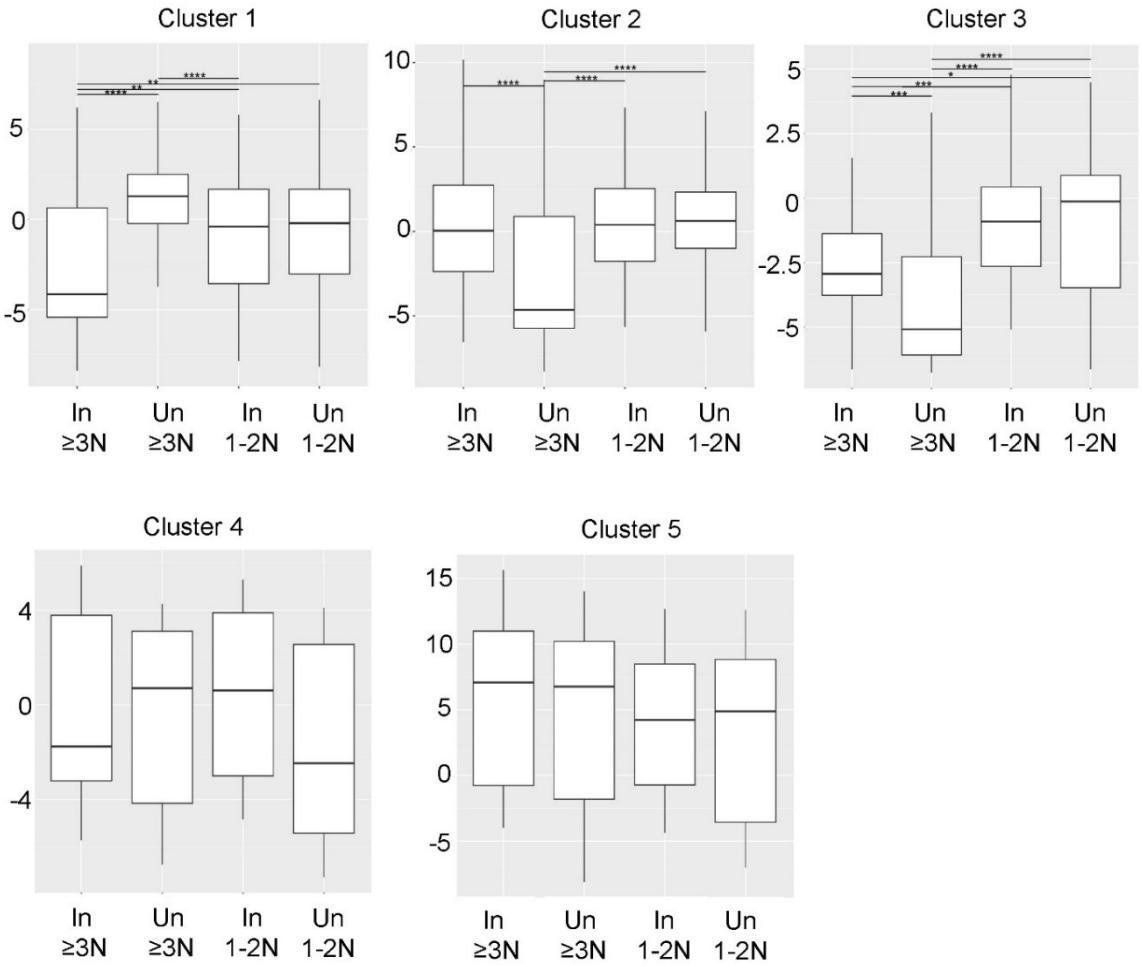

Figure 5.7 Significant transcriptomic changes were found in clusters 1, 2, and 3

Box plots for Z-score of gene expressions averaged over the same conditions for N=5 clusters and of the same condition on each cluster. Significance of transcriptomic changes were determined by Wilcoxon statistical tests. (p-values in Table SC7, Appendix).

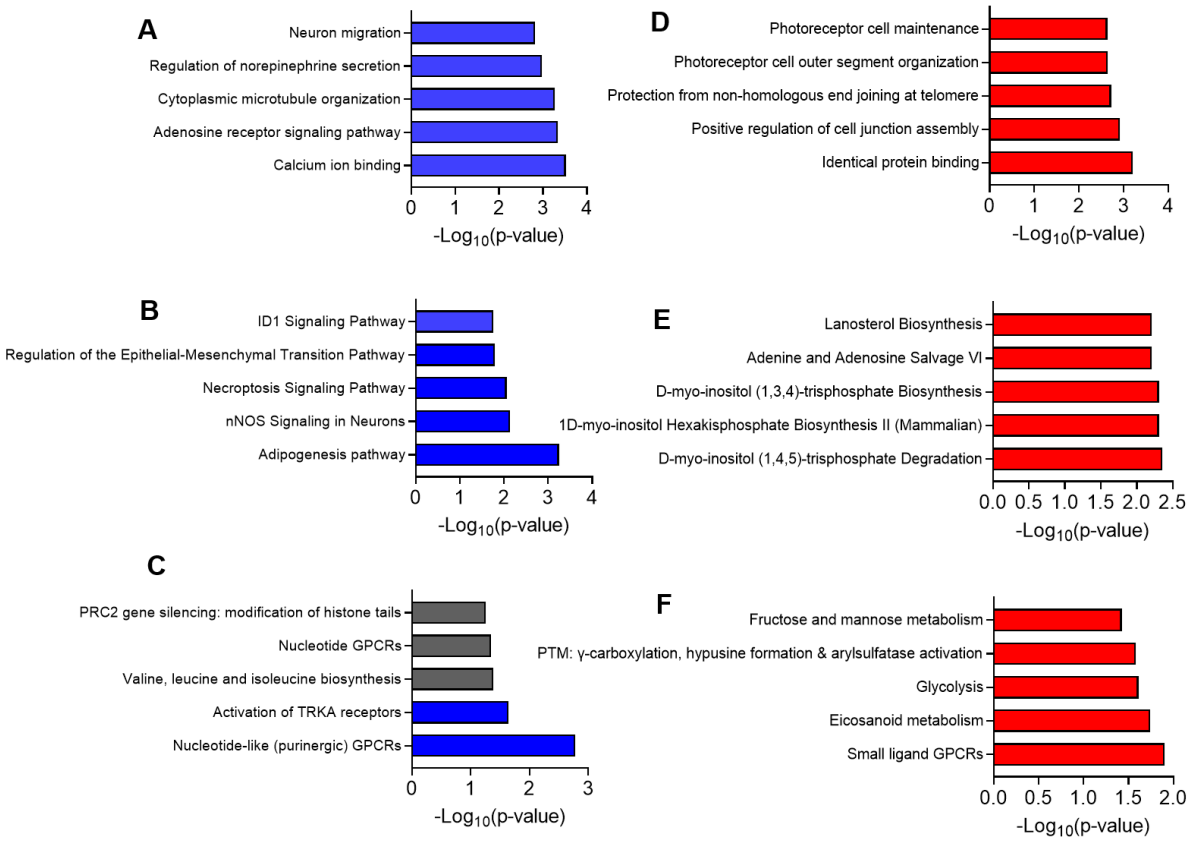

Figure 5.8 Enrichment analysis of cluster 1 and cluster 2 genes

Blue bar graphs denote cluster 1 enrichment analysis of 76 DEGs downregulated upon in vivo BCG infection in ≥3N OCLs (A) Top 5 BPs and MFs from GO enrichment analysis. (B) Top 5 canonical pathways from IPA analysis. (C) Top 5 processes highlighted from BioPlanet (2019) enrichment analysis. -log(p-value) cut off at 1.5 is considered significant. Red bar graphs denote cluster 2 enrichment analysis of 180 DEGs upregulated upon in ≥3N OCLs generated from BM of BCG-infected mice compared to those generated from uninfected mice. (D) Top 5 BPs and MFs from GO enrichment analysis. (E) Top 5 canonical pathways from IPA analysis. (F) Top 5 processes highlighted from BioPlanet (2019) enrichment analysis.

BioPlanet enrichment analysis of cluster 1 genes found nucleotide-like (purinergic) GPCRs (*P2ry12* and *Adora2a)* and activation of TRKA receptors (*Adora2a*) (figure 5.8C). *P2ry12* (In ≥3N vs Un ≥3N: log2FC=-7.972798, *padj*=0.038215) codes for the adenosine diphosphate (ADP) receptor P2RY12 (purinergic receptor P2Y, G protein coupled, 12). One study has shown that *P2ry12*$^{-/-}$ murine OCs exhibited intact differentiation markers, but diminished resorptive function (Su, Floyd et al. 2012). Of note, *Adora2a* (In ≥3N vs Un ≥3N: log2FC=-7.636627, *padj*=2.17E-06) codes for adenosine A_{2A} receptor (A2AR).

Adenosine is a purine nucleoside involved in the regulation of bone homeostasis via its binding to A2AR, (as well as A1R, A2BR, and A3R). It has been shown that activation of A2AR reduces formation of osteoclasts (via PKA- and ERK1/2-mediated suppression of N-FκB nuclear translocation) (Mediero, Perez-Aso et al. 2013). It also impairs osteoclastogenesis through the AP-1 pathway. The use of exogenous adenosine /A2AR agonists show promise as a novel method to facilitate bone repair (Zheng and Wang 2020, Cheng, Yin et al. 2022).

Cluster 2, which contains 180 DEGs upregulated upon *in vivo BCG* infection in ≥3N OCLs specifically, found identical protein binding (*Inpp5f, Apoe, Erbb3, Usp15, H2-M3, Itga2b, Recql5, Lyz1, Pfkfb1, Pfkl, Pkd2, Traf4, Snx33, Spag4, Ercc4, Ahi1, Hsd17b14, Ddx39, Heximˆ2, Castor1*), positive regulation of cell junction assembly (*Epha2, Nrp1, Nphp4*) and protection from non-homologous end joining at telomere (*Ercc4, Dclre1a*) (figure 5.8D). Other notable processes from GO analysis that were not listed in figure 5.8 include Cdc42 protein signal transduction (*Apoe, Nrp1*) (p=0.0027), regulation of innate immune response (*Smpdl3b, Apoe, H2-M3, Lrp8*) (p=0.0037) and regulation of apoptotic processes (*Card11, Apoe, Erbb3, Lpar1, H2-M3, Lrp8, Kitl, Nrp1, Osm, Tnfrsf8, Traf4, Alms1, Mydgf, Ahi1, Gsdme, Cul7,* and *Bfar*) (p=0.0038). Notably, cluster 2 genes are downregulated in Un ≥3N cells compared to Un 1-2N cells (figure 5.5, 5.7), indicating the importance of these genes in differentiating between 1-2N and ≥3N OCLs. IPA analysis of cluster 2 genes revealed D-myo-inositol (1,4,5)-trisphosphate degradation and biosynthesis as the top pathways (*Inpp5f, Inpp5j*) (figure 5.8E). In addition, BioPlanet enrichment analysis of cluster 2 genes found small ligand GPCRs (*Ptger2* and *Lpar1*), eicosanoid metabolism (*Ptger2* and *Ptges*), and glycolysis (*Ptger2* and *Ptges*) to be enriched processes (figure 5.8F).

5.2.3.2 Pairwise analysis of OCLs from *in vivo* BCG-infected mice

Next, I conducted enrichment analysis of pairwise comparisons of DEGs from the comparisons In 1-2N vs Un 1-2N (61 DEGs) as well as In ≥3N vs Un ≥3N (194 DEGs). For reference, raw DEGs for these comparisons are listed in Tables SC6B-C, Appendix. I used MetaCore software for enrichment analysis of cell processes with upregulated / downregulated DEGs analysed separately. Top 5 enriched

process networks for each comparison are listed in table 5.4. Top canonical pathways for the pairwise comparisons identified by IPA are listed in Table SC9, Appendix.

Table 5.4 Enrichment analysis among differentially expressed genes in OCLs from in vivo BCG-infected mice

MetaCore cell process networks enrichment analysis for upregulated and downregulated genes. Upregulated/ downregulated genes were analysed separately.

Comparison	**Enrichment of Process Networks**	***p*-value**
In 1-2N vs Un 1-2N (53 genes upregulated in In 1-2N)	Signal transduction: ESR1-membrane pathway	2.28E-03
	Apoptosis: Anti-Apoptosis mediated by external signals by Oestrogen	2.58E-03
	Signal transduction: Androgen receptor signalling crosstalk	1.87E-02
	Transcription: Nuclear receptors transcriptional regulation	1.88E-02
	Reproduction: Progesterone signalling	2.45E-02
In 1-2N vs Un 1-2N (8 genes downregulated in In 1-2N)	Immune response: Th17-derived cytokines	1.83E-03
	Proteolysis: ECM remodelling	5.84E-02
	Signal transduction: Leptin signalling	7.30E-02
	Proteolysis: Connective tissue degradation	8.03E-02
	Inflammation: IL-6 signalling	8.09E-02
In ≥3N vs Un ≥3N (151 genes upregulated in In ≥3N)	Cell cycle: Mitosis	5.76E-04
	Development: Neurogenesis Axonal guidance	1.07E-02
	Cytoskeleton: Regulation of cytoskeleton rearrangement	2.22E-02
	Cytoskeleton: Spindle microtubules	2.61E-02
	Apoptosis: Death Domain receptors & caspases in apoptosis	3.55E-02
In ≥3N vs Un ≥3N (43 genes downregulated in In ≥3N)	Transport: Synaptic vesicle exocytosis	7.72E-03
	Development: Neurogenesis Synaptogenesis	8.09E-03
	Proliferation: Positive regulation cell proliferation	1.46E-02
	Cytoskeleton: Intermediate filaments	1.56E-02
	Development: Blood vessel morphogenesis	1.57E-02

Synaptic vesicle exocytosis was the top process revealed by MetaCore in the downregulated genes from the In ≥3N vs Un ≥3N comparison (*Bsn, Syt3*) (table 5.4). *Syt3,* Synaptotagmin 3 is a Ca^{2+} sensor involved in exocytosis of secretory vesicles in a Ca^{2+} dependent manner. Synaptotagmins are usually found in synaptic vesicle membranes but another isoform of Syt, Syt7, plays a role in regulating secretory pathways in osteoclasts (Zhao 2008). Bassoon is a scaffolding protein present at the presynaptic cytomatrix at the active zone

where the neurotransmitter is secreted. The gene is expressed primarily in neurons in the brain and there is no evidence of Bassoon playing a major role in osteoclasts or mycobacterial infections. The top process network highlighted from the 53 genes upregulated in In 1-2N vs Un 1-2N was signal transduction: ESR1-membrane pathway (Caveolin-1, Esr1) and anti-apoptosis mediated by external signals by oestrogen (*Esr1*). Intriguingly, regulation of cytoskeleton rearrangement (*Capza1, Tubb3*), and spindle microtubules (*Kif22, Tubb3*) were also enriched in the In ≥3N vs Un ≥3N. Apoptosis related death domain receptors and caspases were similarly enriched among upregulated genes in the In ≥3N vs Un ≥3N comparison (*Tnfrsf8, Traf4, Card11*) (table 5.4).

In summary, mRNA levels of genes involved in cell death pathways were repeatedly found to be upregulated upon infection in OCLs, both *in vitro* (figure 5.4F) and *in vivo* (table 5.4) data sets.

5.2.4 Probing host cell death pathways in BCG infected OCLs

As apoptotic processes were enriched in BCG-exposed OCLs, we decided to probe cell death pathways further using various methods. First, we used the trypan blue exclusion assay and the CytoTox 96® Non-Radioactive Cytotoxicity Assay to determine cell viability of OCLs infected by BCG *in vitro* (figure 5.9). The trypan blue method showed a reduction in cell viability from an average of 95.8 % in uninfected to 74 % in infected OCLs (figure 5.9A). Similarly, the lactose dehydrogenase (LDH) assay showed an average 21.8 % reduction in relative cell viability of *in vitro* BCG-infected OCLs compared to uninfected (figure 5.9B).

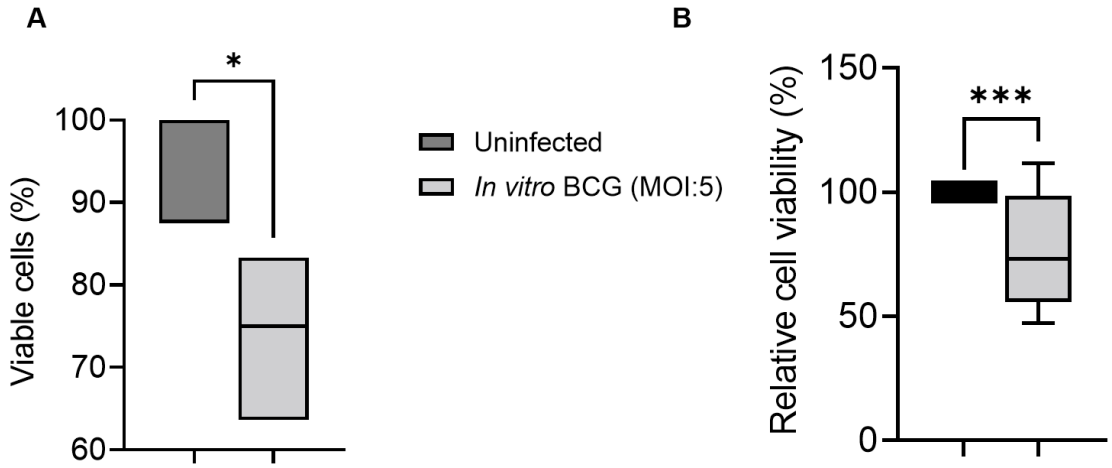

Figure 5.9 The effect of in vitro BCG infection on cell viability in OCLs.

(A) Floating bar plot to show cell death quantified by trypan blue exclusion assay. Data was analysed using unpaired t-test, P=0.0365. N=13 experiments. (B) Cell death quantified by CytoTox 96® Non-Radioactive Cytotoxicity Assay, measuring lactate dehydrogenase (LDH) released during cell death in uninfected OCLs and OCLs that had been infected in vitro with BCG (MOI:5) for 3 hrs followed by incubation for 24 hrs. Cell viability is expressed relative to the uninfected control. Data was analysed using Mann Whitney test as data did not pass the normality test, P=0.0007. N=13 experiments.

5.2.4.1 Apoptotic cell death in BCG infected OCLs

The role of the apoptotic processes during infection was assessed further using Annexin V/ Propidium iodide (PI) staining. Annexin V/PI is a sensitive method to detect whether cells are viable, early apoptotic, or late apoptotic/necrotic due to the differences in the integrity and permeability of the plasma membrane. Viable cells are both Annexin V and PI negative as the plasma membrane is intact. During early apoptosis, the integrity of the plasma membrane deteriorates. Phosphatidylserine (PS) becomes exposed on the external leaflet of the lipid bilayer and Annexin V binds with high affinity to PS so early apoptotic cells are Annexin V positive and PI negative. During late apoptosis, integrity of both the plasma and nuclear membranes deteriorates, allowing PI to get through, intercalate into nucleic acids, and emit red fluorescence. Therefore, late apoptotic cells are both Annexin V and PI positive. During necrosis, the cell membranes are

no longer intact to take up the Annexin V stain. Therefore, necrotic cells are defined as Annexin V negative and PI positive.

From Annexin V/PI staining we observed a trend of reduction in both early and late apoptosis, albeit not significant, in *in vitro* infected OCLs compared to uninfected (figure 5.10A,B). On average, early apoptotic cells decreased from 7.837 % in uninfected to 4.860 % in infected. As for late apoptotic cells, there was reduction from an average of 2.507 % in uninfected to 1.560 % in infected. For necrotic cells, there was an average of 0.590 % in uninfected cell compared to 0.2200 % in infected.

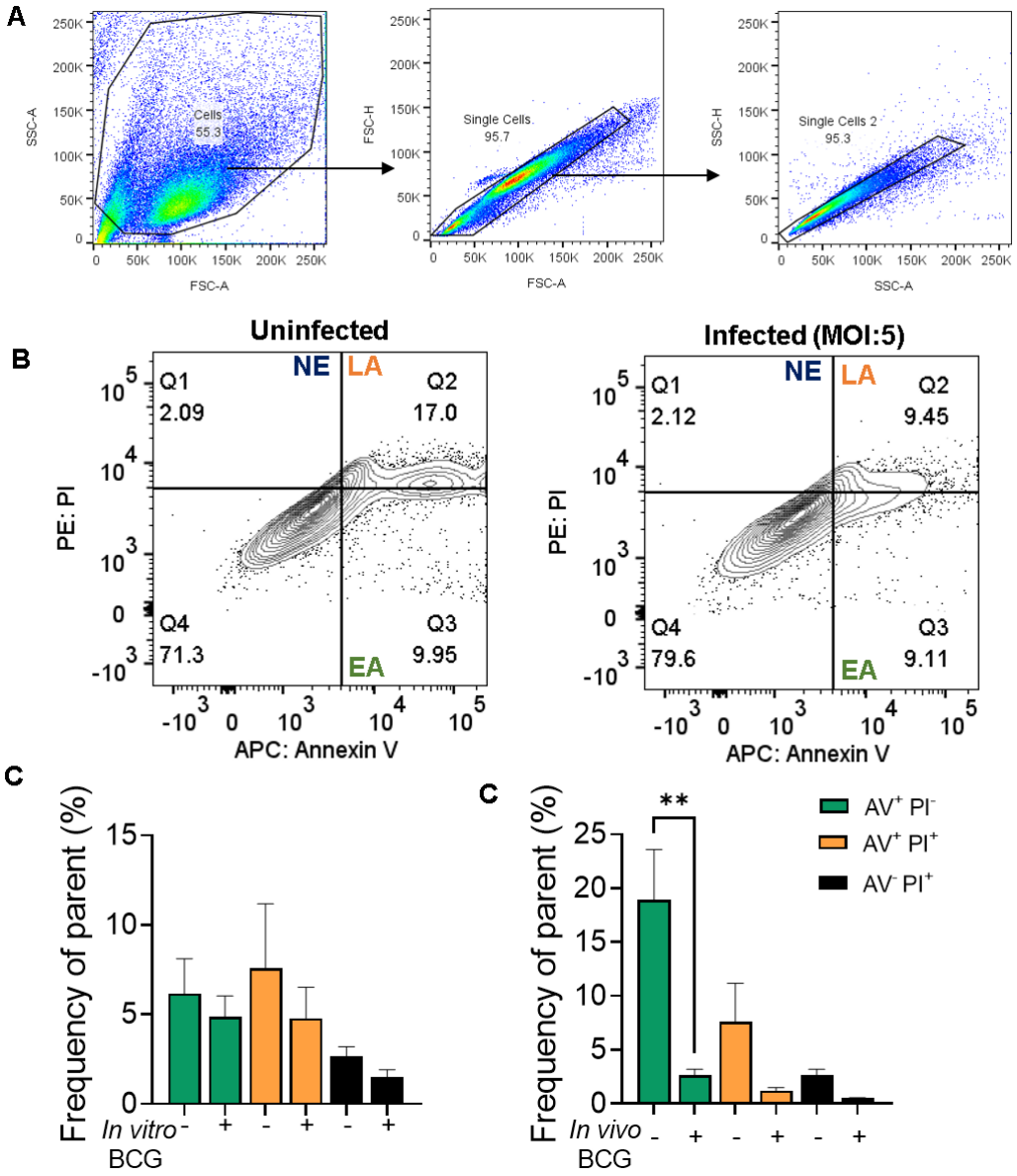

Figure 5.10 Apoptosis of OCLs is inhibited by BCG infection

(A) Gating strategy showing representative Annexin V/PI experiment to probe for early/late apoptosis and necrosis in uninfected versus infected OCLs. EA=Early apoptosis; LA=Late apoptosis; NE=Necrosis. (B) Bar graph of compiled data showing compiled Annexin/PI staining for early apoptotic (Annexin$^+$/PI$^-$) and late apoptotic (Annexin V$^+$/PI$^+$) and necrotic (Annexin$^-$/PI$^+$) cells during uninfected and in vitro BCG infected states. N=4 experiments. One-Way ANOVA. (C) Bar graph of compiled data showing compiled Annexin/PI staining of OCLs generated from BM of mock-infected mice compared to those from BCG infected mice. N=4. One-Way ANOVA showed significant differences between the groups ($F_{5, 12}$ = 6.163, P=0.004). Tukey's multiple comparison test showed significant differences in AV$^+$/PI$^-$ between uninfected and in vivo infected (P=0.0068). Graphs show mean ±SD. N=4 mice in each group.

The trend of apoptosis inhibition was also observed in the OCLs generated from BM of BCG-infected mice (figure 5.10C). Early apoptotic cells significantly decreased from 18.95 % in OCLs from BM of uninfected mice to 2.665 % in the OCLs generated from BM of BCG-infected mice. For late apoptotic cells, the frequency reduced from 7.588 % in OCLs from BM of uninfected to 1.225 % in the OCLs generated from BM of BCG-infected mice. As for necrotic cells, the percentage of necrotic cells was also decreased from an average of 2.665 % in OCLs from BM of uninfected OCLs to 0.530 % in the OCLs generated from BM of BCG-infected mice.

As Annexin/PI experiments showed a trend of inhibition of early and late apoptosis as well as necrosis in BCG-exposed OCLs, we decided to delve further into apoptosis by examining caspase activity. Both intrinsic and extrinsic pathways of apoptosis converge at the executioner caspases 3 and 7 (Cavalcante 2019). Western blots for caspase-3 did not find cleavage of procaspase-3 (32kDa) into their active forms (12, 17kDa) upon *in vitro* infection by BCG (figure 5.11A). Therefore, we calculated the relative density of procaspase-3 relative to that of housekeeping protein β-actin and found a non-significant accumulation of procaspase-3 in *in vitro* infected OCLs (figure 5.11B). Next, caspase-3/7 luminescence assays were used to quantify relative caspase-3/7 activity. As a positive control to induce (non-specific) apoptosis, OCLs were challenged with 1μM staurosporine for 4 hrs. In line with increased procaspase 3 in BCG-infected

OCLs (figure 5.11B), we found a significant reduction in relative caspase-3/7 activity in *in vitro* infected OCLs (figure 5.11C).

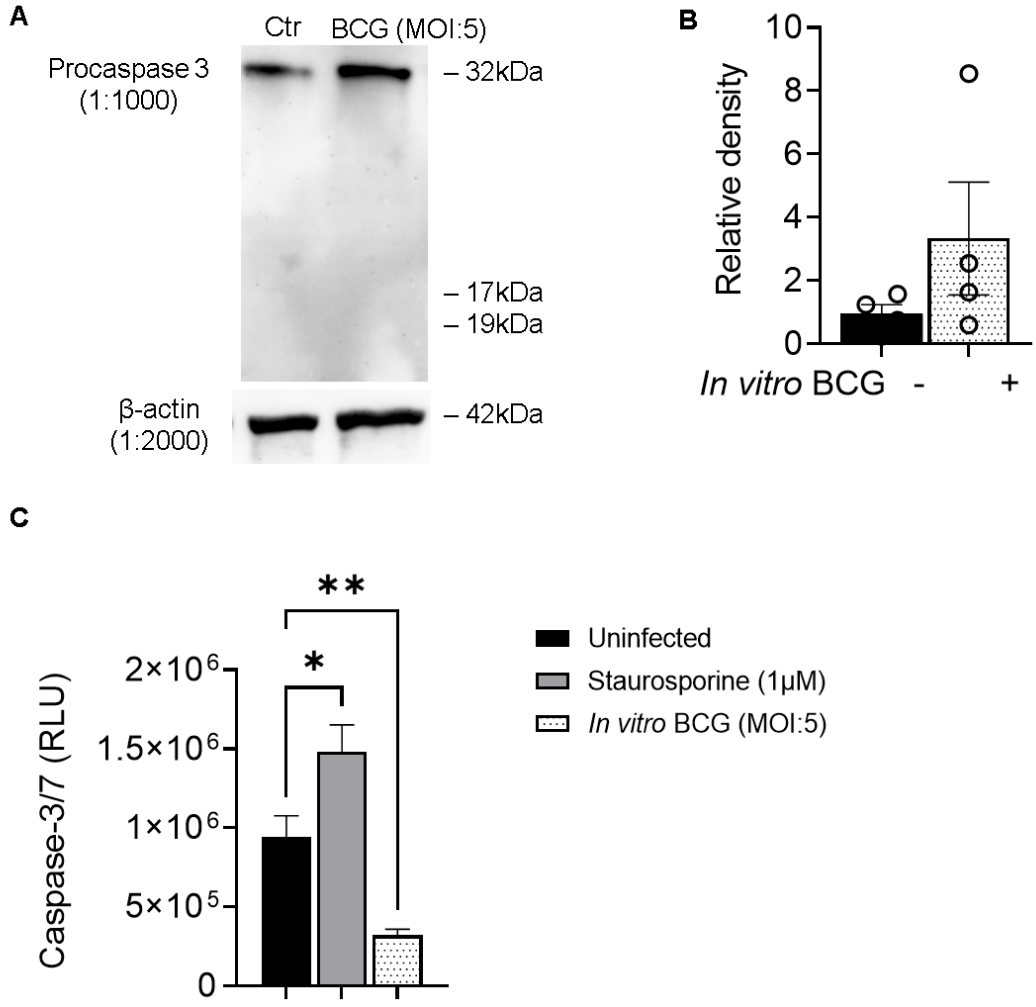

Figure 5.11 Reduction in executioner caspase activity in vitro BCG infected OCLs

(A) Immunoblot for the detection of procaspase 3 (32kDa) and cleaved caspase-3 (17,19kDa) from uninfected or in vitro BCG infected OCLs. The numbers on the right indicate the molecular masses in kDa. (B) Bar graph shows mean relative density of procaspase 3 band normalised to β-actin; each dot represents a biological repeat. Statistical analysis was performed using Mann Whitney test, P=0.2. (C) Caspase 3/7 activity of uninfected murine OCLs, OCLs that had been challenged with Staurosporine (1μM) for 4 hrs and in vitro BCG-infected OCLs (24 hrs p.i). One-way ANOVA showed significant differences between the groups ($F_{2, 33}$ = 20.76, P<0.0001). Tukey's multiple comparison test showed significant differences between uninfected and Staurosporine treated (P=0.0137), uninfected and in vitro infected (p=0.0045). Graphs show mean ±SD. N=4.

As it was clear the process of apoptosis was being perturbed (figure 5.10, 5.11) whist cell viability was reduced (figure 5.9), we decided to investigate other cell

death pathways. Pyroptosis was chosen due to its well noted significance in promoting inflammation in *Mtb* infected macrophages (Qu 2020). We noticed an increased expression of *Gsdme* gene in In ≥3N cells compared to Un ≥3N cells (Log2FC=1.48803, *padj*=0.016722). *Gsdme* is Gasdermin E, a pore-forming protein produced by cleavage from caspase 3, essentially a molecular switch converting apoptosis to pyroptosis (Jiang 2020, Zhou 2021).

Pyroptosis is also triggered by *Caspase-1* after its activation by various inflammasomes and results in lysis of the affected cell, so a Caspase-1 glo luminescence assay was used to quantify caspase-1 levels. We found a reduction of caspase-1 RLU in *in vitro* BCG-infected OCLs at 24-hr p.i. (figure 5.12A). This reduction, however, had no impact on IL-1β release from *in vitro* infected OCLs compared to uninfected OCLs (figure 5.12B).

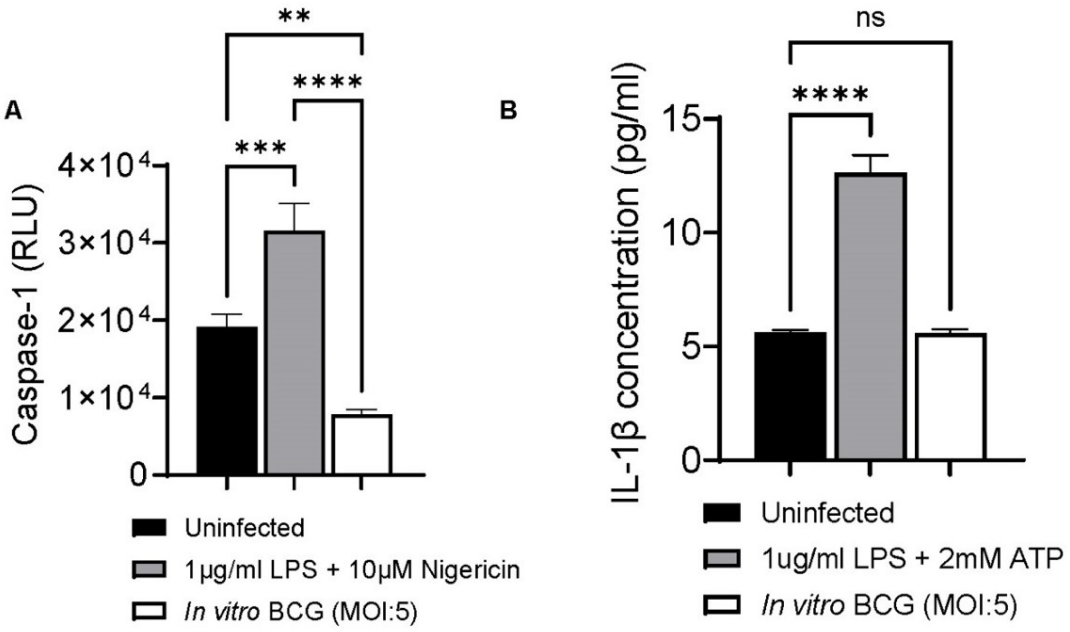

Figure 5.12 NLRP3 inflammasome activity is dampened during in vitro BCG infection of OCLs

*(A) Caspase-1 glo luminescence assay was used to quantify caspase-1 activity in murine osteoclast-like cells uninfected or infected at day 6 with BCG MOI:5 for 24-hrs. OCLs stimulated with 1µg/ml LPS for 4 hrs followed by 30 mins of 10µM Nigericin at day 7 were used as a positive control. Graph shows mean ±SD. N=4 experiments. One-way ANOVA showed significant differences between the groups. ($F_{2,28}$= 33.11, P<0.0001). Tukey's multiple comparison test found significant differences between uninfected and LPS + nigericin (***P=0.0009), uninfected and infected (**P=0.0013) and LPS + nigericin and infected (****P<0.0001). (B)*

Quantification of IL-1β in uninfected and infected OCLs. Response to 1μg/ml LPS for 4 hrs followed by 1 hr of 2mM ATP treatment was used as positive control. N=3 experiments. Analysis was performed using One-Way ANOVA. Tukey's multiple comparison test showed significant differences between uninfected levels of IL-1β and the test concentrations of LPS + ATP positive control (P<0.0001).

One of the major inflammasomes that is crucial in mediating caspase-1 activation is the NLRP3 inflammasome, which results in the secretion of proinflammatory cytokines IL-1β/IL-18 (Huang 2021). We found an accumulation of NLRP3 and ASC protein in *in vitro* BCG-infected OCLs by western immunoblotting (figure 5.13), though this increase does not correlate with IL-1β concentration and caspase-1 activity in *in vitro* BCG-infected OCLs (figure 5.12).

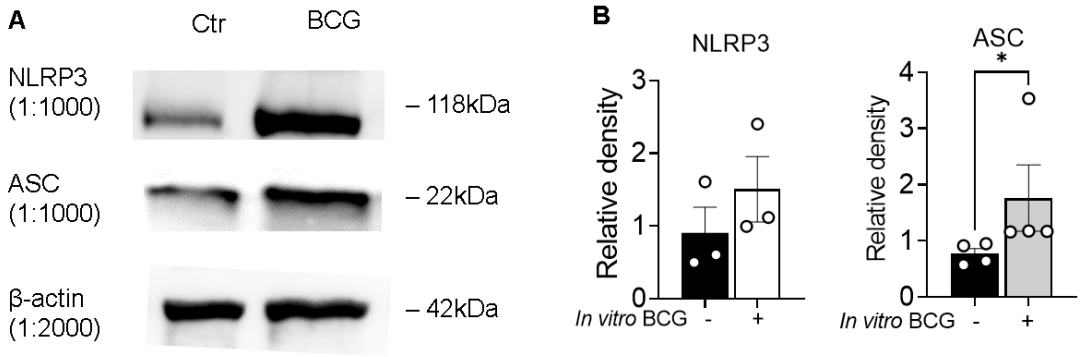

Figure 5.13 NLRP3 and ASC components are activated during BCG infection but NLRP3 inflammasome activity is dampened

(A) OCLs were left untreated at day 7 (control) or infected with BCG for 3 hrs at day 6 followed by wash and 24-h time point. Cell lysates were separated by SDS-PAGE and analysed by western blotting using the indicated antibodies. The numbers on the right indicate the molecular masses in kDa. (B) Bar graphs show mean relative density of western blot bands normalised to β-actin, each point represents a biological repeat. Statistical analysis was performed using Mann-Whitney test. ASC: P=0.0286.

Taken together, our data indicates mycobacterial mediated inhbition of cell death pathway in OCLs, which might be via dampening of NLRP3 inflammasome. These findings envisage the role of NLRP3 in BCG-induced osteoclastogenisis (figures 5.12, 5.13).

5.2.5 The effect of NLRP3 deficiency on BCG infection of OCLs

To further probe into NLRP3 involvement in BCG infection of OCLs, we used NLRP3 deficient mice. First, we investigated a link between NLRP3 and BCG mediated osteoclastogenesis using our previously described method of nuclear staining and analysis using FACS (Chapter 2.2.3). To this end, we discovered that *in vitro* BCG infection of OCLs from NLRP3$^{-/-}$ mice displayed almost no expansion of ≥3N cells compared to the OCLs from WT mice (figure 5.14). Upon BCG infection WT OCLs displayed an average 2.5-fold increase of the ≥3N population of cells, compared to almost no increase in NLRP3$^{-/-}$ OCLs, suggesting an important role of NLRP3 in BCG mediated multinucleation of murine OCLs.

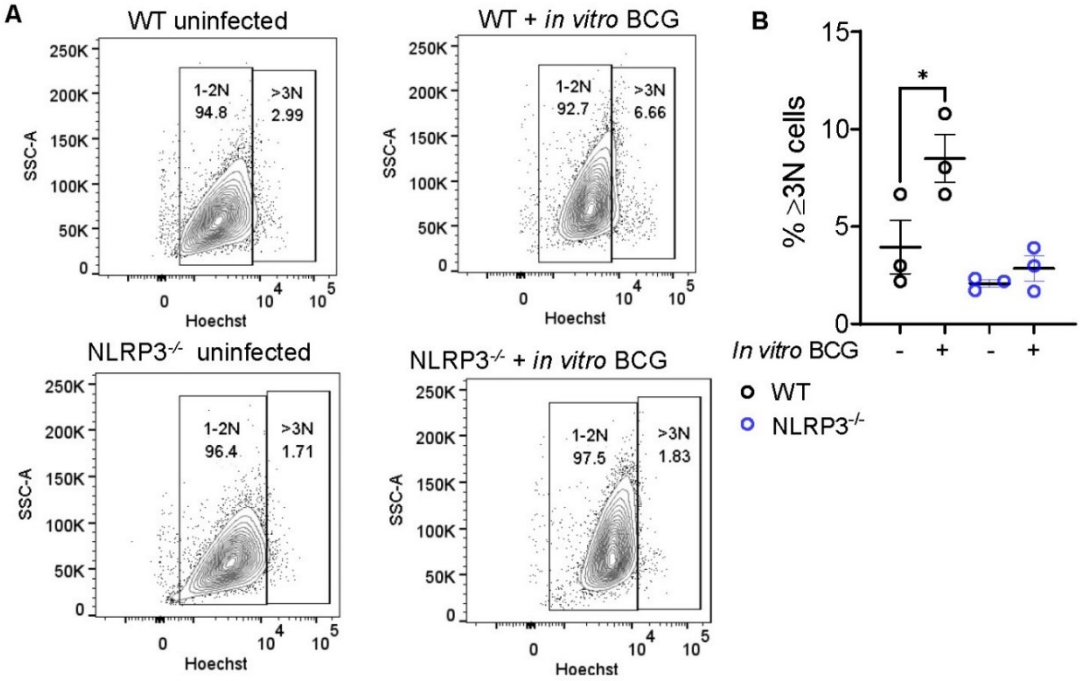

Figure 5.14 NLRP3-/- OCLs have reduced frequency of ≥3N cells during in vitro BCG infection

(A) Representative contour plots to gate 1-2N cells from ≥3N cells from uninfected WT control mice and age and gender matched NLRP3$^{-/-}$ mice that were infected in vitro with BCG MOI 5 for 3 hrs followed by a 24-hr time point. Gated on single and live cells. (B) Scatter plot depicting compiled percentages of ≥3N cells from uninfected WT control mice and ≥3N cells from in vitro BCG infected NLRP3$^{-/-}$. Statistical analyses were performed using 2 Way-ANOVA and showed significant differences between groups. Column factor: ($F_{3,6}$ = 12.46, P=0.0055). N=3. Tukey's

multiple comparison test showed a significant difference between WT uninfected vs WT infected (P=0.0286), and WT infected vs NLRP3 infected (P=0.0107).

Our findings were also strengthened by reproducing the above *in vitro* data with *in vivo* infection of NLRP3$^{-/-}$ mice. Due to N=2 mice for each sample group (8 mice in total) which in turn leads to the lack of a statistically significant positive control (significant difference in ≥3N OCLs between WT uninfected and infected), this data is in supplementary figure SC3, Appendix. It does however show the same trend seen with *in vitro* infected NLRP3$^{-/-}$ mice (2.21-fold increase in ≥3N OCL in WT upon *in vivo* BCG infection compared to a 0.93-fold increase in NLRP3$^{-/-}$).

Next, we investigated the impact of NLRP3 on the expression of pro-inflammatory factors during infection of OCLs. We performed Luminex on supernatants collected from *in vitro* BCG infected WT and NLRP3$^{-/-}$ OCLs (figure 5.15). As shown before (figure 4.9), we found IL-10, TNF-α, IL-18 CCL3, CCL11 and IL-6 to be upregulated in BCG-infected OCLs compared to uninfected OCLs from WT mice (figure 5.15). This upregulation was not observed in BCG-infected OCLs from NLRP3$^{-/-}$ mice. Also, the increase in GRO-α (CXCL1) and RANTES (CCL5) in WT infected OCLs was not seen in infected NLRP3$^{-/-}$ OCLs. Taken together, this data suggests NLRP3 dependent osteoclastogenic differentiation during mycobacterial infection.

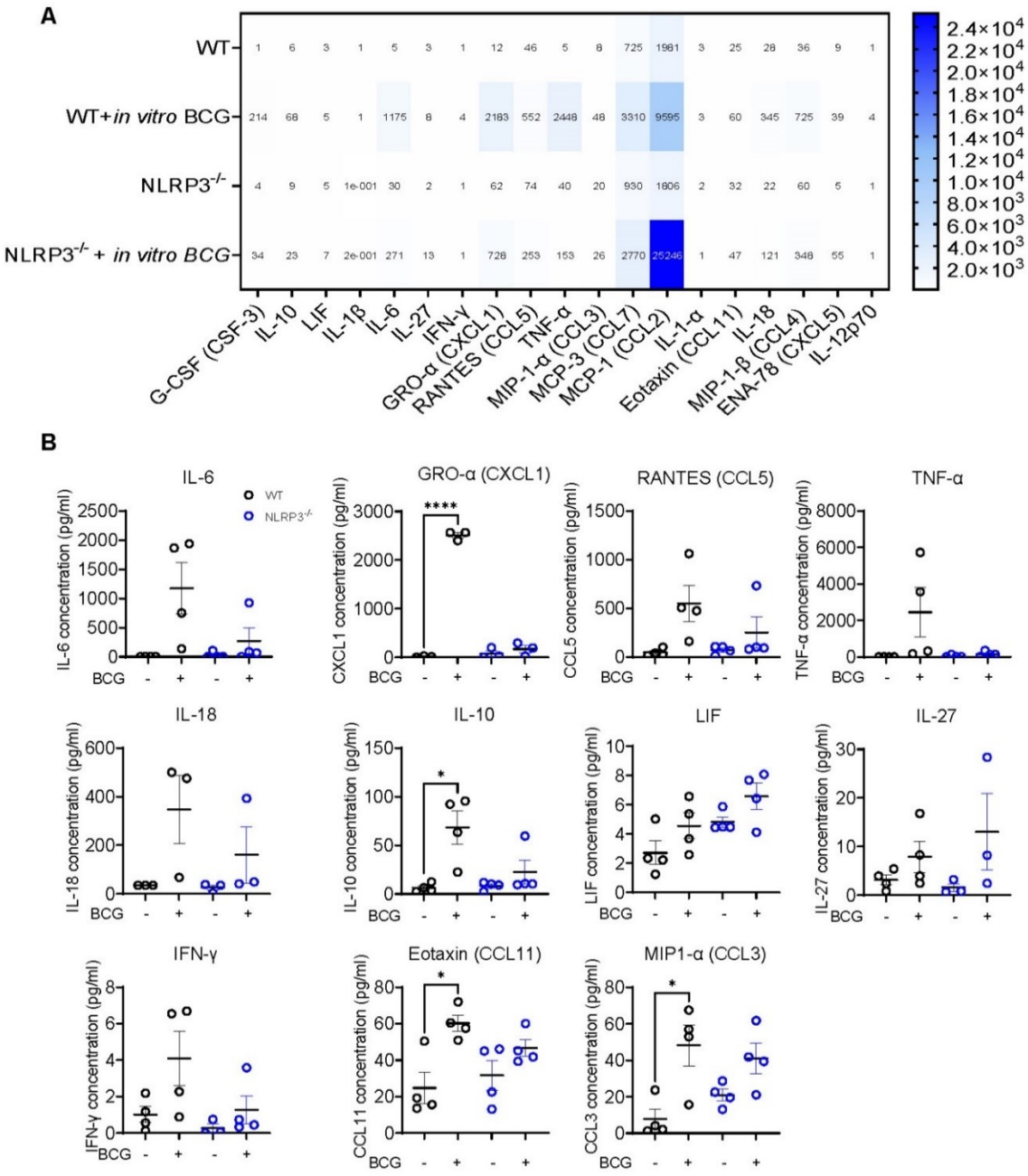

Figure 5.15 In vitro BCG infection of NLRP3$^{-/-}$ mice inhibits osteoclastogenic and proinflammatory cytokine release

Luminex assay of pre-determined panel of cytokines released into the supernatant by uninfected WT and NLRP3$^{-/-}$ OCLs and the supernatant of in vitro BCG infected WT and NLRP3$^{-/-}$ OCLs. OCLs were infected at day 6 with BCG MOI 5 for 24 hrs. (A) Heatmap of cytokine panel assay of cytokine levels that were determined by Luminex including values that were within range, or able to be extrapolated. Values that were out of range (higher than the HLOQ or lower than the LLOQ) are plotted as the HLOQ or LLOQ accordingly. The average of side-by-side replicates were plotted with a double gradient colourmap. (B) Scatter plots depicting the cytokines that are upregulated upon in vitro BCG infection of WT OCLs but not NLRP3$^{-/-}$ OCLs. Individual replicates are plotted on the graphs for N=3 at least. Statistical analyses

were performed using 2 Way-ANOVA. Significant differences were found in CXCL1, IL-10, CCL11 and CCL3.

5.3 Discussion

The ability of mycobacteria to survive within osteoclasts and modulate their cell death pathways has been previously studied, where it was found that *Mtb* could escape the phagosome of osteoclasts, survive in the cytosol, and inhibit apoptotic cell death (Hoshino 2014). However, molecular details underpinning the osteoclast responses to mycobacterium are unclear. To enhance our understanding of BCG-osteoclast interactions, we performed transcriptomic analysis to investigate infection-dependent genes during *in vitro* BCG infection of OCLs, as well as OCLs generated from BM of *in vivo* infected mice. This forms a large portion of the results of this chapter.

We utilised two analysis strategies from the output of DESeq2 DEG data for *in vitro* BCG infected samples. Clustered analysis was performed to observe changes across all groups (Un 1-2N, In 1-2N, Un ≥3N and In ≥3N) and pairwise analysis was adopted to study selected comparisons (Un 1-2N vs In 1-2N and Un ≥3N vs In ≥3N). Clustered analysis was performed using GO enrichment analysis using R statistics, IPA and BioPlanet (2019). Pairwise analyses were accomplished using MetaCore.

From *in vitro* data, expected changes seen were the enrichment of myeloid leukocyte mediated immunity and myeloid cell activation involved in the immune response genes upregulated in In 1-2N cells compared to Un 1-2N (table 5.2). Enrichment analysis of *in vitro* infected OCLs also revealed the novel finding that serotonin receptor signalling genes *Htr1b* and *Slc6a4* were upregulated upon *in vitro* infection, particularly in ≥3N cells. Osteoclasts do in fact express neurotransmitters such as the serotonin transporter SLC6A4 (short for solute carrier family 6 member 4), which is a selective serotonin reuptake inhibitor (SSRI) target. Notably, it has been found that SSRI treatment decreased SLC6A4 expression as well as reduced apoptosis of murine pre-osteoclasts (Durham,

Zhang et al. 2020). SSRIs, which are widely used clinically to treat depression, have been linked to increased bone fracture risk and lower bone mineral density. SLC6A4 specifically has been verified to be linked to bone loss (Lapid, Kung et al. 2017). Based on our findings and correlation to previous data, SLC6A4 could be a potential novel biomarker for bone TB, although further validation is needed.

In vitro transcriptomics data also highlighted the downregulation of genes related to regulation of cell death in infected ≥3N (*Nr4a1, Ccn2, Id3, Timp3, Gata1, Alox12, Irak3, Rnf144b, Hpgd, Eno2*) (figure 5.2, table 5.2). *Alox12* and *Hpgd* genes showed overlap with the lipoxygenase pathway, along with *Alox15*. ALOX12/15 also known as lipoxygenase-12/15 are enzymes that oxidise polyunsaturated fatty acids, such as omega-6 and −3 fatty acids, to generate bioactive lipid metabolites (Mashima and Okuyama 2015). It would have been interesting to investigate the involvement of lipid metabolism and the lipoxygenase pathway further. However, ALOX12/15 have different substrate specificities in humans and mice and as their differences have not been fully confirmed, we decided against looking at this further in this instance.

Transcriptomic analysis of OCLs generated from BM of BCG-infected mice led to novel insights on the possible impact of *Mycobacterium* on osteoclasts *in vivo*. Our data highlighted genes involved in the organisation of cytoskeleton to be upregulated as well as downregulated in ≥3N OCLs from BCG-infected mice. Genes *Ccdc88a, Spast,* and *Chp1* were downregulated in ≥3N OCLs from BCG-infected mice. In contrast cytoskeleton rearrangement (*Capza1, Tubb3*), and spindle microtubules (*Kif22, Tubb3*) were found to be upregulated in In ≥3N (table 5.4). Cytoskeletal intermediate filaments gene (*Tubb2b*) was also found to be downregulated in In ≥3N from pairwise analysis of In ≥3N vs Un ≥3N. Both tubulin β2 and 3 have not been associated with osteoclasts before and it remains to be seen what the role of these tubulins are and how they affect osteoclast development during infection.

The cytoskeleton is a highly co-ordinated 3D network of actin filaments, microtubules (MTs, α- and β-tubulin dimers), and intermediate filaments (IFs)

that allows the cell to assemble and disassemble the podosome to the bone matrix via αvβ3 integrins to create resorption pits inside the lacunae. The cytoskeleton can also be rearranged to promote the internalisation of bacteria, traffic vesicles, and promote actin-dependent cell motility (Colonne, Winchell et al. 2016). Osteoclasts express four α- and four β-tubulin genes, with high levels of tubulin β6, which has been shown to control MT shaping and podosome patterning (Guérit, Marie et al. 2020).

The role of the cytoskeleton in mycobacteria of macrophages, however, has been studied. It was unveiled that bacterial load was controlled during internalisation by interference with actin polymerisation at the phagocytic cup (actin-dependent reorganisation of the membrane) (Bettencourt, Marion et al. 2013). Interference with actin nucleation at the cell membrane in *Mtb* infected cells, resulted in the expression of microRNA 142-3p, which was responsible for low intracellular bacteria load, and prevented apoptosis of the host cell to promote bacilli survival (Welin, Eklund et al. 2011, Naqvi, Fordham et al. 2015). As well as regulating bacterial uptake, the manipulation of the cytoskeleton by *Mtb* occurs intracellularly during late-stage phagocytosis. Indeed, pathogenic *Mtb* but not non-pathogenic *Mycobacterium smegmatis* was shown to prevent actin polymerisation on phagosome membranes (Anes, Kühnel et al. 2003, Anes, Peyron et al. 2006). Due to the similarities between osteoclasts and macrophages, it is possible they share similar cytoskeleton dynamics during infection. *Mtb* has already been shown to escape the phagosome of human osteoclasts (a similarity shared with macrophages) (Hoshino 2014). This is a useful survival strategy as osteoclasts express more acid-producing vacuolar type H^+-ATPase (V-ATPase) than other cells for their osteolytic function (Hoshino 2014). Only one study to date has looked at osteoclast cytoskeletal dynamics during infection i.e in Zika virus infected pre-OCs. This study showed that infected pre-OCs showed a reduced number of actin rings and increased discontinuation of the rings compared to the uninfected controls, meaning an inhibition of overall osteoclastogenesis (Mumtaz, Koedam et al. 2022). Therefore, if pre-OCs are infected with mycobacteria, we would expect that the opposite is true (increased

number of actin rings, decreased discontinuation of the rings). Targeting the cytoskeleton may be a useful potential treatment strategy in the future.

GO enrichment analysis of cluster 2 genes (upregulated in ≥3N OCLs from BCG infected mice) found an enrichment of innate immune response genes (*Smpdl3b, Apoe, H2-M3, Lrp8*). Furthermore, analysis of cluster 2 DEGs found regulation of apoptotic processes to be enriched (*Card11, Apoe, Erbb3, Lpar1, H2-M3, Lrp8, Kitl, Nrp1, Osm, Tnfrsf8, Traf4, Alms1, Mydgf, Ahi1, Gsdme, Cul7, Bfar*). Pairwise analysis of In ≥3N vs Un ≥3N also highlighted regulation of death domain receptors and caspases (*Tnfrsf8, Traf4, Card11*). On the contrary, pairwise analysis of In 1-2N vs Un 1-2N featured anti-apoptosis mediated by external signals by oestrogen (*Esr1*) (table 5.4). Due to the recurrence of apoptosis as a theme in transcriptomic profiling in both *in vitro* and *in vivo* data, we decided to probe into this further. By performing Annexin V/PI staining, we were able to confirm that apoptotic processes were being inhibited by BCG in OCLs both *in vitro* and *in vivo*. Apoptosis is an integral to the life cycle of an osteoclast due to their limited lifespan. Hence, any change that increases their viability and reduces apoptosis has been linked to an increase in osteoclast activity and resorption (Soysa and Alles 2019). Indeed, apoptosis inhibition has been utilised by *Mtb* while infecting macrophages, and thus heightening its intracellular survival (Velmurugan 2007). *Mtb* infection has been shown to inhibit apoptosis in human osteoclasts by inducing TNF-α mediated autophagic processes (Liu, Zhou et al. 2020). In the present study, we show that BCG also inhibits apoptosis in mouse OCLs. Of note, it contradicts the idea that only virulent *Mtb* strains can inhibit apoptotic processes whereas non-pathogenic and attenuated mycobacteria trigger apoptosis (Lam, Prabhu et al. 2017).

As induction of cell death in the presence of intracellular pathogens is an effective approach for innate cells in controlling infection, pyroptosis was then investigated in conjunction with NLRP3 inflammasome activity. Recent studies have revealed that various effectors of cell death have been reported to regulate NLRP3 inflammasome activation, suggesting that cell death is closely related to NLRP3 inflammasome activation (Huang, 2021). Activation of the NLRP3

inflammasome requires priming and activation. Signal 1 is triggered by PAMPs, such as lipopolysaccharide (LPS), or cytokines, such as TNF-α and IL-1 (Huang 2021). The priming signal leads to transcriptional activation of NLRP3 inflammasome-related genes, such as *NLRP3, pro-IL-1β*, and *pro-IL-18*, through activation of the nuclear factor-κB (NF-κB) signalling pathway. Signal 2 is the trigger step for activation and is induced by specific PAMPs or DAMPs, such as bacterial infection, extracellular ATP, Ca^{2+} influx, lysosomal rupture, mitochondrial damage, and ER stress. The trigger signal induces the assembly of NLRP3, ASC, and pro-caspase-1, leading to the activation of the NLRP3 inflammasome, pyroptotic cell death, IL-18 and IL-1β release (Kelley, Jeltema et al. 2019).

We show that protein levels of NLRP3 and the adaptor ASC are increased upon BCG infection of OCLs from WT mice, but caspase-1 activity was dampened (figures 5.12, 5.13). During *Mtb* infection of murine macrophages, caspase-1 activation (and secretion of IL-1β) has been reported, which was found to be mediated by ESX-1 secreted protein ESAT-6 (Wong and Jacobs 2011, Shah, Cannon et al. 2015). ESAT6 has roles in apoptosis induction and has previously been shown to activate NLRP3 (Derrick 2007, Mishra 2010). Nevertheless, in the context of osteoclast infection, the involvement of NLRP3 inflammasome and caspase-1 has been poorly studied and remains unclear. One study showed that the NLRP3 inflammasome negatively regulates RANKL-induced osteoclastogenesis of murine BMDMs but positively regulates it in the presence of LPS (Alam, Mae et al. 2022). Furthermore, overexpression of the NLRP3 protein has been correlated to aggravated bone resorption (Jiang, An et al. 2021). It is possible that NLRP3 levels increase during BCG infection was due to successful priming of the inflammasome, but activation (due to insignificant increased levels of NLRP3/ASC and significant reduction in caspase-1 activity and lack of IL-1β release) was hampered. This could be due to mycobacteria interfering with the 2nd signal required for NLRP3 inflammasome activation, such as interference with Ca^{2+} signalling. It is interesting to note that live *Mtb* induces a change in $[Ca^{2+}]_c$ in human macrophages, whereas killed *Mtb* does not. Viable *Mtb* causes an inhibition of Ca^{2+} signalling, while mediating Ca^{2+} efflux (Malik,

Denning et al. 2000). A surge in cytosolic Ca^{2+} concentration has been associated with antimicrobial phagosome processes, and *Mtb* can inhibit this process partly due to manipulation of Ca^{2+} signalling, mediated by *Mtb* LAM through sphingosine kinase inhibition (Malik, 2003).

Certainly, the findings in this study are limited to using BCG as a model. BCG strains possess a deletion of the genomic region *RD1* which is responsible for encoding two immunogenic antigens and virulence factors— ESAT-6 and CFP-10, along with several structural components of the ESAT-6 secretion system (ESX)-1 type VII secretion system, which together are responsible for ESAT-6 and CFP-10 secretion. Therefore, the mechanism by which mycobacteria might be regulating the NLRP3 inflammasome in osteoclasts should be further validated with *Mtb.* Despite this, our results provide evidence for phenotypic and transcriptomic changes in osteoclasts that favour osteoclastogenesis and result in bone loss. Modulating cell death pathways may be a mechanism of mycobacterial survival strategy within osteoclast-like cells, along with the dampening of the NLRP3 inflammasome, through the reduction in caspase-1 activity and lack of IL-1β secretion.

Chapter 6 Final Discussion

M. tuberculosis is a successful intracellular pathogen that has evolved various mechanisms to evade host immunity. This project aimed to investigate the molecular mechanisms of mycobacterial pathogenesis in bone cells, focusing on osteoclasts due to their shared characteristics with innate immune cells.

Firstly, chapter 3 describes the characterisation of osteoclasts like cells (OCLs) generated from murine BM cells. Standardisation and validation of the protocol was important to establish before moving onto infection models. After determining that a 7-day protocol was optimal, we used biochemical, microscopic, and molecular techniques to confirm the authenticity of OCLs. We first characterised the OCLs by their multinucleation and TRAP activity. Following this, flow cytometry was used to sort 1-2N and ≥3N OCLs, which underwent transcriptomic profiling to identify differentially expressed genes (DEGs) relating to osteoclast differentiation. To the best of my knowledge, the transcriptomic profiling of sorted 1-2N, ≥3N OCLs has not been performed before. It was unveiled that 1-N and ≥3N OCLs differed by their NADH dehydrogenase (ubiquinone) activity and calcium ion binding processes – the annotated genes may be useful as novel molecular markers of osteoclastogenesis.

Chapter 4 results unravelled phenotypic changes in BCG-infected osteoblasts and osteoclasts. BCG infection of osteoblasts showed some evidence of a proinflammatory response through the differential modulation of TLR2/4 surface and mRNA expression and IL-1β cytokine release. Evidence of cytokine release from osteoblasts is in line with previously reported responses to *Mtb* and other bacteria. For example, human bone tissue derived osteoblasts infected with *Mtb* resulted in IL-6 cytokine release (Ma, Jin et al. 2022). Similarly, when challenged with *S. aureus* and *S. epidermidis,* primary human osteoblasts saw an increase in mRNA and cytokine release of IL-6, IL-8 (CXCL8) and CCL2 (MCP-1) (Dapunt, Giese et al. 2016). The release of CXCL8 and CCL2 may increase the local inflammatory response through the recruitment of leukocytes. Furthermore, IL-1β, along with IL-6 and TNF-α are soluble factors involved in osteoclastogenesis.

The release of IL-1β (which induces RANKL expression to enhance OC differentiation) from osteoblasts in response to BCG provides an insight into the role of osteoblasts in pathogenic bone resorption during bacterial infection (Ruscitti, Cipriani et al. 2015, Amarasekara, Yun et al. 2018).

BCG infection of MG-63 demonstrated an increase in *ALP* mRNA expression, with a reduction in ALP staining data, which gave an indication of reduced ALP activity (figure 4.2B-C). To confirm a reduction in ALP activity, we could have performed ELISA for ALP to show that enzymatic activity was being affected. Increased *TNFSF11* (RANKL) gene expression seen in BCG-infected MG-63 (figure 4.2A) could also be correlated with an increase in RANKL enzymatic activity, which could have been shown with ELISA. Additionally, the crosstalk between osteoblasts and osteoclasts could have been studied, where the supernatant from infected osteoblasts could have been exposed to OCPs to see whether this induces osteoclastogenesis within a co-culture system. Of note, the use of human osteoblasts (MG-63) and mouse osteoclasts during this project made these investigations complex.

Another point to note was that BCG internalisation and persistence within MG-63 cells was generally low (around 5 %) between 3 and 24 hrs p.i. and still resulted in proinflammatory responses. Although we decided to probe into the OCL response to BCG infection in detail, it has been recorded that the contact of bacteria with osteoblasts that results in binding but not uptake is still enough to stimulate cytokine production (Dapunt, Giese et al. 2016).

The key findings in the current work were that BCG infection of OCLs resulted in an increased OCL frequency, pro-osteoclastogenic activity, and resorption potential, agreeing with the literature regarding *Mtb* infection of osteoclasts (Liu, Jia et al. 2015, Liu, Zhou et al. 2020). A fascinating aspect of the increase in OCL frequency not touched on in this project was the cell biology behind this process. For instance, the cytoskeleton remodelling, as our transcriptome analysis of OCLs generated from BM cells of BCG-infected mice unveiled rearrangement of cytoskeleton remodelling in infected OCLs (table 5.4). The cytoskeleton is a

tempting therapeutic target to inhibit aberrant osteoclast activity. The current therapeutic options that target the cytoskeleton are limited by their side effects. For example, current treatments of osteoporosis, Denosumab and biphosphates, work by inhibiting differentiation or causing apoptosis of osteoclasts but also inhibit bone forming activities of osteoblasts (Blangy, Bompard et al. 2020). Targeting the osteoclast cytoskeleton via the αVβ3 (integrin receptor for vitronectin) to control osteoclast activity may be one such approach (Blangy, Bompard et al. 2020), and thus investigating the mechanics of the osteoclast cytoskeleton during pathologies is important. Particularly, a selective inhibitor of αvβ3 had successfully made it to phase 1 clinical trial stage, where its use helped protect women from postmenopausal bone loss by diminishing osteoclast activity (Murphy, Cerchio et al. 2005).

We also employed μCT to quantify parameters of porosity and thickness, which directly relate to bone strength, in BCG-infected mice bones. BCG infection increased epiphysis and diaphysis porosity of the mouse femur, along with a significant reduction in the average thickness of the epiphysis (figures 4.21, 4.22). We believe this is the first time that μCT has been used to image the femurs from BCG infected mice. In *S. aureus* infected mice, μCT analysis demonstrated osteolysis and bone loss (Li, Chen et al. 2022). Intriguingly, μCT performed on SARS-CoV-2-infected hamsters showed significant decreases in bone trabeculae volume at the proximal metaphysis of the tibia (Qiao, Lau et al. 2022). We did not investigate the tibia in our μCT experiments. Ideally, live mice infected with BCG/*Mtb* would be subject to μCT across a time course which would give more insight into the temporal changes during infection, as well as changes across different sites in the skeleton. As our μCT experiments were performed in collaboration with Warwick Manufacturing Group, we did not have the necessary permissions for live animals with this equipment at the time.

Transcriptomic profiling of OCLs infected with BCG *in vitro* and those generated from BM cells of *in vivo* BCG-infected mice in chapter 5 led to the finding that, in both scenarios, genes related to the cell death processes were differentially regulated (figure 5.4F, table 5.2, figure 5.8B, table 5.4). However, we found

disparity viz. *in vitro* data showed a downregulation of genes regulating cell death upon BCG infection while *in vivo* data showed an upregulation of genes regulating apoptotic processes. This could be due to the direct effect of BCG on OCLs in *in vitro* experiments, compared to the *in vivo* dataset where OCLs were differentiated for 7 days *in vitro* from BM cells of BCG-infected mice. If we were able to extract and sort osteoclasts directly from bone tissue, we might have observed more stark differences.

Mtb has been shown to evade clearance by inhibiting host macrophage apoptosis via several anti-apoptotic virulence factors including SodA, NuoG, Eis, Rv3364c, and Rv3033 (Edwards, Cynamon et al. 2001, Velmurugan, Chen et al. 2007, Miller, Velmurugan et al. 2010, Shin, Jeon et al. 2010, Zhang, Lu et al. 2018). These anti-apoptotic virulence factors exert their functions by limiting host ROS production, inhibiting the mitochondrial pathway, or the TNF-α-mediated pathway. *Mtb* also modulates the host by way of affecting the expression of Mg^{2+}/Mn^{2+}-dependent 1A (PPM1A), a protein phosphatase involved in innate immunity in macrophages, to block apoptosis (Sun 2016, Schaaf, 2017). Furthermore, *Mtb* targets host eicosanoid Lipoxin A4 (LTA_4), which inhibits pro-apoptotic PGE2 biosynthesis and cyclooxygenase 2 (COX2), resulting in necrosis rather than apoptosis (Chen, Divangahi et al. 2008). Furthermore, *Mtb* mediated decreased apoptosis in THP-1 and alveolar macrophages has been found to be attenuated during infection of macrophages by BCG (Riendeau 2003).

This intriguing tempering of apoptotic cell death has been less defined in *Mtb* / BCG infected osteoclasts. We have shown, through Annexin V/PI staining, that early and late-stage apoptosis (along with necrosis) was reduced in BCG infected OCLs (figure 5.10). This was supported through evidence of reduced caspase-3/7 activity and protein accumulation of inactive procaspase-3 in BCG infected OCLs (figure 5.11). Reduction of apoptosis in *Mtb*-infected OCs has been shown previously by Liu *et al.* where they indicate an induction of autophagy via the increased expression level of TNF-α, with the use of immunoblotting, RT-qPCR, transmission electron microscopy and TUNEL staining to detect autophagy and

apoptosis in lesions from patients with osteoarticular TB compared with osteoarthritis samples (Liu, Zhou et al. 2020).

As signalling pathways of cell death overlap, we probed pyroptosis as well as the NLRP3 inflammasome in our experiments. Pyroptosis is a well characterised mode of cell death triggered by the NLRP3 inflammasome and results in cleavage of caspase-1 and pro- IL-1β and pro-IL-18 into their active forms. Pyroptosis and NLRP3 involvement in BCG-infected OCLs was investigated through a caspase-1 activity assay, IL-1β cytokine release and immunoblots for NLRP3 and ASC. We found reduced caspase-1 activity upon infection along with no release of proinflammatory IL-1β (figure 5.12). Along with this, we found non-significant accumulation of protein levels of NLRP3 and ASC upon infection (figure 5.13). To investigate further into the role NLRP3 plays in mycobacterial infection, we used NLRP3 deficient mice to link our findings to BCG-mediated osteoclastogenesis. Indeed, we found a role of NLRP3 in BCG-induced osteoclastogenesis of OCLs (figure 5.14). This was evidenced through the fact that OCLs from $NLRP3^{-/-}$ mice did not display an increase in ≥3N OCL frequency upon BCG infection compared to the WT mice. Importantly, NLRP3 has been linked to osteoclastogenesis previously. $NLRP3^{-/-}$ mice show attenuated OC differentiation *in vitro* (Alippe, Kress et al. 2021). Likewise, other studies show the protective role of NLRP3 deficiency on bone loss caused by cytokine or hormonal challenges, as well as aging (Youm, Grant et al. 2013, Alippe, Wang et al. 2017, Furman, Chang et al. 2017). Furthermore, ligature-induced periodontitis models of $NLRP3^{-/-}$ and WT mice showed that NLRP3 promotes alveolar bone loss through promoting OC differentiation (Chen, Yang et al. 2021).

NLRP3 and how it links to bone disorders has gained traction in recent years, although at present no studies have specifically examined this interaction regarding mycobacteria. A recent study showed that the NLRP3 inflammasome negatively regulates RANKL-induced osteoclastogenesis in murine BMMs but positively regulates it in the presence of LPS, with the use of BMMs with or without NLRP3 inflammasome inhibitors (Alam, Mae et al. 2022). Pit assays were used to show functional bone resorption, ASC speck formation was visualised to

confirm inflammasome assembly, as well as ELISA and RT-qPCR for IL-1β levels and cytotoxicity to investigate pyroptotic cell death (Alam, Mae et al. 2022).

Our study links mycobacterial infection of the bone with NLRP3. As well as a positive role of NLRP3 in BCG mediated osteoclastogenesis, we found NLRP3 to be involved in the production of several cytokines and chemokines. Luminex analysis on supernatants from WT and NLRP3$^{-/-}$ BCG-infected OCLs showed that BCG infected NLRP3$^{-/-}$ OCLs did not show as high of a release in IL-6, CXCL1, CCL5, TNF-α, IL-10, CCL11 and CCL3 as in WT BCG-infected OCLs. This was most notable in CXCL1 (figure 5.15). CXCL1 is recognised by its G-protein-coupled receptor CXCR2 (also recognising chemokine CXCL2) and notably is another activator of the NLRP3 inflammasome. CXCL1 (and CXCL2) act on CXCR2 activate NLRP3 in a PKCμ and ILK dependent manner (Boro and Balaji 2017).

These findings linking mycobacterial infection of the bone with the NLRP3 inflammasome would of course first have to be validated in *Mtb.* The remaining questions about the involvement of the NLRP3 inflammasome relate to how the components NLRP3 and ASC are activated whilst dampening the overall activity of the NLRP3 inflammasome. Other methods could be used to confirm the NLRP3 inflammasome is dampened upon infection. Visualisation of ASC oligomers ('specks') with immunofluorescence or quantification with flow cytometry are often-used tools to quantify NLRP3 activation, and the formation of these oligomers precede pyroptotic cell death (Beilharz, De Nardo et al. 2016). Immunofluorescence can also give insight into NLRP3 localisation within the cell – interestingly, under some conditions NLRP3 is localised on the mitochondrial membranes for optimal activation (Beilharz, De Nardo et al. 2016, Zito, Buscetta et al. 2020).

Signal 1 which induces the activation of NF-kB and genes *NLRP3, ASC, PRO-IL-1β,* and *PRO-IL-18* under NF-κB control, is also involved in the post-translational modifications (PTMs) that confer NLRP3 into its active state (Yang, Liu et al. 2017). These PTMs could be investigated. So could the involvement of the second signal, including K^+ efflux and Ca^{2+} influx. Inhibition of Ca^{2+} signalling is seen in

Mtb infected human macrophages and mediates Ca^{2+} efflux (Malik, Denning et al. 2000). A calcium mobilisation assay could thus be performed in *Mtb* infected OCLs to investigate if calcium signalling is linked to the perturbation of the NLRP3 inflammasome.

To summarise, our data shows that bone TB, which is characterised by chronic inflammation and mass bone resorption, is driven by (1) the induction of osteoclastogenesis or multinucleation of OCPs (2) inhibition of apoptosis which lengthens the lifespan of the OC to mediate increased resorption (3) activation of the NLRP3 inflammasome components but dampening of the overall NLRP3 inflammasome activity which is beneficial to the intracellular survival of mycobacteria, as has been shown in *Mtb* infection of macrophages (Rastogi 2022).

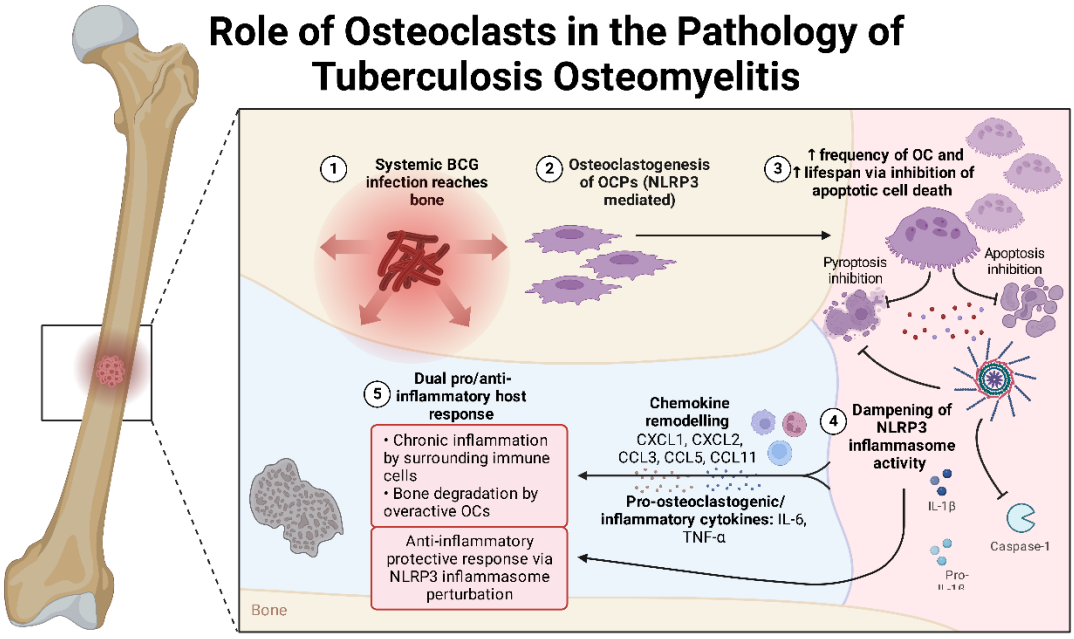

Figure 6.1 Working hypothesis for mycobacterial mediated pathogenic bone resorption in tuberculosis osteomyelitis

Dual response of host osteoclast cell in response to mycobacterial infection. 1. Mycobacteria reaches the bone marrow. 2. Mycobacteria directly or indirectly induces multinucleation and fusion of OCPs, inducing osteoclastogenesis. 3. The resulting increase in osteoclast frequency results in an increase in osteoclast-mediated bone resorption. Lifespan of the osteoclast is increased by inhibition of cell death by apoptosis and pyroptosis. 4. Inhibition of pyroptosis is due to the dampening of NLRP3 inflammasome activity, which is also evidenced through a

lack of IL-1β secretion. 5. Pro/anti-inflammatory host response with a stronger overall pro-inflammatory response, evidenced by aberrant bone resorption.

6.1 Limitations of Study

A major limitation of this study was the use of BCG as a model for *Mtb.* BCG can be handled in a BSL2 laboratory and mitigates health and safety risks. Although BCG and *Mtb* share 99 % of their genome sequence, BCG contains genomic modifications that confer its lack of virulence. For example, BCG does not contain Region of Difference 1 (*RD1*) which encodes the ESX-1 system. The ESX-1 secretion system is indispensable for the secretion of CFP-10/ESAT-6 virulence factors (Guo, Xue et al. 2012). Although BCG lacks this system, it is noted that the use of BCG as a model captures the general metabolic processes crucial for intracellular survival, such as the induction of the glyoxylate shunt, methyl citrate cycle, cholesterol catabolism, and iron homeostasis signatures upon macrophage infection (Medley, Goff et al. 2022). This project intended to incorporate the use of *Mtb* but due to the unfortunate timing of BSL3 closures at both Warwick and A*STAR during my project timeline, along with the advent of the COVID-19 pandemic, this was not feasible.

Although murine primary OCLs are a very good model for osteoclasts, the gold standard would be human derived osteoclasts. Ideally, we could have worked with bone TB patient samples and directly isolate osteoclasts.

Our *in vivo* infection model uses an intravenous injection of BCG to induce systemic infection to allow BCG to migrate to the bone where CFU could be recovered from the BM. Obviously, dissemination of *Mtb* to the bones in EPTB is secondary to the primary infection site of the lungs. In order to replicate this in mice, we could have used an aerosol model to induce pulmonary TB and then study the effects on the bone, but this method does not guarantee the bacteria will interact with the bone cells specifically.

Another unfortunate limitation of this study includes the small number of OCLs with ≥3N recovered after sorting by FACS. This means that studies using larger numbers of cells (as needed for protein and other studies) were not feasible. Single cell RNA-seq (sc-RNA seq) in conjunction with sc-ATAC-seq was supposed to be performed on ≥3N OCLs from *in vivo* infected mice to unravel epigenomic and transcriptomic changes. However, after sorting, there were only enough cells to perform sc-ATAC-seq. Due to a lack of data in the literature to annotate our sc-ATAC-seq to, our analysis reached a bottleneck, and we could not annotate the clusters and complete the data analysis in the time frame of this project.

6.2 Future Directions

Even with the use of BCG, my project helps shed light on its effects on the bone. The interest in BCG in conjunction with the concept of trained immunity is a hot topic in recent years in light of the COVID-19 pandemic, especially as it has been reported that BCG vaccination could decrease suspensibility to respiratory tract infections and boost long term innate immunity (O'Neill and Netea 2020).

Trained immunity specifically refers to the long-term boost in innate immune cell (monocytes, macrophages, dendritic cells, NK cells, etc) responses as a result of vaccination, infection or antigen exposure. Examples include BCG, *Candida albicans*, β-glucan (a polysaccharide of fungal cell walls), as well as LPS. It involves the rewiring of HSCs cells of the myeloid lineage in the BM or in circulation through signalling pathways, along with the rewiring of metabolism and epigenetic modelling. This exposure strengthens the host cell response to a secondary infection (Cumming, Addicott et al. 2018).

BCG vaccination has been found to induce trained immunity in the monocytes from mice (Kaufmann 2018) and humans (Cirovic 2020). A future direction this project could take is to delve into whether osteoclasts from BCG-immunised mice display this aspect of trained immunity. To do this, mice would receive *in vivo* training via inoculation with BCG for a determined amount of time (e.g. 1 month),

then the BM would be harvested and differentiated into OCLs and receive an *ex vivo* challenge with a second stimulus such as virulent *Mtb* / LPS. If the cells undergo sorting to purify ≥3N cells, a larger number of mice could be pooled together to generate more ≥3N OCLs. Then, ATAC-seq or ChIP-seq would be the appropriate method(s) to employ in order to unravel epigenetic changes by identifying the state of open chromatin. Metabolic rewiring of OCLs could be performed using Seahorse, which measures oxygen consumption rate (OCR) and extracellular acidification rate (ECAR) of live cells - OCR and ECAR rates are key indicators of mitochondrial respiration and glycolysis. Increased glycolysis is a hallmark of BCG-trained monocytes, but metabolic remodelling signatures of other tissue-specific innate immune cells is lacking (Arts, Joosten et al. 2016, Zahalka, Starkl et al. 2022). As OCs behave like innate immune cells in various ways, this novel insight would be a valuable contribution to the field of osteoimmunology and build on our understanding of OC participation in immunity.

Another interesting add on to studying the link between NLRP3 and pathogenic bone loss due to mycobacterial infection, would be to use μCT to ascertain the differences in bone architecture between WT and NLRP3$^{-/-}$ *in vivo Mtb* infected mice.

In conclusion, this project has been successful in highlighting several phenomena associated with mycobacterial infection of the bone, with the use of BCG as a model. Our findings help reveal underlying molecular mechanisms of mycobacterial survival and offer many suggestions for further study.

Chapter 7 Bibliography

Abdurrahman, S. T., N. Emenyonu, O. J. Obasanya, L. Lawson, R. Dacombe, M. Muhammad, O. Oladimeji and L. E. Cuevas (2014). "The hidden costs of installing Xpert machines in a tuberculosis high-burden country: experiences from Nigeria." Pan Afr Med J 18: 277.

Agashe, V. M., A. N. Johari, M. Shah, R. Anjum, C. Romano, L. Drago, H. K. Sharma and T. Benzakour (2020). "Diagnosis of Osteoarticular Tuberculosis: Perceptions, Protocols, Practices, and Priorities in the Endemic and Non-Endemic Areas of the World-A WAIOT View." Microorganisms 8(9).

Aitken, C. J., J. M. Hodge, Y. Nishinaka, T. Vaughan, J. Yodoi, C. J. Day, N. A. Morrison and G. C. Nicholson (2004). "Regulation of human osteoclast differentiation by thioredoxin binding protein-2 and redox-sensitive signalling." J Bone Miner Res 19(12): 2057-2064.

Akchurin, T., T. Aissiou, N. Kemeny, E. Prosk, N. Nigam and S. V. Komarova (2008). "Complex dynamics of osteoclast formation and death in long-term cultures." PLoS One 3(5): e2104.

Alam, I., D. L. Koller, T. Cañete, G. Blázquez, R. López-Aumatell, E. Martínez-Membrives, S. Díaz-Morán, A. Tobeña, A. Fernández-Teruel, P. Stridh, M. Diez, T. Olsson, M. Johannesson, A. Baud, M. J. Econs and T. Foroud (2014). "High-resolution genome screen for bone mineral density in heterogeneous stock rat." J Bone Miner Res 29(7): 1619-1626.

Alam, M. I., M. Mae, F. Farhana, M. Oohira, Y. Yamashita, Y. Ozaki, E. Sakai and A. Yoshimura (2022). "NLRP3 Inflammasome Negatively Regulates RANKL-Induced Osteoclastogenesis of Mouse Bone Marrow Macrophages but Positively Regulates It in the Presence of Lipopolysaccharides." International Journal of Molecular Sciences 23(11): 6096.

Alippe, Y., D. Kress, B. Ricci, K. Sun, T. Yang, C. Wang, J. Xiao, Y. Abu-Amer and G. Mbalaviele (2021). "Actions of the NLRP3 and NLRC4 inflammasomes overlap in bone resorption." Faseb j 35(9): e21837.

Alippe, Y., C. Wang, B. Ricci, J. Xiao, C. Qu, W. Zou, D. V. Novack, Y. Abu-Amer, R. Civitelli and G. Mbalaviele (2017). "Bone matrix components activate the NLRP3

inflammasome and promote osteoclast differentiation." Scientific Reports 7(1): 6630.

Alnaeeli, M., J. M. Penninger and Y. T. Teng (2006). "Immune interactions with CD4+ T cells promote the development of functional osteoclasts from murine CD11c+ dendritic cells." J Immunol 177(5): 3314-3326.

Alonso-Pérez, A., E. Franco-Trepat, M. Guillán-Fresco, A. Jorge-Mora, V. López, J. Pino, O. Gualillo and R. Gómez (2018). "Role of Toll-Like Receptor 4 on Osteoblast Metabolism and Function." Frontiers in Physiology 9.

AlQranei, M. S., L. T. Senbanjo, H. Aljohani, T. Hamza and M. A. Chellaiah (2021). "Lipopolysaccharide- TLR-4 Axis regulates Osteoclastogenesis independent of RANKL/RANK signalling." BMC Immunology 22(1): 23.

Amaral, E. P., D. L. Costa, S. Namasivayam, N. Riteau, O. Kamenyeva, L. Mittereder, K. D. Mayer-Barber, B. B. Andrade and A. Sher (2019). "A major role for ferroptosis in Mycobacterium tuberculosis-induced cell death and tissue necrosis." J Exp Med 216(3): 556-570.

Amaral, E. P., N. Riteau, M. Moayeri, N. Maier, K. D. Mayer-Barber, R. M. Pereira, S. L. Lage, A. Kubler, W. R. Bishai, M. R. D'Império-Lima, A. Sher and B. B. Andrade (2018). "Lysosomal Cathepsin Release Is Required for NLRP3-Inflammasome Activation by Mycobacterium tuberculosis in Infected Macrophages." Front Immunol 9: 1427.

Amarasekara, D. S., H. Yun, S. Kim, N. Lee, H. Kim and J. Rho (2018). "Regulation of Osteoclast Differentiation by Cytokine Networks." Immune Netw 18(1): e8.

Andersen, P., M. E. Munk, J. M. Pollock and T. M. Doherty (2000). "Specific immune-based diagnosis of tuberculosis." Lancet 356(9235): 1099-1104.

Anes, E., M. P. Kühnel, E. Bos, J. Moniz-Pereira, A. Habermann and G. Griffiths (2003). "Selected lipids activate phagosome actin assembly and maturation resulting in killing of pathogenic mycobacteria." Nat Cell Biol 5(9): 793-802.

Anes, E., P. Peyron, L. Staali, L. Jordao, M. G. Gutierrez, H. Kress, M. Hagedorn, I. Maridonneau-Parini, M. A. Skinner, A. G. Wildeman, S. A. Kalamidas, M. Kuehnel and G. Griffiths (2006). "Dynamic life and death interactions between Mycobacterium smegmatis and J774 macrophages." Cell Microbiol 8(6): 939-960.

Ansari, S., M. F. Amanullah, K. Ahmad and R. K. Rauniyar (2013). "Pott's Spine: Diagnostic Imaging Modalities and Technology Advancements." N Am J Med Sci 5(7): 404-411.

Arai, F., T. Miyamoto, O. Ohneda, T. Inada, T. Sudo, K. Brasel, T. Miyata, D. M. Anderson and T. Suda (1999). "Commitment and differentiation of osteoclast precursor cells by the sequential expression of c-Fms and receptor activator of nuclear factor kappaB (RANK) receptors." J Exp Med 190(12): 1741-1754.

Arnett, T. R. and D. W. Dempster (1986). "Effect of pH on bone resorption by rat osteoclasts *in vitro*." Endocrinology 119(1): 119-124.

Arnvig, K. B., I. Comas, N. R. Thomson, J. Houghton, H. I. Boshoff, N. J. Croucher, G. Rose, T. T. Perkins, J. Parkhill, G. Dougan and D. B. Young (2011). "Sequence-based analysis uncovers an abundance of non-coding RNA in the total transcriptome of Mycobacterium tuberculosis." PLoS Pathog 7(11): e1002342.

Arts, R. J., L. A. Joosten and M. G. Netea (2016). "Immunometabolic circuits in trained immunity." Semin Immunol 28(5): 425-430.

Avalle, L., A. Camporeale, G. Morciano, N. Caroccia, E. Ghetti, V. Orecchia, D. Viavattene, C. Giorgi, P. Pinton and V. Poli (2019). "STAT3 localizes to the ER, acting as a gatekeeper for ER-mitochondrion Ca(2+) fluxes and apoptotic responses." Cell Death Differ 26(5): 932-942.

Ayed, H. (2018). "Extrapulmonary Tuberculosis: Update on the Epidemiology, Risk Factors and Prevention Strategies " International Journal of Tropical Diseases.

Baykan, A. H., H. S. Sayiner, E. Aydin, M. Koc, I. Inan and S. M. Erturk (2022). "Extrapulmonary tuberculosıs: an old but resurgent problem." Insights into Imaging 13(1): 39.

Beckwith, K. S., M. S. Beckwith, S. Ullmann, R. S. Sætra, H. Kim, A. Marstad, S. E. Åsberg, T. A. Strand, M. Haug, M. Niederweis, H. A. Stenmark and T. H. Flo (2020). "Plasma membrane damage causes NLRP3 activation and pyroptosis during Mycobacterium tuberculosis infection." Nature Communications 11(1): 2270.

Beilharz, M., D. De Nardo, E. Latz and B. S. Franklin (2016). "Measuring NLR Oligomerization II: Detection of ASC Speck Formation by Confocal Microscopy and Immunofluorescence." Methods Mol Biol 1417: 145-158.

Bettencourt, P., S. Marion, D. Pires, L. F. Santos, C. Lastrucci, N. Carmo, J. Blake, V. Benes, G. Griffiths, O. Neyrolles, G. Lugo-Villarino and E. Anes (2013). "Actin-binding protein regulation by microRNAs as a novel microbial strategy to modulate phagocytosis by host cells: the case of N-Wasp and miR-142-3p." Front Cell Infect Microbiol 3: 19.

Binesh, F., S. T. Zahir and T. R. Bovanlu (2013). "Isolated cerebellar tuberculoma mimicking posterior cranial fossa tumour." BMJ Case Rep 2013.

Blangy, A., G. Bompard, D. Guerit, P. Marie, J. Maurin, A. Morel and V. Vives (2020). "The osteoclast cytoskeleton – current understanding and therapeutic perspectives for osteoporosis." Journal of Cell Science 133(13).

Blin-Wakkach, C., A. Wakkach, P. M. Sexton, N. Rochet and G. F. Carle (2004). "Hematological defects in the oc/oc mouse, a model of infantile malignant osteopetrosis." Leukemia 18(9): 1505-1511.

Boabaid, F., P. S. Cerri and E. Katchburian (2001). "Apoptotic bone cells may be engulfed by osteoclasts during alveolar bone resorption in young rats." Tissue Cell 33(4): 318-325.

Boissy, P., F. Saltel, C. Bouniol, P. Jurdic and I. Machuca-Gayet (2002). "Transcriptional Activity of Nuclei in Multinucleated Osteoclasts and Its Modulation by Calcitonin." Endocrinology 143(5): 1913-1921.

Boro, M. and K. N. Balaji (2017). "CXCL1 and CXCL2 Regulate NLRP3 Inflammasome Activation via G-Protein-Coupled Receptor CXCR2." J Immunol 199(5): 1660-1671.

Boyde, A., N. N. Ali and S. J. Jones (1984). "Resorption of dentine by isolated osteoclasts *in vitro*." Br Dent J 156(6): 216-220.

Broderick, C., S. Hopkins, D. J. F. Mack, W. Aston, R. Pollock, J. A. Skinner and S. Warren (2018). "Delays in the diagnosis and treatment of bone and joint tuberculosis in the United Kingdom." Bone Joint J 100-b(1): 119-124.

Brosch, R., S. V. Gordon, M. Marmiesse, P. Brodin, C. Buchrieser, K. Eiglmeier, T. Garnier, C. Gutierrez, G. Hewinson, K. Kremer, L. M. Parsons, A. S. Pym, S. Samper, D. van Soolingen and S. T. Cole (2002). "A new evolutionary scenario for the Mycobacterium tuberculosis complex." Proc Natl Acad Sci U S A 99(6): 3684-3689.

Butler, R. E., P. Brodin, J. Jang, M. S. Jang, B. D. Robertson, B. Gicquel and G. R. Stewart (2012). "The balance of apoptotic and necrotic cell death in Mycobacterium tuberculosis infected macrophages is not dependent on bacterial virulence." PLoS One 7(10): e47573.

Cao, Y., I. D. Jansen, S. Sprangers, J. Stap, P. J. Leenen, V. Everts and T. J. de Vries (2016). "IL-1β differently stimulates proliferation and multinucleation of distinct mouse bone marrow osteoclast precursor subsets." J Leukoc Biol 100(3): 513-523.

Cavalcante, G. C., A. P. Schaan, G. F. Cabral, M. N. Santana-da-Silva, P. Pinto, A. F. Vidal and Â. Ribeiro-dos-Santos (2019) "A Cell's Fate: An Overview of the Molecular Biology and Genetics of Apoptosis." International Journal of Molecular Sciences 20 DOI: 10.3390/ijms20174133.

Chabadel, A., I. Bañon-Rodríguez, D. Cluet, B. B. Rudkin, B. Wehrle-Haller, E. Genot, P. Jurdic, I. M. Anton and F. Saltel (2007). "CD44 and beta3 integrin organize two functionally distinct actin-based domains in osteoclasts." Mol Biol Cell 18(12): 4899-4910.

Chambers, T. J. (1979). "Phagocytosis and trypsin-resistant glass adhesion by osteoclasts in culture." J Pathol 127(2): 55-60.

Chambers, T. J., P. A. Revell, K. Fuller and N. A. Athanasou (1984). "Resorption of bone by isolated rabbit osteoclasts." J Cell Sci 66: 383-399.

Chandra, P., S. Ghanwat, S. K. Matta, S. S. Yadav, M. Mehta, Z. Siddiqui, A. Singh and D. Kumar (2015). "Mycobacterium tuberculosis Inhibits RAB7 Recruitment to Selectively Modulate Autophagy Flux in Macrophages." Sci Rep 5: 16320.

Chang, E. J., H. J. Kim, J. Ha, H. J. Kim, J. Ryu, K. H. Park, U. H. Kim, Z. H. Lee, H. M. Kim, D. E. Fisher and H. H. Kim (2007). "Hyaluronan inhibits osteoclast differentiation via Toll-like receptor 4." J Cell Sci 120(Pt 1): 166-176.

Charles, J. F. and A. O. Aliprantis (2014). "Osteoclasts: more than 'bone eaters'." Trends Mol Med 20(8): 449-459.

Charles, J. F., L. Y. Hsu, E. C. Niemi, A. Weiss, A. O. Aliprantis and M. C. Nakamura (2012). "Inflammatory arthritis increases mouse osteoclast precursors with myeloid suppressor function." J Clin Invest 122(12): 4592-4605.

Chellaiah, M. A., N. Kizer, R. Biswas, U. Alvarez, J. Strauss-Schoenberger, L. Rifas, S. R. Rittling, D. T. Denhardt and K. A. Hruska (2003). "Osteopontin deficiency

produces osteoclast dysfunction due to reduced CD44 surface expression." Mol Biol Cell 14(1): 173-189.
Chen, M., M. Divangahi, H. Gan, D. S. Shin, S. Hong, D. M. Lee, C. N. Serhan, S. M. Behar and H. G. Remold (2008). "Lipid mediators in innate immunity against tuberculosis: opposing roles of PGE2 and LXA4 in the induction of macrophage death." J Exp Med 205(12): 2791-2801.
Chen, Y., Q. Yang, C. Lv, Y. Chen, W. Zhao, W. Li, H. Chen, H. Wang, W. Sun and H. Yuan (2021). "NLRP3 regulates alveolar bone loss in ligature-induced periodontitis by promoting osteoclastic differentiation." Cell Prolif 54(2): e12973.
Cheng, X., C. Yin, Y. Deng and Z. Li (2022). "Exogenous adenosine activates A2A adenosine receptor to inhibit RANKL-induced osteoclastogenesis via AP-1 pathway to facilitate bone repair." Molecular Biology Reports 49(3): 2003-2014.
Cheng, Z. and Y. Li (2007). "What is responsible for the initiating chemistry of iron-mediated lipid peroxidation: an update." Chem Rev 107(3): 748-766.
Chevalier, C., M. Çolakoğlu, J. Brun, C. Thouverey, N. Bonnet, S. Ferrari and M. Trajkovski (2021). "Primary mouse osteoblast and osteoclast culturing and analysis." STAR Protocols 2(2): 100452.
Chiu, Y. H. and C. T. Ritchlin (2016). "DC-STAMP: A Key Regulator in Osteoclast Differentiation." J Cell Physiol 231(11): 2402-2407.
Cirovic, B., L. C. J. de Bree, L. Groh, B. A. Blok, J. Chan, W. van der Velden, M. E. J. Bremmers, R. van Crevel, K. Händler, S. Picelli, J. Schulte-Schrepping, K. Klee, M. Oosting, V. Koeken, J. van Ingen, Y. Li, C. S. Benn, J. L. Schultze, L. A. B. Joosten, N. Curtis, M. G. Netea and A. Schlitzer (2020). "BCG Vaccination in Humans Elicits Trained Immunity via the Hematopoietic Progenitor Compartment." Cell Host Microbe 28(2): 322-334.e325.
Colonne, P. M., C. G. Winchell and D. E. Voth (2016). "Hijacking Host Cell Highways: Manipulation of the Host Actin Cytoskeleton by Obligate Intracellular Bacterial Pathogens." Front Cell Infect Microbiol 6: 107.
Copp, D. H. and B. Cheney (1962). "Calcitonin-a hormone from the parathyroid which lowers the calcium-level of the blood." Nature 193: 381-382.
Coury, F., O. Peyruchaud and I. Machuca-Gayet (2019). "Osteoimmunology of Bone Loss in Inflammatory Rheumatic Diseases." Front Immunol 10: 679.

Croucher, P. I., M. M. McDonald and T. J. Martin (2016). "Bone metastasis: the importance of the neighbourhood." Nat Rev Cancer 16(6): 373-386.
Cumming, B. M., K. W. Addicott, J. H. Adamson and A. J. C. Steyn (2018). "Mycobacterium tuberculosis induces decelerated bioenergetic metabolism in human macrophages." eLife 7: e39169.
Daniel, T. M. (2006). "The history of tuberculosis." Respir Med 100(11): 1862-1870.
Dapunt, U., T. Giese, S. Stegmaier, A. Moghaddam and G. M. Hänsch (2016). "The osteoblast as an inflammatory cell: production of cytokines in response to bacteria and components of bacterial biofilms." BMC Musculoskeletal Disorders 17(1): 243.
Dapunt, U., S. Maurer, T. Giese, M. M. Gaida and G. M. Hänsch (2014). "The macrophage inflammatory proteins MIP1α (CCL3) and MIP2α (CXCL2) in implant-associated osteomyelitis: linking inflammation to bone degradation." Mediators Inflamm 2014: 728619.
Das, B., S. S. Kashino, I. Pulu, D. Kalita, V. Swami, H. Yeger, D. W. Felsher and A. Campos-Neto (2013). "CD271(+) bone marrow mesenchymal stem cells may provide a niche for dormant Mycobacterium tuberculosis." Sci Transl Med 5(170): 170ra113.
Das, B., S. S. Kashino, I. Pulu, D. Kalita, V. Swami, H. Yeger, D. W. Felsher and A. Campos-Neto (2013). "CD271(+) bone marrow mesenchymal stem cells may provide a niche for dormant Mycobacterium tuberculosis." Sci Transl Med 5(170): 170ra113.
Day, T. F., X. Guo, L. Garrett-Beal and Y. Yang (2005). "Wnt/beta-catenin signalling in mesenchymal progenitors controls osteoblast and chondrocyte differentiation during vertebrate skeletogenesis." Dev Cell 8(5): 739-750.
Deng, Z., Q. Zhang, Z. Zhao, Y. Li, X. Chen, Z. Lin, Z. Deng, J. Liu, L. Duan, D. Wang and W. Li (2021). "Crosstalk between immune cells and bone cells or chondrocytes." International Immunopharmacology 101: 108179.
Derrick, S. C. and S. L. Morris (2007). "The ESAT6 protein of Mycobacterium tuberculosis induces apoptosis of macrophages by activating caspase expression." Cell Microbiol 9(6): 1547-1555.

Dolma, S., S. L. Lessnick, W. C. Hahn and B. R. Stockwell (2003). "Identification of genotype-selective antitumor agents using synthetic lethal chemical screening in engineered human tumor cells." Cancer Cell 3(3): 285-296.

Dorhoi, A., G. Nouailles, S. Jörg, K. Hagens, E. Heinemann, L. Pradl, D. Oberbeck-Müller, M. A. Duque-Correa, S. T. Reece, J. Ruland, R. Brosch, J. Tschopp, O. Gross and S. H. Kaufmann (2012). "Activation of the NLRP3 inflammasome by Mycobacterium tuberculosis is uncoupled from susceptibility to active tuberculosis." Eur J Immunol 42(2): 374-384.

Du, Y. and Z. Guo (2022). "Recent progress in ferroptosis: inducers and inhibitors." Cell Death Discovery 8(1): 501.

Dudareva, M., A. J. Hotchen, J. Ferguson, S. Hodgson, M. Scarborough, B. L. Atkins and M. A. McNally (2019). "The microbiology of chronic osteomyelitis: Changes over ten years." J Infect 79(3): 189-198.

Durham, E., Y. Zhang, A. LaRue, A. Bradshaw and J. Cray (2020). "Selective serotonin reuptake inhibitors (SSRI) affect murine bone lineage cells." Life Sci 255: 117827.

Dutta, R. K., M. Kathania, M. Raje and S. Majumdar (2012). "IL-6 inhibits IFN-γ induced autophagy in Mycobacterium tuberculosis H37Rv infected macrophages." Int J Biochem Cell Biol 44(6): 942-954.

Edwards, K. M., M. H. Cynamon, R. K. Voladri, C. C. Hager, M. S. DeStefano, K. T. Tham, D. L. Lakey, M. R. Bochan and D. S. Kernodle (2001). "Iron-cofactored superoxide dismutase inhibits host responses to Mycobacterium tuberculosis." Am J Respir Crit Care Med 164(12): 2213-2219.

Eklund, D., A. Welin, H. Andersson, D. Verma, P. Söderkvist, O. Stendahl, E. Särndahl and M. Lerm (2014). "Human gene variants linked to enhanced NLRP3 activity limit intramacrophage growth of Mycobacterium tuberculosis." J Infect Dis 209(5): 749-753.

Etna, M. P., A. Sinigaglia, A. Grassi, E. Giacomini, A. Romagnoli, M. Pardini, M. Severa, M. Cruciani, F. Rizzo, E. Anastasiadou, B. Di Camillo, L. Barzon, G. M. Fimia, R. Manganelli and E. M. Coccia (2018). "Mycobacterium tuberculosis-induced miR-155 subverts autophagy by targeting ATG3 in human dendritic cells." PLoS Pathog 14(1): e1006790.

Evans, K. E. and S. W. Fox (2007). "Interleukin-10 inhibits osteoclastogenesis by reducing NFATc1 expression and preventing its translocation to the nucleus." BMC Cell Biol 8: 4.

Fatima, S., S. S. Kamble, V. P. Dwivedi, D. Bhattacharya, S. Kumar, A. Ranganathan, L. Van Kaer, S. Mohanty and G. Das (2020). "Mycobacterium tuberculosis programs mesenchymal stem cells to establish dormancy and persistence." J Clin Invest 130(2): 655-661.

Ferguson, J. S., J. J. Weis, J. L. Martin and L. S. Schlesinger (2004). "Complement protein C3 binding to Mycobacterium tuberculosis is initiated by the classical pathway in human bronchoalveolar lavage fluid." Infect Immun 72(5): 2564-2573.

Fernandes-Alnemri, T., J. Wu, J. W. Yu, P. Datta, B. Miller, W. Jankowski, S. Rosenberg, J. Zhang and E. S. Alnemri (2007). "The pyroptosome: a supramolecular assembly of ASC dimers mediating inflammatory cell death via caspase-1 activation." Cell Death Differ 14(9): 1590-1604.

Ferrier, J., S. L. Xia, E. Lagan, J. E. Aubin and J. N. Heersche (1994). "Displacement and translocation of osteoblast-like cells by osteoclasts." J Bone Miner Res 9(9): 1397-1405.

Fessler, J., R. Husic, V. Schwetz, E. Lerchbaum, F. Aberer, P. Fasching, A. Ficjan, B. Obermayer-Pietsch, C. Duftner, W. Graninger, M. H. Stradner and C. Dejaco (2018). "Senescent T-Cells Promote Bone Loss in Rheumatoid Arthritis." Front Immunol 9: 95.

Furlan, F., C. Galbiati, N. R. Jorgensen, J. E. Jensen, E. Mrak, A. Rubinacci, F. Talotta, P. Verde and F. Blasi (2007). "Urokinase plasminogen activator receptor affects bone homeostasis by regulating osteoblast and osteoclast function." J Bone Miner Res 22(9): 1387-1396.

Furman, D., J. Chang, L. Lartigue, C. R. Bolen, F. Haddad, B. Gaudilliere, E. A. Ganio, G. K. Fragiadakis, M. H. Spitzer, I. Douchet, S. Daburon, J. F. Moreau, G. P. Nolan, P. Blanco, J. Déchanet-Merville, C. L. Dekker, V. Jojic, C. J. Kuo, M. M. Davis and B. Faustin (2017). "Expression of specific inflammasome gene modules stratifies older individuals into two extreme clinical and immunological states." Nat Med 23(2): 174-184.

Gao, X., C. Wu, W. He, X. Wang, Y. Li, Y. Wang, Y. Jia, R. Yuan, H. Li and B. Zhang (2019). "DosR antigen Rv1737c induces activation of macrophages dependent on the TLR2 pathway." Cellular Immunology 344: 103947.

Garcia-Moreno, M., P. M. Jordan, K. Günther, T. Dau, C. Fritzsch, M. Vermes, A. Schoppa, A. Ignatius, B. Wildemann, O. Werz, B. Löffler and L. Tuchscherr (2022). "Osteocytes Serve as a Reservoir for Intracellular Persisting Staphylococcus aureus Due to the Lack of Defense Mechanisms." Frontiers in Microbiology 13.

Gharun, K., J. Senges, M. Seidl, A. Lösslein, J. Kolter, F. Lohrmann, M. Fliegauf, M. Elgizouli, M. Vavra, K. Schachtrup, A. L. Illert, M. Gilleron, C. J. Kirschning, A. Triantafyllopoulou and P. Henneke (2017). "Mycobacteria exploit nitric oxide-induced transformation of macrophages into permissive giant cells." EMBO reports 18(12): 2144-2159.

Gomes da Rocha Dias, A. P., B. von Amann, J. Costeira, C. Gomes and C. Bárbara (2016). "Extrapulmonary tuberculosis in HIV infected patients admitted to the hospital." European Respiratory Journal 48(suppl 60): PA2761.

Grigoriadis, A. E., M. Kennedy, A. Bozec, F. Brunton, G. Stenbeck, I. H. Park, E. F. Wagner and G. M. Keller (2010). "Directed differentiation of hematopoietic precursors and functional osteoclasts from human ES and iPS cells." Blood 115(14): 2769-2776.

Grosz, M., J. Kolter, K. Paprotka, A. C. Winkler, D. Schäfer, S. S. Chatterjee, T. Geiger, C. Wolz, K. Ohlsen, M. Otto, T. Rudel, B. Sinha and M. Fraunholz (2014). "Cytoplasmic replication of Staphylococcus aureus upon phagosomal escape triggered by phenol-soluble modulin α." Cell Microbiol 16(4): 451-465.

Grover, S., T. Sharma, Y. Singh, S. Kohli, M. P, A. Singh, T. Semmler, L. H. Wieler, K. Tedin, N. Z. Ehtesham and S. E. Hasnain (2018). "The PGRS Domain of Mycobacterium tuberculosis PE_PGRS Protein Rv0297 Is Involved in Endoplasmic Reticulum Stress-Mediated Apoptosis through Toll-Like Receptor 4." mBio 9(3).

Guérit, D., P. Marie, A. Morel, J. Maurin, C. Verollet, B. Raynaud-Messina, S. Urbach and A. Blangy (2020). "Primary myeloid cell proteomics and transcriptomics: importance of β-tubulin isotypes for osteoclast function." Journal of Cell Science 133(10).

Guo, S., R. Xue, Y. Li, S. M. Wang, L. Ren and J. J. Xu (2012). "The CFP10/ESAT6 complex of Mycobacterium tuberculosis may function as a regulator of macrophage cell death at different stages of tuberculosis infection." Med Hypotheses 78(3): 389-392.

Gutierrez, M. C., S. Brisse, R. Brosch, M. Fabre, B. Omaïs, M. Marmiesse, P. Supply and V. Vincent (2005). "Ancient origin and gene mosaicism of the progenitor of Mycobacterium tuberculosis." PLoS Pathog 1(1): e5.

Gutierrez, M. G., S. S. Master, S. B. Singh, G. A. Taylor, M. I. Colombo and V. Deretic (2004). "Autophagy is a defense mechanism inhibiting BCG and Mycobacterium tuberculosis survival in infected macrophages." Cell 119(6): 753-766.

Ha, J., H.-S. Choi, Y. Lee, H.-J. Kwon, Y.-W. Song and H.-H. Kim (2010). "CXC Chemokine Ligand 2 Induced by Receptor Activator of NF-κB Ligand Enhances Osteoclastogenesis." The Journal of Immunology 184: 4717 - 4724.

Halder, P., R. Kumar, K. Jana, S. Chakraborty, Z. Ghosh, M. Kundu and J. Basu (2015). "Gene expression profiling of Mycobacterium tuberculosis Lipoarabinomannan-treated macrophages: A role of the Bcl-2 family member A1 in inhibition of apoptosis in mycobacteria-infected macrophages." IUBMB Life 67(9): 726-736.

Hardaway, A. L., M. K. Herroon, E. Rajagurubandara and I. Podgorski (2015). "Marrow adipocyte-derived CXCL1 and CXCL2 contribute to osteolysis in metastatic prostate cancer." Clin Exp Metastasis 32(4): 353-368.

Harre, U., H. Keppeler, N. Ipseiz, A. Derer, K. Poller, M. Aigner, G. Schett, M. Herrmann and K. Lauber (2012). "Moonlighting osteoclasts as undertakers of apoptotic cells." Autoimmunity 45(8): 612-619.

Harty, R. and M. S. Jones (2021). Principles of Diagnosis and Treatment of Bone Remodeling Disorders. Clinical Foundations of Musculoskeletal Medicine: A Manual for Medical Students. R. J. Esther. Cham, Springer International Publishing: 57-65.

Hayashi, Y., Y. Okamatsu, M. Usui and M. Yamamoto (2009). "CCL7 and CCL25 promote RANKL-induced osteoclast formation." Nihon Shishubyo Gakkai Kaishi (Journal of the Japanese Society of Periodontology) 51(1): 51-61.

Hayward, S. E., K. Rustage, L. B. Nellums, M. J. van der Werf, T. Noori, D. Boccia, J. S. Friedland and S. Hargreaves (2021). "Extrapulmonary tuberculosis among migrants in Europe, 1995 to 2017." Clin Microbiol Infect 27(9): 1347.e1341-1347.e1347.

Heinemann, C., J. Adam, B. Kruppke, V. Hintze, H. P. Wiesmann and T. Hanke (2021). "How to Get Them off?-Assessment of Innovative Techniques for Generation and Detachment of Mature Osteoclasts for Biomaterial Resorption Studies." Int J Mol Sci 22(3).

Held, M. F. G., S. Hoppe, M. Laubscher, S. Mears, S. Dix-Peek, H. J. Zar and R. N. Dunn (2017). "Epidemiology of Musculoskeletal Tuberculosis in an Area with High Disease Prevalence." Asian Spine J 11(3): 405-411.

Henriksen, K., M. A. Karsdal, A. Taylor, D. Tosh and F. P. Coxon (2012). "Generation of human osteoclasts from peripheral blood." Methods Mol Biol 816: 159-175.

Heymann, D., J. Guicheux and A. V. Rousselle (2001). "Ultrastructural evidence *in vitro* of osteoclast-induced degradation of calcium phosphate ceramic by simultaneous resorption and phagocytosis mechanisms." Histol Histopathol 16(1): 37-44.

Hobolt-Pedersen, A.-S., J.-M. Delaissé and K. Søe (2014). "Osteoclast Fusion is Based on Heterogeneity Between Fusion Partners." Calcified Tissue International 95(1): 73-82.

Hoeffel, G. and F. Ginhoux (2018). "Fetal monocytes and the origins of tissue-resident macrophages." Cell Immunol 330: 5-15.

Hoshino, A., S. Hanada, H. Yamada, S. Mii, M. Takahashi, S. Mitarai, K. Yamamoto and Y. Manome (2014). "Mycobacterium tuberculosis escapes from the phagosomes of infected human osteoclasts reprograms osteoclast development via dysregulation of cytokines and chemokines." Pathogens and Disease 70(1): 28-39.

Hou, G. Q., C. Guo, G. H. Song, N. Fang, W. J. Fan, X. D. Chen, L. Yuan and Z. Q. Wang (2013). "Lipopolysaccharide (LPS) promotes osteoclast differentiation and activation by enhancing the MAPK pathway and COX-2 expression in RAW264.7 cells." Int J Mol Med 32(2): 503-510.

Houri-Haddad, Y., W. A. Soskolne, A. Halabi and L. Shapira (2007). "IL-10 Gene Transfer Attenuates P. gingivalis-induced Inflammation." Journal of Dental Research 86(6): 560-564.

Hu, Y., L. Wang, Z. Zhao, W. Lu, J. Fan, B. Gao, Z. Luo, Q. Jie, X. Shi and L. Yang (2020). "Cytokines CCL2 and CXCL1 may be potential novel predictors of early bone loss." Mol Med Rep 22(6): 4716-4724.

Huang, L., E. V. Nazarova, S. Tan, Y. Liu and D. G. Russell (2018). "Growth of Mycobacterium tuberculosis *in vivo* segregates with host macrophage metabolism and ontogeny." Journal of Experimental Medicine 215(4): 1135-1152.

Huang, Y., W. Xu and R. Zhou (2021). "NLRP3 inflammasome activation and cell death." Cell Mol Immunol 18(9): 2114-2127.

Ibáñez, L., G. Abou-Ezzi, T. Ciucci, V. Amiot, N. Belaïd, D. Obino, A. Mansour, M. Rouleau, A. Wakkach and C. Blin-Wakkach (2016). "Inflammatory Osteoclasts Prime TNFα-Producing CD4(+) T Cells and Express CX(3) CR1." J Bone Miner Res 31(10): 1899-1908.

Ikeda, T., K. Ikeda, K. Sasaki, K. Kawakami, K. Hatake, Y. Kaji, H. Norimatsu, M. Harada and J. Takahara (1998). "IL-13 as well as IL-4 induces monocytes/macrophages and a monoblastic cell line (UG3) to differentiate into multinucleated giant cells in the presence of M-CSF." Biochem Biophys Res Commun 253(2): 265-272.

Izawa, K. (2015). "[HISTOLOGICAL ANALYSIS OF BONE DESTRUCTION IN SPINAL TUBERCULOSIS]." Kekkaku 90(3): 415-420.

Jacome-Galarza, C. E. (2013). Phenotypic Characterization of Peripheral Osteoclast Precursors their Lineage Relation to Macrophages and Dendritic Cells and their Population Dynamics Influenced by Parathyroid Hormone and Inflammatory Signals. Doctor of Philosophy
University of Connecticut.

Jacome-Galarza, C. E., S.-K. Lee, J. A. Lorenzo and H. L. Aguila (2013). "Identification, characterization, and isolation of a common progenitor for osteoclasts, macrophages, and dendritic cells from murine bone marrow and periphery." Journal of Bone and Mineral Research 28(5): 1203-1213.

Jacome-Galarza, C. E., G. I. Percin, J. T. Muller, E. Mass, T. Lazarov, J. Eitler, M. Rauner, V. K. Yadav, L. Crozet, M. Bohm, P. L. Loyher, G. Karsenty, C. Waskow and F. Geissmann (2019). "Developmental origin, functional maintenance and genetic rescue of osteoclasts." Nature 568(7753): 541-545.

Jacquin, C., D. E. Gran, S. K. Lee, J. A. Lorenzo and H. L. Aguila (2006). "Identification of multiple osteoclast precursor populations in murine bone marrow." J Bone Miner Res 21(1): 67-77.

Jamwal, S. V., P. Mehrotra, A. Singh, Z. Siddiqui, A. Basu and K. V. S. Rao (2016). "Mycobacterial escape from macrophage phagosomes to the cytoplasm represents an alternate adaptation mechanism." Scientific Reports 6(1): 23089.

Jayaraman, P., I. Sada-Ovalle, T. Nishimura, A. C. Anderson, V. K. Kuchroo, H. G. Remold and S. M. Behar (2013). "IL-1β promotes antimicrobial immunity in macrophages by regulating TNFR signalling and caspase-3 activation." J Immunol 190(8): 4196-4204.

Jiang, M., L. Qi, L. Li and Y. Li (2020). "The caspase-3/GSDME signal pathway as a switch between apoptosis and pyroptosis in cancer." Cell Death Discov 6: 112.

Jiang, N., J. An, K. Yang, J. Liu, C. Guan, C. Ma and X. Tang (2021). "NLRP3 Inflammasome: A New Target for Prevention and Control of Osteoporosis?" Frontiers in Endocrinology 12.

Jiang, Q., X. Huang, W. Yu, R. Huang, X. Zhao and C. Chen (2022). "mTOR Signalling in the Regulation of CD4+ T Cell Subsets in Periodontal Diseases." Front Immunol 13: 827461.

Jilka, R. L. (2003). "Biology of the basic multicellular unit and the pathophysiology of osteoporosis." Med Pediatr Oncol 41(3): 182-185.

Jordan, L. A., M. C. Erlandsson, B. F. Fenner, R. Davies, A. K. Harvey, E. H. Choy, R. Errington, M. I. Bokarewa and A. S. Williams (2018). "Inhibition of CCL3 abrogated precursor cell fusion and bone erosions in human osteoclast cultures and murine collagen-induced arthritis." Rheumatology (Oxford) 57(11): 2042-2052.

Kang, P. B., A. K. Azad, J. B. Torrelles, T. M. Kaufman, A. Beharka, E. Tibesar, L. E. DesJardin and L. S. Schlesinger (2005). "The human macrophage mannose receptor directs Mycobacterium tuberculosis lipoarabinomannan-mediated phagosome biogenesis." J Exp Med 202(7): 987-999.

Kassem, A., C. Lindholm and U. H. Lerner (2016). "Toll-Like Receptor 2 Stimulation of Osteoblasts Mediates Staphylococcus Aureus Induced Bone Resorption and Osteoclastogenesis through Enhanced RANKL." PLoS One 11(6): e0156708.
Katsimbri, P. (2017). "The biology of normal bone remodelling." Eur J Cancer Care (Engl) 26(6).
Kaufmann, E., J. Sanz, J. L. Dunn, N. Khan, L. E. Mendonça, A. Pacis, F. Tzelepis, E. Pernet, A. Dumaine, J. C. Grenier, F. Mailhot-Léonard, E. Ahmed, J. Belle, R. Besla, B. Mazer, I. L. King, A. Nijnik, C. S. Robbins, L. B. Barreiro and M. Divangahi (2018). "BCG Educates Hematopoietic Stem Cells to Generate Protective Innate Immunity against Tuberculosis." Cell 172(1-2): 176-190.e119.
Kaur, K., S. Sharma, S. A. Sinha, P. Kaur, U. C. Saini, M. S. Dhillon, P. C. Karakousis and I. Verma (2022). "Metabolic switching and cell wall remodelling of Mycobacterium tuberculosis during bone tuberculosis." bioRxiv: 2022.2001.2013.476285.
Kawai, T. and S. Akira (2007). "Signalling to NF-kB by Toll-like receptors." Trends in Molecular Medicine 13(11): 460-469.
Kearns, A. E., S. Khosla and P. J. Kostenuik (2008). "Receptor activator of nuclear factor kappaB ligand and osteoprotegerin regulation of bone remodeling in health and disease." Endocr Rev 29(2): 155-192.
Keller, J., P. Catala-Lehnen, A. K. Huebner, A. Jeschke, T. Heckt, A. Lueth, M. Krause, T. Koehne, J. Albers, J. Schulze, S. Schilling, M. Haberland, H. Denninger, M. Neven, I. Hermans-Borgmeyer, T. Streichert, S. Breer, F. Barvencik, B. Levkau, B. Rathkolb, E. Wolf, J. Calzada-Wack, F. Neff, V. Gailus-Durner, H. Fuchs, M. H. de Angelis, S. Klutmann, E. Tsourdi, L. C. Hofbauer, B. Kleuser, J. Chun, T. Schinke and M. Amling (2014). "Calcitonin controls bone formation by inhibiting the release of sphingosine 1-phosphate from osteoclasts." Nat Commun 5: 5215.
Kelley, N., D. Jeltema, Y. Duan and Y. He (2019). "The NLRP3 Inflammasome: An Overview of Mechanisms of Activation and Regulation." Int J Mol Sci 20(13).
Kenkre, J. S. and J. Bassett (2018). "The bone remodelling cycle." Ann Clin Biochem 55(3): 308-327.
Kim, H. R., H. J. Chae, M. Thomas, T. Miyazaki, A. Monosov, E. Monosov, M. Krajewska, S. Krajewski and J. C. Reed (2007). "Mammalian dap3 is an essential

gene required for mitochondrial homeostasis *in vivo* and contributing to the extrinsic pathway for apoptosis." Faseb j 21(1): 188-196.
Kim, J., J. Yang, O. J. Park, S. S. Kang, W. S. Kim, K. Kurokawa, C. H. Yun, H. H. Kim, B. L. Lee and S. H. Han (2013). "Lipoproteins are an important bacterial component responsible for bone destruction through the induction of osteoclast differentiation and activation." J Bone Miner Res 28(11): 2381-2391.
Kim, K., J. H. Kim, J. Lee, H. M. Jin, S. H. Lee, D. E. Fisher, H. Kook, K. K. Kim, Y. Choi and N. Kim (2005). "Nuclear factor of activated T cells c1 induces osteoclast-associated receptor gene expression during tumor necrosis factor-related activation-induced cytokine-mediated osteoclastogenesis." J Biol Chem 280(42): 35209-35216.
Kim, M. S., C. J. Day and N. A. Morrison (2005). "MCP-1 is induced by receptor activator of nuclear factor-{kappa}B ligand, promotes human osteoclast fusion, and rescues granulocyte macrophage colony-stimulating factor suppression of osteoclast formation." J Biol Chem 280(16): 16163-16169.
Kim, Y. and S. Kumar (2014). "CD44-mediated adhesion to hyaluronic acid contributes to mechanosensing and invasive motility." Mol Cancer Res 12(10): 1416-1429.
Kindstedt, E., C. K. Holm, R. Sulniute, I. Martinez-Carrasco, R. Lundmark and P. Lundberg (2017). "CCL11, a novel mediator of inflammatory bone resorption." Scientific Reports 7(1): 5334.
Kirschke, H. (2007). Cathepsin K. xPharm: The Comprehensive Pharmacology Reference. S. J. Enna and D. B. Bylund. New York, Elsevier: 1-12.
Kleinnijenhuis, J., J. Quintin, F. Preijers, L. A. B. Joosten, D. C. Ifrim, S. Saeed, C. Jacobs, J. van Loenhout, D. de Jong, H. G. Stunnenberg, R. J. Xavier, J. W. M. van der Meer, R. van Crevel and M. G. Netea (2012). "Bacille Calmette-Guérin induces NOD2-dependent nonspecific protection from reinfection via epigenetic reprogramming of monocytes." Proceedings of the National Academy of Sciences 109(43): 17537-17542.
Koch, R. (1882). "The Etiology of Tuberculosis " Zentralbl Bakteriol Mikrobiol Hyg A Med Mikrobiol Infekt Parasitol 251(3): 287-296.
Kylmäoja, E., M. Nakamura, S. Turunen, C. Patlaka, G. Andersson, P. Lehenkari and J. Tuukkanen (2018). "Peripheral blood monocytes show increased

osteoclast differentiation potential compared to bone marrow monocytes." Heliyon 4(9): e00780.
Lacey, D. L., E. Timms, H. L. Tan, M. J. Kelley, C. R. Dunstan, T. Burgess, R. Elliott, A. Colombero, G. Elliott, S. Scully, H. Hsu, J. Sullivan, N. Hawkins, E. Davy, C. Capparelli, A. Eli, Y. X. Qian, S. Kaufman, I. Sarosi, V. Shalhoub, G. Senaldi, J. Guo, J. Delaney and W. J. Boyle (1998). "Osteoprotegerin ligand is a cytokine that regulates osteoclast differentiation and activation." Cell 93(2): 165-176.
Lachmandas, E., L. Boutens, J. M. Ratter, A. Hijmans, G. J. Hooiveld, L. A. Joosten, R. J. Rodenburg, J. A. Fransen, R. H. Houtkooper, R. van Crevel, M. G. Netea and R. Stienstra (2016). "Microbial stimulation of different Toll-like receptor signalling pathways induces diverse metabolic programmes in human monocytes." Nat Microbiol 2: 16246.
Lam, A., R. Prabhu, C. M. Gross, L. A. Riesenberg, V. Singh and S. Aggarwal (2017). "Role of apoptosis and autophagy in tuberculosis." Am J Physiol Lung Cell Mol Physiol 313(2): L218-l229.
Lapid, M. I., S. Kung, M. A. Frye, J. M. Biernacka, J. R. Geske, M. T. Drake, M. D. Jankowski and B. L. Clarke (2017). "Association of the serotonin transporter-linked polymorphic region genotype with lower bone mineral density." Translational Psychiatry 7(8): e1213-e1213.
Larousserie, F., L. Bsiri, V. Dumaine, C. Dietrich, A. Audebourg, B. Radenen-Bussière, P. Anract, M. C. Vacher-Lavenu and O. Devergne (2017). "Frontline Science: Human bone cells as a source of IL-27 under inflammatory conditions: role of TLRs and cytokines." J Leukoc Biol 101(6): 1289-1300.
Lee, H. M., D. M. Shin, K. K. Kim, J. S. Lee, T. H. Paik and E. K. Jo (2009). "Roles of reactive oxygen species in CXCL8 and CCL2 expression in response to the 30-kDa antigen of Mycobacterium tuberculosis." J Clin Immunol 29(1): 46-56.
Lee, S. H., J. Rho, D. Jeong, J. Y. Sul, T. Kim, N. Kim, J. S. Kang, T. Miyamoto, T. Suda, S. K. Lee, R. J. Pignolo, B. Koczon-Jaremko, J. Lorenzo and Y. Choi (2006). "v-ATPase V0 subunit d2-deficient mice exhibit impaired osteoclast fusion and increased bone formation." Nat Med 12(12): 1403-1409.
Lees, R. L., V. K. Sabharwal and J. N. Heersche (2001). "Resorptive state and cell size influence intracellular pH regulation in rabbit osteoclasts cultured on collagen-hydroxyapatite films." Bone 28(2): 187-194.

Leisching, G., R. D. Pietersen, C. van Heerden, P. van Helden, I. Wiid and B. Baker (2017). "RNAseq reveals hypervirulence-specific host responses to M. tuberculosis infection." Virulence 8(6): 848-858.

Lemma, S., M. Sboarina, P. E. Porporato, N. Zini, P. Sonveaux, G. Di Pompo, N. Baldini and S. Avnet (2016). "Energy metabolism in osteoclast formation and activity." Int J Biochem Cell Biol 79: 168-180.

Leonard, M. K. and H. M. Blumberg (2017). "Musculoskeletal Tuberculosis." Microbiol Spectr 5(2).

Leu, J. S., M. L. Chen, S. Y. Chang, S. L. Yu, C. W. Lin, H. Wang, W. C. Chen, C. H. Chang, J. Y. Wang, L. N. Lee, C. J. Yu, I. Kramnik and B. S. Yan (2017). "SP110b Controls Host Immunity and Susceptibility to Tuberculosis." Am J Respir Crit Care Med 195(3): 369-382.

Li, B., W. C. Lee, C. Song, L. Ye, E. D. Abel and F. Long (2020). "Both aerobic glycolysis and mitochondrial respiration are required for osteoclast differentiation." Faseb j 34(8): 11058-11067.

Li, F., L. Feng, C. Jin, X. Wu, L. Fan, S. Xiong and Y. Dong (2018). "LpqT improves mycobacteria survival in macrophages by inhibiting TLR2 mediated inflammatory cytokine expression and cell apoptosis." Tuberculosis (Edinb) 111: 57-66.

Li, H., S. Hong, J. Qian, Y. Zheng, J. Yang and Q. Yi (2010). "Cross talk between the bone and immune systems: osteoclasts function as antigen-presenting cells and activate CD4+ and CD8+ T cells." Blood 116(2): 210-217.

Li, H., S. Hong, J. Qian, Y. Zheng, J. Yang and Q. Yi (2010). "Cross talk between the bone and immune systems: osteoclasts function as antigen-presenting cells and activate CD4+ and CD8+ T cells." Blood 116(2): 210-217.

Li, Z. H., Y. Si, G. Xu, X. M. Chen, H. Xiong, L. Lai, Y. Q. Zheng and Z. G. Zhang (2017). "High-dose PMA with RANKL and MCSF induces THP-1 cell differentiation into human functional osteoclasts *in vitro*." Mol Med Rep 16(6): 8380-8384.

Liao, R., Z. Feng, W. Li, R. Liu, X. Xu, S. Yao and J. Tian (2021). "Interleukin-1 induces receptor activator of nuclear factor-κB ligand-independent osteoclast differentiation in RAW264.7 cells." Exp Ther Med 21(6): 640.

Lin, J., Q. Chang, X. Dai, D. Liu, Y. Jiang and Y. Dai (2019). "Early secreted antigenic target of 6-kDa of Mycobacterium tuberculosis promotes caspase-9/caspase-3-mediated apoptosis in macrophages." Mol Cell Biochem 457(1-2): 179-189.

Lin, W., P. F. de Sessions, G. H. Teoh, A. N. Mohamed, Y. O. Zhu, V. H. Koh, M. L. Ang, P. C. Dedon, M. L. Hibberd and S. Alonso (2016). "Transcriptional Profiling of Mycobacterium tuberculosis Exposed to *In vitro* Lysosomal Stress." Infect Immun 84(9): 2505-2523.

Lindsay M. Biga, S. D., Amy Harwell, Robin Hopkins, Joel Kaufmann, Mike LeMaster, Philip Matern, Katie Morrison-Graham, Devon Quick & Jon Runyeon (2022). Anatomy & Physiology

Liu, W., J. Zhou, F. Niu, F. Pu, Z. Wang, M. Huang, X. Zhao, L. Yang, P. Tao, P. Xia and J. Feng (2020). "Mycobacterium tuberculosis infection increases the number of osteoclasts and inhibits osteoclast apoptosis by regulating TNF-α-mediated osteoclast autophagy." Exp Ther Med 20(3): 1889-1898.

Liu, X., W. Jia, H. Wang, Y. Wang, J. Ma, H. Wang, X. Zhou and G. Li (2015). "Establishment of a rabbit model of spinal tuberculosis using Mycobacterium tuberculosis strain H37Rv." Jpn J Infect Dis 68(2): 89-97.

López-Agudelo, V. A., A. Baena, V. Barrera, F. Cabarcas, J. F. Alzate, D. J. V. Beste, R. Ríos-Estepa and L. F. Barrera (2022). "Dual RNA Sequencing of Mycobacterium tuberculosis-Infected Human Splenic Macrophages Reveals a Strain-Dependent Host–Pathogen Response to Infection." International Journal of Molecular Sciences 23(3): 1803.

Lu, A., V. G. Magupalli, J. Ruan, Q. Yin, M. K. Atianand, M. R. Vos, G. F. Schröder, K. A. Fitzgerald, H. Wu and E. H. Egelman (2014). "Unified polymerization mechanism for the assembly of ASC-dependent inflammasomes." Cell 156(6): 1193-1206.

Luo, G., F. Li, X. Li, Z. G. Wang and B. Zhang (2018). "TNF-α and RANKL promote osteoclastogenesis by upregulating RANK via the NF-κB pathway." Mol Med Rep 17(5): 6605-6611.

Lv, J., X. He, H. Wang, Z. Wang, G. T. Kelly, X. Wang, Y. Chen, T. Wang and Z. Qian (2017). "TLR4-NOX2 axis regulates the phagocytosis and killing of

Mycobacterium tuberculosis by macrophages." BMC Pulmonary Medicine 17(1): 194.
Ma, W., W. Jin, X. He, Y. Sun, H. Yin, Z. Wang and S. Shi (2022). "Mycobacterium tuberculosis Induced Osteoblast Dysregulation Involved in Bone Destruction in Spinal Tuberculosis." Front Cell Infect Microbiol 12: 780272.
Madel, M. B., L. Ibáñez, A. Wakkach, T. J. de Vries, A. Teti, F. Apparailly and C. Blin-Wakkach (2019). "Immune Function and Diversity of Osteoclasts in Normal and Pathological Conditions." Front Immunol 10: 1408.
Madel, M.-B., L. Ibáñez, M. Rouleau, A. Wakkach and C. Blin-Wakkach (2018). "A Novel Reliable and Efficient Procedure for Purification of Mature Osteoclasts Allowing Functional Assays in Mouse Cells." Frontiers in Immunology 9.
Malik, Z. A., G. M. Denning and D. J. Kusner (2000). "Inhibition of Ca(2+) signalling by Mycobacterium tuberculosis is associated with reduced phagosome-lysosome fusion and increased survival within human macrophages." J Exp Med 191(2): 287-302.
Malik, Z. A., C. R. Thompson, S. Hashimi, B. Porter, S. S. Iyer and D. J. Kusner (2003). "Cutting edge: Mycobacterium tuberculosis blocks Ca2+ signalling and phagosome maturation in human macrophages via specific inhibition of sphingosine kinase." J Immunol 170(6): 2811-2815.
Maphasa, R. E., M. Meyer and A. Dube (2020). "The Macrophage Response to Mycobacterium tuberculosis and Opportunities for Autophagy Inducing Nanomedicines for Tuberculosis Therapy." Front Cell Infect Microbiol 10: 618414.
Marciniuk, D. D., B. D. Mc Nab, W. T. Martin and V. H. Hoeppner (1999). "Detection of Pulmonary Tuberculosis in Patients With a Normal Chest Radiograph." CHEST 115(2): 445-452.
Marino, S., J. G. Logan, D. Mellis and M. Capulli (2014). "Generation and culture of osteoclasts." Bonekey Rep 3: 570.
Martinon, F., V. Pétrilli, A. Mayor, A. Tardivel and J. Tschopp (2006). "Gout-associated uric acid crystals activate the NALP3 inflammasome." Nature 440(7081): 237-241.

Mashima, R. and T. Okuyama (2015). "The role of lipoxygenases in pathophysiology; new insights and future perspectives." Redox Biology 6: 297-310.

Master, S. S., S. K. Rampini, A. S. Davis, C. Keller, S. Ehlers, B. Springer, G. S. Timmins, P. Sander and V. Deretic (2008). "Mycobacterium tuberculosis prevents inflammasome activation." Cell Host Microbe 3(4): 224-232.

Masters, E. A., B. F. Ricciardi, K. L. d. M. Bentley, T. F. Moriarty, E. M. Schwarz and G. Muthukrishnan (2022). "Skeletal infections: microbial pathogenesis, immunity and clinical management." Nature Reviews Microbiology 20(7): 385-400.

Matsumoto, M., M. Kogawa, S. Wada, H. Takayanagi, M. Tsujimoto, S. Katayama, K. Hisatake and Y. Nogi (2004). "Essential role of p38 mitogen-activated protein kinase in cathepsin K gene expression during osteoclastogenesis through association of NFATc1 and PU.1." J Biol Chem 279(44): 45969-45979.

Mayer-Barber, K. D., B. B. Andrade, D. L. Barber, S. Hieny, C. G. Feng, P. Caspar, S. Oland, S. Gordon and A. Sher (2011). "Innate and adaptive interferons suppress IL-1α and IL-1β production by distinct pulmonary myeloid subsets during Mycobacterium tuberculosis infection." Immunity 35(6): 1023-1034.

Mayer-Barber, K. D., D. L. Barber, K. Shenderov, S. D. White, M. S. Wilson, A. Cheever, D. Kugler, S. Hieny, P. Caspar, G. Núñez, D. Schlueter, R. A. Flavell, F. S. Sutterwala and A. Sher (2010). "Caspase-1 independent IL-1beta production is critical for host resistance to mycobacterium tuberculosis and does not require TLR signalling *in vivo*." J Immunol 184(7): 3326-3330.

McKinney-Freeman, S. L., O. Naveiras, F. Yates, S. Loewer, M. Philitas, M. Curran, P. J. Park and G. Q. Daley (2009). "Surface antigen phenotypes of hematopoietic stem cells from embryos and murine embryonic stem cells." Blood 114(2): 268-278.

Mediero, A., M. Perez-Aso and B. N. Cronstein (2013). "Activation of adenosine A2A receptor reduces osteoclast formation via PKA- and ERK1/2-mediated suppression of NFκB nuclear translocation." British Journal of Pharmacology 169(6): 1372-1388.

Medley, J., A. Goff, P. J. G. Bettencourt, M. Dare, L. Cole, D. Cantillon and S. J. Waddell (2022) "Dissecting the Mycobacterium bovis BCG Response to

Macrophage Infection to Help Prioritize Targets for Anti-Tuberculosis Drug and Vaccine Discovery." Vaccines 10 DOI: 10.3390/vaccines10010113.
Medzhitov, R., P. Preston-Hurlburt and C. A. Janeway, Jr. (1997). "A human homologue of the Drosophila Toll protein signals activation of adaptive immunity." Nature 388(6640): 394-397.
Meghji, S., P. A. White, S. P. Nair, K. Reddi, K. Heron, B. Henderson, A. Zaliani, G. Fossati, P. Mascagni, J. F. Hunt, M. M. Roberts and A. R. Coates (1997). "Mycobacterium tuberculosis chaperonin 10 stimulates bone resorption: a potential contributory factor in Pott's disease." J Exp Med 186(8): 1241-1246.
Mehandru, S., M. A. Poles, K. Tenner-Racz, A. Horowitz, A. Hurley, C. Hogan, D. Boden, P. Racz and M. Markowitz (2004). "Primary HIV-1 infection is associated with preferential depletion of CD4+ T lymphocytes from effector sites in the gastrointestinal tract." J Exp Med 200(6): 761-770.
Merrild, D. M., D. C. Pirapaharan, C. M. Andreasen, P. Kjærsgaard-Andersen, A. M. Møller, M. Ding, J. M. Delaissé and K. Søe (2015). "Pit- and trench-forming osteoclasts: a distinction that matters." Bone Res 3: 15032.
Miller, J. L., K. Velmurugan, M. J. Cowan and V. Briken (2010). "The type I NADH dehydrogenase of Mycobacterium tuberculosis counters phagosomal NOX2 activity to inhibit TNF-alpha-mediated host cell apoptosis." PLoS Pathog 6(4): e1000864.
Mira-Pascual, L. (2019). Role of Tatrate-Resistant Acid Phosphatase in Bone Remodelling. PhD, Karolinska Institutet, Stockholm, Sweden

Mishra, B. B., P. Moura-Alves, A. Sonawane, N. Hacohen, G. Griffiths, L. F. Moita and E. Anes (2010). "Mycobacterium tuberculosis protein ESAT-6 is a potent activator of the NLRP3/ASC inflammasome." Cell Microbiol 12(8): 1046-1063.
Mishra, B. B., P. Moura-Alves, A. Sonawane, N. Hacohen, G. Griffiths, L. F. Moita and E. Anes (2010). "Mycobacterium tuberculosis protein ESAT-6 is a potent activator of the NLRP3/ASC inflammasome." Cell Microbiol 12(8): 1046-1063.
Miyamoto, H., T. Suzuki, Y. Miyauchi, R. Iwasaki, T. Kobayashi, Y. Sato, K. Miyamoto, H. Hoshi, K. Hashimoto, S. Yoshida, W. Hao, T. Mori, H. Kanagawa, E. Katsuyama, A. Fujie, H. Morioka, M. Matsumoto, K. Chiba, M. Takeya, Y. Toyama and T. Miyamoto (2012). "Osteoclast stimulatory transmembrane protein and

dendritic cell–specific transmembrane protein cooperatively modulate cell–cell fusion to form osteoclasts and foreign body giant cells." J Bone Miner Res 27(6): 1289-1297.
Moon, M. S. (2014). "Tuberculosis of spine: current views in diagnosis and management." Asian Spine J 8(1): 97-111.
Moon, M. S., S. S. Kim, B. J. Lee and J. L. Moon (2012). "Spinal tuberculosis in children: Retrospective analysis of 124 patients." Indian J Orthop 46(2): 150-158.
Morse, D., D. R. Brothwell and P. J. Ucko (1964). "TUBERCULOSIS IN ANCIENT EGYPT." Am Rev Respir Dis 90: 524-541.
Mumtaz, N., M. Koedam, J. van Leeuwen, M. P. G. Koopmans, B. C. J. van der Eerden and B. Rockx (2022). "Zika virus infects human osteoclasts and blocks differentiation and bone resorption." Emerg Microbes Infect 11(1): 1621-1634.
Murakami, T., J. Ockinger, J. Yu, V. Byles, A. McColl, A. M. Hofer and T. Horng (2012). "Critical role for calcium mobilization in activation of the NLRP3 inflammasome." Proc Natl Acad Sci U S A 109(28): 11282-11287.
Murphy, M. G., K. Cerchio, S. A. Stoch, K. Gottesdiener, M. Wu and R. Recker (2005). "Effect of L-000845704, an αVβ3 Integrin Antagonist, on Markers of Bone Turnover and Bone Mineral Density in Postmenopausal Osteoporotic Women." The Journal of Clinical Endocrinology & Metabolism 90(4): 2022-2028.
Muthukuru, M. and R. P. Darveau (2014). "TLR signalling that induces weak inflammatory response and SHIP1 enhances osteogenic functions." Bone Research 2(1): 14031.
Naqvi, A. R., J. B. Fordham and S. Nares (2015). "miR-24, miR-30b, and miR-142-3p regulate phagocytosis in myeloid inflammatory cells." J Immunol 194(4): 1916-1927.
Newa, M., K. H. Bhandari, L. Tang, R. Kalvapalle, M. Suresh and M. R. Doschak (2011). "Antibody-mediated "universal" osteoclast targeting platform using calcitonin as a model drug." Pharm Res 28(5): 1131-1143.
NHS. (2019). "Symptoms - Tuberculosis (TB)." from https://www.nhs.uk/conditions/tuberculosis-tb/symptoms/.

NHS. (2022). "Treatment -Tuberculosis (TB)." from https://www.nhs.uk/conditions/tuberculosis-tb/treatment/.

Nigou, J., C. Zelle-Rieser, M. Gilleron, M. Thurnher and G. Puzo (2001). "Mannosylated lipoarabinomannans inhibit IL-12 production by human dendritic cells: evidence for a negative signal delivered through the mannose receptor." J Immunol 166(12): 7477-7485.

Nikoletopoulou, V., M. Markaki, K. Palikaras and N. Tavernarakis (2013). "Crosstalk between apoptosis, necrosis and autophagy." Biochim Biophys Acta 1833(12): 3448-3459.

Nisa, A., F. C. Kipper, D. Panigrahy, S. Tiwari, A. Kupz and S. Subbian (2022). "Different modalities of host cell death and their impact on Mycobacterium tuberculosis infection." Am J Physiol Cell Physiol 323(5): C1444-c1474.

Okada, H., K. Okabe and S. Tanaka (2020). "Finely-Tuned Calcium Oscillations in Osteoclast Differentiation and Bone Resorption." Int J Mol Sci 22(1).

O'Neill, L. A. J. and M. G. Netea (2020). "BCG-induced trained immunity: can it offer protection against COVID-19?" Nat Rev Immunol 20(6): 335-337.

Osorio, E. Y., Z. Gugala, G. T. Patterson, G. Palacios, E. Cordova, A. Uscanga-Palomeque, B. L. Travi and P. C. Melby (2022). "Inflammatory stimuli alter bone marrow composition and compromise bone health in the malnourished host." Front Immunol 13: 846246.

Pai, M., M. P. Nicol and C. C. Boehme (2016). "Tuberculosis Diagnostics: State of the Art and Future Directions." Microbiol Spectr 4(5).

Paik, S., S. Choi, K. I. Lee, Y. W. Back, Y. J. Son, E. K. Jo and H. J. Kim (2019). "Mycobacterium tuberculosis acyl carrier protein inhibits macrophage apoptotic death by modulating the reactive oxygen species/c-Jun N-terminal kinase pathway." Microbes Infect 21(1): 40-49.

Patel, C., L. Shi, J. F. Whitesides, B. M. Foster, R. J. Fajardo, E. E. Quillen and B. A. Kerr (2022). "A New Method of Bone Stromal Cell Characterization by Flow Cytometry." Current Protocols 2(3): e400.

Peek, C. T., C. A. Ford, K. R. Eichelberger, J. Jacobse, T. P. Torres, D. Maseda, Y. L. Latour, M. B. Piazuelo, J. R. Johnson, M. X. Byndloss, K. T. Wilson, J. C. Rathmell, J. A. Goettel and J. E. Cassat (2022). "Intestinal Inflammation Promotes MDL-1(+)

Osteoclast Precursor Expansion to Trigger Osteoclastogenesis and Bone Loss." Cell Mol Gastroenterol Hepatol 14(4): 731-750.

Pellin, D., P. Miotto, A. Ambrosi, D. M. Cirillo and C. Di Serio (2012). "A genome-wide identification analysis of small regulatory RNAs in Mycobacterium tuberculosis by RNA-Seq and conservation analysis." PLoS One 7(3): e32723.

Picelli, S., Å. K. Björklund, O. R. Faridani, S. Sagasser, G. Winberg and R. Sandberg (2013). "Smart-seq2 for sensitive full-length transcriptome profiling in single cells." Nature Methods 10(11): 1096-1098.

Pilli, M., J. Arko-Mensah, M. Ponpuak, E. Roberts, S. Master, M. A. Mandell, N. Dupont, W. Ornatowski, S. Jiang, S. B. Bradfute, J. A. Bruun, T. E. Hansen, T. Johansen and V. Deretic (2012). "TBK-1 promotes autophagy-mediated antimicrobial defense by controlling autophagosome maturation." Immunity 37(2): 223-234.

Piper, K., A. Boyde and S. J. Jones (1992). "The relationship between the number of nuclei of an osteoclast and its resorptive capability *in vitro*." Anat Embryol (Berl) 186(4): 291-299.

Pisu, D., L. Huang, J. K. Grenier and D. G. Russell (2020). "Dual RNA-Seq of Mtb-Infected Macrophages *In vivo* Reveals Ontologically Distinct Host-Pathogen Interactions." Cell Rep 30(2): 335-350.e334.

Place, D. E., R. K. S. Malireddi, J. Kim, P. Vogel, M. Yamamoto and T. D. Kanneganti (2021). "Osteoclast fusion and bone loss are restricted by interferon inducible guanylate binding proteins." Nat Commun 12(1): 496.

Qian, X., D. T. Nguyen, J. Lyu, A. E. Albers, X. Bi and E. A. Graviss (2018). "Risk factors for extrapulmonary dissemination of tuberculosis and associated mortality during treatment for extrapulmonary tuberculosis." Emerg Microbes Infect 7(1): 102.

Qiao, W., H. E. Lau, H. Xie, V. K. Poon, C. C. Chan, H. Chu, S. Yuan, T. T. Yuen, K. K. Chik, J. O. Tsang, C. C. Chan, J. P. Cai, C. Luo, K. Y. Yuen, K. M. Cheung, J. F. Chan and K. W. Yeung (2022). "SARS-CoV-2 infection induces inflammatory bone loss in golden Syrian hamsters." Nat Commun 13(1): 2539.

Qu, Z., J. Zhou, Y. Zhou, Y. Xie, Y. Jiang, J. Wu, Z. Luo, G. Liu, L. Yin and X. L. Zhang (2020). "Mycobacterial EST12 activates a RACK1-NLRP3-gasdermin D pyroptosis-IL-1β immune pathway." Sci Adv 6(43).

Queval, C. J., A. Fearns, L. Botella, A. Smyth, L. Schnettger, M. Mitermite, E. Wooff, B. Villarreal-Ramos, W. Garcia-Jimenez, T. Heunis, M. Trost, D. Werling, F. J. Salguero, S. V. Gordon and M. G. Gutierrez (2021). "Macrophage-specific responses to human- and animal-adapted tubercle bacilli reveal pathogen and host factors driving multinucleated cell formation." PLoS Pathog 17(3): e1009410.

Raghuvanshi, S., P. Sharma, S. Singh, L. Van Kaer and G. Das (2010). "Mycobacterium tuberculosis evades host immunity by recruiting mesenchymal stem cells." Proc Natl Acad Sci U S A 107(50): 21653-21658.

Rahyussalim Ahmad, J., R. Andriansjah, S. Ifran and K. Tri (2017). The Existence of Mycobacterium tuberculosis in Microenvironment of Bone. Mycobacterium. R. Wellman. Rijeka, IntechOpen: Ch. 3.

Rajasekaran, S., D. C. R. Soundararajan, A. P. Shetty and R. M. Kanna (2018). "Spinal Tuberculosis: Current Concepts." Global Spine J 8(4 Suppl): 96s-108s.

Rastogi, S. and V. Briken (2022). "Interaction of Mycobacteria With Host Cell Inflammasomes." Front Immunol 13: 791136.

Raynaud-Messina, B., C. Verollet and I. Maridonneau-Parini (2019). "The osteoclast, a target cell for microorganisms." Bone 127: 315-323.

Reddy, S. V., C. Menaa, F. R. Singer, A. Demulder and G. D. Roodman (1999). "Cell biology of Paget's disease." J Bone Miner Res 14 Suppl 2: 3-8.

Riendeau, C. J. and H. Kornfeld (2003). "THP-1 cell apoptosis in response to Mycobacterial infection." Infect Immun 71(1): 254-259.

Rodrigues, L. C., P. Mangtani and I. Abubakar (2011). "How does the level of BCG vaccine protection against tuberculosis fall over time?" Bmj 343: d5974.

Root, S. H. and H. L. Aguila (2021). "Novel population of human monocyte and osteoclast progenitors from pluripotent stem cells and peripheral blood." Blood Adv 5(21): 4435-4446.

Rossol, M., M. Pierer, N. Raulien, D. Quandt, U. Meusch, K. Rothe, K. Schubert, T. Schöneberg, M. Schaefer, U. Krügel, S. Smajilovic, H. Bräuner-Osborne, C. Baerwald and U. Wagner (2012). "Extracellular Ca2+ is a danger signal activating the NLRP3 inflammasome through G protein-coupled calcium sensing receptors." Nat Commun 3: 1329.

Ruscitti, P., P. Cipriani, F. Carubbi, V. Liakouli, F. Zazzeroni, P. Di Benedetto, O. Berardicurti, E. Alesse and R. Giacomelli (2015). "The role of IL-1β in the bone loss during rheumatic diseases." Mediators Inflamm 2015: 782382.
Rutkovskiy, A., K. O. Stensløkken and I. J. Vaage (2016). "Osteoblast Differentiation at a Glance." Med Sci Monit Basic Res 22: 95-106.
Saelens, J. W., M. I. Sweeney, G. Viswanathan, A. M. Xet-Mull, K. L. Jurcic Smith, D. M. Sisk, D. D. Hu, R. M. Cronin, E. J. Hughes, W. J. Brewer, J. Coers, M. M. Champion, P. A. Champion, C. B. Lowe, C. M. Smith, S. Lee, J. E. Stout and D. M. Tobin (2022). "An ancestral mycobacterial effector promotes dissemination of infection." Cell 185(24): 4507-4525.e4518.
Sakowski, E. T., S. Koster, C. Portal Celhay, H. S. Park, E. Shrestha, S. E. Hetzenecker, K. Maurer, K. Cadwell and J. A. Philips (2015). "Ubiquilin 1 Promotes IFN-γ-Induced Xenophagy of Mycobacterium tuberculosis." PLoS Pathog 11(7): e1005076.
Salhotra, A., H. N. Shah, B. Levi and M. T. Longaker (2020). "Mechanisms of bone development and repair." Nat Rev Mol Cell Biol 21(11): 696-711.
Sanchez, C. J., C. L. Ward, D. R. Romano, B. J. Hurtgen, S. K. Hardy, R. L. Woodbury, A. V. Trevino, C. R. Rathbone and J. C. Wenke (2013). "Staphylococcus aureus biofilms decrease osteoblast viability, inhibits osteogenic differentiation, and increases bone resorption *in vitro*." BMC Musculoskeletal Disorders 14(1): 187.
Saraste, A. and K. Pulkki (2000). "Morphologic and biochemical hallmarks of apoptosis." Cardiovasc Res 45(3): 528-537.
Sarkar, S., M. G. Dlamini, D. Bhattacharya, O. T. Ashiru, A. W. Sturm and P. Moodley (2016). "Strains of Mycobacterium tuberculosis differ in affinity for human osteoblasts and alveolar cells *in vitro*." Springerplus 5: 163.
Schaaf, K., S. R. Smith, A. Duverger, F. Wagner, F. Wolschendorf, A. O. Westfall, O. Kutsch and J. Sun (2017). "Mycobacterium tuberculosis exploits the PPM1A signalling pathway to block host macrophage apoptosis." Sci Rep 7: 42101.
Shah, S., J. R. Cannon, C. Fenselau and V. Briken (2015). "A Duplicated ESAT-6 Region of ESX-5 Is Involved in Protein Export and Virulence of Mycobacteria." Infect Immun 83(11): 4349-4361.

Sharma, D. and T. D. Kanneganti (2016). "The cell biology of inflammasomes: Mechanisms of inflammasome activation and regulation." J Cell Biol 213(6): 617-629.

Shimada, K., T. R. Crother, J. Karlin, J. Dagvadorj, N. Chiba, S. Chen, V. K. Ramanujan, A. J. Wolf, L. Vergnes, D. M. Ojcius, A. Rentsendorj, M. Vargas, C. Guerrero, Y. Wang, K. A. Fitzgerald, D. M. Underhill, T. Town and M. Arditi (2012). "Oxidized mitochondrial DNA activates the NLRP3 inflammasome during apoptosis." Immunity 36(3): 401-414.

Shin, D. M., B. Y. Jeon, H. M. Lee, H. S. Jin, J. M. Yuk, C. H. Song, S. H. Lee, Z. W. Lee, S. N. Cho, J. M. Kim, R. L. Friedman and E. K. Jo (2010). "Mycobacterium tuberculosis eis regulates autophagy, inflammation, and cell death through redox-dependent signalling." PLoS Pathog 6(12): e1001230.

Shivtiel, S., O. Kollet, K. Lapid, A. Schajnovitz, P. Goichberg, A. Kalinkovich, E. Shezen, M. Tesio, N. Netzer, I. Petit, A. Sharir and T. Lapidot (2008). "CD45 regulates retention, motility, and numbers of hematopoietic progenitors, and affects osteoclast remodeling of metaphyseal trabecules." J Exp Med 205(10): 2381-2395.

Sholeye, A. R., A. A. Williams, D. T. Loots, A. M. Tutu van Furth, M. van der Kuip and S. Mason (2022). "Tuberculous Granuloma: Emerging Insights From Proteomics and Metabolomics." Front Neurol 13: 804838.

Sigal, G. B., M. R. Segal, A. Mathew, L. Jarlsberg, M. Wang, S. Barbero, N. Small, K. Haynesworth, J. L. Davis, M. Weiner, W. C. Whitworth, J. Jacobs, J. Schorey, D. M. Lewinsohn and P. Nahid (2017). "Biomarkers of Tuberculosis Severity and Treatment Effect: A Directed Screen of 70 Host Markers in a Randomized Clinical Trial." EBioMedicine 25: 112-121.

Silvério, D., R. Gonçalves, R. Appelberg and M. Saraiva (2021). "Advances on the Role and Applications of Interleukin-1 in Tuberculosis." mBio 12(6): e0313421.

Sims, N. A. and T. J. Martin (2020). "Osteoclasts Provide Coupling Signals to Osteoblast Lineage Cells Through Multiple Mechanisms." Annual Review of Physiology 82(1): 507-529.

Søe, K. (2020). "Osteoclast Fusion: Physiological Regulation of Multinucleation through Heterogeneity—Potential Implications for Drug Sensitivity." International Journal of Molecular Sciences 21(20): 7717.

Søe, K., A. S. Hobolt-Pedersen and J. M. Delaisse (2015). "The elementary fusion modalities of osteoclasts." Bone 73: 181-189.
Soskolne, W. A. (1978). "Phagocytosis of osteocytes by osteoclasts in femora of two week-old rabbits." Cell Tissue Res 195(3): 557-564.
Soysa, N. S. and N. Alles (2019). "Positive and negative regulators of osteoclast apoptosis." Bone Rep 11: 100225.
Stattin, E.-L., P. Henning, J. Klar, E. McDermott, C. Stecksen-Blicks, P.-E. Sandström, T. G. Kellgren, P. Rydén, G. Hallmans, T. Lönnerholm, A. Ameur, M. H. Helfrich, F. P. Coxon, N. Dahl, J. Wikström and U. H. Lerner (2017). "SNX10 gene mutation leading to osteopetrosis with dysfunctional osteoclasts." Scientific Reports 7(1): 3012.
Stein, G. S., J. B. Lian, A. J. van Wijnen, J. L. Stein, M. Montecino, A. Javed, S. K. Zaidi, D. W. Young, J. Y. Choi and S. M. Pockwinse (2004). "Runx2 control of organization, assembly and activity of the regulatory machinery for skeletal gene expression." Oncogene 23(24): 4315-4329.
Stenbeck, G. and M. A. Horton (2000). "A new specialized cell-matrix interaction in actively resorbing osteoclasts." J Cell Sci 113 (Pt 9): 1577-1587.
Sugawara, I., H. Yamada, H. Kaneko, S. Mizuno, K. Takeda and S. Akira (1999). "Role of interleukin-18 (IL-18) in mycobacterial infection in IL-18-gene-disrupted mice." Infect Immun 67(5): 2585-2589.
Sumi, K., T. Abe, R. Kunimatsu, N. Oki, Y. Tsuka, T. Awada, K. Nakajima, K. Ando and K. Tanimoto (2018). "The effect of mesenchymal stem cells on chemotaxis of osteoclast precursor cells." J Oral Sci 60(2): 221-225.
Sun, J., K. Schaaf, A. Duverger, F. Wolschendorf, A. Speer, F. Wagner, M. Niederweis and O. Kutsch (2016). "Protein phosphatase, Mg2+/Mn2+-dependent 1A controls the innate antiviral and antibacterial response of macrophages during HIV-1 and Mycobacterium tuberculosis infection." Oncotarget 7(13): 15394-15409.
Tăbăran, A. F., C. T. Matea, T. Mocan, A. Tăbăran, M. Mihaiu, C. Iancu and L. Mocan (2020). "Silver Nanoparticles for the Therapy of Tuberculosis." Int J Nanomedicine 15: 2231-2258.
Takala, R., D. P. Ramji, R. Andrews, Y. Zhou, M. Farhat, M. Elmajee, S. Rundle and E. Choy (2022). "Pinolenic acid exhibits anti-inflammatory and anti-atherogenic

effects in peripheral blood-derived monocytes from patients with rheumatoid arthritis." Sci Rep 12(1): 8807.
Takayanagi, H. (2021). "RANKL as the master regulator of osteoclast differentiation." J Bone Miner Metab 39(1): 13-18.
Takayanagi, H., S. Kim, T. Koga, H. Nishina, M. Isshiki, H. Yoshida, A. Saiura, M. Isobe, T. Yokochi, J. Inoue, E. F. Wagner, T. W. Mak, T. Kodama and T. Taniguchi (2002). "Induction and activation of the transcription factor NFATc1 (NFAT2) integrate RANKL signalling in terminal differentiation of osteoclasts." Dev Cell 3(6): 889-901.
Takeshita, S., T. Fumoto, K. Matsuoka, K. A. Park, H. Aburatani, S. Kato, M. Ito and K. Ikeda (2013). "Osteoclast-secreted CTHRC1 in the coupling of bone resorption to formation." J Clin Invest 123(9): 3914-3924.
Tang, T., X. Lang, C. Xu, X. Wang, T. Gong, Y. Yang, J. Cui, L. Bai, J. Wang, W. Jiang and R. Zhou (2017). "CLICs-dependent chloride efflux is an essential and proximal upstream event for NLRP3 inflammasome activation." Nat Commun 8(1): 202.
Tang, Y., L. Yin, S. Tang, H. Zhang and J. Lan (2018). "Application of molecular, microbiological, and immunological tests for the diagnosis of bone and joint tuberculosis." J Clin Lab Anal 32(2).
Thompson, A. L. (2020). Morphine Induced Osteolysis and Hyperalgesia in Models of Traumatic and Pathologic Fracture: Potential for Cannabinoid-Based Therapeutics, The University of Arizona.
Toman, K., T. R. Frieden and O. World Health (2004). Toman's tuberculosis : case detection, treatment, and monitoring : questions and answers / edited by T. Frieden. Geneva, World Health Organization.
Toor, S. M., S. Wani and O. M. E. Albagha (2021). "Comprehensive Transcriptomic Profiling of Murine Osteoclast Differentiation Reveals Novel Differentially Expressed Genes and LncRNAs." Front Genet 12: 781272.
Trunz, B. B., P. Fine and C. Dye (2006). "Effect of BCG vaccination on childhood tuberculous meningitis and miliary tuberculosis worldwide: a meta-analysis and assessment of cost-effectiveness." Lancet 367(9517): 1173-1180.
Tsenova, L. and A. Singhal (2020). "Effects of host-directed therapies on the pathology of tuberculosis." J Pathol 250(5): 636-646.

Tsukasaki, M., N. C. Huynh, K. Okamoto, R. Muro, A. Terashima, Y. Kurikawa, N. Komatsu, W. Pluemsakunthai, T. Nitta, T. Abe, H. Kiyonari, T. Okamura, M. Sakai, T. Matsukawa, M. Matsumoto, Y. Kobayashi, J. M. Penninger and H. Takayanagi (2020). "Stepwise cell fate decision pathways during osteoclastogenesis at single-cell resolution." Nat Metab 2(12): 1382-1390.

Tural Önür, S., S. Iliaz, R. Iliaz, S. Sökücü and C. Özdemir (2016). "Serum alkaline phosphatase may play a role in the differential diagnosis of sarcoidosis and tuberculosis?" European Respiratory Journal 48(suppl 60): PA3722.

Udagawa, N., N. Takahashi, T. Akatsu, H. Tanaka, T. Sasaki, T. Nishihara, T. Koga, T. J. Martin and T. Suda (1990). "Origin of osteoclasts: mature monocytes and macrophages are capable of differentiating into osteoclasts under a suitable microenvironment prepared by bone marrow-derived stromal cells." Proc Natl Acad Sci U S A 87(18): 7260-7264.

Underhill, D. M., A. Ozinsky, K. D. Smith and A. Aderem (1999). "Toll-like receptor-2 mediates mycobacteria-induced proinflammatory signalling in macrophages." Proc Natl Acad Sci U S A 96(25): 14459-14463.

Velmurugan, K., B. Chen, J. L. Miller, S. Azogue, S. Gurses, T. Hsu, M. Glickman, W. R. Jacobs, Jr., S. A. Porcelli and V. Briken (2007). "Mycobacterium tuberculosis nuoG is a virulence gene that inhibits apoptosis of infected host cells." PLoS Pathog 3(7): e110.

Verma, D., M. Lerm, R. Blomgran Julinder, P. Eriksson, P. Söderkvist and E. Särndahl (2008). "Gene polymorphisms in the NALP3 inflammasome are associated with interleukin-1 production and severe inflammation: relation to common inflammatory diseases?" Arthritis Rheum 58(3): 888-894.

Wang, L., M. Zuo, H. Chen, S. Liu, X. Wu, Z. Cui, H. Yang, H. Liu and B. Ge (2017). "Mycobacterium tuberculosis Lipoprotein MPT83 Induces Apoptosis of Infected Macrophages by Activating the TLR2/p38/COX-2 Signalling Pathway." J Immunol 198(12): 4772-4780.

Welin, A., D. Eklund, O. Stendahl and M. Lerm (2011). "Human macrophages infected with a high burden of ESAT-6-expressing M. tuberculosis undergo caspase-1- and cathepsin B-independent necrosis." PLoS One 6(5): e20302.

WHO (2022). The WHO Global Tuberculosis Report 2022.

WHO (2022). WHO operational handbook on tuberculosis. Module 3: diagnosis. Tests for tuberculosis infection.

Wilkinson, R. J., P. Patel, M. Llewelyn, C. S. Hirsch, G. Pasvol, G. Snounou, R. N. Davidson and Z. Toossi (1999). "Influence of polymorphism in the genes for the interleukin (IL)-1 receptor antagonist and IL-1beta on tuberculosis." J Exp Med 189(12): 1863-1874.

Wintges, K., F. T. Beil, J. Albers, A. Jeschke, M. Schweizer, B. Claass, G. Tiegs, M. Amling and T. Schinke (2013). "Impaired bone formation and increased osteoclastogenesis in mice lacking chemokine (C-C motif) ligand 5 (Ccl5)." J Bone Miner Res 28(10): 2070-2080.

Wong, K. W. and W. R. Jacobs, Jr. (2011). "Critical role for NLRP3 in necrotic death triggered by Mycobacterium tuberculosis." Cell Microbiol 13(9): 1371-1384.

Wright, K. M. and J. S. Friedland (2002). "Differential regulation of chemokine secretion in tuberculous and staphylococcal osteomyelitis." J Bone Miner Res 17(9): 1680-1690.

Wright, K. M. and J. S. Friedland (2004). "Regulation of monocyte chemokine and MMP-9 secretion by proinflammatory cytokines in tuberculous osteomyelitis." J Leukoc Biol 75(6): 1086-1092.

Wu, H., G. Xu and Y. P. Li (2009). "Atp6v0d2 is an essential component of the osteoclast-specific proton pump that mediates extracellular acidification in bone resorption." J Bone Miner Res 24(5): 871-885.

Xiao, Y., J.-Y. Song, T. J. de Vries, C. Fatmawati, D. B. Parreira, G. E. J. Langenbach, N. Bąbała, M. A. Nolte, V. Everts and J. Borst (2013). "Osteoclast precursors in murine bone marrow express CD27 and are impeded in osteoclast development by CD70 on activated immune cells." Proceedings of the National Academy of Sciences 110(30): 12385-12390.

Xing, L., Y. Xiu and B. F. Boyce (2012). "Osteoclast fusion and regulation by RANKL-dependent and independent factors." World J Orthop 3(12): 212-222.

Xu, X., L. Zheng, Q. Yuan, G. Zhen, J. L. Crane, X. Zhou and X. Cao (2018). "Transforming growth factor-β in stem cells and tissue homeostasis." Bone Research 6(1): 2.

Yagi, M., T. Miyamoto, Y. Sawatani, K. Iwamoto, N. Hosogane, N. Fujita, K. Morita, K. Ninomiya, T. Suzuki, K. Miyamoto, Y. Oike, M. Takeya, Y. Toyama and T. Suda (2005). "DC-STAMP is essential for cell-cell fusion in osteoclasts and foreign body giant cells." J Exp Med 202(3): 345-351.

Yahara, Y., T. Barrientos, Y. J. Tang, V. Puviindran, P. Nadesan, H. Zhang, J. R. Gibson, S. G. Gregory, Y. Diao, Y. Xiang, Y. J. Qadri, T. Souma, M. L. Shinohara and B. A. Alman (2020). "Erythromyeloid progenitors give rise to a population of osteoclasts that contribute to bone homeostasis and repair." Nat Cell Biol 22(1): 49-59.

Yahara, Y., T. Nguyen, K. Ishikawa, K. Kamei and B. A. Alman (2022). "The origins and roles of osteoclasts in bone development, homeostasis and repair." Development 149(8).

Yao, Z., P. Li, Q. Zhang, E. M. Schwarz, P. Keng, A. Arbini, B. F. Boyce and L. Xing (2006). "Tumor necrosis factor-alpha increases circulating osteoclast precursor numbers by promoting their proliferation and differentiation in the bone marrow through up-regulation of c-Fms expression." J Biol Chem 281(17): 11846-11855.

Yasuda, H., N. Shima, N. Nakagawa, K. Yamaguchi, M. Kinosaki, S. Mochizuki, A. Tomoyasu, K. Yano, M. Goto, A. Murakami, E. Tsuda, T. Morinaga, K. Higashio, N. Udagawa, N. Takahashi and T. Suda (1998). "Osteoclast differentiation factor is a ligand for osteoprotegerin/osteoclastogenesis-inhibitory factor and is identical to TRANCE/RANKL." Proc Natl Acad Sci U S A 95(7): 3597-3602.

Yazid, M. D., S. H. Z. Ariffin, S. Senafi, M. A. Razak and R. M. A. Wahab (2010). "Determination of the differentiation capacities of murines' primary mononucleated cells and MC3T3-E1 cells." Cancer Cell International 10(1): 42.

Yi, F., J. Hu, X. Zhu, Y. Wang, Q. Yu, J. Deng, X. Huang, Y. Ma and Y. Xie (2021). "Transcriptional Profiling of Human Peripheral Blood Mononuclear Cells Stimulated by Mycobacterium tuberculosis PPE57 Identifies Characteristic Genes Associated With Type I Interferon Signalling." Front Cell Infect Microbiol 11: 716809.

Yi, L., Z. Li, H. Jiang, Z. Cao, J. Liu and X. Zhang (2018). "Gene Modification of Transforming Growth Factor β (TGF-β) and Interleukin 10 (IL-10) in

Suppressing Mt Sonicate Induced Osteoclast Formation and Bone Absorption." Med Sci Monit 24: 5200-5207.

Yorgan, T. A. and T. Schinke (2014). "Relevance of Wnt signalling for osteoanabolic therapy." Mol Cell Ther 2: 22.

Yorulmaz, H. (2015). Apoptosis and Infections. Cell Death. M. N. Tobias. Rijeka, IntechOpen: Ch. 12.

Yoshii, T., S. Magara, D. Miyai, H. Nishimura, E. Kuroki, S. Furudoi, T. Komori and C. Ohbayashi (2002). "Local levels of interleukin-1beta, -4, -6 and tumor necrosis factor alpha in an experimental model of murine osteomyelitis due to staphylococcus aureus." Cytokine 19(2): 59-65.

Youm, Y. H., R. W. Grant, L. R. McCabe, D. C. Albarado, K. Y. Nguyen, A. Ravussin, P. Pistell, S. Newman, R. Carter, A. Laque, H. Münzberg, C. J. Rosen, D. K. Ingram, J. M. Salbaum and V. D. Dixit (2013). "Canonical Nlrp3 inflammasome links systemic low-grade inflammation to functional decline in aging." Cell Metab 18(4): 519-532.

Yukie, H., O. Yoshimasa and U. Michihiko (2009). "CCL7 and CCL25 promote RANKL-induced osteoclast formation." Nihon Shishubyo Gakkai Kaishi (Journal of the Japanese Society of Periodontology) 51(1): 51-61.

Zahalka, S., P. Starkl, M. L. Watzenboeck, A. Farhat, M. Radhouani, F. Deckert, A. Hladik, K. Lakovits, F. Oberndorfer, C. Lassnig, B. Strobl, K. Klavins, M. Matsushita, D. E. Sanin, K. M. Grzes, E. J. Pearce, A.-D. Gorki and S. Knapp (2022). "Trained immunity of alveolar macrophages requires metabolic rewiring and type 1 interferon signalling." Mucosal Immunology 15(5): 896-907.

Zhang, G., B. Zhou, S. Li, J. Yue, H. Yang, Y. Wen, S. Zhan, W. Wang, M. Liao, M. Zhang, G. Zeng, C. G. Feng, C. M. Sassetti and X. Chen (2014). "Allele-specific induction of IL-1β expression by C/EBPβ and PU.1 contributes to increased tuberculosis susceptibility." PLoS Pathog 10(10): e1004426.

Zhang, W., Q. Lu, Y. Dong, Y. Yue and S. Xiong (2018). "Rv3033, as an Emerging Anti-apoptosis Factor, Facilitates Mycobacteria Survival via Inhibiting Macrophage Intrinsic Apoptosis." Front Immunol 9: 2136.

Zhao, H., Y. Ito, J. Chappel, N. W. Andrews, S. L. Teitelbaum and F. P. Ross (2008). "Synaptotagmin VII regulates bone remodeling by modulating osteoclast and osteoblast secretion." Dev Cell 14(6): 914-925.

Zheng, C. (2021). "The emerging roles of NOD-like receptors in antiviral innate immune signalling pathways." Int J Biol Macromol 169: 407-413.
Zheng, X. and D. Wang (2020). "The Adenosine A2A Receptor Agonist Accelerates Bone Healing and Adjusts Treg/Th17 Cell Balance through Interleukin 6." BioMed Research International 2020: 2603873.
Zhou, B. and D. W. Abbott (2021). "Gasdermin E permits interleukin-1 beta release in distinct sublytic and pyroptotic phases." Cell Rep 35(2): 108998.
Zhou, R., A. S. Yazdi, P. Menu and J. Tschopp (2011). "A role for mitochondria in NLRP3 inflammasome activation." Nature 469(7329): 221-225.
Zito, G., M. Buscetta, M. Cimino, P. Dino, F. Bucchieri and C. Cipollina (2020) "Cellular Models and Assays to Study NLRP3 Inflammasome Biology." International Journal of Molecular Sciences 21 DOI: 10.3390/ijms21124294.
Zwerina, J., S. Hayer, M. Tohidast-Akrad, H. Bergmeister, K. Redlich, U. Feige, C. Dunstan, G. Kollias, G. Steiner, J. Smolen and G. Schett (2004). "Single and combined inhibition of tumor necrosis factor, interleukin-1, and RANKL pathways in tumor necrosis factor-induced arthritis: effects on synovial inflammation, bone erosion, and cartilage destruction." Arthritis Rheum 50(1): 277-290.

Chapter 8 Appendix

Supplementary figures for chapter 3

Table SA 1 p-values determined by for Wilcoxon statistical test to determine the statistical significance of transcriptomic changes in each cluster of the heatmap of 1568 unique DEGs.

Cluster	Comparison	Day 7 ≥3N	Day 7 1-2N
1	Day 7 1-2N	0.183265	-
1	Day 3 OCP	8.92E-47	5.87E-40
2	Day 7 1-2N	0.221134	-
2	Day 3 OCP	1.34E-38	7.16E-38
3	Day 7 1-2N	5.82E-24	-
3	Day 3 OCP	9.13E-29	0.000468
4	Day 7 1-2N	3.36E-05	-
4	Day 3 OCP	6.95E-08	0.014776

Table SA 2: List of genes in each cluster for unbiased clustering analysis for transcriptomic OCL validation

Cluster			
1	**2**	**3**	**4**
Gene ID	**Gene ID**	**Gene ID**	**Gene ID**
Cav2	Itgb2l	Mx1	Polr3d
Sdhd	Alox12	Hk2	Col1a1
Ckmt1	Lck	Icam2	Dtx2
Pdgfb	Sept1	Mxd1	Clcnkb
Gm2a	Haao	Foxm1	Fzd3
Mmp14	Dnmt3l	Napsa	Plcd1
Epn2	Icosl	Hltf	Ptprs
Poldip2	Hip1r	Mcm2	Slc9a5
Ckb	Scn4a	Ppp5c	Actn1
Acp5	Ergic1	Slc2a3	Gata3
Col18a1	Acap1	Rnf215	Actr8
Gstt1	Cldn15	Ruvbl2	Stac2
Tcirg1	Smo	Zfp81	Frk
Naglu	Cpa3	Dnmt1	Tns3
Slc1a5	Gria3	Angptl2	Arsg
Idh3g	Il17ra	Rab11a	Ddx52
Ltbp2	Cd36	Asf1b	Lpcat1
Rab34	Apoe	Kit	Sema5a
Slc39a13	Hmgn2	Prss16	Mtdh
Mov10	Cd79a	Tmco6	Deptor
Ppm1j	Cyp4f18	Cers4	Arsa
Irf9	Ier3	Tex15	Ccdc80
Use1	Mmd	Ankrd28	Nckap5l
Scin	Cacna1e	Rbsn	Pla2g7
Prkra	Bid	Gata2	Lox
Adgre5	Ctse	Sash1	Rin1

Bcam	Nkg7	Xk	Peli3
Relb	Cnn2	Fcrls	Vldlr
Atp5d	Abca13	Cacna1d	Echs1
Pld3	Hdac9	Mtrex	Pnpla2
Klc4	Mapk13	Foxred2	D3Ertd751e
Gys1	Thop1	Nup50	Vim
Cavin1	Spc25	Cmah	Lrsam1
Dnaja3	Mcm5	Traf4	Gfra4
Lpcat3	Hmox1	Cd40	Adam33
Pgf	Ddx39	Wsb1	Mcm8
Grap	Por	Erbb3	Ndufaf5
Matk	Mef2c	Chtf18	Gss
Rasa4	Mrvi1	Ahr	Vangl1
Cstb	Zfp592	Mydgf	Lrrc47
Prdx2	Mmp8	Kitl	Guf1
Corin	Bcl2l1	Ahi1	Wsb2
P2rx5	Dio2	Mtfr2	Pxn
Htra1	Id3	Hal	Ptms
Fblim1	Spib	Usp15	Sipa1l3
Atp6v1b2	Mgst1	Castor1	Syt3
Zbtb32	Cd163	Limk2	Gga2
Pdk1	Trpm2	Pctp	Cask
Ezh1	Mpo	Pik3cg	Mrps31
M6pr	Tnpo1	Recql5	Kat6a
Cav1	Mcu	Spns3	Cbr4
Mid1ip1	Slc3a2	Nxn	Gab1
Fgfrl1	Adam19	Abcc3	Ap1g1
Gprc5b	Kif11	Aurkb	Ldhd
Met	Etv5	Entpd5	Bco2
Nav1	Mcemp1	Wars	Calml4
Apobec3	Pax5	Irf4	Ank2
Sdhb	Klhl3	Dnajc9	Ucp2
Hyal2	Lta4h	Rnase6	Mga
Hyal1	Chdh	Pspc1	Lif
Ifi35	Cd34	Amer2	Lars2
Mcoln2	Pacsin2	Ppp3cc	Gnptab
Steap4	Slpi	Cmbl	Bbs9
Card14	Tns4	Tbc1d31	Tmtc2
St3gal1	Rab11fip4	Litaf	Phf24
Nit1	Elmo2	Ciita	Bicral
Chp1	Trim37	Cldn1	Tcaf1
Cox6c	Lsp1	Ercc4	Dchs1
Abca1	Alox15	Gpaa1	Mllt6
Itga2	Ccl6	Alcam	Spsb2
Atp6v0e	Ccl4	Trmt2a	Nos1ap
Pls3	BC005537	Lmln	Lrrc56
Lnx2	Cd164	Ccdc14	Rreb1
Sdc4	Rab32	Donson	Tmem246
Nbr1	Pkib	Rttn	Plpp6
Rnd3	Dusp6	Kcnk5	Sgsm1
Aldoc	Myb	Prkn	Zc3h6
Timp2	Hsp90b1	Satb1	D830039M14Rik
Mmp9	Igf1	Rfx2	Apol7c
Pltp	Plek	Ip6k3	Col27a1

Slc12a7	Cpm	Nudt12	Mtmr11
Hist1h2bc	Stk10	Ltb	Lhfp
Myo1b	Pfkl	Psat1	F2r
Slc13a3	Prss57	Grk2	Ogfr
Acadvl	Btg2	Arhgap19	Spats2
Atox1	Mfap3	Pfkfb1	Pla2r1
Slc25a39	Sypl	Aatk	Mok
Cd68	Pdia6	Prkar1b	Ttc26
Avpi1	Rnf144a	Smad7	Capn11
Wwc1	Id2	Cxcr2	Fam57b
Cxcl16	Rrm2	Gpr35	mt-Rnr1
Nars2	Pecam1	Inpp5d	mt-Rnr2
Atp6ap1	Atp2a3	Atp1b1	mt-Co1
Mdh2	Blmh	Nuf2	mt-Nd4
Atp6v1e1	Rflnb	Slc25a25	mt-Nd5
Cyb561	Lrrc59	Usp20	mt-Nd6
Aig1	Stat5b	Dhrs9	Anks6
Crybg1	Dcakd	Pacsin3	Capn6
Slc16a7	Rtn1	Rassf2	Adgrf3
Hmg20b	Rdh12	Acss1	Gm10222
Mdh1	Arg2	Hps3	Trim6
Tnip1	Ccdc88c	Ppid	Ppp1r3e
Sdc1	Slc25a29	Slc27a3	Gm5532
Cmpk2	Fdft1	Cd1d1	Gm23935
Rsad2	Gadd45g	Eif4e	BC022960
Adcy3	Ctsl	Wls	Gm13340
Dnmt3a	Cxcl14	Ptgr1	Vgll3
Itgb3	Agtpbp1	Snx30	Neat1
Mink1	Glrx	Glipr2	Itpripl2
Pld2	F2rl2	Pdpn	Gm4076
Slc46a1	Iqgap2	Lrp8	Gm20594
Pik3r5	Scamp1	Sema3c	Gm26546
Nfkbia	Plk2	Smpdl3b	Gm26917
Atp6v1d	Plau	H6pd	Gm28439
Akr1c12	Gpr65	Acox3	Gm29216
Akr1c18	Sh3bp5	Rgs12	Gm37569
Npc2	Extl3	Rnf4	Gm43858
Fos	Olfm4	Klf3	Gm43071
Tnfaip2	Dok2	Rhoh	C430019N01Rik
Gpr132	Rcbtb2	Gsdme	CT010467.1
Gpr137b	Dab2	Tmf1	Gm43571
Sema4d	Slc7a8	Emp1	Gm44950
Golm1	Ctnnd2	Atf7ip	Gm44745
Sdha	Angpt1	Sbk2	AC119228.1
Hexb	Rangap1	Cd22	
Slc4a7	Parvg	Ppme1	
Pdhb	Ly6g	Il21r	
Plpp1	Ly6c2	Itgal	
Nr1d2	Cep97	F9	
Ktn1	Retnlg	Mtcp1	
Tsc22d1	Sdf2l1	Rps6ka3	
Epsti1	Muc13	Flna	
Ephx2	Dgkg	G6pdx	
Acod1	Samsn1	Dkc1	

Lrp10	Ets2	Proz	
Oxct1	Tmem50b	Thsd1	
Rai14	Tuba1b	Eri1	
Myo10	Creld2	Plpp5	
Atp6v1c1	Mmp25	Hpgd	
Dcstamp	Cyp39a1	Il34	
Oxr1	Treml1	Bbs2	
Aco2	Emilin2	Adgrg1	
Ppp1r1a	Prkd3	Hyou1	
1810013L24Rik	H2-Oa	Dock6	
Zfp263	Rab27b	Rab27a	
Mefv	Lmnb1	Mns1	
Cyc1	Cd74	Acsbg1	
Plec	Cndp2	Csk	
Gsdmd	Rab3il1	Amigo3	
Ly6e	Ms4a1	Pwp2	
Cd200	Ms4a3	Cip2a	
Boc	Tcf7l2	Afap1l1	
Serpind1	Dntt	Lss	
Tmem41a	Tm9sf3	Dis3	
St6gal1	Msr1	Szt2	
Parp9	Hdgfl3	Galnt9	
Slc11a2	Cd7	Lpar6	
Nus1	Adpgk	Tlr13	
Ivns1abp	Padi4	Pkd2	
Acy1	Esyt1	Zfp418	
Mx2	Adam8	Itga2b	
Tmem176a	Nrp1	Tmx4	
Agpat4	Pdia4	Acot11	
Igf2r	Hk3	Ncaph	
Slc29a1	Tram1	Rubcnl	
Nfkbie	Slc40a1	Ncapd3	
Calcr	Il18rap	1110059E24Rik	
Abcg1	Il1rl1	Emsy	
Cyp4f13	Il1r2	Iqce	
Spast	Slc11a1	Zfp280c	
Atp6v0c	Ing5	Stag3	
Hagh	Lrrfip1	Map11	
Tmem204	Rgs1	Ralgapa2	
Rgs11	Rassf5	Ddx1	
Fam234a	Ppfia4	Fam168b	
Plin3	Pycr2	Ptger2	
Cox7a2l	Vangl2	Ankrd9	
Tapbp	F5	Ccdc138	
Tap2	Sell	Ttc39b	
Sil1	Fam107b	Pgap3	
Lims2	Nek6	Mfsd14b	
Ppic	Prkcq	Bcl9	
Slc14a2	Lcn2	Dennd2a	
Dctn4	Cytip	Cul7	
Camk2a	Fcnb	Tctn1	
Anxa1	Hspa5	Rap1gap2	
Ms4a6b	Ly75	Zfp653	
Ehd1	Prg3	Txndc5	

Coro1b	Prg2	Taf4	
Pitpnm1	Itga6	Runx2	
Ltbp3	Api5	Cybc1	
Tctn3	Gatm	Nphp4	
Gsto1	Pcna	Gorab	
Ubtd1	Hdc	Gpr176	
Scd2	Il1b	Lrp1	
Nfkb2	Cd93	Olfr56	
Hexa	Tnik	Milr1	
Hsd17b10	Nceh1	Adam22	
Sat1	Mbnl1	Madd	
Cd63	P2ry1	Fzd7	
Baiap2	Il12a	Amot	
Pstpip2	Nup210l	Trem3	
Ifitm3	Tpm3	Ptpre	
Irf7	Adam15	Hnrnpf	
Tmem192	Zbtb7b	Slc26a9	
Clybl	Pear1	Stab1	
Uqcrc1	Gclm	AA986860	
Mcrip2	Zfp618	Crppa	
Ccr1	Reck	Hexim2	
Iscu	Plin2	Dpy19l3	
Pdgfa	Ak4	Slc36a4	
Nrp2	Slc2a1	Il1f9	
Raph1	Cap1	9930012K11Rik	
Stat1	Tinagl1	Ubtd2	
Ptpn18	Csf3r	Dipk2a	
Col19a1	Prom1	Hcar2	
Speg	Lrpap1	Wnk1	
Sp100	Emilin1	Pkd1l1	
Serpine2	Spp1	Stbd1	
Serpinb8	Pf4	Ldlrad3	
Slc45a3	Kdm2b	Mcat	
Klhl12	Anxa3	Pkd1l3	
Xpr1	Actb	Zfp689	
Coq8a	Dtx1	Ndnf	
Ifi211	Irf5	C5ar1	
Pter	Zyx	Ctu2	
Pkn3	Ephb6	Spty2d1	
Ralgds	Rpn1	Ccdc69	
Traf1	Ruvbl1	Suox	
Ifih1	Nup210	Amz1	
Fcna	Clec4d	Eif5a2	
Uap1l1	Olr1	B230217C12Rik	
Ube2l6	Klrd1	Zscan29	
Cd82	Plbd1	Gp1ba	
Pex16	Erp27	Ptges	
Snap23	Kras	P2ry10	
Idh3b	Dennd5b	Map10	
Cst3	Dmpk	2900026A02Rik	
Zbp1	Pglyrp1	Plpp7	
Fabp5	Siglecg	Gm45902	
Car2	Mef2a	Bbs12	
Pcmtd2	Ctsc	Wdfy4	

Epb41l1	Xylt1	Cebpe	
Src	Coro1a	Tmem171	
Gnb4	Cd19	Uba2	
Ocstamp	Dgat2	Tarm1	
Sucnr1	Nomo1	Zfp472	
Stxbp3	Mki67	Exoc6	
Adar	Slc9a9	Spcs3	
Ifi44	Gata1	Cadps	
Lmna	Awat2	Tmem62	
Ctsk	Bmx	Mmrn1	
Bdh2	Hcfc1	Tmem119	
Adgrl2	Zcchc18	Smim10l2a	
Atp6v0d2	Prps1	Rab39	
Gbp3	Mcf2l	Klf2	
Gbp2	F7	Rtl6	
Col15a1	F10	Izumo4	
Slc44a1	Cd209a	Ms4a4b	
Tmem38b	Tnfsf13b	Slc44a2	
Cd72	Hp	Chst3	
Nfia	Cx3cl1	Ece1	
Mycl	Crispld2	Zfp420	
Aldh4a1	Usp10	Akap17b	
Ak2	Ets1	Tmem26	
Rnf19b	Mcam	Zfp937	
Sh3bgrl3	Tle3	Zfp128	
Padi2	Ctsh	Sntb1	
Nub1	Plod2	Flot2	
Slc4a2	Dapk2	Glrp1	
Tnfrsf9	Nt5e	Brwd3	
Nmnat1	Ngp	Alms1	
Pex10	Ltf	Mocs1	
Morn1	Trib1	Zfp772	
Nadk	Acpp	Ifit1bl2	
Fosl2	Mapkapk3	Ninl	
Nsun7	Lmo2	Cst7	
Uchl1	Abcc4	Zfp120	
Abcg3	P2ry2	Apol9b	
Antxr2	Rasgrp2	Zfp975	
Rilpl1	Rnf125	B3gnt9	
Rilpl2	Slc22a15	Mmp27	
Rhof	Card10	Capza1	
Acad10	Gucy1a1	Fam217b	
Brap	Cd226	Peg12	
Oasl2	Ccnd3	Rbm44	
Asns	Cbl	Treml2	
Plxna4	Ramp1	Smim15	
Hibadh	Cyb561a3	Gspt2	
Fkbp9	Snx2	6720489N17Rik	
Tmem176b	Pik3ip1	4930522L14Rik	
Anxa4	Ly6d	Bhlhb9	
Slc6a6	Dgkh	Armcx5	
Bhlhe40	Dpp4	Efcab7	
Usp18	Egln3	Ceacam1	
Plxnd1	Pcyt1b	Sirpb1c	

Clec4a2	Ccl7	H60b	
Clec2d	Ccl2	Mon1b	
Ptpro	Ggta1	D130040H23Rik	
Ldhb	Ripor2	Tlr5	
Srgap3	Cd200r3	Gbp4	
Camk1	March1	Mroh2a	
Ccdc91	Card11	Nhsl2	
Rab38	H2-Aa	3110001I22Rik	
Mfge8	Chst12	Gm12708	
Pik3c2a	Dennd3	Slc2a4rg-ps	
Mvp	Smad6	AI427809	
Fchsd2	Rab8b	BC064078	
Nupr1	Lrg1	Med20	
Lat	Ldlrap1	Gm20939	
Pak1	Traf3ip3	Zfp799	
Bcat2	Map4k1	Zfp994	
Rgs10	Paqr7	Zfp850	
Uqcrc2	Azin1	Gm16712	
Fam53b	H2-DMa	9230114K14Rik	
Atp6ap2	Ppp1r16b	2700038G22Rik	
St5	Camp	A930007I19Rik	
Arhgef6	C1rl	4933404O12Rik	
Plp2	Akap12	Gm29170	
Wdr13	Vill	Gm43696	
Il2rg	Siglecf	Gm43775	
Psmd10	F13a1	Nup62	
Col4a2	Akna	9330162G02Rik	
Smim19	Gimap3	Gm36445	
Fgfr1	Rftn1	Gm3325	
Mt3	Ncam1	Gm5165	
Coq9	Cpeb2	Gm50010	
B3gnt3	Hip1	AC132148.1	
Ifi30	Gnaz	AC154328.1	
Rrad	Tbc1d10c		
Aplp2	Bach2		
Birc3	Suco		
Clmp	Ctsg		
Acat1	Klhl32		
Slc37a2	Tex2		
Myo1e	Cd79b		
Tcf12	Clcf1		
Anxa2	Phc1		
Sh3bgrl2	Chil3		
Pstpip1	Phf8		
Stoml1	Inhba		
Tpm1	Irf8		
Atp1b3	H2-Ob		
Mst1r	Tmem273		
Uba7	Pde3a		
Oas3	Ipo9		
Cd59a	Slc16a6		
Oas2	Zfp239		
Kank1	Trem1		
Resf1	Itga1		

Tpcn1	Ubash3a		
Cspg4	Id1		
Chpf	Flt3		
Nfatc1	Sbk1		
Gas7	Fam129c		
Lpcat2	Filip1l		
Rac2	2510009E07Rik		
Rtp4	B430306N03Rik		
Atp6v0b	S1pr4		
Gucd1	Serpinb1a		
Cryzl2	6330549D23Rik		
Rbfox2	Fpr1		
Myo6	Penk		
St18	Mtus1		
Atp6v1h	Plaur		
Ppargc1b	Unc119b		
Lgals3bp	Tifa		
Ifit1	Ckap4		
Uaca	Ltb4r1		
Ppm1h	Cd24a		
Gns	Cd300lf		
Grn	Gp5		
Ttyh2	Nat8l		
Cnot6l	Smim5		
Mfsd12	Jaml		
Cxcl10	Mrgpre		
Pip5k1c	Ccr2		
Myo1d	Sorl1		
Isg15	Tifab		
Cox8a	Mmp12		
Acaa1a	Gpr171		
Hist1h1c	Haspin		
Slc18a1	Gpr18		
Kidins220	Sept6		
Ubac1	Mmp13		
P2ry14	Adgb		
Ppfibp2	Ffar2		
Ndrg4	Tacstd2		
Eepd1	Siglech		
Clcn7	Mafg		
Pnpla7	Kctd14		
Acaa2	Btla		
C1qa	Cd177		
Pml	Fpr2		
Apbb1	Ankrd44		
Smpd1	Nrros		
Scd1	Nup188		
Syn1	Rab7b		
Aagab	Lamb2		
Tap1	Gpr141		
Nudt22	Phgdh		
Icam1	Cnn3		
Rapgef6	Pkp3		
Vash2	Adam10		

Vopp1	Lrrc8c		
Fbxw17	Elp6		
Ifi206	Per2		
Ankrd13b	S100a8		
Ndufv1	S100a9		
Slc9b2	St3gal5		
Trappc11	Pard6g		
Phf20	Prss34		
Prdm1	Tmem154		
Pde4dip	Chst13		
F11r	Ebf1		
Snx10	Eif1a		
Uqcrfs1	Prtn3		
Mcl1	Tubb2a		
Ctss	Nfe2		
Dgki	Slc14a1		
Ephx1	B3gnt8		
A230050P20Rik	Fcgr3		
Ctu1	Tmem40		
Supt3	Adgrg3		
Slco4a1	H2-Eb1		
Cpq	Gmfg		
Arpin	Stat4		
Anpep	Tmed5		
Atp6v1g1	Nr6a1		
Fam102a	Ipcef1		
Dap	Rab44		
1110008P14Rik	Chil1		
Znfx1	H2-Q10		
Ccser1	Clec4b2		
Mrps6	Tnfrsf13c		
Fnbp1l	Mgam		
Orai2	4930438A08Rik		
Arhgap29	Mpzl3		
Gsap	Ccnd1		
Dtx4	Hs3st3b1		
Ifi203	Skint3		
Stat2	9830107B12Rik		
Mrps35	H2-Ab1		
Gbp7	Kti12		
Ddx58	Gm1966		
Sec1	Nxpe3		
Etfrf1	Carns1		
Spns2	Igkc		
Xaf1	Ighm		
Ofd1	Iglv1		
Sft2d2	Iglc2		
Mul1	Iglv3		
Shtn1	Iglv2		
Cdc42ep4	F630028O10Rik		
Tdrkh	Gm3550		
AW549877	Nlrp12		
Agrn	Zfp970		
Pkp2	Gm14221		

S100a10	Gm8818		
Rapgef5	Ccr5		
Igsf3	Slc48a1		
Abhd14b	Snhg17		
Arsb	F730016J06Rik		
Tent2	4933424M12Rik		
Sestd1	Gm8113		
Fam83g	Gimap1		
Abcb4	Serpinb10		
Trafd1	Igha		
Hebp1	Nim1k		
Krba1	Mrgpra2b		
Serpinb6b	Gm26724		
Ppp2r3a	Peak1os		
Hpdl	Gm16675		
Fbrsl1	Mirt1		
Clec4a3	Bin2		
Als2cl	Ly6a2		
S100a1	Gm37168		
Pheta1	Gm38248		
Dock5	C130089K02Rik		
Fahd1	Gm37510		
Proser2	Gm42462		
Fndc7	Iglc3		
Epcam	Iglc1		
Cdc42ep2	4921529L05Rik		
Pqlc3	Gm5086		
Ifit2	Mirt2		
Cd109	Gm35853		
Bdh1	Itprip		
Bst2			
Irgm1			
Flrt2			
Gpr68			
Ust			
Diras2			
Phldb1			
Acap2			
Chchd10			
Vsig8			
Gpr55			
Lig4			
2810025M15Rik			
C77080			
Ncald			
Irf2bp2			
Acvr2a			
Slc39a1			
Atp6v1a			
Oas1a			
Junb			
Clec12a			
Gm9920			
Sh2d4a			

Ndst1			
Slfn5			
Oscar			
Nyap2			
Agap1			
Sugct			
Kbtbd11			
H2-T22			
Pgpep1			
Trim12c			
Sdhc			
Nfam1			
Tspan7			
Wdr91			
Pirb			
Vwa8			
Kcp			
Fxyd2			
Clec4a4			
Dbp			
Kmt5c			
Serpinb6a			
Zfp462			
Tor3a			
Eno3			
B2m			
H2-K1			
Akap6			
Gdpd1			
Ext1			
Akr1b10			
Rufy4			
Zfp27			
Iah1			
Nectin2			
Tmem65			
Ifit3b			
Klhl24			
Acadm			
Msln			
Rnf183			
Ifi27			
Tank			
mt-Nd1			
mt-Nd2			
mt-Atp6			
mt-Co3			
mt-Cytb			
Ifi208			
Oas1g			
H2-T23			
Trmt2b			
Phf11d			
Htra2			

Hist2h2be			
Ahnak			
Irgm2			
Rnf213			
Tmem35b			
Klhl9			
Ubxn1			
Csf2rb2			
Ncf4			
Slfn2			
Ahnak2			
H2-D1			
Ifi204			
Ifi207			
Ppp1r12b			
Plekhf1			
Dnajb14			
Spint2			
Gm14548			
Gm15448			
Fat3			
Ifit3			
Ly6a			
Ass1			
Plekhn1			
Ifi47			
Ifi27l2a			
Serpinb1c			
Cyp4v3			
Ifit1bl1			
St6galnac4			
Tm4sf19			
Xlr4a			
Spaca6			
Gm15922			
Gm15931			
Gm12366			
Gm12892			
Esrp2			
Tmem250-ps			
Slc5a3			
Gm16536			
Pira2			
Ifi203-ps			
Siglec15			
Malat1			
Gm21188			
4930556M19Rik			
2210008F06Rik			
Gpr137b-ps			
Ptprv			
2310069B03Rik			
Gm10925			
Gm28437			

Gm37949			
Tstd1			
Gm19026			
Gm20056			
Gm20559			
4833415N18Rik			
4833438C02Rik			

Supplementary figures for chapter 4

Table SB 1, Table SB 2: Raw values from Luminex cytokine/chemokine profiling experiments from supernatants of in vitro infected OCLs from WT mice. OCLs were infected in vitro at day 6 of differentiation with BCG of an MOI of 5 for 3 hrs. After 3 hrs, extracellular bacteria were washed, and cells were harvested for 24 hrs. 24 h.p.i, supernatants were harvested and stored at -20°C before being sent for Luminex. OOR< : Values are lower than LLOQ and unable to extrapolate, OOR> : Values are higher than HLOQ and unable to extrapolate. HLOQ=highest limit of quantification. LLOQ=lowest limit of quantification. Un=uninfected. In=in vitro infected.

Table SB1

	G-CSF	IL-10 (13)	IL-3 (14)	LIF (18)	IL-1 beta	IL-2 (20)	M-CSF	IP-10	IL-4 (26)	IL-5 (27)	IL-6 (28)	IFN alpha	IL-22 (33)	IL-9 (34)	IL-13 (35)	IL-27 (36)	IL-23 (37)	IFN	IL-12p70	GM-CSF	GRO alpha	RANTES	TNF alpha	MIP-1	MCP-3	MCP-1	IL-17A	IL-15 (54)	MIP-2	IL-1 alpha	ENA-78	Eotaxin	IL-28 (64)	IL-18 (66)	MIP-1	IL-31 (76)
LLOQ	1.42	2.05	0.38	1.55	1.44	1.84	0.18	0.72	1.35	2.18	5.5	2.94	12.82	21.3	2.77	11.12	11.45	2.2	2.35	3.2	2.44	2.34	3.67	0.59	0.26	11.49	2.37	1.97	0.82	3.25	6.99	0.67	30.96	35.43	0.84	10.07
HLOQ	1372.18	2086.5	387.94	1703.84	1505.51	1924.73	187.06	749.93	1464.87	2249.61	5683.61	3599.83	13383.87	21916.18	3084.05	2475.38	11989.16	1996.24	606.8	3596.41	2566.15	2606.1	3575.95	614.98	231.47	9594.68	2513.48	2085.5	1053.71	3443.69	6896.69	686.58	32731.19	36531.79	778.46	10361.15
(1) Un	OOR <	2.41	OOR <	2.33	OOR <	OOR <	OOR <	OOR >	OOR <	OOR <	OOR <	*0.80	*1.88	OOR <	OOR <	*5.42	OOR <	*0.56	*0.08	OOR <	*2.19	14.41	*2.35	1.32	163.88	1652.79	*0.23	OOR <	8.55	3.2	15.53	13.6	OOR <	OOR <	8.74	OOR <
(1) In	319.11	95.54	OOR <	6.57	2.03	2.9	*0.06	OOR >	*0.32	*1.84	1939.56	OOR <	OOR <	OOR <	OOR <	*8.28	OOR <	6.69	6.6	8.75	OOR >	475.41	OOR >	56.96	*3302.77	OOR >	OOR <	*0.47	OOR >	3.2	50.19	57.55	OOR <	500.34	OOR >	*0.42
(2) Un	OOR <	6.54	OOR <	*1.24	OOR <	OOR <	OOR <	OOR >	OOR <	*0.03	OOR <	39.31	OOR <	OOR <	OOR <	*3.96	OOR <	*0.13	OOR <	OOR <	11.26	41.92	4.53	4.19	*1228.62	2931.6	OOR <	OOR <	14.14	OOR <	38.32	19.29	OOR <	OOR <	26.66	OOR <
(2) In	251.1	92.28	OOR <	3.68	1.7	2.46	*0.01	OOR >	*0.10	*1.93	1866.35	OOR <	OOR <	OOR <	3.05	16.81	OOR <	6.55	5.75	7.38	OOR >	1063.19	*5730.13	52.87	*3392.79	OOR >	OOR <	*0.34	OOR >	3.72	38.32	71.94	OOR <	475.19	OOR >	OOR <

(3) In	(3) Un
251.1	OOR <
22.53	3.83
OOR <	OOR <
2.58	2.22
*0.16	OOR <
*0.09	OOR <
OOR <	OOR <
OOR >	OOR >
OOR <	OOR <
OOR <	OOR <
139.54	OOR <
OOR <	OOR <
OOR <	OOR <
OOR <	OOR <
*2.46	*0.84
OOR <	OOR <
*0.88	*0.18
*0.92	OOR <
OOR <	OOR <
1199.14	7.27
162.48	27.27
171.51	4.55
15.7	2.16
*3233.58	782.29
OOR >	1358.77
OOR <	OOR <
OOR <	OOR <
OOR >	17.79
*1.93	OOR <
27.26	OOR <
50.98	15.65
OOR <	OOR <
67.99	OOR <
470.52	10.5
OOR <	OOR <

Table SB2

(4) In	(4) Un	HLOQ	LLOQ	
34.46	*0.98	343.81	1.34	**G-CSF**
63.57	12.41	8086.53	2.04	**IL-10**
*0.16	*0.14	1497.97	0.38	**IL-3**
5.38	5.03	1681.87	1.75	**LIF**
*0.57	*0.12	1036.89	1.44	**IL-1 beta**
1.91	*0.02	1913.48	1.86	**IL-2**
*0.04	*0.09	184.23	0.18	**M-CSF**
OOR >	OOR >	3002.16	2.38	**IP-10**
OOR <	OOR <	6071.2	1.37	**IL-4**
*0.63	OOR <	8677.37	2.14	**IL-5**
753.4	*3.36	22658.99	5.56	**IL-6**
*11.48	29.38	2577.43	13.22	**IFN alpha**
*6.90	*6.38	60843.38	12.93	**IL-22**
*10.47	*12.47	20036.21	21.34	**IL-9**
6.72	3.44	2945.74	2.81	**IL-13**
3.97	OOR <	11899.11	2.41	**IL-27**
17.12	*9.63	47104.62	11.52	**IL-23**
2.28	OOR <	1885.26	2.19	**IFN**
*2.10	*0.29	532.58	2.33	**IL-12p70**
5.17	OOR <	2427.07	3.21	**GM-CSF**
OOR >	27.36	2401.97	3.09	**GRO alpha**
508.43	101.85	2018.21	2.03	**RANTES**
313.48	8.88	813.54	3.63	**TNF alpha**
67.47	23.72	593.05	0.69	**MIP-1**
OOR >	OOR >	249.8	0.25	**MCP-3**
OOR >	OOR >	9575.13	29.1	**MCP-1**
*1.38	*1.24	10838.55	2.39	**IL-17A**
*1.05	*0.87	1816.18	1.99	**IL-15**
OOR >	63.79	1031.79	3.84	**MIP-2**
*2.36	*1.05	3573.95	3.25	**IL-1 alpha**
322.92	OOR <	6889.73	7.4	**ENA-78**
60.42	50.42	2970.39	0.62	**Eotaxin**
*5.18	OOR <	147260.9	31	**IL-28**
338.38	*5.87	36309.75	35.64	**IL-18**
OOR >	96.91	871.91	0.8	**MIP-1 beta**
OOR <	OOR <	9631.45	10.1	**IL-31**

Table SB 3: Raw values from Luminex cytokine/chemokine profiling experiments from supernatants of in vivo BCG infected murine OCLs. Mice were infected with in vivo for 30 days with a CFU of 10^6 BCG or PBS in 100µl. After 30 days, mice were sacrificed and OCLs were differentiated for 7 days. At day 7, supernatants were harvested and stored at -20°C before being sent for Luminex. OOR< : Values are lower than LLOQ and unable to extrapolate, OOR> : Values are higher than HLOQ and unable to extrapolate. HLOQ=highest limit of quantification. LLOQ=lowest limit of quantification. Un=mock infected/'uninfected'. In=in vivo infected.

(3) In	(2) In	(1) In	(3) Un	(2) Un	(1) Un	HLOQ	LLOQ	
32.97	3.32	1.57	OOR <	OOR <	*0.98	343.81	1.34	**G-CSF (CSF-3)**
76.23	9.47	13.16	6.54	2.41	12.41	8086.53	2.04	**IL-10**
*0.16	0.44	*0.22	OOR <	OOR <	*0.14	1497.97	0.38	**IL-3**
6.06	4.19	4.98	*1.24	2.33	5.03	1681.87	1.75	**LIF**
*0.59	*0.62	*0.17	OOR <	OOR <	*0.12	1036.89	1.44	**IL-1 beta**
2.52	2.78	*0.82	OOR <	OOR <	*0.02	1913.48	1.86	**IL-2**
*0.10	*0.11	*0.09	OOR <	OOR <	*0.09	184.23	0.18	**M-CSF**
OOR >	OOR >	OOR >	OOR >	OOR >	OOR >	3002.16	2.38	**IP-10**
OOR <	OOR <	OOR <	OOR <	OOR <	OOR <	6071.2	1.37	**IL-4**
*0.80	*0.52	OOR <	*0.03	OOR <	OOR <	8677.37	2.14	**IL-5**
836.11	7.06	8.14	OOR <	OOR <	*3.36	22658.99	5.56	**IL-6**
40.12	42.68	41.7	39.31	*0.80	29.38	2577.43	13.22	**IFN alpha**
*6.90	13.73	*6.38	OOR <	*1.88	*6.38	60843.38	12.93	**IL-22**
*18.10	34.47	*9.78	OOR <	OOR <	*12.47	20036.21	21.34	**IL-9**
7.6	5.95	3.22	OOR <	OOR <	3.44	2945.74	2.81	**IL-13**
5.97	*1.36	OOR <	*3.96	*5.42	OOR <	11899.11	2.41	**IL-27**
20.82	39.12	11.52	OOR <	OOR <	*9.63	47104.62	11.52	**IL-23**
4.22	*0.85	*0.21	*0.13	*0.56	OOR <	1885.26	2.19	**IFN GAMMA**
2.96	*1.82	*0.31	OOR <	*0.08	*0.29	532.58	2.33	**IL-12p70**
6.01	4.37	OOR <	OOR <	OOR <	OOR <	2427.07	3.21	**GM-CSF**
OOR >	15.76	33.49	11.26	*2.19	27.36	2401.97	3.09	**GRO alpha**
602.18	92.02	105.3	41.92	14.41	101.85	2018.21	2.03	**RANTES**
739.4	9.28	12.32	4.53	*2.35	8.88	813.54	3.63	**TNF alpha**
73.57	27.05	22.04	4.19	1.32	23.72	593.05	0.69	**MIP-1 alpha**
OOR >	*4641.53	OOR >	*1228.62	163.88	OOR >	249.8	0.25	**MCP-3 (CCL7)**
OOR >	5291.25	OOR >	2931.6	1652.79	OOR >	9575.13	29.1	**MCP-1 (CCL2)**
*1.76	*2.27	*1.89	OOR <	*0.23	*1.24	10838.55	2.39	**IL-17A (CTLA-**
*1.19	*1.53	*1.01	OOR <	OOR <	*0.87	1816.18	1.99	**IL-15**
OOR >	47.1	117.77	14.14	8.55	63.79	1031.79	3.84	**MIP-2 alpha**
3.66	4.07	*1.65	OOR <	OOR <	*1.05	3573.95	3.25	**IL-1 alpha**
118.12	100.93	38.9	OOR <	15.53	OOR <	6889.73	7.4	**ENA-78**
59.15	38.12	48.99	19.29	13.6	50.42	2970.39	0.62	**Eotaxin**
*13.12	61.73	*5.18	OOR <	OOR <	OOR <	147260.9	31	**IL-28**
342.65	*16.38	*16.38	OOR <	OOR <	*5.87	36309.75	35.64	**IL-18**
OOR >	24.11	110.98	26.66	8.74	96.91	871.91	0.8	**MIP-1 beta**
OOR <	*7.09	OOR <	OOR <	OOR <	OOR <	9631.45	10.1	**IL-31**

Supplementary figures for chapter 5

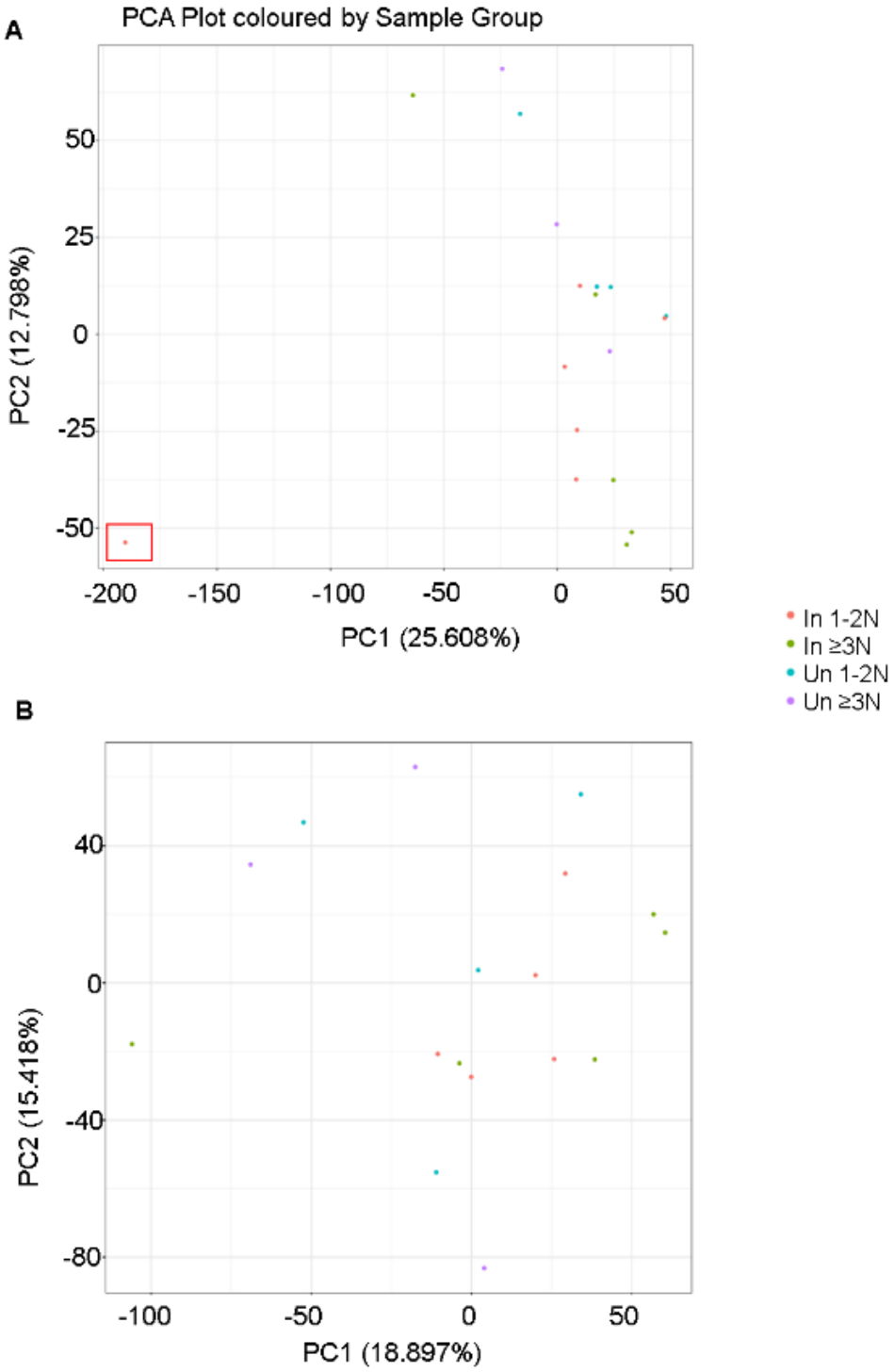

Figure SC 1: Plots of the principal component analysis (PCA) coloured by sample group. The plots represent a biological replicate. PCA plot (A) before and (B) after the removal of an outlier sample (outlined in red box).

Table SC 1: Differentially expressed genes between uninfected OCLs and in vitro BCG infected OCLs with a FDR<0.05 and Log_2FoldChange > |0.6.: (A) Un 1-2N vs Un ≥3N (B) Un 1-2N vs In 1-2N (C) Un ≥3N vs In ≥3N.

A Un 1-2N vs Un ≥3N: 89 DEGs

Gene_ID	Gene_name	Gene_type	Log2FoldChange	padj
ENSMUSG00000048232.12	Fbxo10	protein_coding	-9.90857	4.04E-09
ENSMUSG00000039634.12	Zfp189	protein_coding	-11.0124	9.57E-09
ENSMUSG00000074364.6	Ehd2	protein_coding	-3.384	5.15E-08
ENSMUSG00000020160.18	Meis1	protein_coding	-5.77592	1.66E-07
ENSMUSG00000072066.7	6720489N17Rik	protein_coding	-8.62652	3.54E-07
ENSMUSG00000051034.7	Zfp11	protein_coding	-8.7829	5.06E-07
ENSMUSG00000046380.3	Jrk	protein_coding	-9.41733	9.51E-07
ENSMUSG00000021696.9	Elovl7	protein_coding	-9.82253	1.56E-06
ENSMUSG00000079659.5	Tmem243	protein_coding	-5.33709	7.7E-06
ENSMUSG00000102861.1	Gm37637	lncRNA	-8.73815	7.7E-06
ENSMUSG00000028578.8	Caap1	protein_coding	-6.98128	3.77E-05
ENSMUSG00000037583.2	Nr0b2	protein_coding	-8.14949	3.77E-05
ENSMUSG00000024970.5	Spindoc	protein_coding	-8.11191	3.9E-05
ENSMUSG00000025453.18	Nnt	protein_coding	-8.0395	3.9E-05
ENSMUSG00000102664.1	Gm38380	TEC	8.58358	4.08E-05
ENSMUSG00000037007.17	Zfp113	protein_coding	-5.98255	7E-05
ENSMUSG00000043153.6	Crppa	protein_coding	-7.5875	7.7E-05
ENSMUSG00000109781.1	Gm45509	lncRNA	9.069079	0.000114
ENSMUSG00000097429.1	Gm26520	lncRNA	-6.71385	0.000138
ENSMUSG00000024597.11	Slc12a2	protein_coding	-6.6256	0.000138
ENSMUSG00000014686.8	Ceacam16	protein_coding	-8.006	0.000484
ENSMUSG00000029664.10	Tfpi2	protein_coding	-8.76936	0.00058
ENSMUSG00000057894.10	Zfp329	protein_coding	-6.33073	0.000585
ENSMUSG00000060336.6	Zfp937	protein_coding	-5.56504	0.000585
ENSMUSG00000021906.14	Oxnad1	protein_coding	-1.71699	0.000635
ENSMUSG00000042279.13	H1foo	protein_coding	-7.33888	0.00069
ENSMUSG00000049038.3	Mterf2	protein_coding	-8.31783	0.000732
ENSMUSG00000074634.12	Tmem267	protein_coding	-8.04636	0.001045
ENSMUSG00000045071.14	E130308A19Rik	protein_coding	-8.71486	0.00109
ENSMUSG00000064339.1	mt-Rnr2	Mt_rRNA	3.337697	0.001149
ENSMUSG00000019437.17	Tlcd1	protein_coding	-4.49136	0.001281
ENSMUSG00000039678.12	Tbc1d13	protein_coding	-1.91369	0.001391
ENSMUSG00000032281.11	Acsbg1	protein_coding	-9.87577	0.001391
ENSMUSG00000020669.15	Sh3yl1	protein_coding	-7.81264	0.001536
ENSMUSG00000014164.15	Klhl3	protein_coding	-8.17846	0.002091
ENSMUSG00000101225.1	1700008J07Rik	lncRNA	-7.30201	0.002254
ENSMUSG00000091474.2	2610021A01Rik	protein_coding	-5.95493	0.003193
ENSMUSG00000105176.1	Gm43668	TEC	-8.48813	0.003464

ENSMUSG00000083563.1	Gm13340	unprocessed_pseudogene	3.068724	0.003494
ENSMUSG00000031549.16	Ido2	protein_coding	-8.2657	0.003936
ENSMUSG00000031390.8	Avpr2	protein_coding	-7.36737	0.004052
ENSMUSG00000067276.5	Capn6	protein_coding	-10.5029	0.004073
ENSMUSG00000033478.5	Fam160b1	protein_coding	-3.14049	0.004973
ENSMUSG00000032280.16	Tle3	protein_coding	4.214652	0.005498
ENSMUSG00000028309.14	Rnf20	protein_coding	1.11158	0.006124
ENSMUSG00000009292.18	Trpm2	protein_coding	-4.46091	0.006574
ENSMUSG00000096887.2	Gm20594	protein_coding	3.375726	0.007748
ENSMUSG00000021179.8	Nrde2	protein_coding	1.084024	0.010196
ENSMUSG00000003123.15	Lipe	protein_coding	1.18067	0.010196
ENSMUSG00000039831.16	Arhgap29	protein_coding	-5.35055	0.010196
ENSMUSG00000064337.1	mt-Rnr1	Mt_rRNA	2.995125	0.0106
ENSMUSG00000095325.3	Zfp870	protein_coding	-8.99834	0.011544
ENSMUSG00000021693.20	Kif2a	protein_coding	1.401452	0.011544
ENSMUSG00000043284.12	Tmem11	protein_coding	-0.87493	0.01165
ENSMUSG00000027805.16	Pfn2	protein_coding	-4.31446	0.014897
ENSMUSG00000104388.1	Gm37033	TEC	7.953499	0.018176
ENSMUSG00000029370.10	Rassf6	protein_coding	-7.99047	0.018176
ENSMUSG00000104761.1	Gm43511	TEC	-5.57521	0.019038
ENSMUSG00000026196.7	Bard1	protein_coding	-4.07395	0.019653
ENSMUSG00000063535.7	Zfp773	protein_coding	-9.49535	0.019653
ENSMUSG00000020894.16	Vamp2	protein_coding	-1.48796	0.019653
ENSMUSG00000101249.1	Gm29216	unprocessed_pseudogene	2.934532	0.021003
ENSMUSG00000064351.1	mt-Co1	protein_coding	2.87042	0.021381
ENSMUSG00000027983.13	Cyp2u1	protein_coding	-5.20029	0.022242
ENSMUSG00000060098.11	Prmt7	protein_coding	-0.81221	0.024711
ENSMUSG00000031750.15	Il34	protein_coding	-7.36377	0.024711
ENSMUSG00000100862.1	Gm10925	unprocessed_pseudogene	3.375142	0.025387
ENSMUSG00000109390.1	Gm45718	TEC	-8.13827	0.025387
ENSMUSG00000024604.7	Rbm22	protein_coding	-0.71425	0.029643
ENSMUSG00000073755.4	5730409E04Rik	protein_coding	-6.84647	0.03001
ENSMUSG00000100131.1	Gm28439	unprocessed_pseudogene	2.528857	0.030176
ENSMUSG00000097354.7	2310001H17Rik	lncRNA	-3.80143	0.030176
ENSMUSG00000115249.1	Gm49085	lncRNA	-7.7372	0.031203
ENSMUSG00000020475.3	Pgam2	protein_coding	-7.49434	0.031949
ENSMUSG00000030393.8	Zik1	protein_coding	-9.13399	0.033121
ENSMUSG00000068744.12	Psrc1	protein_coding	1.123688	0.035125
ENSMUSG00000027797.15	Dclk1	protein_coding	-6.34076	0.035828
ENSMUSG00000026768.10	Itga8	protein_coding	-9.38314	0.035865
ENSMUSG00000022074.6	Tnfrsf10b	protein_coding	-4.93358	0.03717
ENSMUSG00000047766.15	Lrrc49	protein_coding	2.804083	0.03717
ENSMUSG00000044847.13	Lsm11	protein_coding	-9.00661	0.03717
ENSMUSG00000029403.14	Cdkl2	protein_coding	-9.45251	0.038317
ENSMUSG00000005220.10	Corin	protein_coding	-9.2213	0.038317
ENSMUSG00000041797.7	Abca9	protein_coding	2.857344	0.044045
ENSMUSG00000027722.14	Spata5	protein_coding	-1.56651	0.044943
ENSMUSG00000002504.15	Slc9a3r2	protein_coding	-4.83551	0.045592
ENSMUSG00000049999.4	Ppp1r3d	protein_coding	-6.28382	0.048368

ENSMUSG00000102344.1	9430053O09Rik	TEC	-5.60443	0.048369
ENSMUSG00000072568.4	Fam84b	protein_coding	-1.26553	0.048838

B: ***Un 1-2N vs In 1-2N: 48 DEGs***

Gene_ID	Gene_name	Gene_type	Log2FoldChange	padj
ENSMUSG00000038429.10	Usp5	protein_coding	-0.64217	0.0189
ENSMUSG00000041926.15	Rnpep	protein_coding	-0.67779	0.042201
ENSMUSG00000030062.7	Rpn1	protein_coding	-0.71992	0.042755
ENSMUSG00000030956.15	Fam53b	protein_coding	-0.72217	0.026243
ENSMUSG00000034757.15	Tmub2	protein_coding	-0.77623	0.000824
ENSMUSG00000001211.15	Agpat3	protein_coding	-0.81831	0.006284
ENSMUSG00000037251.5	Pomk	protein_coding	-1.1453	0.026243
ENSMUSG00000014778.10	Fhod1	protein_coding	-1.23646	0.0189
ENSMUSG00000041143.16	Tmco4	protein_coding	-1.95028	3.04E-06
ENSMUSG00000045917.17	Tmem268	protein_coding	-2.08268	0.001336
ENSMUSG00000024140.10	Epas1	protein_coding	-2.69352	0.025852
ENSMUSG00000013974.3	Mcemp1	protein_coding	-2.76776	0.036354
ENSMUSG00000005800.3	Mmp8	protein_coding	-3.28182	3.5E-05
ENSMUSG00000032280.16	Tle3	protein_coding	-3.99313	0.006117
ENSMUSG00000042265.13	Trem1	protein_coding	-5.7474	0.007217
ENSMUSG00000116702.1	Gm6553	processed_pseudogene	-5.85751	0.000876
ENSMUSG00000074738.2	Fndc10	protein_coding	-7.2308	0.007915
ENSMUSG00000087385.8	Frg2f1	protein_coding	-7.29811	0.007217
ENSMUSG00000028071.12	Sh2d2a	protein_coding	-7.45337	0.042201
ENSMUSG00000025867.8	Cplx2	protein_coding	-7.76851	0.004408
ENSMUSG00000027894.14	Slc6a17	protein_coding	-8.24652	0.011745
ENSMUSG00000100291.6	2310069B03Rik	lncRNA	-8.31118	0.003407
ENSMUSG00000043648.7	Pld6	protein_coding	-8.34302	0.025852
ENSMUSG00000087242.2	C78197	lncRNA	-8.37844	0.003383
ENSMUSG00000091764.3	Zfp964	protein_coding	-8.93199	0.001363
ENSMUSG00000020017.14	Hal	protein_coding	-8.94554	1.53E-06
ENSMUSG00000023032.12	Slc4a8	protein_coding	-9.78477	6.63E-10

C*: In ≥3N vs Un ≥3N: 83 DEGs*

Gene_ID	Gene_name	Gene_type	Log2FoldChange	padj
ENSMUSG00000018678.13	Sp2	protein_coding	1.046719	0.047246
ENSMUSG00000007872.3	Id3	protein_coding	1.580899	0.047439
ENSMUSG00000031093.14	Dock11	protein_coding	1.635952	0.000855
ENSMUSG00000020227.10	Irak3	protein_coding	1.679429	0.046513
ENSMUSG00000046341.5	Gm11223	processed_pseudogene	1.828864	0.001949
ENSMUSG00000029687.16	Ezh2	protein_coding	2.417193	0.002869
ENSMUSG00000031613.9	Hpgd	protein_coding	4.398036	0.009577
ENSMUSG00000020044.13	Timp3	protein_coding	5.19676	0.002683

ENSMUSG00000053931.11	Cnn3	protein_coding	5.263862	0.007259
ENSMUSG00000023034.7	Nr4a1	protein_coding	5.464056	0.039253
ENSMUSG00000028328.13	Tmod1	protein_coding	5.506594	0.009043
ENSMUSG00000028082.14	Sh3d19	protein_coding	5.579991	0.034122
ENSMUSG00000088504.1	Gm26490	snoRNA	6.753806	0.02047
ENSMUSG00000030782.16	Tgfb1i1	protein_coding	6.843384	0.027968
ENSMUSG00000038068.15	Rnf144b	protein_coding	7.01979	6.86E-06
ENSMUSG00000050503.9	Fbxl22	protein_coding	7.097148	0.022464
ENSMUSG00000031162.14	Gata1	protein_coding	7.179614	0.039253
ENSMUSG00000075502.2	Kbtbd6	protein_coding	7.445313	1.41E-05
ENSMUSG00000019997.11	Ccn2	protein_coding	7.668743	0.020432
ENSMUSG00000109781.1	Gm45509	lncRNA	7.726205	0.001727
ENSMUSG00000033436.13	Armcx2	protein_coding	7.75646	7.29E-05
ENSMUSG00000023993.7	Treml1	protein_coding	7.824836	0.001949
ENSMUSG00000038793.8	Lefty1	protein_coding	8.062539	0.007993
ENSMUSG00000063383.5	Zfp947	protein_coding	8.470779	0.00388
ENSMUSG00000072653.14	Zfp783	transcribed_unprocessed_pseudogene	9.276158	0.04252
ENSMUSG00000000320.10	Alox12	protein_coding	9.770536	0.018852
ENSMUSG00000047786.12	Lix1	protein_coding	9.789625	1.6E-10
ENSMUSG00000004267.16	Eno2	protein_coding	10.91361	0.032554

Table SC 2: p-values determined by for Wilcoxon statistical test to determine the statistical significance of transcriptomic changes in each cluster of the heatmap of 199 unique DEGs.

Cluster 1	**Comparison**	**Infected ≥3N**	**Uninfected ≥3N**	**Infected 1-2N**
1	Uninfected ≥3N	1.57E-05		
1	Infected 1-2N	0.803104934	0.000123889	
1	Uninfected 1-2N	0.000155709	0.119804055	0.001145022
2	Uninfected ≥3N	0.422782272		
2	Infected 1-2N	0.422782272	0.973411315	
2	Uninfected 1-2N	0.973411315	0.422782272	0.422782272
3	Uninfected ≥3N	3.40E-07		

3	Infected 1-2N	0.24331141	1.26E-09	
3	Uninfected 1-2N	1.04E-07	1.59E-13	2.64E-06
4	Uninfected ≥3N	2.52E-05		
4	Infected 1-2N	0.359392025	4.09E-06	
4	Uninfected 1-2N	0.286370234	0.009195102	0.10084378
5	Uninfected ≥3N	0.8384088		
5	Infected 1-2N	0.822877541	0.8384088	
5	Uninfected 1-2N	0.822877541	0.8384088	0.8384088

Table SC 3: List of genes in each cluster for unbiased clustering analysis for in vitro dataset

Gene Name	Gene ID	Cluster
Alox12	ENSMUSG00000000320.10	1
Eno2	ENSMUSG00000004267.16	1
Cmah	ENSMUSG00000016756.17	1
Sp2	ENSMUSG00000018678.13	1
Timp3	ENSMUSG00000020044.13	1
Pbk	ENSMUSG00000022033.9	1
Ctnnd2	ENSMUSG00000022240.10	1
Knstrn	ENSMUSG00000027331.15	1
Rnf20	ENSMUSG00000028309.14	1
Tmod1	ENSMUSG00000028328.13	1
Ezh2	ENSMUSG00000029687.16	1
Ddias	ENSMUSG00000030641.10	1
Dock11	ENSMUSG00000031093.14	1
Gata1	ENSMUSG00000031162.14	1
L1cam	ENSMUSG00000031391.18	1
Hpgd	ENSMUSG00000031613.9	1
Bbs10	ENSMUSG00000035759.4	1
Rnf144b	ENSMUSG00000038068.15	1
Dock10	ENSMUSG00000038608.15	1
Lefty1	ENSMUSG00000038793.8	1
Abca9	ENSMUSG00000041797.7	1
Odf3l1	ENSMUSG00000045620.7	1
Gm11223	ENSMUSG00000046341.5	1
Lix1	ENSMUSG00000047786.12	1
Gigyf2	ENSMUSG00000048000.15	1
Fbxl22	ENSMUSG00000050503.9	1
Gprc5c	ENSMUSG00000051043.16	1
Cnn3	ENSMUSG00000053931.11	1
Zfp947	ENSMUSG00000063383.5	1
Syne2	ENSMUSG00000063450.14	1
Zfp783	ENSMUSG00000072653.14	1

Kbtbd6	ENSMUSG00000075502.2	1
Gm26490	ENSMUSG00000088504.1	1
Gm38377	ENSMUSG00000102662.1	1
Gm38380	ENSMUSG00000102664.1	1
Gm37566	ENSMUSG00000104044.1	1
Gm45435	ENSMUSG00000110202.1	1
1700012D14Rik	ENSMUSG00000110424.1	1
Agpat3	ENSMUSG00000001211.15	2
Lipe	ENSMUSG00000003123.15	2
Id3	ENSMUSG00000007872.3	2
Mcemp1	ENSMUSG00000013974.3	2
Fhod1	ENSMUSG00000014778.10	2
Ccn2	ENSMUSG00000019997.11	2
Irak3	ENSMUSG00000020227.10	2
Nrde2	ENSMUSG00000021179.8	2
Kif2a	ENSMUSG00000021693.20	2
Nr4a1	ENSMUSG00000023034.7	2
Mmp25	ENSMUSG00000023903.8	2
Treml1	ENSMUSG00000023993.7	2
Epas1	ENSMUSG00000024140.10	2
Sh3d19	ENSMUSG00000028082.14	2
Afap1	ENSMUSG00000029094.12	2
Cdkl2	ENSMUSG00000029403.14	2
Tgfb1i1	ENSMUSG00000030782.16	2
Armcx2	ENSMUSG00000033436.13	2
Tmub2	ENSMUSG00000034757.15	2
Pomk	ENSMUSG00000037251.5	2
Mex3c	ENSMUSG00000037253.8	2
Ttc12	ENSMUSG00000040219.4	2
Trem1	ENSMUSG00000042265.13	2
Dcst1	ENSMUSG00000042672.15	2
Lsm11	ENSMUSG00000044847.13	2
Lrrc49	ENSMUSG00000047766.15	2
Psrc1	ENSMUSG00000068744.12	2
Fndc10	ENSMUSG00000074738.2	2
Zfp964	ENSMUSG00000091764.3	2
Pcdhgb5	ENSMUSG00000103749.1	2
Gm37033	ENSMUSG00000104388.1	2
Gm45509	ENSMUSG00000109781.1	2
Slc9a3r2	ENSMUSG00000002504.15	3
Corin	ENSMUSG00000005220.10	3
Trpm2	ENSMUSG00000009292.18	3
Klhl3	ENSMUSG00000014164.15	3
Meis1	ENSMUSG00000020160.18	3
Pgam2	ENSMUSG00000020475.3	3
Sh3yl1	ENSMUSG00000020669.15	3

Vamp2	ENSMUSG00000020894.16	3
Elovl7	ENSMUSG00000021696.9	3
Tnfrsf10b	ENSMUSG00000022074.6	3
Slc12a2	ENSMUSG00000024597.11	3
Rbm22	ENSMUSG00000024604.7	3
Spindoc	ENSMUSG00000024970.5	3
Nnt	ENSMUSG00000025453.18	3
Itga8	ENSMUSG00000026768.10	3
Spata5	ENSMUSG00000027722.14	3
Dclk1	ENSMUSG00000027797.15	3
Pfn2	ENSMUSG00000027805.16	3
Cyp2u1	ENSMUSG00000027983.13	3
Caap1	ENSMUSG00000028578.8	3
Zik1	ENSMUSG00000030393.8	3
Avpr2	ENSMUSG00000031390.8	3
Ido2	ENSMUSG00000031549.16	3
Acsbg1	ENSMUSG00000032281.11	3
Zfyve9	ENSMUSG00000034557.14	3
Zfp113	ENSMUSG00000037007.17	3
Nr0b2	ENSMUSG00000037583.2	3
1700028J19Rik	ENSMUSG00000038782.7	3
Zfp189	ENSMUSG00000039634.12	3
Tbc1d13	ENSMUSG00000039678.12	3
Clcf1	ENSMUSG00000040663.9	3
H1foo	ENSMUSG00000042279.13	3
Crppa	ENSMUSG00000043153.6	3
E130308A19Rik	ENSMUSG00000045071.14	3
Fbxo10	ENSMUSG00000048232.12	3
Ppp1r3d	ENSMUSG00000049999.4	3
Zfp11	ENSMUSG00000051034.7	3
Zfp329	ENSMUSG00000057894.10	3
Zfp937	ENSMUSG00000060336.6	3
Intu	ENSMUSG00000060798.7	3
Zfp773	ENSMUSG00000063535.7	3
6720489N17Rik	ENSMUSG00000072066.7	3
Fam84b	ENSMUSG00000072568.4	3
5730409E04Rik	ENSMUSG00000073755.4	3
Tmem243	ENSMUSG00000079659.5	3
2610021A01Rik	ENSMUSG00000091474.2	3
2310001H17Rik	ENSMUSG00000097354.7	3
Gm26520	ENSMUSG00000097429.1	3
Gm26637	ENSMUSG00000097567.1	3
1700008J07Rik	ENSMUSG00000101225.1	3
9430053O09Rik	ENSMUSG00000102344.1	3
Gm37637	ENSMUSG00000102861.1	3
Gm43511	ENSMUSG00000104761.1	3

Gm43668	ENSMUSG00000105176.1	3
Gm45718	ENSMUSG00000109390.1	3
Gm49085	ENSMUSG00000115249.1	3
Mmp8	ENSMUSG00000005800.3	4
Ceacam16	ENSMUSG00000014686.8	4
Tlcd1	ENSMUSG00000019437.17	4
Calr3	ENSMUSG00000019732.14	4
Hal	ENSMUSG00000020017.14	4
Tcam1	ENSMUSG00000020712.11	4
Slc6a4	ENSMUSG00000020838.12	4
Oxnad1	ENSMUSG00000021906.14	4
Slc4a8	ENSMUSG00000023032.12	4
Krt7	ENSMUSG00000023039.17	4
Tbc1d5	ENSMUSG00000023923.10	4
Pdcd11	ENSMUSG00000025047.9	4
Echs1	ENSMUSG00000025465.13	4
Fbxl16	ENSMUSG00000025738.8	4
Cplx2	ENSMUSG00000025867.8	4
Bard1	ENSMUSG00000026196.7	4
Slc6a17	ENSMUSG00000027894.14	4
Sh2d2a	ENSMUSG00000028071.12	4
Rassf6	ENSMUSG00000029370.10	4
Tfpi2	ENSMUSG00000029664.10	4
Rpn1	ENSMUSG00000030062.7	4
Strn4	ENSMUSG00000030374.15	4
Sorbs2	ENSMUSG00000031626.17	4
Il34	ENSMUSG00000031750.15	4
Fam160b1	ENSMUSG00000033478.5	4
Smyd5	ENSMUSG00000033706.13	4
N4bp2	ENSMUSG00000037795.14	4
Usp5	ENSMUSG00000038429.10	4
Arhgap29	ENSMUSG00000039831.16	4
Tmco4	ENSMUSG00000041143.16	4
Rnpep	ENSMUSG00000041926.15	4
Itpr3	ENSMUSG00000042644.9	4
Tmem11	ENSMUSG00000043284.12	4
Pld6	ENSMUSG00000043648.7	4
Alkbh2	ENSMUSG00000044339.12	4
Epcam	ENSMUSG00000045394.9	4
Jrk	ENSMUSG00000046380.3	4
Mterf2	ENSMUSG00000049038.3	4
Htr1b	ENSMUSG00000049511.5	4
Glis3	ENSMUSG00000052942.13	4
Tmem119	ENSMUSG00000054675.5	4
Prmt7	ENSMUSG00000060098.11	4
Glrp1	ENSMUSG00000062310.7	4

Capn6	ENSMUSG00000067276.5	4
Flnc	ENSMUSG00000068699.12	4
B3gnt9	ENSMUSG00000069920.10	4
Ehd2	ENSMUSG00000074364.6	4
Tmem267	ENSMUSG00000074634.12	4
C78197	ENSMUSG00000087242.2	4
Frg2f1	ENSMUSG00000087385.8	4
Zfp870	ENSMUSG00000095325.3	4
Tdgf1-ps1	ENSMUSG00000095834.2	4
2310069B03Rik	ENSMUSG00000100291.6	4
Pcdhgc3	ENSMUSG00000102918.1	4
Gm6553	ENSMUSG00000116702.1	4
AC115752.1	ENSMUSG00000118106.1	4
1700061G19Rik	ENSMUSG00000024209.9	5
Scd2	ENSMUSG00000025203.6	5
Nbea	ENSMUSG00000027799.12	5
Fam53b	ENSMUSG00000030956.15	5
Tle3	ENSMUSG00000032280.16	5
Tmem268	ENSMUSG00000045917.17	5
mt-Rnr1	ENSMUSG00000064337.1	5
mt-Rnr2	ENSMUSG00000064339.1	5
mt-Co1	ENSMUSG00000064351.1	5
Trp53i11	ENSMUSG00000068735.14	5
Gm13340	ENSMUSG00000083563.1	5
Gm20594	ENSMUSG00000096887.2	5
Gm28439	ENSMUSG00000100131.1	5
Gm10925	ENSMUSG00000100862.1	5
Gm29216	ENSMUSG00000101249.1	5
4933400F21Rik	ENSMUSG00000102009.6	5
Gm37101	ENSMUSG00000102448.1	5

Table SC 4: Top 5 canonical pathways identified by IPA analysis for unbiased clustering analysis of in vitro dataset

Cluster	Ingenuity Canonical Pathways	-log(p-value)	Molecules
1	Gluconeogenesis I	1.52E+00	ENO2
	Glycolysis I	1.50E+00	ENO2
	Inhibition of Matrix Metalloproteases	1.35E+00	TIMP3
	Oncostatin M Signalling	1.31E+00	TIMP3
	Transcriptional Regulatory Network in Embryonic Stem Cells	1.21E+00	L1CAM
2	Apelin Cardiac Fibroblast Signalling Pathway	1.56E+00	CCN2
	CDP-diacylglycerol Biosynthesis I	1.52E+00	AGPAT3
	Phosphatidylglycerol Biosynthesis II (Non-plastidic)	1.49E+00	AGPAT3
	Inhibition of Matrix Metalloproteases	1.33E+00	MMP25
	Oncostatin M Signalling	1.29E+00	EPAS1

3	LPS/IL-1 Mediated Inhibition of RXR Function	2.05E+00	ACSBG1,CYP2U1,NR0B2
	Rapoport-Luebering Glycolytic Shunt	2.00E+00	PGAM2
	Regulation of Actin-based Motility by Rho	1.79E+00	ITGA8,PFN2
	Insulin Receptor Signalling	1.63E+00	PPP1R3D,VAMP2
	Fatty Acid Activation	1.60E+00	ACSBG1
4	Inhibition of Matrix Metalloproteases	2.52E+00	MMP8,TFPI2
	Serotonin Receptor Signalling	2.39E+00	HTR1B,SLC6A4
	Histidine Degradation III	1.78E+00	HAL
	Choline Biosynthesis III	1.51E+00	Pld6
	Isoleucine Degradation I	1.43E+00	ECHS1
5	Regulation of eIF4 and p70S6K Signalling	2.71E+00	MT-RNR1,MT-RNR2
	Coronavirus Pathogenesis Pathway	2.60E+00	MT-RNR1,MT-RNR2
	mTOR Signalling	2.56E+00	MT-RNR1,MT-RNR2
	EIF2 Signalling	2.52E+00	MT-RNR1,MT-RNR2
	Oleate Biosynthesis II (Animals)	2.31E+00	Scd2

Table SC 5: Top 5 canonical pathways identified by IPA analysis for pairwise analysis of in vitro dataset

Upregulated and downregulated genes analysed separately. Un 1-2N vs In 1-2N – 48 total DEGs – 27 genes upregulated in In 1-2N, 21 genes downregulated in In 1-2N.

Un ≥3N vs In ≥3N – 83 total DEGs – 55 genes upregulated in In ≥3N, 28 genes downregulated in In ≥3N.

Comparison	**Up/Down**	**Top canonical pathways**	***p*-value**	**Molecules**
Un 1-2N vs In 1-2N	Up	Histidine Degradation III	7.71E-03	HAL
		Choline Biosynthesis III	1.44E-02	Pld6
		CDP-diacylglycerol Biosynthesis I	2.39E-02	AGPAT3
		Phosphatidylglycerol Biosynthesis II (Non-plastidic)	2.58E-02	AGPAT3
		Histidine Degradation VI	2.67E-02	HAL
Un 1-2N vs In 1-2N	Down	Gluconeogenesis I	1.63E-02	ENO2
		Glycolysis I	1.69E-02	ENO2
		Transcriptional Regulatory Network in Embryonic Stem Cells	3.35E-02	L1CAM
		Regulation Of The Epithelial Mesenchymal Transition by Growth Factors Pathway	1.14E-01	DOCK10
		Axonal Guidance Signalling	2.77E-01	L1CAM
Un ≥3N vs In ≥3N	Up	Inhibition of Matrix Metalloproteases	2.70E-03	MMP25,TFPI2
		Serotonin Receptor Signalling	3.58E-03	HTR1B,SLC6A4

		Oleate Biosynthesis II (Animals)	2.54E-02	Scd2
		Isoleucine Degradation I	3.50E-02	ECHS1
		Valine Degradation I	4.07E-02	ECHS1
Un ≥3N vs In ≥3N	Down	Hepatic Fibrosis Signalling Pathway	6.60E-03	CCN2,EZH2 ,IRAK3
		Apelin Cardiac Fibroblast Signalling	2.11E-02	CCN2
		Gluconeogenesis I	2.38E-02	ENO2
		Glycolysis I	2.47E-02	ENO2
		Inhibition of Matrix Metalloproteases	3.55E-02	TIMP3

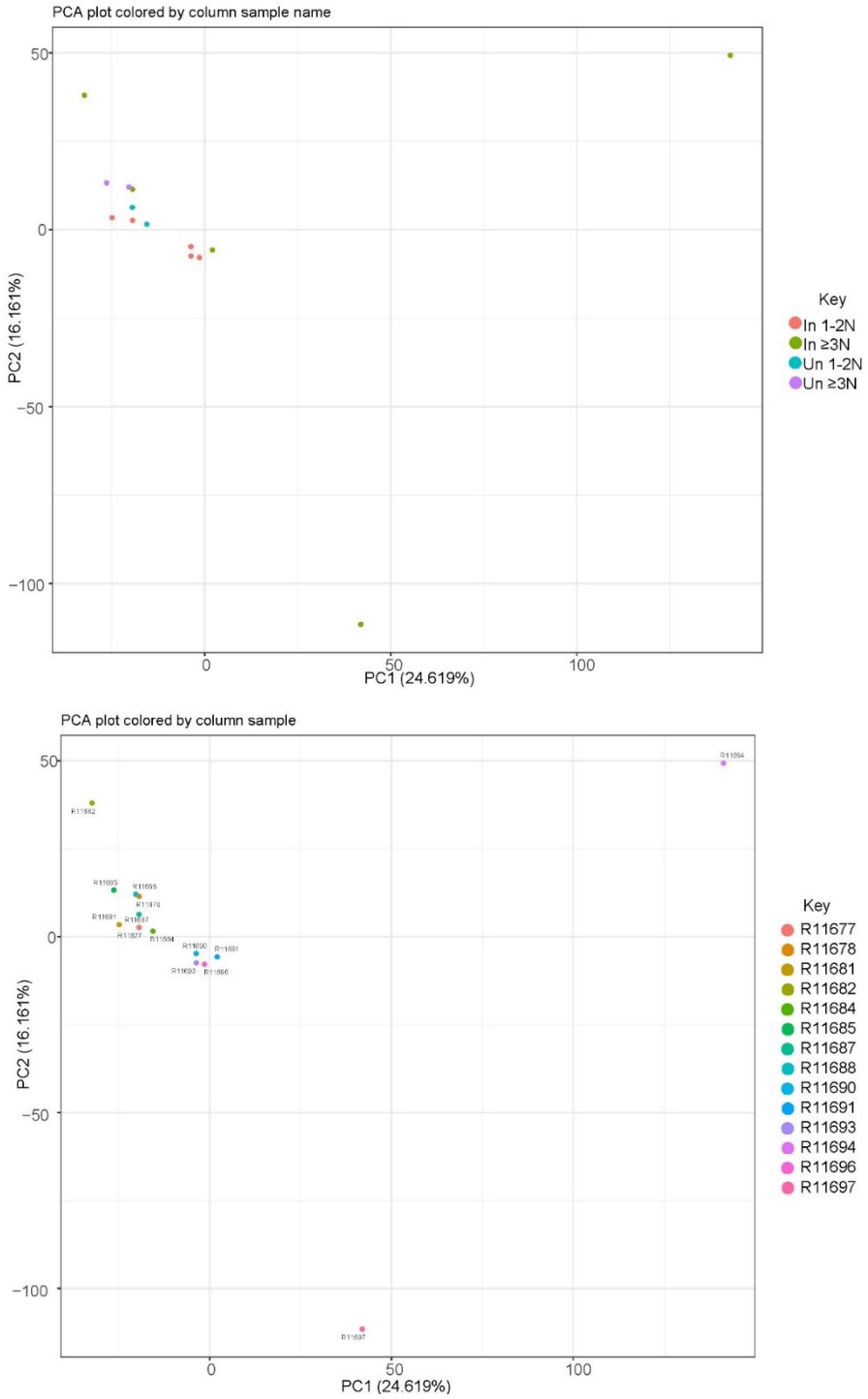

Figure SC 2: Plots of the principal component analysis (PCA) coloured by sample name and description. PCA plots show variation between the samples. The plots represent a biological replicate.

Table SC 6: Differentially expressed genes between uninfected OCLs and in vivo BCG infected OCLs with an FDR<0.05 and Log_2FoldChange > |0.6.: (A) Un 1-2N vs Un ≥3N; (B) Un 1-2N vs In 1-2N; (C) Un ≥3N vs In ≥3N.

A: Un 1-2N vs Un ≥3N (132 DEGs)

Gene_ID	Gene_name	Log2FoldChange	padj
ENSMUSG00000064337.1	mt-Rnr1	3.631008	1.87E-23
ENSMUSG00000064339.1	mt-Rnr2	2.587427	1.21E-14
ENSMUSG00000064363.1	mt-Nd4	1.601176	1.48E-12
ENSMUSG00000064351.1	mt-Co1	1.526144	3.54E-10
ENSMUSG00000048332.13	Lhfp	23.24466	9.77E-10
ENSMUSG00000064367.1	mt-Nd5	1.941022	1.14E-08
ENSMUSG00000064368.1	mt-Nd6	2.228637	7.11E-08
ENSMUSG00000022231.10	Sema5a	22.65568	7.11E-08
ENSMUSG00000058626.16	Capn11	22.65223	7.11E-08
ENSMUSG00000042268.10	Slc26a9	-23.066	7.83E-08
ENSMUSG00000022833.7	Ccdc14	-11.0645	4.64E-07
ENSMUSG00000000386.16	Mx1	-10.8561	2.07E-06
ENSMUSG00000017607.9	Tns4	11.153	3.89E-06
ENSMUSG00000096433.2	Zfp994	-6.5643	6.44E-06
ENSMUSG00000066838.7	Zfp772	-8.42496	6.86E-06
ENSMUSG00000083563.1	Gm13340	2.542291	1E-05
ENSMUSG00000036916.13	Zfp280c	-6.38803	1E-05
ENSMUSG00000053600.8	Zfp472	-9.65548	1E-05
ENSMUSG00000020798.14	Spns3	-10.5143	2.6E-05
ENSMUSG00000048755.9	Mcat	-8.25519	2.62E-05
ENSMUSG00000031755.6	Bbs2	-6.9222	3.67E-05
ENSMUSG00000097908.7	4933404O12Rik	-10.4298	3.8E-05
ENSMUSG00000068246.6	Apol9b	-10.4141	3.8E-05
ENSMUSG00000018166.8	Erbb3	-10.3218	6.42E-05
ENSMUSG00000064370.1	mt-Cytb	1.482925	6.42E-05
ENSMUSG00000064345.1	mt-Nd2	1.530254	8.49E-05
ENSMUSG00000023243.9	Kcnk5	-10.28	8.49E-05
ENSMUSG00000072244.11	Trim6	6.747168	9.06E-05
ENSMUSG00000113836.1	Gm3325	-4.88439	0.000183
ENSMUSG00000058402.14	Zfp420	-10.1819	0.000183
ENSMUSG00000043372.12	Hexim2	-10.1482	0.000185
ENSMUSG00000049858.8	Suox	-10.1673	0.000185

ENSMUSG00000016018.4	Mtrex	-1.94608	0.000185
ENSMUSG00000023826.16	Prkn	-8.28665	0.000187
ENSMUSG00000050930.5	Map10	-7.97659	0.00019
ENSMUSG00000038545.13	Cul7	-7.21636	0.000245
ENSMUSG00000040669.14	Phc1	7.967472	0.00026
ENSMUSG00000024883.8	Rin1	2.806623	0.000436
ENSMUSG00000095253.4	Zfp799	-7.89137	0.000614
ENSMUSG00000044551.13	9930012K11Rik	-9.92891	0.000694
ENSMUSG00000038593.18	Tctn1	-7.15073	0.000769
ENSMUSG00000041688.16	Amot	-7.75202	0.000987
ENSMUSG00000028613.15	Lrp8	-9.81896	0.001255
ENSMUSG00000105304.1	Gm43696	-7.68115	0.001263
ENSMUSG00000025375.15	Aatk	-6.18367	0.001372
ENSMUSG00000031750.15	Il34	-7.70168	0.001372
ENSMUSG00000027257.13	Pacsin3	-9.79085	0.001372
ENSMUSG00000046634.12	Pkd1l1	-7.68224	0.001372
ENSMUSG00000032593.5	Amigo3	-10.0602	0.001372
ENSMUSG00000086712.2	AI427809	-7.78776	0.001372
ENSMUSG00000034538.8	Zfp418	-9.9168	0.001372
ENSMUSG00000019986.17	Ahi1	-10.0105	0.001372
ENSMUSG00000040133.2	Gpr176	-9.76285	0.001405
ENSMUSG00000006850.8	Tmco6	-7.89744	0.001405
ENSMUSG00000101249.1	Gm29216	2.275653	0.001483
ENSMUSG00000069727.5	Zfp975	-5.58447	0.00195
ENSMUSG00000076258.1	Gm23935	3.693763	0.002023
ENSMUSG00000016756.17	Cmah	-7.23548	0.00229
ENSMUSG00000100131.1	Gm28439	2.427032	0.00242
ENSMUSG00000070323.11	Mmp27	-5.72038	0.002923
ENSMUSG00000042851.17	Zc3h6	9.674813	0.003038
ENSMUSG00000095193.2	Gm20939	-6.78367	0.003075
ENSMUSG00000024210.3	Ip6k3	-9.60573	0.003478
ENSMUSG00000020424.3	Castor1	-7.50467	0.004246
ENSMUSG00000055745.4	Rtl6	-7.61692	0.004476
ENSMUSG00000015342.6	Xk	-9.53343	0.00463
ENSMUSG00000051373.5	Plpp7	-6.37889	0.004687
ENSMUSG00000054423.14	Cadps	-6.26763	0.005232
ENSMUSG00000062310.7	Glrp1	-9.50678	0.005302

ENSMUSG00000054484.14	Tmem62	-9.59244	0.005331
ENSMUSG00000038172.14	Ttc39b	-3.47123	0.006268
ENSMUSG00000063810.7	Alms1	-9.49566	0.006942
ENSMUSG00000035202.8	Lars2	1.401924	0.006948
ENSMUSG00000079038.3	D130040H23Rik	-7.32794	0.007503
ENSMUSG00000026854.16	Usp20	-2.13625	0.007507
ENSMUSG00000037904.14	Ankrd9	-5.79261	0.00776
ENSMUSG00000042510.7	AA986860	-9.69607	0.007985
ENSMUSG00000038456.9	Dennd2a	-4.81758	0.008404
ENSMUSG00000033105.12	Lss	-1.44569	0.008462
ENSMUSG00000051444.9	Bbs12	-9.38634	0.008864
ENSMUSG00000038895.16	Zfp653	-9.44418	0.008864
ENSMUSG00000029178.14	Klf3	-3.15602	0.008864
ENSMUSG00000022545.13	Ercc4	-3.15799	0.009544
ENSMUSG00000031480.15	Thsd1	-9.4036	0.009569
ENSMUSG00000056458.16	Mok	9.379454	0.010996
ENSMUSG00000043153.6	Crppa	-8.22614	0.011053
ENSMUSG00000079737.4	3110001I22Rik	-9.32636	0.011195
ENSMUSG00000071068.7	Treml2	-9.68565	0.011199
ENSMUSG00000055069.3	Rab39	-6.03163	0.011199
ENSMUSG00000060336.6	Zfp937	-7.2273	0.011199
ENSMUSG00000108455.1	Gm44745	9.354985	0.011948
ENSMUSG00000040297.12	Suco	1.873841	0.013273
ENSMUSG00000025271.13	Pfkfb1	-5.94631	0.014259
ENSMUSG00000110393.2	Gm36445	-9.2895	0.014424
ENSMUSG00000024673.9	Ms4a1	7.245955	0.014424
ENSMUSG00000117964.1	AC119228.1	7.337647	0.014495
ENSMUSG00000097971.3	Gm26917	1.734032	0.01489
ENSMUSG00000118330.1	AC132148.1	-9.31305	0.016158
ENSMUSG00000064341.1	mt-Nd1	1.086632	0.017664
ENSMUSG00000091243.2	Vgll3	10.41227	0.019331
ENSMUSG00000109536.1	9330162G02Rik	-5.50738	0.01961
ENSMUSG00000033253.18	Szt2	-3.4191	0.01961
ENSMUSG00000025766.14	D3Ertd751e	2.293506	0.019632
ENSMUSG00000007989.7	Fzd3	9.221575	0.019632
ENSMUSG00000030433.15	Sbk2	-5.89492	0.019632
ENSMUSG00000049588.13	Ccdc69	-7.10209	0.019632

ENSMUSG00000072969.2	Armcx5	-6.35879	0.021696
ENSMUSG00000036469.16	March1	3.118831	0.023212
ENSMUSG00000022092.11	Ppp3cc	-9.14685	0.024047
ENSMUSG00000096887.2	Gm20594	3.298802	0.024616
ENSMUSG00000092274.3	Neat1	0.979699	0.024902
ENSMUSG00000030577.14	Cd22	-7.07679	0.025401
ENSMUSG00000039577.17	Nphp4	-9.09971	0.030986
ENSMUSG00000050737.13	Ptges	-9.27196	0.032026
ENSMUSG00000072762.9	4930522L14Rik	-5.37956	0.033897
ENSMUSG00000070732.2	Rbm44	-9.20533	0.034129
ENSMUSG00000025855.13	Prkar1b	-7.11618	0.03488
ENSMUSG00000038010.9	Ccdc138	-9.04342	0.035073
ENSMUSG00000036928.14	Stag3	-6.9931	0.036193
ENSMUSG00000056832.14	Ttc26	10.10596	0.036397
ENSMUSG00000032246.14	Calml4	9.083901	0.036735
ENSMUSG00000015305.6	Sash1	-4.5292	0.038936
ENSMUSG00000024228.12	Nudt12	-9.19491	0.039696
ENSMUSG00000050192.8	Eif5a2	-6.92739	0.039778
ENSMUSG00000019966.18	Kitl	-2.4829	0.04297
ENSMUSG00000053886.4	Sh2d4a	10.04067	0.04442
ENSMUSG00000026792.16	Lrsam1	1.49639	0.045491
ENSMUSG00000038256.15	Bcl9	-6.56837	0.048536
ENSMUSG00000036568.7	Bicral	3.537999	0.049145
ENSMUSG00000030213.12	Atf7ip	-1.22701	0.04978
ENSMUSG00000059708.12	Akap17b	-8.93761	0.04978
ENSMUSG00000034906.15	Ncaph	-1.18688	0.04978

B: Un 1-2N vs In 1-2N (61 DEGs)

Gene_ID	Gene_name	Gene_type	log2FoldChange	padj
ENSMUSG00000007989.7	Fzd3	protein_coding	-22.8541	2.8E-06
ENSMUSG00000007655.16	Cav1	protein_coding	-1.54986	2.8E-06
ENSMUSG00000105748.1	Gm43088	TEC	-22.4125	5.81E-06
ENSMUSG00000035107.13	Dcbld2	protein_coding	-22.3535	5.81E-06
ENSMUSG00000070305.10	Mpzl3	protein_coding	-22.0166	2.35E-05
ENSMUSG00000054715.11	Zscan22	protein_coding	-1.31819	2.64E-05
ENSMUSG00000103039.1	Gm37123	TEC	-21.6471	5.63E-05

ENSMUSG00000097534.3	Gm16675	lncRNA	-9.82723	5.91E-05
ENSMUSG00000042097.17	Zfp239	protein_coding	-9.78544	0.000144
ENSMUSG00000049723.14	Mmp12	protein_coding	-2.85047	0.000165
ENSMUSG00000023232.17	Serinc2	protein_coding	-7.89775	0.00021
ENSMUSG00000040415.15	Dtx3	protein_coding	-2.06809	0.000348
ENSMUSG00000087177.7	E130307A14Rik	lncRNA	-5.08064	0.000639
ENSMUSG00000075266.5	Cenpw	protein_coding	-1.64505	0.000639
ENSMUSG00000045441.5	Gprin3	protein_coding	5.706964	0.001113
ENSMUSG00000118106.1	AC115752.1	TEC	-9.30455	0.001113
ENSMUSG00000103867.1	9630010A21Rik	TEC	-5.80912	0.001113
ENSMUSG00000024056.10	Ndc80	protein_coding	-0.80229	0.001703
ENSMUSG00000058755.3	Osm	protein_coding	-10.16	0.004141
ENSMUSG00000006241.16	Ccdc159	protein_coding	-9.08618	0.004234
ENSMUSG00000029833.17	Trim24	protein_coding	-3.56252	0.004234
ENSMUSG00000026939.12	Tmem141	protein_coding	0.915133	0.004693
ENSMUSG00000038860.15	Garnl3	protein_coding	-7.94069	0.004744
ENSMUSG00000029001.15	Fbxo44	protein_coding	-5.01669	0.004744
ENSMUSG00000027306.15	Nusap1	protein_coding	-0.78152	0.005742
ENSMUSG00000031951.8	Tmem231	protein_coding	-8.76912	0.005742
ENSMUSG00000037855.15	Zfp365	protein_coding	-5.44508	0.005815
ENSMUSG00000033502.14	Cdc14a	protein_coding	-2.69602	0.006644
ENSMUSG00000025010.14	Ccnj	protein_coding	-3.29491	0.007814
ENSMUSG00000066647.8	Gm5113	transcribed_unprocessed_pseudogene	-2.26047	0.008272
ENSMUSG00000046718.8	Bst2	protein_coding	0.803966	0.008392
ENSMUSG00000027316.15	Gfra4	protein_coding	-5.36354	0.008394
ENSMUSG00000036469.16	March1	protein_coding	-1.86721	0.009851
ENSMUSG00000102930.1	Gm38115	lncRNA	-8.53284	0.012336
ENSMUSG00000038393.14	Txnip	protein_coding	1.476364	0.012418

ENSMUSG00000075033.4	Nxpe3	protein_coding	-8.38634	0.013038
ENSMUSG00000027447.6	Cst3	protein_coding	0.609727	0.0131
ENSMUSG00000073409.12	H2-Q6	protein_coding	-1.91238	0.013703
ENSMUSG00000019768.16	Esr1	protein_coding	-2.10949	0.015557
ENSMUSG00000000282.12	Mnt	protein_coding	-1.59594	0.016334
ENSMUSG00000005374.13	Tbl2	protein_coding	-0.9463	0.018595
ENSMUSG00000057836.12	Xlr3a	protein_coding	-7.42867	0.019344
ENSMUSG00000047757.16	Fancb	protein_coding	-1.59882	0.020262
ENSMUSG00000048922.18	Cdca2	protein_coding	-0.65286	0.020262
ENSMUSG00000090124.7	Ugt1a7c	protein_coding	-0.65427	0.020262
ENSMUSG00000045411.16	2410002F23Rik	protein_coding	-1.01757	0.020262
ENSMUSG00000040451.18	Sgms1	protein_coding	-1.13414	0.024241
ENSMUSG00000025395.14	Prim1	protein_coding	-0.85704	0.024241
ENSMUSG00000006463.13	Zdhhc24	protein_coding	-1.78605	0.025311
ENSMUSG00000043391.10	2510009E07Rik	protein_coding	-1.61394	0.025851
ENSMUSG00000008035.12	Mid1ip1	protein_coding	0.836463	0.027223
ENSMUSG00000071637.5	Cebpd	protein_coding	1.554558	0.03254
ENSMUSG00000056418.3	BC043934	lncRNA	-7.99532	0.034942
ENSMUSG00000022292.16	Rrm2b	protein_coding	1.319844	0.035043
ENSMUSG00000017607.9	Tns4	protein_coding	-9.40545	0.039728
ENSMUSG00000028525.16	Pde4b	protein_coding	-1.51581	0.040525
ENSMUSG00000064138.14	Fam172a	protein_coding	-0.73221	0.04596
ENSMUSG00000031883.13	Car7	protein_coding	-7.52697	0.047647
ENSMUSG00000041187.16	Prkd2	protein_coding	-2.89725	0.047647
ENSMUSG00000029869.7	Ephb6	protein_coding	-6.68352	0.047647
ENSMUSG00000025145.13	Lrrc45	protein_coding	-1.01997	0.047647

C: Un ≥3N vs In ≥3N (194 DEGs)

Gene_ID	Gene_name	Gene_type	log2FoldChange	padj
ENSMUSG00000086503.4	Xist	lncRNA	-25.3348	1.05E-10
ENSMUSG00000034664.13	Itga2b	protein_coding	-23.939	1.8E-08

ENSMUSG00000106475.1	Gm43011	TEC	-23.0105	1.22E-05
ENSMUSG00000097077.1	Gm16712	lncRNA	-23.0089	6.29E-07
ENSMUSG00000096916.7	Zfp850	protein_coding	-22.9179	1.32E-05
ENSMUSG00000026069.15	Il1rl1	protein_coding	-22.8758	1.33E-05
ENSMUSG00000017386.10	Traf4	protein_coding	-22.7979	1.35E-05
ENSMUSG00000040133.2	Gpr176	protein_coding	-22.7806	1.35E-05
ENSMUSG00000056145.5	AI504432	lncRNA	-22.7627	1.35E-05
ENSMUSG00000043487.4	Acot6	protein_coding	-22.619	1.57E-05
ENSMUSG00000024544.9	Ldlrad4	protein_coding	-22.6008	1.57E-05
ENSMUSG00000109946.1	Brd3os	protein_coding	-22.5682	1.58E-05
ENSMUSG00000068246.6	Apol9b	protein_coding	-22.4258	1.8E-05
ENSMUSG00000070305.10	Mpzl3	protein_coding	-22.3997	1.8E-05
ENSMUSG00000034570.12	Inpp5j	protein_coding	-22.3946	1.8E-05
ENSMUSG00000102982.1	Gm38319	TEC	-22.232	2.11E-05
ENSMUSG00000028602.12	Tnfrsf8	protein_coding	-22.1602	2.17E-05
ENSMUSG00000049811.16	Fam161a	protein_coding	-22.1335	2.17E-05
ENSMUSG00000054409.5	Tmem74	protein_coding	-22.1245	2.17E-05
ENSMUSG00000024530.8	Prelid3a	protein_coding	-22.1228	2.17E-05
ENSMUSG00000050954.15	Zfp169	protein_coding	-22.0595	2.28E-05
ENSMUSG00000030486.9	Zfp108	protein_coding	-22.0142	2.28E-05
ENSMUSG00000118138.1	AC132253.6	lncRNA	-21.9817	2.28E-05
ENSMUSG00000018924.6	Alox15	protein_coding	-21.978	2.28E-05
ENSMUSG00000038180.11	Spag4	protein_coding	-21.9663	2.28E-05
ENSMUSG00000086894.2	Gm15708	lncRNA	-21.9534	2.28E-05
ENSMUSG00000113128.1	Gm47813	TEC	-21.9353	2.28E-05
ENSMUSG00000097574.2	C920006O11Rik	transcribed_unprocessed_pseudogene	-21.9018	2.3E-05
ENSMUSG00000024210.3	Ip6k3	protein_coding	-21.8819	2.3E-05
ENSMUSG00000036526.8	Card11	protein_coding	-21.8608	2.3E-05
ENSMUSG00000062380.4	Tubb3	protein_coding	-21.8445	2.3E-05
ENSMUSG00000048534.7	Jaml	protein_coding	-21.8302	2.3E-05
ENSMUSG00000118423.1	AC154328.1	transcribed_unitary_pseudogene	-21.8199	2.3E-05
ENSMUSG00000030825.19	Hsd17b14	protein_coding	-21.7959	2.33E-05
ENSMUSG00000006445.3	Epha2	protein_coding	-21.6382	2.77E-05
ENSMUSG00000057337.13	Chst3	protein_coding	-21.5954	2.88E-05
ENSMUSG00000113687.1	Gm49703	TEC	-21.4911	3.19E-05
ENSMUSG00000024330.17	Col11a2	protein_coding	-21.1561	4.56E-05
ENSMUSG00000097660.1	Gm26762	lncRNA	-20.8868	6.39E-05
ENSMUSG00000074807.3	Gm10762	lncRNA	-20.7475	7.41E-05
ENSMUSG00000000386.16	Mx1	polymorphic_pseudogene	-11.4394	3.66E-09
ENSMUSG00000032733.6	Snx33	protein_coding	-11.4191	1.8E-08
ENSMUSG00000022833.7	Ccdc14	protein_coding	-11.1342	0.000102
ENSMUSG00000037759.6	Ptger2	protein_coding	-11.0539	4.15E-05
ENSMUSG00000054484.14	Tmem62	protein_coding	-10.8986	3.89E-06
ENSMUSG00000042265.13	Trem1	protein_coding	-10.3571	0.000168
ENSMUSG00000079737.4	3110001I22Rik	protein_coding	-10.3383	0.00501
ENSMUSG00000038010.9	Ccdc138	protein_coding	-10.3306	0.006404
ENSMUSG00000059956.14	Serpinb12	protein_coding	-10.2715	0.006404
ENSMUSG00000028613.15	Lrp8	protein_coding	-10.199	0.005707
ENSMUSG00000038895.16	Zfp653	protein_coding	-10.181	0.006404
ENSMUSG00000110457.1	Gm45752	lncRNA	-10.0654	0.004243

ENSMUSG00000045075.3	Gm9796	lncRNA	-10.0136	0.006691
ENSMUSG00000053600.8	Zfp472	protein_coding	-9.99897	5.17E-08
ENSMUSG00000044551.13	9930012K11Rik	protein_coding	-9.79869	0.006454
ENSMUSG00000097136.1	Gm26772	lncRNA	-9.67958	0.004229
ENSMUSG00000034156.16	Tspoap1	protein_coding	-9.65871	0.044187
ENSMUSG00000020798.14	Spns3	protein_coding	-9.63078	0.00106
ENSMUSG00000110393.2	Gm36445	lncRNA	-9.58241	0.011324
ENSMUSG00000073791.11	Efcab7	protein_coding	-9.26203	0.018212
ENSMUSG00000034959.8	Rubcnl	protein_coding	-9.25585	0.041631
ENSMUSG00000022421.19	Nptxr	protein_coding	-8.94197	0.004202
ENSMUSG00000102353.1	Gm38345	TEC	-8.93732	0.005078
ENSMUSG00000050192.8	Eif5a2	protein_coding	-8.82097	7.08E-11
ENSMUSG00000047654.6	Tssk6	protein_coding	-8.47616	4.01E-05
ENSMUSG00000006850.8	Tmco6	protein_coding	-8.17787	0.000558
ENSMUSG00000072066.7	6720489N17Rik	protein_coding	-7.86249	0.000677
ENSMUSG00000003581.14	Rnf215	protein_coding	-7.68906	0.017146
ENSMUSG00000097180.5	2700038G22Rik	lncRNA	-7.51581	2.28E-05
ENSMUSG00000104656.1	Gm44483	miRNA	-7.51279	0.001594
ENSMUSG00000085687.1	Gm16153	lncRNA	-7.45226	0.046328
ENSMUSG00000031444.16	F10	protein_coding	-7.3006	0.046328
ENSMUSG00000016552.13	Foxred2	protein_coding	-7.27726	0.027867
ENSMUSG00000025271.13	Pfkfb1	protein_coding	-6.62047	0.002703
ENSMUSG00000019992.8	Mtfr2	protein_coding	-6.53858	2.3E-05
ENSMUSG00000036916.13	Zfp280c	protein_coding	-6.49593	0.001722
ENSMUSG00000034853.16	Acot11	protein_coding	-6.47761	8.81E-05
ENSMUSG00000034462.9	Pkd2	protein_coding	-6.36987	0.001252
ENSMUSG00000040146.9	Rgl3	protein_coding	-6.22012	0.046872
ENSMUSG00000038593.18	Tctn1	protein_coding	-6.07416	0.03616
ENSMUSG00000025420.13	Katnal2	protein_coding	-5.92029	0.017625
ENSMUSG00000096433.2	Zfp994	protein_coding	-5.74605	0.00501
ENSMUSG00000020752.11	Recql5	protein_coding	-5.3465	0.041848
ENSMUSG00000037913.12	Tmem156	protein_coding	-4.50392	0.00019
ENSMUSG00000048058.17	Ldlrad3	protein_coding	-4.44713	0.016657
ENSMUSG00000038668.14	Lpar1	protein_coding	-4.13418	0.001722
ENSMUSG00000038456.9	Dennd2a	protein_coding	-4.1218	1.45E-07
ENSMUSG00000053101.3	Gpr141	protein_coding	-3.94411	2.46E-06
ENSMUSG00000035356.17	Nfkbiz	protein_coding	-3.92572	0.005764
ENSMUSG00000078877.11	Gm14295	protein_coding	-3.89108	0.046328
ENSMUSG00000039879.9	Heca	protein_coding	-3.77097	0.03616
ENSMUSG00000029153.11	Ociad2	protein_coding	-3.71366	0.004202
ENSMUSG00000034858.16	Fam214a	protein_coding	-3.5092	0.007997
ENSMUSG00000022545.13	Ercc4	protein_coding	-3.08334	2.71E-05
ENSMUSG00000028885.8	Smpdl3b	protein_coding	-2.99583	1.83E-16
ENSMUSG00000033373.16	Fntb	protein_coding	-2.9743	0.008784
ENSMUSG00000042225.3	Ammecr1	protein_coding	-2.95929	0.00015
ENSMUSG00000049866.12	Arl4c	protein_coding	-2.67821	0.002477
ENSMUSG00000049723.14	Mmp12	protein_coding	-2.58454	0.019336
ENSMUSG00000098090.8	2700099C18Rik	transcribed_unprocessed_pseudogene	-2.44267	0.001059
ENSMUSG00000026873.9	Phf19	protein_coding	-2.37477	0.029486
ENSMUSG00000092558.3	Med20	protein_coding	-2.21136	0.002503

ENSMUSG00000043885.14	Slc36a4	protein_coding	-2.14811	0.000129
ENSMUSG00000074677.11	Sirpb1c	protein_coding	-2.11315	4.46E-05
ENSMUSG00000037649.10	H2-DMa	protein_coding	-2.0632	0.017335
ENSMUSG00000044991.10	Shld1	protein_coding	-2.02699	0.014423
ENSMUSG00000022364.14	Tbc1d31	protein_coding	-2.02412	0.049198
ENSMUSG00000016018.4	Mtrex	protein_coding	-1.99348	0.037361
ENSMUSG00000038871.5	Bpgm	protein_coding	-1.96352	0.026805
ENSMUSG00000019214.14	Chtf18	protein_coding	-1.85724	0.001206
ENSMUSG00000064120.14	Mocs1	protein_coding	-1.84752	0.014423
ENSMUSG00000020493.8	Prr11	protein_coding	-1.83155	0.003281
ENSMUSG00000031441.15	Atp11a	protein_coding	-1.80054	0.008454
ENSMUSG00000018927.3	Ccl6	protein_coding	-1.79461	0.000106
ENSMUSG00000053950.10	Adnp2	protein_coding	-1.78382	0.019258
ENSMUSG00000016206.6	H2-M3	protein_coding	-1.7827	0.024055
ENSMUSG00000038775.14	Vill	protein_coding	-1.71997	0.00019
ENSMUSG00000000530.16	Acvrl1	protein_coding	-1.66373	0.046872
ENSMUSG00000045248.6	Med26	protein_coding	-1.58342	0.029798
ENSMUSG00000029821.15	Gsdme	protein_coding	-1.48803	0.016722
ENSMUSG00000025077.13	Dclre1a	protein_coding	-1.46027	0.002044
ENSMUSG00000062421.13	Arf2	protein_coding	-1.41771	0.000659
ENSMUSG00000042105.18	Inpp5f	protein_coding	-1.37658	0.036063
ENSMUSG00000035171.9	1110059E24Rik	protein_coding	-1.34836	0.007169
ENSMUSG00000039356.15	Exosc2	protein_coding	-1.30589	2.09E-05
ENSMUSG00000024370.17	Cdc23	protein_coding	-1.29521	0.000148
ENSMUSG00000056310.14	Tyw1	protein_coding	-1.28061	0.039319
ENSMUSG00000002985.16	Apoe	protein_coding	-1.24864	0.000447
ENSMUSG00000022102.13	Dok2	protein_coding	-1.24238	1.73E-10
ENSMUSG00000058587.9	Tmod3	protein_coding	-1.23856	0.032825
ENSMUSG00000020124.10	Usp15	protein_coding	-1.22293	0.048887
ENSMUSG00000025810.9	Nrp1	protein_coding	-1.20919	0.005151
ENSMUSG00000022540.16	Rogdi	protein_coding	-1.19521	0.005343
ENSMUSG00000020277.10	Pfkl	protein_coding	-1.17829	0.012297
ENSMUSG00000034641.2	Cd300ld	protein_coding	-1.16887	0.00032
ENSMUSG00000034290.9	Nek9	protein_coding	-1.16374	0.030763
ENSMUSG00000042729.11	Wdr74	protein_coding	-1.13773	0.029486
ENSMUSG00000030677.8	Kif22	protein_coding	-1.13064	0.000301
ENSMUSG00000021811.7	Dnajc9	protein_coding	-1.11033	0.041848
ENSMUSG00000061981.14	Flot2	protein_coding	-1.10718	0.01702
ENSMUSG00000052087.14	Rgs14	protein_coding	-1.09472	0.045231
ENSMUSG00000005470.8	Asf1b	protein_coding	-1.08456	0.000391
ENSMUSG00000039197.10	Adk	protein_coding	-1.03736	0.003277
ENSMUSG00000027306.15	Nusap1	protein_coding	-1.02962	0.006404
ENSMUSG00000021384.14	Susd3	protein_coding	-0.88906	2.94E-05
ENSMUSG00000082062.1	Ftl2-ps	processed_pseudogene	-0.81549	0.039319
ENSMUSG00000018040.9	Rrp7a	protein_coding	-0.80436	0.044187
ENSMUSG00000005481.18	Ddx39	protein_coding	-0.76945	0.048887
ENSMUSG00000070372.11	Capza1	protein_coding	-0.70589	0.049774
ENSMUSG00000069515.6	Lyz1	protein_coding	-0.62296	0.006646
ENSMUSG00000019579.13	Mydgf	protein_coding	-0.60501	0.007072
ENSMUSG00000024603.8	Dctn4	protein_coding	0.864731	0.041848
ENSMUSG00000020400.17	Tnip1	protein_coding	1.016269	0.03765
ENSMUSG00000014077.13	Chp1	protein_coding	1.039416	0.00031

ENSMUSG00000008035.12	Mid1ip1	protein_coding	1.097946	0.046848
ENSMUSG00000024622.8	Hmgxb3	protein_coding	1.233408	0.000634
ENSMUSG00000021608.15	Lpcat1	protein_coding	1.280559	2.26E-10
ENSMUSG00000069769.13	Msi2	protein_coding	1.3427	0.046792
ENSMUSG00000032740.16	Ccdc88a	protein_coding	1.350745	0.030789
ENSMUSG00000035311.16	Gnptab	protein_coding	1.361462	0.016108
ENSMUSG00000043140.10	Tmem186	protein_coding	1.418507	0.004802
ENSMUSG00000071637.5	Cebpd	protein_coding	1.586912	0.000776
ENSMUSG00000024068.8	Spast	protein_coding	1.678555	0.016926
ENSMUSG00000097971.3	Gm26917	lncRNA	1.992257	1.13E-06
ENSMUSG00000024505.16	Dtwd2	protein_coding	2.073355	0.009025
ENSMUSG00000039473.8	Ubn1	protein_coding	2.311503	0.013395
ENSMUSG00000045136.6	Tubb2b	protein_coding	3.547993	0.000957
ENSMUSG00000075254.12	Heg1	protein_coding	5.330845	0.03616
ENSMUSG00000055137.7	Sugct	protein_coding	5.839588	0.000301
ENSMUSG00000027797.15	Dclk1	protein_coding	6.007421	0.005707
ENSMUSG00000008090.14	Fgfrl1	protein_coding	6.356865	0.009356
ENSMUSG00000041351.16	Rap1gap	protein_coding	7.355752	0.006454
ENSMUSG00000020178.6	Adora2a	protein_coding	7.636627	2.17E-06
ENSMUSG00000043419.11	Rnf227	protein_coding	7.680143	0.0029
ENSMUSG00000032589.14	Bsn	protein_coding	7.931195	0.041848
ENSMUSG00000094942.7	Gm3604	protein_coding	7.968645	0.000649
ENSMUSG00000036353.13	P2ry12	protein_coding	7.972798	0.038215
ENSMUSG00000108455.1	Gm44745	TEC	8.012673	0.030687
ENSMUSG00000045394.9	Epcam	protein_coding	8.437834	0.006454
ENSMUSG00000043155.4	Hpdl	protein_coding	8.884697	0.001345
ENSMUSG00000104852.1	Gm43201	TEC	9.002548	0.046872
ENSMUSG00000030446.17	Zfp273	protein_coding	9.237518	3.66E-05
ENSMUSG00000030309.16	Caprin2	protein_coding	9.337128	0.000541
ENSMUSG00000105509.1	C130013H08Rik	lncRNA	9.49451	0.046872
ENSMUSG00000074505.5	Fat3	protein_coding	9.497779	0.038215
ENSMUSG00000030731.13	Syt3	protein_coding	9.717584	0.021563
ENSMUSG00000020389.19	Cdkl3	protein_coding	9.784157	0.013888
ENSMUSG00000100291.6	2310069B03Rik	lncRNA	9.840291	0.014889
ENSMUSG00000044309.8	Apol7c	protein_coding	10.06245	0.0055
ENSMUSG00000005220.10	Corin	protein_coding	10.28782	0.006404
ENSMUSG00000034394.14	Lif	protein_coding	10.34294	0.001206
ENSMUSG00000084128.10	Esrp2	protein_coding	10.84798	7.09E-05
ENSMUSG00000038042.10	Ptpdc1	protein_coding	23.91619	1.09E-06
ENSMUSG00000045071.14	E130308A19Rik	protein_coding	24.00149	1.03E-06

Table SC 7: p-values determined by for Wilcoxon statistical test to determine the statistical significance of transcriptomic changes in each cluster of the heatmap of 354 common DEGs. In this instance, Un=mock infected/'uninfected', In=in vivo infected.

Cluster	**Comparison**	**In ≥3N**	**Un ≥3N**	**In 1-2N**
1	Un ≥3N	3.3E-08	-	-
1	In 1-2N	0.006862	0.000315	-
1	Un 1-2N	0.00742	0.00128	0.778021
2	Un ≥3N	3.42E-14	-	-
2	In 1-2N	0.595236	1.29E-14	-
2	Un 1-2N	0.289855	1.91E-14	0.460114
3	Un ≥3N	0.000236	-	-
3	In 1-2N	0.000316	1.33E-07	-
3	Un 1-2N	0.020564	2.24E-05	0.946212
4	Un ≥3N	0.73446	-	-
4	In 1-2N	0.73446	0.601895	-
4	Un 1-2N	0.580736	0.601895	0.580736
5	Un ≥3N	0.898329	-	-
5	In 1-2N	0.612693	0.612693	-
5	Un 1-2N	0.612693	0.612693	0.898329

Table SC 8: List of genes in each cluster for unbiased clustering analysis for in vivo dataset

Gene ID	Cluster
Mnt	1
Corin	1
Tbl2	1
Fzd3	1
Mid1ip1	1
Fgfrl1	1
Chp1	1
Tns4	1
Adora2a	1
Cdkl3	1
Tnip1	1
Lpcat1	1
Sema5a	1
Rrm2b	1
Spast	1
Dtwd2	1
Dctn4	1
Hmgxb3	1
Ms4a1	1
Rin1	1
D3Ertd751e	1
Lrsam1	1

Dclk1	1
Caprin2	1
Zfp273	1
Syt3	1
Calml4	1
Bsn	1
Ccdc88a	1
Lif	1
Lars2	1
Gnptab	1
P2ry12	1
March1	1
Bicral	1
Ptpdc1	1
Txnip	1
Ubn1	1
Suco	1
Phc1	1
Rap1gap	1
Zc3h6	1
Tmem186	1
Hpdl	1
Rnf227	1
Apol7c	1
E130308A19Rik	1
Tubb2b	1
Epcam	1
Gprin3	1
Bst2	1
Fancb	1
Lhfp	1
Zscan22	1
Sugct	1
Ttc26	1
Capn11	1
Gm5113	1
Msi2	1
Cebpd	1
Trim6	1
Fat3	1
Heg1	1
Cenpw	1
Gm23935	1
Esrp2	1
Vgll3	1
Neat1	1
Gm3604	1
Gm26917	1
2310069B03Rik	1
Gm43201	1
C130013H08Rik	1
Gm43088	1
Gm44745	1
AC119228.1	1

Mx1	2
Acvrl1	2
Apoe	2
Rnf215	2
Asf1b	2
Ddx39	2
Epha2	2
Tmco6	2
Sash1	2
Xk	2
Mtrex	2
H2-M3	2
Foxred2	2
Cmah	2
Traf4	2
Rrp7a	2
Erbb3	2
Alox15	2
Ccl6	2
Chtf18	2
Mydgf	2
Kitl	2
Ahi1	2
Mtfr2	2
Usp15	2
Pfkl	2
Castor1	2
Prr11	2
Recql5	2
Spns3	2
Susd3	2
Dnajc9	2
Dok2	2
Tbc1d31	2
Nptxr	2
Rogdi	2
Ercc4	2
Ccdc14	2
Kcnk5	2
Ip6k3	2
Nudt12	2
Cdc23	2
Dclre1a	2
Pfkfb1	2
Aatk	2
Prim1	2
Katnal2	2
Nrp1	2
Prkar1b	2
Phf19	2
Nusap1	2
Tnfrsf8	2
Lrp8	2
Smpdl3b	2

Ociad2	2
Gsdme	2
Atf7ip	2
Cd22	2
Kif22	2
Hsd17b14	2
Atp11a	2
F10	2
Bbs2	2
Snx33	2
Lss	2
Szt2	2
Fntb	2
Tspoap1	2
Nek9	2
Pkd2	2
Inpp5j	2
Cd300ld	2
Itga2b	2
Acot11	2
Fam214a	2
Rubcnl	2
1110059E24Rik	2
Nfkbiz	2
Card11	2
Zfp280c	2
Stag3	2
H2-DMa	2
Ptger2	2
Ankrd9	2
Tmem156	2
Ccdc138	2
Spag4	2
Bcl9	2
Dennd2a	2
Cul7	2
Tctn1	2
Lpar1	2
Vill	2
Bpgm	2
Zfp653	2
Adk	2
Exosc2	2
Nphp4	2
Heca	2
Gpr176	2
Rgl3	2
Inpp5f	2
Ammecr1	2
Trem1	2
Slc26a9	2
Wdr74	2
Hexim2	2
Acot6	2

Slc36a4	2
9930012K11Rik	2
Shld1	2
Gm9796	2
Med26	2
Pkd1l1	2
Tssk6	2
Ldlrad3	2
Mcat	2
Ccdc69	2
Arl4c	2
Eif5a2	2
Ptges	2
Map10	2
Zfp169	2
Bbs12	2
Rgs14	2
Gpr141	2
Zfp472	2
Adnp2	2
Tmem74	2
Cadps	2
Tmem62	2
Rab39	2
AI504432	2
Tyw1	2
Chst3	2
Tmod3	2
Osm	2
Serpinb12	2
Flot2	2
Glrp1	2
Arf2	2
Alms1	2
Zfp772	2
Apol9b	2
Lyz1	2
Zfp975	2
Capza1	2
6720489N17Rik	2
4930522L14Rik	2
Efcab7	2
Sirpb1c	2
Gm10762	2
Gm14295	2
D130040H23Rik	2
3110001I22Rik	2
Ftl2-ps	2
Gm16153	2
AI427809	2
Gm15708	2
Med20	2
Zfp994	2
Zfp850	2

Gm16712	2
Gm26772	2
2700038G22Rik	2
Gm26762	2
4933404O12Rik	2
2700099C18Rik	2
Gm38345	2
Gm38319	2
Gm44483	2
9330162G02Rik	2
Brd3os	2
Gm36445	2
Gm45752	2
Gm47813	2
Gm49703	2
Gm3325	2
AC132148.1	2
AC154328.1	2
Ccdc159	3
Zdhhc24	3
Cav1	3
Esr1	3
Ppp3cc	3
Serinc2	3
Prkn	3
Ldlrad4	3
Lrrc45	3
Il1rl1	3
Usp20	3
Pacsin3	3
Pde4b	3
Fbxo44	3
Klf3	3
Ephb6	3
Sbk2	3
Zfp108	3
Thsd1	3
Il34	3
Car7	3
Amigo3	3
Cdc14a	3
Zfp418	3
Ncaph	3
Zfp365	3
Ttc39b	3
Dtx3	3
Prkd2	3
Amot	3
Zfp239	3
AA986860	3
Crppa	3
2510009E07Rik	3
2410002F23Rik	3
Jaml	3

Fam161a	3
Suox	3
Plpp7	3
Rtl6	3
BC043934	3
Xlr3a	3
Zfp420	3
Akap17b	3
Zfp937	3
Tubb3	3
Mocs1	3
Fam172a	3
Mmp27	3
Rbm44	3
Treml2	3
Armcx5	3
Nxpe3	3
E130307A14Rik	3
Gm20939	3
Zfp799	3
Gm16675	3
C920006O11Rik	3
Gm38115	3
Gm43696	3
AC115752.1	3
AC132253.6	3
Ndc80	4
Col11a2	4
Prelid3a	4
Gfra4	4
Tmem231	4
Garnl3	4
Sgms1	4
Cdca2	4
Mmp12	4
Mok	4
H2-Q6	4
Ugt1a7c	4
9630010A21Rik	4
Gm43011	4
Ccnj	5
Tmem141	5
Cst3	5
Trim24	5
Dcbld2	5
Sh2d4a	5
mt-Rnr1	5
mt-Rnr2	5
mt-Nd1	5
mt-Nd2	5
mt-Co1	5
mt-Nd4	5
mt-Nd5	5
mt-Nd6	5

mt-Cytb	5
Mpzl3	5
Gm13340	5
Xist	5
Gm20594	5
Gm28439	5
Gm29216	5
Gm37123	5

Table SC 9: Top 5 canonical pathways identified by IPA analysis for unbiased clustering analysis of in vivo dataset

Cluster	Ingenuity Canonical Pathways	-log(p-value)	Molecules
1	D-myo-inositol (1,4,5)-trisphosphate Degradation	2.36E+00	INPP5F,INPP5J
	1D-myo-inositol Hexakisphosphate Biosynthesis II (Mammalian)	2.31E+00	INPP5F,INPP5J
	D-myo-inositol (1,3,4)-trisphosphate Biosynthesis	2.31E+00	INPP5F,INPP5J
	Adenine and Adenosine Salvage VI	2.21E+00	ADK
	Lanosterol Biosynthesis	2.21E+00	LSS
2	D-myo-inositol (1,4,5)-trisphosphate Degradation	2.36E+00	INPP5F,INPP5J
	1D-myo-inositol Hexakisphosphate Biosynthesis II (Mammalian)	2.31E+00	INPP5F,INPP5J
	D-myo-inositol (1,3,4)-trisphosphate Biosynthesis	2.31E+00	INPP5F,INPP5J
	Adenine and Adenosine Salvage VI	2.21E+00	ADK
	Lanosterol Biosynthesis	2.21E+00	LSS
3	Sulfite Oxidation IV	2.67E+00	SUOX
	Role Of Chondrocytes In Rheumatoid Arthritis Signalling Pathway	2.48E+00	IL1RL1,MMP27,PPP3CC
	Gap Junction Signalling	2.07E+00	CAV1,PPP3CC,TUBB3
	Axonal Guidance Signalling	1.65E+00	EPHB6,MMP27,PPP3CC,TUBB3
	Role Of Osteoclasts In Rheumatoid Arthritis Signalling Pathway	1.56E+00	IL1RL1,MMP27,PPP3CC
4	Tumour Microenvironment Pathway	2.44E+00	HLA-A,MMP12
	Sphingomyelin Metabolism	2.39E+00	SGMS1
	Natural Killer Cell Signalling	2.36E+00	COL11A2,HLA-A
	Role Of Osteoclasts In Rheumatoid Arthritis Signalling Pathway	1.99E+00	COL11A2,MMP12
	Pulmonary Fibrosis Idiopathic Signalling Pathway	1.94E+00	COL11A2,MMP12

5	Oxidative Phosphorylation	9.95E+00	MT-CO1,MT-CYB,MT-ND1,MT-ND2,MT-ND4,MT-ND5
	Granzyme A Signalling	8.77E+00	MT-ND1,MT-ND2,MT-ND4,MT-ND5,MT-ND6
	Mitochondrial Dysfunction	8.64E+00	MT-CO1,MT-CYB,MT-ND1,MT-ND2,MT-ND4,MT-ND5,MT-ND6
	Sirtuin Signalling Pathway	7.42E+00	MT-CYB,MT-ND1,MT-ND2,MT-ND4,MT-ND5,MT-ND6
	Estrogen Receptor Signalling	6.56E+00	MT-CYB,MT-ND1,MT-ND2,MT-ND4,MT-ND5,MT-ND6

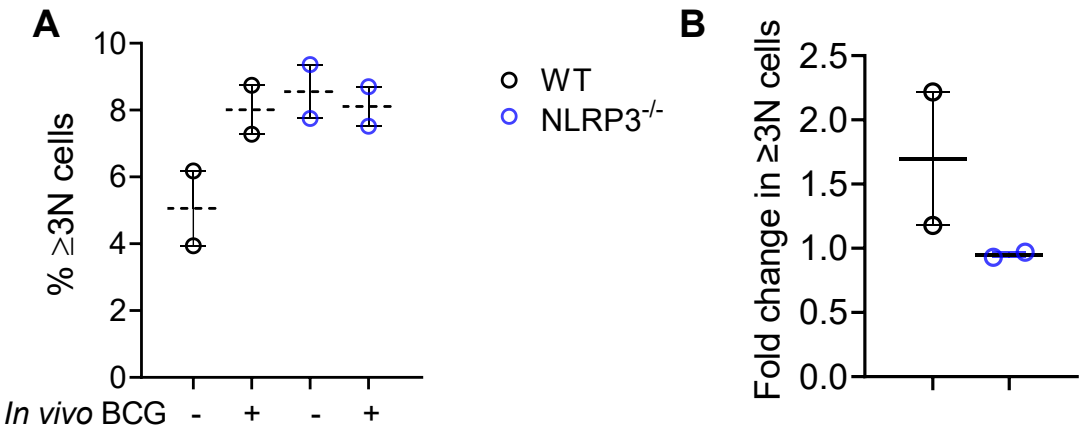

Figure SC 3: NLRP3$^{-/-}$ OCLs have reduced osteoclastogenesis of ≥3N cells during in vivo BCG infection

(A) Scatter plot depicting compiled percentages of ≥3N cells from uninfected WT and NLRP3$^{-/-}$mice comparing mock infected and in vivo BCG infected ≥3N OCLs (B) Fold change in ≥3N OCLs between mock infected and in vivo infected WT and NLRP3$^{-/-}$mice.